Electrostatically Assisted Atomization of a Liquid Jet in the Rayleigh Regime

by

Bilal Bharadia

A thesis submitted in partial fulfillment of the requirements for the degree of

Master of Science

in

Chemical Engineering

Department of Chemical and Materials Engineering
University of Alberta

Abstract

The increased demand for metal powders in the additive manufacturing industry requires reliable, economical and efficient methods for producing metal powders with consistent mechanical, chemical and physical properties. Conventional techniques such as gas and water atomization are commonly used to produce metal powders. However, these techniques have many limitations such particle agglomeration, low particle sphericity, large size distributions, high porosities, and the high cost of inert gas required for atomization. This thesis is thus focussed on designing and testing an electrostatically assisted atomization technique, to overcome these limitations. The atomization method is built on uniform liquid jet breakup using mechanical disturbances, and an electrostatic field to stress the jet into a smaller diameter before breakup.

Several experiments were conducted in this study, using water, ethylene glycol and Tin, with orifice sizes ranging between 0.07 – 2 mm. Using the data collected from these experiments, first the liquid jet formation was tested to ensure that the jet is operating in the laminar Rayleigh regime. Following this, a correlation between the Ohnesorge number and the Reynolds number was generated, allowing the operation velocity to be determined as a function of the thermophysical properties of the liquid and the orifice diameter. The effect of the applied vibration was analyzed next, and it was found that monodispersed droplets were produced with the addition of a vibration of optimal frequency. Drawing from the first principles of liquid jet break up in the Rayleigh regime, and depending on the liquid flow rate, a formulation has been established correlating the droplet size to the jet velocity and required mechanical vibration frequency. During each experiment, three different voltages were applied to create an electric field around the jet. It was found that increasing the voltage applied led to a decrease in the droplet size. However, this effect was not very significant. Therefore, to better understand the effect of the electric field (i.e.,

applied voltage) on reducing the jet diameter, a Bernoulli – Electrostatic model has been created, based on the Bernoulli energy balance, the Young – Laplace surface energy, and the electrostatic pressure balance in electrohydrodynamic atomization. This model shows that increasing the applied voltage (i.e., the electric field strength) leads to a reduction in the jet diameter, and the electric field strength required to constrict the jet diameter increases as the orifice diameter decreases. The work done in this study was also used to present a design of a functioning electrostatically assisted atomization unit. While the application of an applied vibration will successfully provide monodispersed droplets, the effect of the applied electric field will be insignificant in reducing the droplet sizes when using smaller orifices (< 100 μm), even if a high voltage of 100 kV is used.

Therefore, a better approach to produce monodispersed metal powders would be to operate with smaller orifice sizes (e.g., 0.025 – 0.05 mm), and apply the optimal vibration frequencies using the correlation generated and presented in this study. With this, droplets of uniform size with low porosities can be created. Furthermore, it would not require a constant supply of inert gas (i.e., low operation cost), and neither will it require expensive pumps or a large atomization unit (i.e., low capital costs).

Key words: electrostatic metal atomisation, additive manufacturing, metal powders, jet disintegration, Rayleigh regime

Acknowledgements

I would like to express my deepest and most heartfelt gratitude to my supervisor, Dr. Hani Henein, for providing me with the opportunity to work in his most wonderful group. Thank you so much Dr. Henein, for all the guidance, patience, encouragement, and advice through the course of this thesis. Thank you so much for believing in me and having faith in me.

I would also like to thank the AMPL group, and especially Dr. Abdoul Aziz Bogno and Quentin for your continual support and friendship. Thank you for always being there for the discussions and coffee breaks and for always trying to help me solve any issues I may be having.

Thank you to NSERC and HI-AM for the opportunity and funding to work on this project. I would also like to thank the several other professors at the University of Alberta, and the technicians at the CME instrumentation shop for being open to discussions on how to best solve the analytical and experimental problems.

I would also like to thank my friends at the University of Alberta, who were always there for me. Thank you for all the crazy, fun and exciting times, Milla, Monis, Anton and Mwenya.

Finally, I would like to thank my parents and my sister for everything they have done for me through the course of this study and everything before that. This thesis would never have been completed without your support, encouragement, belief, and unconditional love. Thank you so much for everything. I will always be indebted to you.

Table of Contents

List of Figures

List of Tables

Nomenclature

Abbreviations:

AM:	Additive manufacturing
AMPL:	Advanced Materials and Processing Laboratory
EHDA:	Electrohydrodynamic atomization
UDS:	Uniform drop spray process

Latin:

a:	Acceleration
A:	Area along which the liquid flows
A.R:	Aspect ratio
c_1:	Constant of integration
C_D:	Discharge coefficient
d_0:	Orifice diameter
D10:	Average droplet diameter
D32:	Sauter mean diameter
d_d:	Droplet diameter
d_i:	Crucible inner diameter
DV50:	Median droplet diameter
E:	Electrical field
F:	Dimensionless frequency
f_a:	Applied frequency
f_{res}:	Natural frequency of the disturbances on a jet
g:	Acceleration due to gravity
H:	Head of the liquid in the crucible
H_f:	Heat of fusion
I_1:	First expansion term of the Bessel function
I_2:	Second expansion term of the Bessel function
k:	Wavenumber
L:	Nozzle length
L_{BU}:	Length of jet breakup
m:	Mass of the body
P:	Pressure
p_j:	Pressure inside the jet
Q:	Volumetric flow rate
q_r:	Maximum electrical charge on a droplet
r_0:	Orifice radius

R_1, R_2:	Principle radii of curvatures 1, 2
r_d:	Droplet radius
r_j:	Jet radius
T_m:	Melting temperature
t_s:	Solidification time
V:	Applied voltage
v_0:	Jet velocity
v_c:	Critical velocity
x_{trans}:	Jet transition length to semi-turbulent flow

Greek:

α:	Angle of contraction
β:	Contraction ratio
γ:	Liquid surface tension
δ_{ij}:	Kronecker – delta function
ε:	Emissivity
ε_0:	Permittivity of free space
η_0:	Initial amplitude of disturbance
λ:	Wavelength
μ:	Liquid viscosity
ρ:	Liquid density
σ_{eij}:	Maxwell stress tensor
ω:	Rate of growth of disturbances

Subscript:

br:	Breakdown
crit:	Critical value
max:	maximum
n:	Direction in the normal direction
opt:	Optimal value
r:	Radial coordinate axis
t:	Direction in the tangential direction
z:	Axial coordinate axis

Chapter 1: Introduction

Atomization refers to the breakup of continuous liquid streams into smaller droplets or particles. This process of disintegration occurs due to the kinetic energy of the liquid itself, or by exposure to an external force such as a high velocity air or water stream.

Atomization technology producing metal powders has been growing steadily due to the increased need in applications such as catalysis, paints, explosives, welding and many more **[1]**. The past two decades have also seen the growth of another specialized field called additive manufacturing. This is a freeform manufacturing process whereby a three-dimensional object is made by stacking material layer upon layer (commonly known as 3D printing) **[2]**.

There are certain drawbacks when comparing additive manufacturing to traditional production methods (e.g., casting and forging), such as, high production costs, low production rates, and high machining costs. However, there are very significant advantages to using additive manufacturing as opposed to conventional methods. These include reduced time in prototyping, the ability to produce very complex structures, high product quality, and reduced waste of feedstock material **[2, 3]**. This has led to several companies embracing additive manufacturing technologies, with the worldwide revenues of additive manufacturing increasing from $3.07 billion in the year 2013, to over $20 billion dollars in 2020 [**2**]. Therefore, this study is primarily focused on the additive manufacturing industry, with an aim to provide cheaper and more efficient feedstock for the printing processes.

The different additive manufacturing processes can be characterized based on the raw materials they use, as shown by William Frazier **[4]**. These include the wire feed, powder feed, and powder bed processes. The wire feed system uses a continuously fed wire as the feedstock and an energy source such as a laser beam or a plasma arc to melt the wire and deposit it into a 3D object. The wire feed systems are used for producing builds of large sizes (i.e., > 1 m^3). However, the final products require extensive machining and the ability to produce very complex products is reduced in this system. The powder feed and powder bed systems use metal powders of the desired composition. A laser, electron beam or plasma arc is then used to melt and fuse the powders into a 3D object. Extremely complex products such as lattices with dimensions of only a few millimeters can be created using these systems.

In order to ensure efficient and repeatable additive manufacturing processes the metal powders must have distinct physical and chemical characteristics. These include, but are not limited to: uniform particle morphology, low porosity and agglomeration, and a narrow size distribution with low occurrence of satellites. Currently there are several commonly used atomization processes tailored to produce metal powders for additive manufacturing. These include gas atomization, water atomization, rotary electrode atomization and plasma atomization **[5]**.

Gas water, and plasma atomization are considered as two fluid processes, rotary electrode atomization is considered as a single fluid approach **[6]**. During water and gas atomization the metal is first melted into a continuous stream and then struck with a high velocity jet of water or gas to pulverize it into a cloud of fine particles. In plasma atomization a pre alloyed wire is fed into a plasma arc between two electrodes. The very high energy of the arc would melt the wire. A high velocity gas steam is then used to spray the droplets. In the rotary electrode atomization the feedstock is in the form of a pre-alloyed electrode bar that is rotated at very high speeds and melted by a plasma arc. The centrifugal forces due to rotation of the electrode result in the droplets peeling off the surface of the electrode. These droplets are allowed to solidify and are collected as metal powders.

Water and gas atomization processes have the capability to produce very fine powders (< 100 μm) at a very high production rate of several kilograms per minute. However, the resulting powders have a very large size distribution with a large number of satellite particles. The powders may also be irregular shape with high porosity. There is also the risk of contamination as the material is melted in a ceramic, graphite, or metal crucible, and reactive materials at high temperatures can interact with the crucible walls resulting in powders of lower purity. Since plasma and centrifugal atomization both operate using a pre alloyed feedstock that does not need to come in contact with a crucible of any sort, the risks of contamination are much lower. These processes offer several advantages as compared to gas and water atomization, such as, a high degree of particles sphericity, low porosity, excellent flowability and low agglomeration of particles. However, they do have their drawbacks as they do not offer a high yield of fine powders (< 100 μm) and require very high operating and production costs **[5]**.

Since the 1970's several advances have been made in single fluid atomization. The two of greatest interest with respect to this study are the electrohydrodynamic atomization (EHDA), and capillary atomization. EHDA uses electric field energy (electrical stresses) to force the liquid jet into a very thin diameter that eventually disintegrates into a spray of droplets. It has been widely tested using different liquids under various conditions and has a variety of applications in the pharmaceutical and agricultural industry due to its ability to create particles as small as 10 nm in diameter **[7]**. However, the atomization process operates with very high energy requirements and under low flow rates of a few microliters per second, making it inefficient for metal powder production **[8]**.

Capillary atomization can be divided into either a continuous jet breakup method, or a drop on demand method. The continuous jet breakup method patented by Bienvenu and then again by Chun with a few modifications, has produced monodispersed metallic droplets **[9, 10]**. In this technology a laminar liquid jet of the melt is vibrated with an appropriate frequency such that it would break up into droplets of uniform size and morphology. In order to avoid the droplets from agglomerating and sticking together, they can also be charged with a high voltage forcing them to repel each other as they fall and solidify. The main drawback with the continuous jet breakup method is in trying to produce powders of smaller sizes, as very small orifices would be required, and as such the overhead pressure would have to be very high. The drop on demand method is similar to the continuous jet break up method, as vibrations of a given frequency and amplitude are transferred to the molten metal causing a drop of a specific size to be produced one at a time from the nozzle orifice **[11]**. While quite simple and precise, this is a very limited process as the production rate is very low, producing one drop per pulse per orifice.

It goes to show, that while several atomization technologies exist capable of producing metal powders, no single production process meets all the requirements. In order to overcome these problems, a new approach has been described, designed, and tested at the Advanced Materials and Processing Laboratory (AMPL) at the University of Alberta. The mentioned approach combines the knowledge of continuous jet breakup (similar to the works of Bienvenu and Chun), and electrohydrodynamic atomization. It is a single fluid atomization process aimed at producing powders of uniform size at respectable production rates of several kilograms per hour. The first objective of this study is therefore to design and develop the apparatus which overcomes

the disadvantages of other atomization techniques. The next objective is to develop an understanding of the effects of the different operating and experimental variables on powder characteristics. The variables include the applied frequency, the orifice diameter, the applied voltage, the applied overhead pressure, and the liquid temperature. The powder characteristics evaluated are the particle size and size distribution.

The published literature pertaining to this work will be reviewed in Chapter 2. In Chapter 3 different mathematical models will be formulated in order to best understand and predict jet breakup and droplet production. The experimental setup along with the atomization process will be reviewed in Chapter 4. The results obtained under different conditions will be analyzed and discussed in detail in Chapter 5. Finally, the study will be concluded and future work for this technique will be proposed in Chapter 6.

Chapter 2 Literature Review

As this project is based on two different physics phenomena (i.e., continuous jet disintegration and electro-spraying), this chapter will be divided into two sections. Section 2.1 will focus on continuous liquid jet breakup (i.e., factors governing breakup, stability curves, regime diagrams, droplet production and general trends). It should be noted that this is a very vast area of research with thousands of studies done and, therefore, the emphasis will primarily be kept on low velocity laminar jets that break up due to capillary instabilities. Other forms of jet breakup will be mentioned and briefly reviewed but for the most part these mechanisms are beyond the scope of this work. It should also be noted that while this literature review will cover general trends and several empirical equations, it will not cover the mathematical derivation of any of the equations for jet breakup. This will be addressed in the chapter on Mathematical Models.

Section 2.2 will address charged liquid jets and electrohydrodynamic atomization (EHDA). All major discoveries from fundamental theories of maximum charge to modern applications of electro-spraying will be addressed. It should be noted that most of the attention will be placed on the theoretical aspect of electro-spraying to better understand the science of EHDA, particularly in the cone-jet mode. Electrical discharges and other forms of liquid atomisation that incorporate electrohydrodynamics will also be briefly discussed.

2.1 Continuous Liquid Jet Breakup

The review on continuous liquid jet breakup is very extensive. Several theories have been modified or completely altered since they were first introduced. Therefore, this review will be divided into 4 subsections in order to keep it brief while covering all the major areas of interest. The Section 2.1.1 will discuss the classical literature on jet breakup. The several modifications and advancements in jet breakup theories will be discussed in Section 2.1.2. In Section 2.1.3 the different ways of characterizing jet break up mechanisms will be addressed. This in turn will be followed with the recent understandings of jet behavior mechanisms as well as externally manipulated jets and droplet production.

2.1.1 Classical Literature and Fundamentals of Liquid Jet Breakup

The earliest recorded analysis on jet breakup can be traced to the 15th century. Leonardo DaVinci correctly hypothesised that a liquid ligament will break away from a tap, provided that gravity overcomes the cohesive surface tension forces **[12]**. However, he then incorrectly assumed that the same principle would govern the separation of a drop from the ligament after a long enough neck has formed. It was not until the works of Young and Laplace that any significant progress was made on this topic **[12]**. Following their work on surface energy (surface tension), Young and Laplace determined that a low velocity liquid column is naturally driven to an unstable state having a smaller surface area as it flows out from an orifice. The liquid's surface energy is responsible for forcing the jet to break into stable droplets of a larger surface to volume ratio. Therefore, following the original hypothesis of DaVinci, a jet is formed when the inertial force overcomes the surface tension of the liquid. Then according to the works of Young and Laplace, the jet would breakup, paradoxically due to the surface tension, indicating that a larger surface tension leads to a faster rate of disintegration[1].

The first experimental breakthrough in the field of jet disintegration was that by Savart, who found that perturbations (wave like disturbances) would grow along the surface of a jet leading to its breakup into droplets **[13]**. In his work Savart made two distinctive observations. Firstly, he noticed that a smaller satellite drop was almost always formed between two main large drops. This observation is attributed to the "non-linear effects" in jet break up. These effects can be due to a variety of reasons which have troubled researchers to fully understanding jet breakup from an analytical perspective since Savart's discovery in 1833. More on non-linear effects will be covered later in this chapter and the next. Savart also observed that jet breakup always occurred spontaneously and was independent of the external forces or the direction in which it was projected. To this he concluded that jet break up must be an inherent feature of jet dynamics, indicating that a simple static approach can not be used to solve jet break up.

Following these observations, the first analytical work on jet breakup can be attributed to Plateau, who noted that perturbations on a liquid column would grow leading to droplet formation.

[1] It is important to note that throughout this study, unless otherwise specified, surface tension refers to the cohesive liquid property acting unto itself with respect to its cohesion with a surrounding gaseous atmosphere (i.e., it is the gas – liquid surface tension).

Jet breakup occurs when the wavelength of these perturbations is greater than a critical wavelength ($\lambda > \lambda_{crit}$) **[14]**. Such perturbations are described as "unstable disturbances" and have critical wavelengths between 6 and 7.2 times the radius of the office (r_0). Plateau later refined this to be equal to the circumference of the jet (i.e., $\lambda_{crit} = 2\pi r_0 = 6.28r_0$). Plateau also determined from Savart's work that the optimal wavelength (λ_{opt}) was measured as $8.76r_0$ which follows along nicely according to his prediction that only perturbations of wavelength greater than the critical would lead to jet breakup.

In the late 19th century Lord Rayleigh introduced his work on jet breakup. To this day it is hailed as one of the greatest analyses in understanding the breakup of smooth low velocity jets **[15]**. Rayleigh introduced the method of linear stability of jet breakup. This is the foundational cornerstone to several analytical approaches in determining jet behavior for well over the past 100 years. He acknowledged Plateau's work and showed that indeed breakup would only take place if the disturbance was unstable such that its wavelength was greater than the critical wavelength. Rayleigh then went on to show that amongst disturbances of all unstable wavelengths, the one with the fastest growth rate is selected and will be responsible for break up. This is classified as the optimum wavelength (λ_{opt}). Rayleigh found that for an inviscid jet $\lambda_{opt} = 9.01r_0$ (which is in good agreement with that measured by Savart), while the droplets produced should have a diameter (d_d) equal to 1.89 times the diameter of the orifice (d_0), i.e., $dd = 1.89d_0$. From this a dimensionless wavenumber (k) can be defined such that $k = 2\pi r_0/\lambda$. The wavenumber, therefore, obeys the inequality $0 < k < 1$, indicating that the wavelength of disturbances must be greater than the critical value (the jet circumference), but must also be finite in size. By applying the wavelength of the fastest growing disturbance, the optimal wavenumber can be easily calculated as $k = 0.697$. Rayleigh's work laid out the outline for liquid jet break up via capillary instabilities of the simplest from, i.e., inviscid low velocity jets in a quiescent medium. This linear stability approach is used to this day in several industrial applications such as inkjet printing and micro-fabrication, and is a major part of this project **[16, 17]**. The mathematical derivation of his linear stability approach will be presented in Chapter 2.

Weber extended Rayleigh's theory but included the non-linear effects by solving the Navier Stokes equation to incorporate the viscous forces and found the optimal wavelength for inviscid liquids to be $\lambda_{opt} = 8.89r_0$ while the optimal wavelength for viscous fluids to be $\lambda_{opt} =$

$8.89r_0(1 + 2^{0.5Z})^{0.5}$, where Z is a dimensionless number called the Ohnesorge number, presented in Equation 2.1 below **[18]**.

$$Z = \frac{Re}{\sqrt{We}} = \frac{Reynolds\ number}{\sqrt{Weber's number}} = \frac{\mu}{\sqrt{\gamma \rho d_0}} = Oh \qquad 2.1$$

Whereby μ, ρ and γ represent the dynamic viscosity, density, and surface tension of the liquid respectively. From this it is easy to infer that for an inviscid liquid, Weber's analysis agrees quite well with Rayleigh's. However, as the viscosity increases (i.e., Z increases) the optimal wavelength would also increase. Thus, for an extremely viscous liquid, the wavelength would increase indefinitely pushing the jet to extend longitudinally and break up much later. This occurs because viscous forces have a damping effect, and as such they slow the growth rate of disturbances along the jet, as was shown later on by Schweitzer **[19]**. It should be noted however, that for both viscous and non-viscous liquids, Weber found that the critical wavelength below which disturbances would not grow was the same as that determined by Plateau and Rayleigh ($\lambda_{crit} = 2\pi r_0$). Weber also tried to determine the effects of air friction on jet breakup and the transition from rotationally symmetric disturbances (breakup due to capillary instabilities) to wavelike sinusoidal disturbances (breakup due to other effects such as aerodynamics). Weber noticed that as the velocity of the jet is increased the disturbances change from the former to the latter mentioned above. The critical wavelength would also decrease, as the jet becomes more unstable due to the added effects of air friction. This allows shorter waves to grow that eventually lead to jet breakup. It is important to note that in his study, Weber attributes the transition of disturbances from one kind to the other entirely due to the effects of air friction and does not consider other effects such as turbulence, flow profile or nozzle geometry. A schematic of the different disturbances mentioned by Weber are shown in Figure 2.1, below **[20]**:

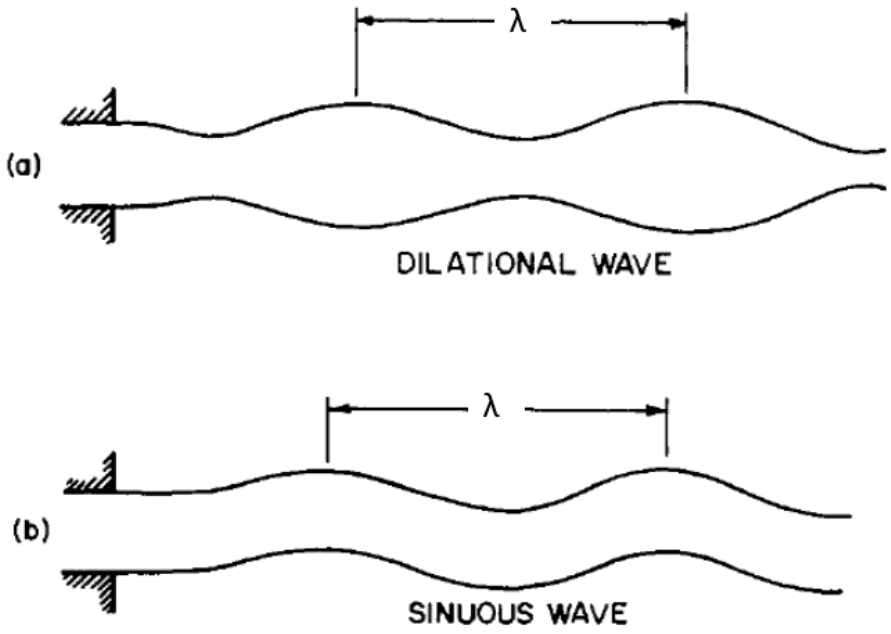

Figure 2.1. A representation of jets with a) rotationally symmetric disturbances, and b) sinusoidal disturbances ***[20]***

Jet breakup due to capillary instabilities (referred to as either "Rayleigh breakup", "varicose breakup" or "rotationally symmetric disturbances" throughout this study) were first proven experimentally by Tyler, and Haenlein **[21, 22]**. Tyler conducted experiments with water, mercury, and aniline. Focusing on just the Rayleigh breakup mode, they found that $\lambda_{opt} = 4.65r_0$. This translates to a droplet diameter $d_d = 1.91d_0$. These results are very consistent with both Rayleigh and Weber's predictions.

Haenlein organized a study to experimentally determine the process of jet disintegration ranging from their simplest form (Rayleigh breakup) to more complicated chaotic atomization breakup. He carried out experiments using water, gas oil, glycerin and castor oil with orifice diameters ranging from 0.1 – 2 mm, and jet velocities ranging from 3.1 – 73 m/s **[22]**. Haenlein, observed that initial disturbances of different wavelengths would occur simultaneously and overlap one another. Depending on the forces acting on the jet, the disturbance of the optimal wavelength would grow in amplitude, eventually leading to disintegration of the jet. When the jet was operated under low velocities the rotationally symmetric disturbances predicted by Rayleigh would be responsible for jet breakup. However, as the jet velocity was increased disturbances generated by

air friction (aerodynamic forces) bend the jet into a wave like sinusoidal shape, as predicted by Weber. These sinusoidal disturbances develop much faster than rotationally symmetric disturbances leading to jet breakup at a much earlier stage. In his study, Haenlein also observed that as the viscosity of the liquid was increased the Rayleigh droplet size prediction was less accurate, as Rayleigh's analysis does not account for liquid viscosity. However, Weber's prediction could be used to determine the droplet size to a much higher level of accuracy for viscous liquids **[22]**.

2.1.2 Modifications and Advancements in Jet Breakup Theories and Hypotheses

While the classical literature on jet breakup outlined by Rayleigh and built upon by Weber had given insight into the disintegration of a continuous liquid column, the complete understanding of the jet break up phenomena is far from complete. Thus, several developments have been made on this subject since then, ranging from different analytical approaches to development of empirical equations from dimensional analysis, to grouping of jet behavior according to quantitative and qualitative observations. This generally creates confusion and makes it difficult to fully understand the breakup processes due to the different approaches that in turn focus on very specific areas of jet break up. To overcome this Miesse outlined that the methods by which jet disintegration theories have been made can be grouped into 3 classes **[23]**. These include the method of small disturbances (the direct analytical approach used by Rayleigh and Weber outlined in Section 2.1.1). The method of plausible conjectures whereby mathematical solutions for jet breakup can be obtained by making reasonable assumptions of the governing processes and creating correlations with experimental data. The method of dimensionless analysis whereby jet disintegration is understood through the combination of the different physical variables in play. While this is a great way to understand the different improvements in jet breakup theories, it would require a very rigorous effort to organize all the previous studies and to scrutinize the work in great detail in order to determine the category they belong to, and not to mention that several studies use a combination of the mentioned approaches. Therefore, in this study the advancements in jet breakup will be divided into 3 categories: the aerodynamic effects and jet breakup length, the influence of turbulence and velocity profiles, and the effects related to nozzle geometry and internal flows.

2.1.2.1 Aerodynamic Effects and Jet Breakup Lengths

The aerodynamic effects and the initial approaches on the jet breakup length can be traced all the way back to the classical literature of Weber, who showed analytically that the breakup length of a jet (L_{BU}) would be directly proportional to the jet velocity (v_0), but inversely to the maximum rate of growth of the disturbances (ω) **[18]**:

$$L_{BU} \propto \frac{v_0}{\omega} \qquad 2.2$$

For a laminar Rayleigh jet, the disturbances grow very slowly along the jet, which would imply that an increase in velocity would lead to an increase in the breakup length. However, as air friction (aerodynamic effects) comes into play the disturbances would grow much more rapidly, leading to a decrease in the jet breakup length. Figure 2.2 below depicts how the breakup length would vary with velocity.

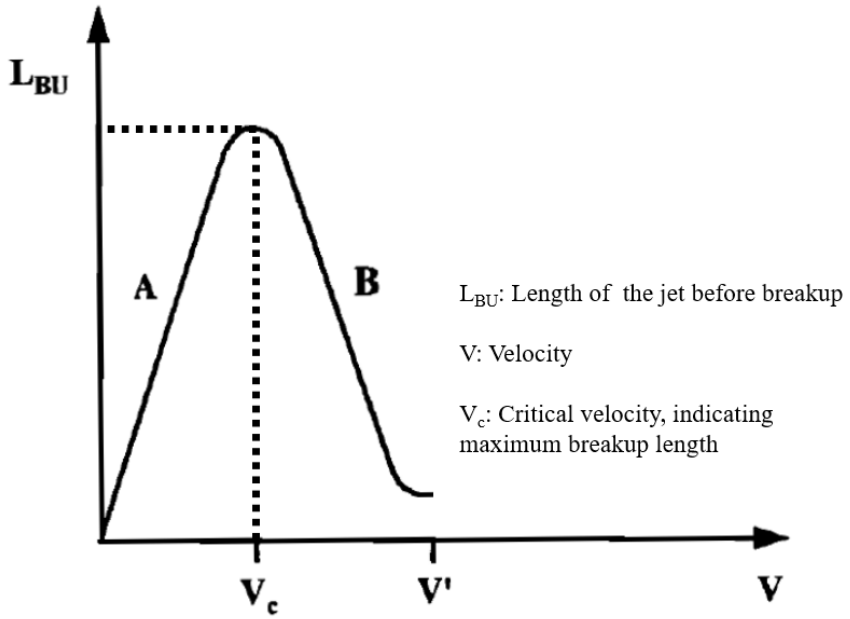

Figure 2.2. A representation of a curve depicting the jet length with respect to its velocity ***[24]***

For the region labeled 'A' on Figure 2.2, the growth of small disturbances would be responsible for jet breakup. From Weber's analytical work, it can be deduced that the length of breakup of the jet (L_{BU}) in region 'A' can be calculated as:

$$\frac{L_{BU}}{d_0} = \ln\left(\frac{r_0}{\eta_0}\right)\left(We^{0.5} + 3\frac{We}{Re}\right) \quad 2.3$$

$$Re = Reynolds\ number = \frac{\rho v_0 d_0}{\mu} \quad 2.4$$

$$We = Weber\ number = \frac{\rho v_0^2 d_0}{\gamma} \quad 2.5$$

Where, the terms ρ, γ and μ are the liquid density, surface tension and viscosity, and 'r_0' and 'η_0' represent the initial jet radius and the initial amplitude of the disturbance respectively. Weber found that for a jet undergoing Rayleigh breakup, the term $\ln(r_0/\eta_0)$ was a constant with a reported value of 12. Therefore, an increase in velocity would lead to a linear increase in the jet breakup length. However, as the aerodynamic forces increased (due to increased velocity) the growth rate of the disturbance would start increasing leading to a maximum as depicted in Figure 2.2, and beyond this point the length of the jet would start decreasing with an increase in velocity.

While Weber's theory allows the prediction of a maximum and the decrease in break up length (as shown in Figure 2.2), it was noted by several researchers that this prediction was very inaccurate. Several studies were organized to modify this theory to yield a better understanding on jet behavior. Fenn and Middlemann organized a study focused on determining the role of the ambient medium on destabilizing the jet **[25]**. They carried out experiments using nozzles with an orifice diameter 0.83 mm and aspect ratios of 52 – 480 (i.e., very long nozzles) in order to ensure the flow was fully developed. In their study silicone oils were used due to their wide range of viscosities and experiments were carried out with jet velocities reaching up to 70 m/s where aerodynamic effects could easily be observed. Fenn and Middlemann noted that the ambient air pressure (i.e., aerodynamic effects) in some cases had no significant influence on the jet stability and the location of the maximum in the breakup curve. It should also be noted that previously Grant and Middlemann had conducted a study with a similar experimental approach and had found that the average value of $\ln(r_0/\eta_0)$ was approximately 13.5. They also went on to suggest that in fact the term $\ln(r_0/\eta_0)$ was dependant on the viscosity of the liquid via the Ohnesorge number (Z) **[26]**:

$$\ln\left(\frac{r_0}{\eta_0}\right) = -2.66\ln(Z) + 7.68 \quad 2.6$$

Grant and Middlemann found that using this correlation along with Equation 2.3 gave a much better result in predicting the maximum point and the regression in the jet length for their experimental data.

Sterling and Sleicher analyzed Grant and Middlemann's modification and concluded that the primary mechanism responsible for the maximum in their breakup curve was due to the liquid flow profile rather than the aerodynamic effects **[27]**. This is because Grant and Middlemann conducted experiments using very long nozzles and as such their liquid jets were undergoing profile relaxation effects changing from fully developed at the exit to flatter profiles downstream. This would destabilize the jet and was the phenomena that Grant and Middlemann unknowingly solved for. Sterling and Sleicher organized a study conducting experiments with much smaller nozzle lengths in order to study the cases whereby aerodynamic effects are the leading cause of the decrease in the breakup length. From this they determined that Weber's theory overestimates the effects of aerodynamics and as such they introduced a correction factor which would give better predictions but with significant errors in many cases nonetheless.

It should be noted that all the mentioned approaches assume the term $\ln(r_0/\eta_0)$ is a constant and independent of jet velocity. Phinney therefore introduced an approach by suggesting that a better way to correlate data was by considering that the initial disturbance (η_0) was a variable i.e., a function of the jet speed **[28]**. Using the experimental data by Fenn and Middlemann, Grant and Middlemann, and Phinney and Humphries a new correlation was created that related the initial disturbance to the Reynolds number **[25, 26, 29]**. Phinney found that at low velocities the disturbances are constant as expected from Rayleigh and Weber's theory as the jet breaks up due to axisymmetric disturbances. However, there exists a critical Reynolds number at which the initial disturbance amplitude increases. At this point the jet stability curve would reach its critical point. This goes to show that as the jet velocity increases it begins to transition to a turbulent flow at the critical Reynolds number and hence the initial disturbance would increase, showing that in fact the maximum on the stability curve is due to a combination of factors, two of which have been highlighted by Phinney, i.e., the aerodynamic effects and jet turbulence. A similar conclusion was reached by Leroux et. al., who compared the models discussed above **[24]**. They found that both Weber's, and Sterling and Sleicher's theories can be used to accurately predict the breakup length in region 'A' of Figure 2.2 (i.e., during varicose breakup). However, none of these models gave a

reasonable correlation of the maximum in breakup length or any data beyond this point, indicating that aerodynamic effects may not be exclusively responsible for jet stability, and several other effects such as jet turbulence, internal instabilities within the jet, velocity profile relaxation, and nozzle geometry also play very significant if not more important roles.

2.1.2.2 Turbulence and Velocity Profiles

When the jet exits the nozzle, it could have either a laminar, turbulent or semi turbulent flow profile. A schematic of the different profiles is shown below in Figure 2.3, obtained from the works of Giffen and Muraszew **[30]**:

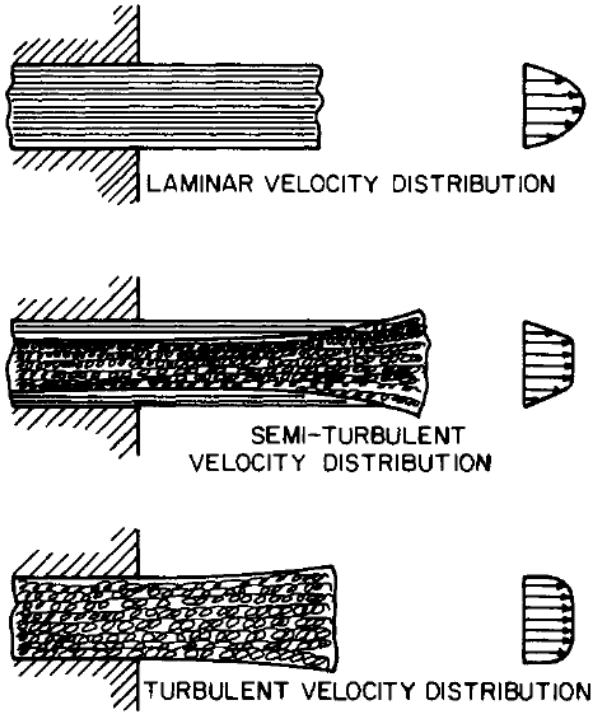

*Figure 2.3. The different velocity distributions in jets suggested by Giffen and Muraszew **[30]***

Laminar jets are dictated by velocity vectors that have a direction parallel to the flow, and to the nozzle axis, and a maximum velocity is recorded at the center line due to the parabolic velocity profile when the flow is fully developed. A turbulent jet on the other hand has a much flatter velocity profile with velocity vectors in both the axial and radial directions. Therefore, in a turbulent jet mixing between layers of velocity is very common which in turn promotes the ruffled

jet appearance, as has been recorded by Sallam et. al., and Wu et. al. in their work on turbulent jet breakup **[31, 32]**. The transition from laminar to turbulent is not sudden and encompasses a wide range of Reynolds numbers. As such there exists an intermediate stage called the semi turbulent flow. In a semi turbulent flow, the core off the jet is turbulent, but is wrapped in a laminar envelope and therefore appears very smooth. The laminar envelope slows down the turbulent particles from the core in reaching the jet surface. However, as the jet flows downstream momentum is redistributed allowing the jet to achieve a flatter velocity profile as the thickness of the laminar envelope is reduced until which the jet becomes completely turbulent.

A laminar jet will breakup into droplets because of growing instabilities due to the surface tension forces. The velocity difference between the laminar jet and the ambient is very small and as such the aerodynamic effects are insignificant. Thus, the jet can stretch for a long distance before eventually breaking up due to capillary instabilities. Sallam et al. showed that a turbulent jet will breakup due to the initial turbulent related disturbances much earlier even with negligible aerodynamic effects **[31]**. Mansour and Chigier studied laminar and turbulent jets under very low ambient pressures in order to mitigate the aerodynamic effects, and found that turbulent jets have a different appearance as compared to laminar jets (i.e., turbulent jets have a much more ruffled appearance as opposed to the smooth laminar jets), but are nonetheless stable and will not disintegrate immediately. However, they also observed that the breakup behavior, as well as droplet formation pattern was different for turbulent jets **[33]**. Sterling and Sleicher, and Lefebvre explain that the decrease in the breakup length after reaching a maximum in the jet length (as shown in Figure 2.2), is therefore when the jet is transitioning from laminar to turbulent and is in the semi-turbulent region **[27, 20]**. As the kinetic energy is redistributed amongst the transverse layers in a semi-turbulent jet, the flow undergoes a change to a completely flat profile. The velocity profile relaxation has effects similar to aerodynamic effects as seen from the work of Fenn and Middlemann, and as such the jet length reduces rapidly **[25]**. Furthermore, Rupe found that due to the profile relaxation effects the jet that emerges as fully turbulent from the nozzle is more stable than the semi-turbulent jet undergoing transition **[34]**. The reasoning behind this is still unclear as they both have a flat velocity profile. However, it is believed that the redistribution of energy during relaxation tends to create further disturbances and causes a sudden violent breakup as can be shown in Figures 2.4.

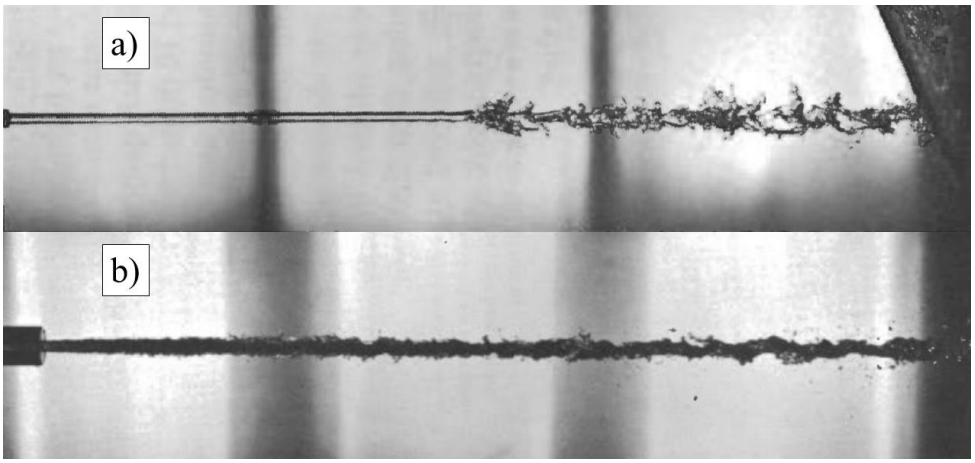

Figure 2.4. Images of jets with a) semi-turbulent and b) turbulent flow profiles, from Rupe ***[34]***

2.1.2.3 Effects of Nozzle Geometry and Internal Flow on Jet Breakup

After analyzing the aerodynamic effects, jet turbulence, and velocity profile relaxation effects it is clear that jet breakup is indeed a combination of these factors. Furthermore, while these effects can enhance breakup, they are not entirely independent. The nozzle geometry and internal flow control the level of turbulence at the nozzle, the shape of the velocity profile and as such the extent of the aerodynamic effects. Leroux et. al., and Malot and Dumouchel took this into account and tried to modify Weber's theory to account for all the mentioned factors and not just aerodynamic effects **[24, 35]**. However, their empirical laws do not apply beyond their particular experimental set up and the cases tested. This is because nozzles come in all shapes and sizes and as such their effects are difficult to understand and perfectly quantify. A simpler approach would be to determine the specific features all nozzles share and as such determine the effects of these features individually on the jet behavior. This methodology has been summarized in detail by McCarthy and Malloy, and by Birouk and Lekic who outline that there are 5 nozzle geometry parameters that have an impact on jet stability **[36, 37]**. These include the contraction ratio (β), the aspect ratio (A.R), the angle of contraction (α), the surface quality (roughness), and streamlining. Figure 2.5 below is a depiction of a typical nozzle showing the different nozzle features.

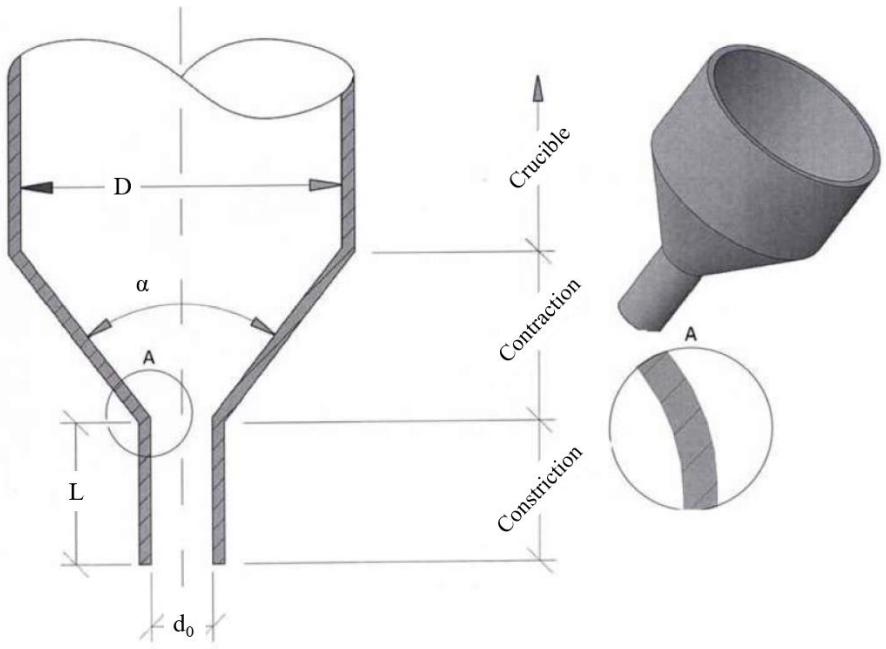

*Figure 2.5. The general nozzle features and nomenclature as described by Birouk and Lekic **[37]***

Contraction Ratio (β):

This is the ratio of the crucible diameter (D) to the nozzle orifice diameter (d_0), i.e., $\beta = D/d_0$. Birouk and Lekic point out that the contraction ratio does not affect the general trend of the jet breakup length, but rather impacts the breakup length itself. This is because as the nozzle diameter decreases the length of breakup increases with respect to the Reynolds number for a fixed crucible diameter **[37]**.

Aspect Ratio (A.R):

This is the ratio of the length of the nozzle to the diameter of the orifice, i.e., $A.R = L/d_0$. It has been noted that the aspect ratio as well does not have much of an effect on the jet breakup trend, but it does have an effect on the breakup length. This has been shown by Hiroyasu and Arai et. al. as they conducted experiments with aspect ratios ranging from 4 – 50 **[38, 39]**. Hiroyasu found that increasing the aspect ratio from 4 to 20 led to jets with shorter break up lengths. This was attributed to flow reattachment along the inner nozzle walls as well as wall friction along the length

of the nozzle. Friction would lead to energy losses and would also act as a turbulence promoter which in turn would increase the disturbances on the jet surface, leading to greater aerodynamic effects and shorter breakup lengths. Van De Sande and Smith found that the critical Reynolds (Recrit) number for the laminar to turbulent transition could be written as a function of the aspect ratio of the nozzle which is as shown in Equation 2.7 below **[40]**:

$$Re_{crit} = 12{,}000\left(\frac{L}{d_0}\right)^{-0.3} \qquad 2.7$$

Equation 2.7 above indicates that as the aspect ratio increases the critical Reynolds number decreases. This is similar to the results obtained by Sterling and Sleicher who found that for shorter nozzles much longer jet lengths were observed due to the lack of turbulence **[27]**. A similar conclusion was reached by Leroux et. al. as well, who noticed that nozzles with very small aspect ratios lead to jets with velocity profiles that are flat and are broken down due to capillary instabilities, whereas larger aspect ratios may lead to semi-turbulent jets **[24]**. Velocity relaxation would thus take place causing a transition to turbulence in the jet and as such aiding in faster breakup. However, on the other hand Hiroyasu also noted that if the aspect ratio was increased to a value of 50 or above then the breakup length was observed to increase as well **[38]**. This is because the jet is allowed to fully transition to turbulent flow before it exits the nozzle, which is more stable than an undeveloped flow in transition.

Birouk et. al., therefore pointed out that a general rule on this regard is that as the aspect ratio increases the breakup length of the jet decreases due to an increase in the frictional forces along the walls of the nozzle. However, when very large aspect ratios are used the jet produced is fully turbulent and as such more stable than a semi-turbulent flow leading to a slight increase in the breakup length **[37]**. This can be seen from the results obtained by McCarthy and Malloy who carried out experiments with aspect ratios of 0, 1, 5 and 10, displayed in Figure 2.6 below **[36]**:

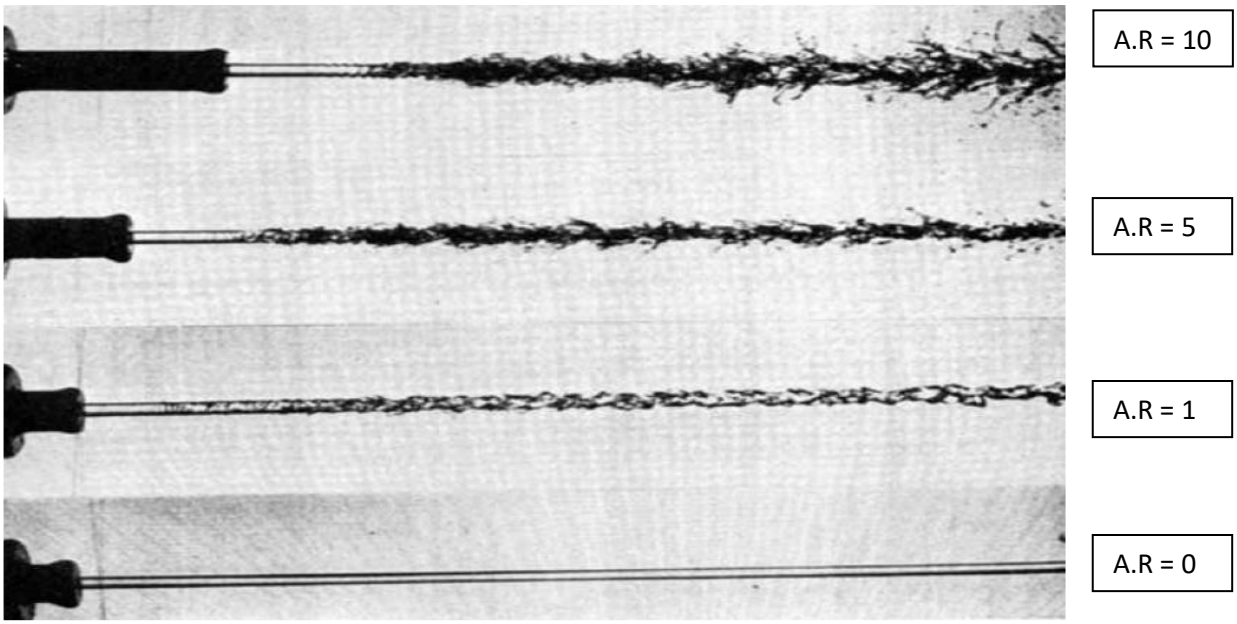

Figure 2.6. Effects of the nozzle aspect ratio on jet behaviour by McCarthy and Malloy ***[3636]***

Angle of Contraction (α):

As the liquid flows from the crucible through the nozzle the potential energy of the liquid is converted into kinetic energy in the emitted jet. McCarthy and Malloy found that an angle of contraction between 15° - 100° allows a minimum energy loss and a smooth jet **[35]**. Unfortunately, very little is known about the effect of the angle of contraction with respect to jet stability. It is only recently this topic has been getting any focus, but that too from studies that are more centered on determining the effect of the angle of contraction with respect to the drag coefficient (C_D) on jet velocity, rather than on jet stability **[41]**.

Surface Roughness and Streamlining:

Surface roughness promotes the transition to turbulence, as pointed out by Marmotaunt and Villermaux, who found that jets would appear very ruffled and irregular if the nozzle was rough, especially at higher Reynolds numbers **[42]**. Similarly with regards to streamlining, Reitz and Bracco found that rounded nozzles promoted smoother jets with lower chances of cavitation **[43]**.

However, it is important to note that while both these nozzle features become important at higher jet velocities, generally they have no effect in jets undergoing Rayleigh breakup **[36]**.

Beside the effects that nozzle geometry has on jet turbulence and velocity profiles, Birouk and Lekic also outline cavitation and hydraulic flip effects taking place inside the nozzle, and their influence on jet flow and breakup **[37]**. Cavitation occurs when the static pressure inside the nozzle is of the same order of magnitude as the liquid vapor pressure. The flow would then detach from the nozzle wall around the areas of cavitation. If the cavitation is very strong then the flow may not re-attach to the wall before exiting the nozzle, leading to a phenomenon known as hydraulic flip. This is shown below in Figure 2.7:

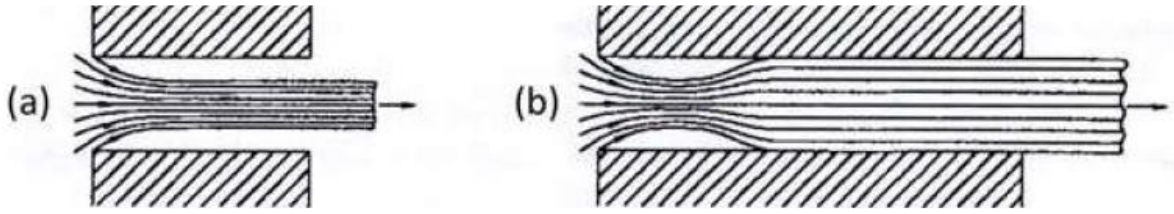

Figure 2.7. A fully detached flow undergoing hydraulic flip (a), and a re-attached flow undergoing cavitation (b) ***[44]***

It is important to note that cavitation is more prominent with sharp edged nozzles and with high velocity jets, as the flow will not be able to negotiate around sharp corners and will detach from the walls. Larger aspect ratios do not necessarily promote cavitation, however reattached flows are usually of an uneven velocity profile and thus reattachment would promote turbulence **[44]**. It can thus be seen that jet breakup is governed by a variety of factors with some more dominant than the others depending on the type of breakup. To fully understand and control jet behavior all these factors must be taken into account. Doing this from an analytical perspective can be very difficult and therefore researchers rely on other methods in order to determine the jet breakup mechanism.

2.1.3 Characterizing Different Jet Breakup Mechanisms

There are several ways of classifying jet breakup mechanisms. The two most common methods include the jet stability curve and the Ohnesorge plot. Both these techniques are widely used in industrial applications and as such will be discussed in this section.

2.1.3.1 The Jet Stability Curve

While Rayleigh had solved for breakup via capillary instabilities, it was noted by several researchers that if the velocity of the jet was increased or decreased beyond a certain point then the appearance and behavior of the jet would also change. Therefore, focus was placed on determining a general classification of jet behavior with respect to jet velocity. The most significant of such classifications was introduced by Smith who observed trends between the length of the jet (i.e., the continuous part before breakup, L_{BU}) and the velocity at which it was ejected (v_0) from an office of a given diameter (d_0) **[45]**. Smith carried out experiments using water, methylated spirit and mercury with orifice diameters ranging from 0.1 to 0.25 mm. He observed similar trends for the length of break up with respect to the velocity for all orifice diameters and reported them in a graph that researchers call the "jet stability curve". This graphical representation of jet behavior has undergone several modifications over the past century, but a general depiction of it recently reported by Bravo and Kweon is shown below in Figure 2.8 **[46]**.

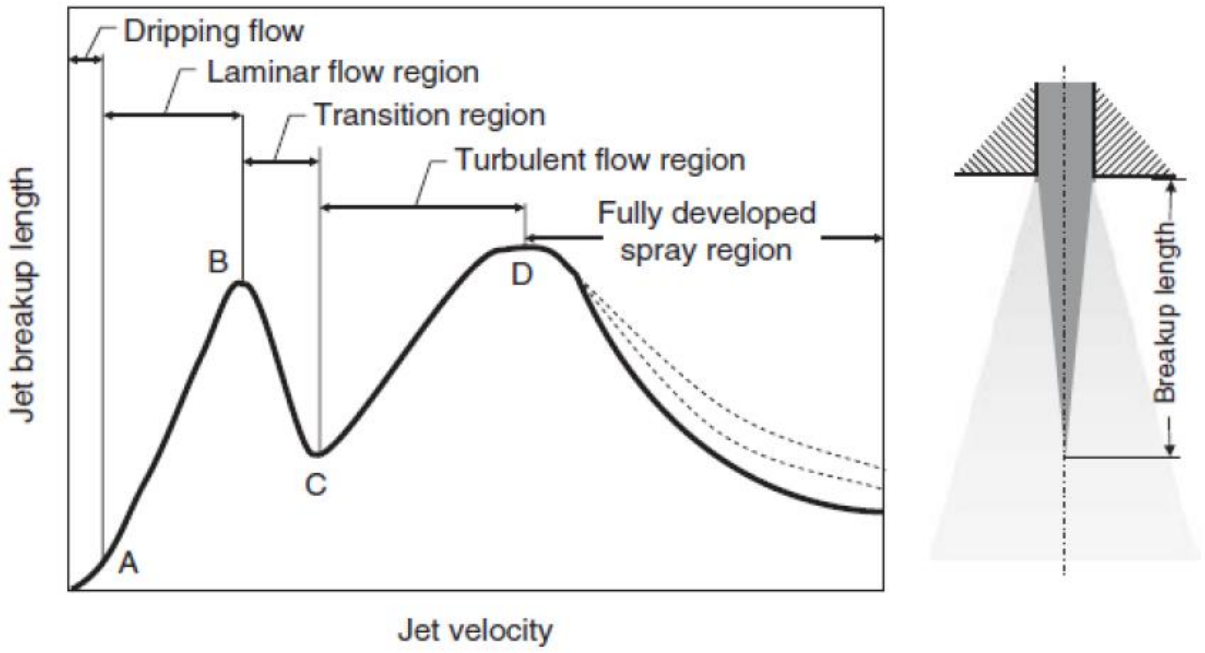

Figure 2.8. The jet stability curve showing the jet breakup length with respect to the jet velocity ***[46]***

From Figure 2.8 it is seen that the jet stability curve is divided into 5 specific regions. These are labeled accordingly as the dripping, laminar flow, transition, turbulent flow and fully developed spray region. It should be noted that Figure 2.8 above is an extension of Figure 2.2 which was a very early adaptation developed by Weber, and only focused on the aerodynamic effects.

Dripping Region:

This region (prior to point A) is when the drops would be produced by simply detaching from the orifice one at a time as gravity overcomes surface tension. Following the work of Tate, the size of the drops (d_d) can easily be calculated knowing the liquid surface tension (γ), density (ρ) and the diameter of the orifice (d_0)[2] **[47]**:

[2] Unless otherwise specified, the wetting phenomena is neglected throughout this study. The jet diameter at the nozzle exit is assumed to be equal to the orifice diameter.

$$d_d = (\frac{6d_0\gamma}{\rho g})^{\frac{1}{3}} \quad 2.8$$

Several other empirical equations are also reported for specific scenarios. For example, the drops produced from a wetted horizontal surface by Tamada and Shiback, or the drops formed from low energy melting of a welding wire by Lowke **[48, 49]**. However, they all follow a similar equation to that shown above, and while the dripping region is useful with applications focused on drop on demand techniques, this region is not studied in as much detail as the others.

Laminar Flow Region:

In this region (between points A – B) the symmetric disturbances described by Rayleigh breakup are most prevalent, and thus the jet would disintegrate due to growing capillary instabilities. It should also be noted that in the laminar region an increase in jet velocity would lead to a linear increase in the jet breakup length until a critical velocity is reached (point B). This point is referred to as the "maximum" or the "critical point" in the jet stability curve throughout this study.

Transition Region:

At the point B in Figure 2.8 both aerodynamic effects and jet turbulence start having profound influences on jet behavior in addition to the already present inertial and surface tension forces. As the jet velocity is increased, Schweitzer outlines that turbulence begins to set in as the Reynolds number surpasses the critical value **[19]**. However, the jet does not jump straight from laminar to turbulent flow, but rather to an intermediate stage called the semi-turbulent flow. The jet would nonetheless become ruffled and with the added aerodynamic effects (due to an increased velocity) surface disturbances would be encouraged to grow much faster. This would therefore not only force the jet to disintegrate sooner but would also cause the jet to break up in a sinusoidal rhythm rather than in the varicose mode. As such the breakup length sharply decreases due to the increased jet instability until a second critical point is reached (point C).

Turbulent Flow Region:

At the second critical point (point C in Figure 2.8) the flow has transitioned from semi turbulent to fully turbulent and as such the next region is called the turbulent flow region (C – D). In this region the aerodynamic forces become more significant. As the velocity is increased both the aerodynamic forces and turbulence increase. However, on the other hand it should be noted that as the velocity is increased the breakup length also increases. Several authors such as Grant and Middleman, and Rupe have argued that this increase in breakup length is because a jet fully transitioned to turbulence at the nozzle exit is more stable than a jet with a semi-turbulent flow still undergoing transition **[26, 34]**. Laminar, semi-turbulent and turbulent jets are discussed in Section 2.1.2.

Fully Developed Spray Region:

Point D marks the onset of atomization. The jet is completely disintegrated into a spray of droplets, of sizes several orders of magnitude smaller than the orifice. The behavior of the jet in the atomization region is not fully understood due to the very chaotic breakup, however, there is a consensus amongst researchers that the jet breakup length would decrease as the velocity increases. While aerodynamic effects are very important in the complete disintegration of the jet in the atomization mode, several other conditions have been seen to be significant as well. DeJuhaz proposed that the most significant cause of complete jet breakup was due to the nozzle geometry which in turn determined the turbulence on the jet; while Sadek proposed that cavitation in the nozzle was the leading effect **[50, 51]**. Sterling and Sleicher on the other hand outlined that the velocity profile relaxation could also have an effect **[27]**. After conducting experiments with water-glycerol mixtures and nozzles of varying geometries, Reitz and Bracco concluded that several of these conditions contribute to the atomization and eventual breakup of the jet. No one proposed mechanism can truly explain the atomization breakup mode **[43]**.

2.1.3.2 Ohnesorge's Classification

Besides the jet stability curve discussed above, the second most common and approved way of characterizing jets is through Ohnesorge's classification. From previous studies, mainly by Rayleigh, Weber and Haenlein, Von Ohnesorge from experimental observations identified four cases of jet breakup as it exits and office **[52]**. These include: dripping due to the effect of gravity without jet formation, break up by axisymmetric surface perturbations (i.e., Rayleigh breakup), wavy breakup due to screw symmetric perturbations following the work of Haenlein and Weber, and atomization of the jet due to aerodynamic forces. Von Ohnesorge realized that jet breakup is governed by the viscous, inertial and surface tension forces, with the dependance on each force changing with different breakup modes. Therefore, Von Ohnesorge took into consideration both Weber's and Reynolds laws of capillarity and viscosity respectively and defined the dimensionless variable Z, presented in Equation 2.1.

The dimensionless variable 'Z' would later be redefined after Von Ohnesorge as the Ohnesorge number or simply the 'Oh' number which relates the viscous forces to the inertial and surface tension forces. After conducting several experiments with water, oil, glycerin, and aniline using long nozzles with orifices of diameters 0.5 – 4mm, Von Ohnesorge organized his results in a plot of Z vs Re depending on the appearance of jet breakup. This plot is another popular way of categorizing jet break up. It is commonly known as Ohnesorge's classification or Ohnesorge's plot and is shown below in Figure 2.9. It should be noted that Ohnesorge's classification is purely qualitative, and is built through the appearance of the jet before breakup and the droplet formation after breakup.

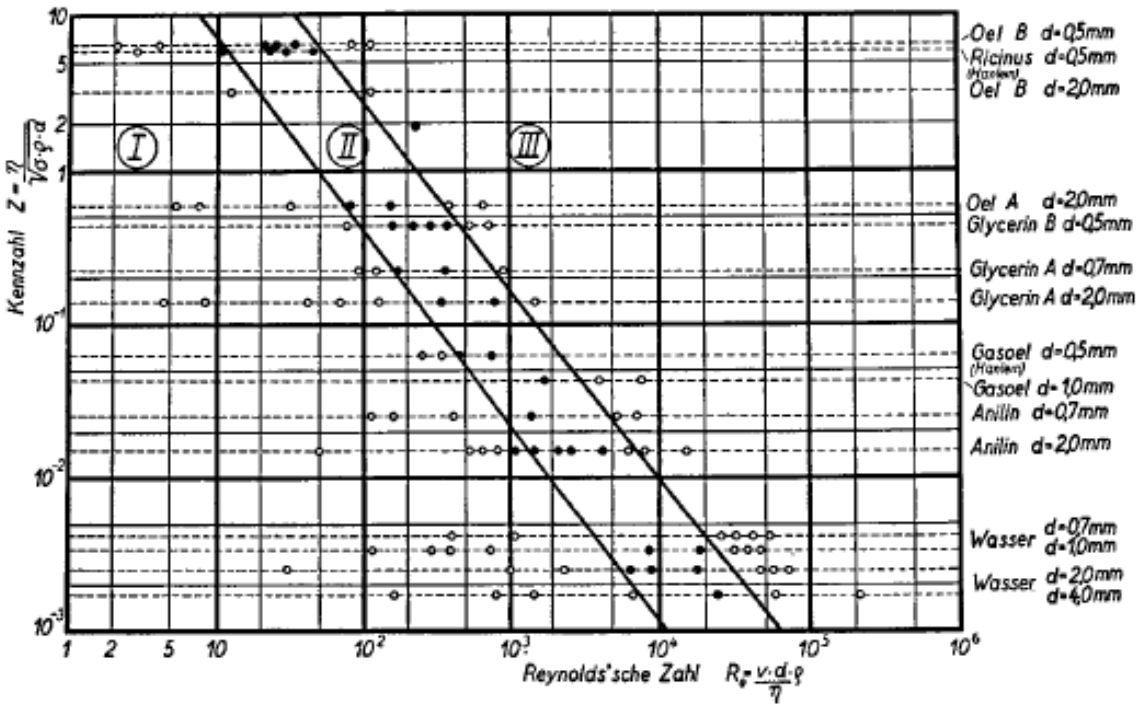

Figure 2.9. Ohnesorge's presentation of his test results on the Z vs Re plot ***[52]***

As shown in Figure 2.9 Ohnesorge classified his results in three different regimes. Regime 1 is a region of small Reynolds numbers describing the breakup defined by Rayleigh and that represented as the region between points B – C on Figure 2.8. Regions 2 and 3 are described as regimes whereby the inertial and aerodynamic forces are increasing, and the instability is changing due to the air friction. The breakup in region 2 is that which is due to sinusoidal instabilities as described by Haenlein, and the breakup in region 3 is due to jet atomization. The Ohnesorge plot has been refined over the past 90 years and not only have specific names been given to the different regimes, but the boundary of regime 3 has been moved and a new regime has been added to make it a total of 4 regimes. The updates on the Ohnesorge plot will be briefly discussed here and the most revised plot will be displayed as well.

The first major update to Ohnesorge's classification was done by Miesse, who conducted experiments with water and liquid nitrogen using orifice diameters of 0.7 – 2.5 mm **[53]**. Miesse observed qualitatively the jets in his study to have an appearance of a wave like sinusoidal breakup and an atomization breakup, indicating that they belong in regions 2 and 3 of Ohnesorge's classification. However, all his data points appeared to fall in region 3 only. Following Littaye's theory of primary and secondary atomization, Miesse showed that if the boundary between regions

2 and 3 were translated somewhat to the right side, then his data points would be correctly segregated in the correct distinct regions following Ohnesorge's classification, Littaye's theory, and the observed breakup **[52, 53]**.

Ohnesorge's original classification is based on a dimensionless analysis approach and simple observations of jet behaviour, allowing it to easily account for any changes in the dominant forces acting on the jet without modification to the plot. However, the liquids used by Ohnesorge have very different thermophysical properties to those tested by Miesse (such as liquid nitrogen), which is why Miesse had to modify the plot. It is also important to note that Ohnesorge's plot does not account for turbulence, velocity profile relaxation or nozzle effects and as such several researchers would find that their experimental data would lie in a different region on the Ohnesorge plot as compared to their qualitative appearance.

The most updated and commonly used Ohnesorge classification was that developed by Reitz during the course of his PhD **[54]**. Reitz compiled the data of several researchers including Haenlein, Von Ohnesorge, and Griffen and Muraszew, and also included his experimental data which was conducted with varying nozzle geometries **[22, 29, 52]**. He found that the modification by Miesse was correct, however the intermediate region (region 2 in Figure 2.9) could in fact be broken into two different regions, and as such a new regime was introduced. A reproduction of the regime diagram from Reitz's work is shown in Figure 2.10 below:

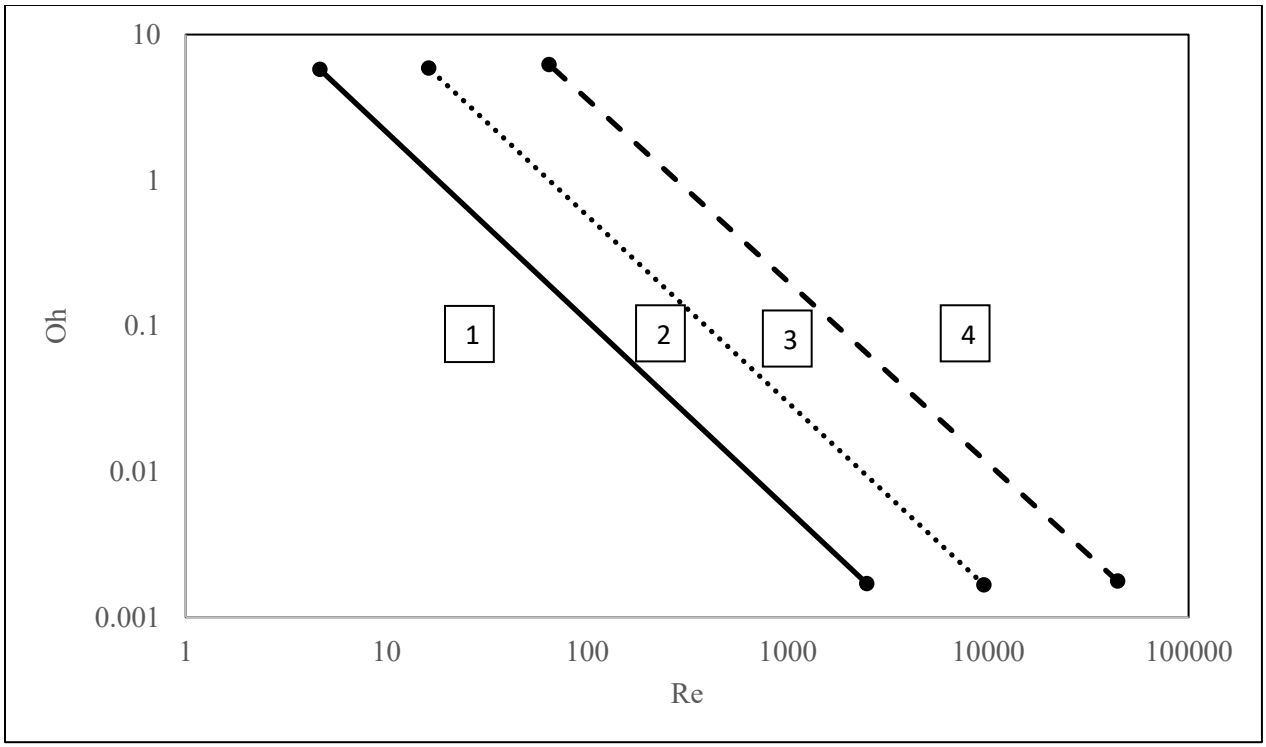

Figure 2.10. Ohnesorge's classification created by Reitz and used in this study. The regions marked 1, 2, 3 and 4, and separated by oblique lines are the Rayleigh, first wind induced, second wind induced, and atomization regimes

Figure 2.11 represents the appearance of the jet as it breaks up in the different regimes, which in turn is followed by the description of the jet breakup with respect to both Figures 2.10 and 2.11.

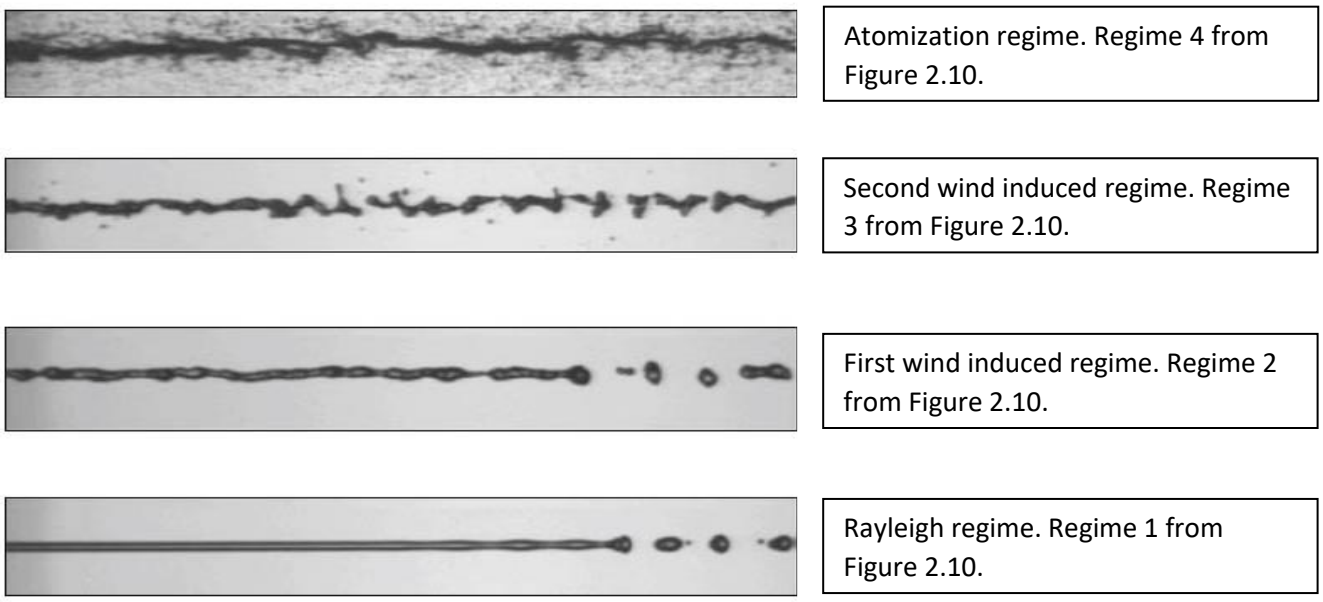

Figure 2.11. Cylindrical jet behaviour identified using the regime names according to the Ohnesorge classification ***[55]***

Regime 1: Rayleigh Breakup: Characterized by low jet velocities (i.e., low Reynolds numbers), where aerodynamic effects are negligible, and breakup is induced by surface tension forces leading to axisymmetric forces on the jet surface. Rayleigh and Weber's theories can adequately predict the jet breakup in this regime (as covered in Section 2.1.1), including the droplet diameter and breakup length, but do not account for the production of satellite droplets.

Regime 2: First Wind Induced Regime: Also called the "sinuous breakup mode" owing to its wavy appearance and sinusoidal vibrations along the jet surface. This is due to the increased relative velocity between jet and the ambient fluid, which indicates that the significance is moving away from surface tension and more towards aerodynamic effects.

Regime 3: Second Wind Induced Regime: Increased aerodynamic forces (due to the increased velocity) lead to the rapid growth of short-wave disturbances, and as such small surface irregularities can disrupt the jet more notably than in the previous regimes. The jet disintegration occurs very close to the nozzle and the drops produced can

vary in size from droplets larger than the orifice diameter to very small droplets several orders of magnitude smaller than the orifice.

Regime 4: Atomization: The complete disintegration of the jet as soon as it exits the nozzle producing tiny droplets several orders of magnitude smaller than the orifice diameter. It was commonly believed that aerodynamic forces are the leading cause of atomization. However, more recent studies have switched focus on understanding other effects such as turbulence and nozzle geometry that could play a significant role as well.

Alternative to the qualitative method mentioned above, a quantitative approach can also be used to classify the regimes to which a jet belongs. From a balance between inertia and surface tension, Ranz noted that a jet is only formed if the Weber number was greater than 8 ($We > 8$), before which droplets would be produced by dripping **[56]**. If the inertial forces increase to a point such that the gas Weber number (We_g, similar to the liquid Weber number except the density of the liquid is replaced by the density of the ambient fluid) exceeded 0.4 then the jet would transition to the first wind induced regime. Sterling and Sleicher noted that this transition can also be correlated to the Ohnesorge number such that transition to the first wind induced regime takes place if $We_g > 1.2 + 3.41Oh^{0.9}$ **[27]**. Ranz also noted that the second wind induced regime and the atomisation regime would take place as the aerodynamic forces increased even further such that $We_g > 13$ and $We_g > 40.3$ for the two regimes respectively. The compilation of this data was presented by Lin and Reitz, and is shown in Table 2.1 below **[57]**.

*Table 2.1. Classification of jet breakup regimes **[57]***

Regime Name	Predominant Factors Affecting Breakup	Conditions for Transition to the Next Regime
Dripping	Gravity and surface tension forces	We > 8
Rayleigh	Surface tension forces	$We_g > 0.4$ $We_g > 1.2 + 3.41Oh^{0.9}$
First Wind Induced	Surface tension and aerodynamic effects	$We_g > 13$
Second Wind Induced	Aerodynamic effects	$We_g > 40.3$
Atomization	Combination of several effects	

Classifying jet behaviour according to either characterization method (i.e., the jet stability curve or Ohnesorge's classification) can be very useful. Engineers and scientists often want to create projects involving jets that operate only in a particular regime. They could, therefore, easily consult either of these characterization methods and determine the necessary operating and experimental conditions. However, this is not to say that these methods are without flaws and inaccuracies. In recent times several researchers have discovered areas of jet breakup not covered in much detail or not covered at all in both the jet stability and Ohnesorge classification, and as such they have proposed their thoughts on how to best tackle this matter. This will be discussed below in Section 2.1.4.

2.1.4 Modern Understandings of Jet Breakup, Including Externally Manipulated Jets and Droplet Production

With advance in technology such as high-speed imaging and computer modelling, the past 100 years or so have seen a number of developments in jet breakup analysis, allowing several factors to be considered and tested. However, the understanding of jet behaviour is far from complete. In this section the most recent updates on jet behaviour will be considered. Furthermore, as this project will focus on externally disturbed jets and droplet production, studies from the past on this regard will be reviewed as well. It should be noted that while a few of these studies have a

target in some form of technological application, most studies with externally excited jets were merely focussed on increasing the understanding of jet behaviour.

2.1.4.1 Modern Understandings of Jet Breakup

Despite the detail into which jet breakup has been studied, it may seem surprising that very few advances have been made on the analytical side, with the most basic and frequently used tools still being the linear stability analysis developed by Rayleigh. This is because of the several nonlinear effects which could sometimes dominate the jet breakup. These effects are very difficult to predict and quantify due to the complexity of jet formation and its relation to several physical, experimental, and geometric factors. This leads to a system of very many degrees of freedom, making it impossible to solve. Most scientists and engineers therefore simply rely on the Ohnesorge classification in order to determine the physical mechanisms causing breakup and the regime to which their operated jet may belong.

Most recently Ben Trettel has carried out several studies arguing that this approach is in fact not reliable, as the Ohnesorge classification (called the "regime diagram" in his study) is constructed from a limited amount of data and is classified by superficial visual characteristics **[58]**. Unfortunately jets in different regimes may have a similar superficial appearance causing this form of qualitative characterization to be quite inaccurate. It is important to note that a quantitative characterization of regime boundaries also exists following the works of Ranz, Reitz, Sterling and Schweitzer and Lin and Reitz as presented in Table 2.1 in Section 2.1.3 **[27, 54, 56, 57]**. However, Trettel points out that these boundaries are purely theoretical, and the derivations seem to be based upon simple scaling laws from assumed physical mechanisms. For example, the transition from one regime to another is attributed solely to aerodynamics, with no regard of the jet turbulence or even the nozzle geometry. Taking this into consideration Trettel aimed at modifying the regime diagram such that the qualitative and quantitative classifications are consistent with the physical mechanisms present in each regime. Therefore, he compiled data from several previous researchers, accumulating hundreds of data points with Weber numbers ranging from 2 – 410,000 and Reynolds numbers ranging from 15 – 730,000. Trettel also went on to redefine the regime names with respect to the dominant physical mechanisms leading to break up.

Table 2.2 shows the regime names proposed by Trettel as well as the conventional names given by Reitz.

*Table 2.2 The proposed changes to the regime names **[58]***

Proposed Regime Name	Conventional Regime Name
Dripping	Dripping
Laminar Rayleigh	Rayleigh
Downstream Transition	First Wind Induced
Turbulent Rayleigh	-
Turbulent Surface Breakup	Second Wind Induced
Atomization	Atomization

From Table 2.2 it can be noted that Trettel places a lot of emphasis on the turbulence of the jet following the regime names proposed. A new regime has also been introduced in this study, called the turbulent Rayleigh regime. Conventional regime diagrams suggest that as the velocity of the jet is increased (i.e., Reynolds number is increased), the jet will transition from the Rayleigh to the first wind induced regime. However, Trettel argues that this is not necessarily true as the transition from one regime to another with the increase in velocity is not universal, and furthermore the transition is not governed entirely by aerodynamic effects. This can be proven further by analyzing the results of previous researchers such as Mansour and Chigier, Sallam et. al., and Sterling and Abbott, who all noticed that sometimes a turbulent jet would be created with an increase in velocity, which would break up in a similar way to the laminar Rayleigh jet (i.e., through the growth of axisymmetric disturbances) **[31, 33, 59]**. A turbulent Rayleigh jet from the work of Asset and Bales is shown in Figure 2.12 below.

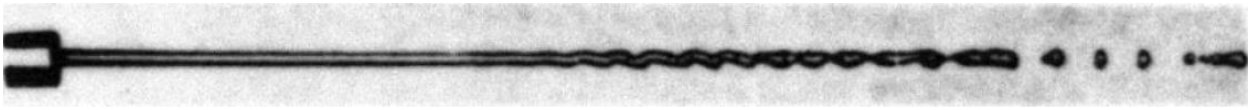

*Figure 2.12. Image of a water jet in the turbulent Rayleigh regime from Asset and Bales **[60]***

In this study Trettel notes that if a purely qualitative approach was used then the regimes could easily be confused with one another, as often happened with the Ohnesorge classification.

Therefore, by considering the superficial qualitative approach as a secondary method of characterization, a primary quantitative approach is introduced that is based on the breakup length of the jets in different regimes. This approach is very intelligent as it combines both forms of jet breakup characterization (i.e., the jet stability curve and the Ohnesorge classification), and as such avoids unnecessary confusion. For example, a jet breaking up in the turbulent Rayleigh regime may seem from a superficial appearance very similar to a jet breaking up in the conventional first wind induced regime as shown in Figure 2.12 above. However, the breakup length decreases as the velocity increases in the first wind induced regime, but the opposite would be true for a jet in the turbulent Rayleigh regime whereby the length would increase with an increase in velocity, thus allowing us to differentiate easily between the regimes. The schematic of the regime diagram generated by Trettel using water flowing through long nozzles (pipe flow) is represented in Figure 2.13 below.

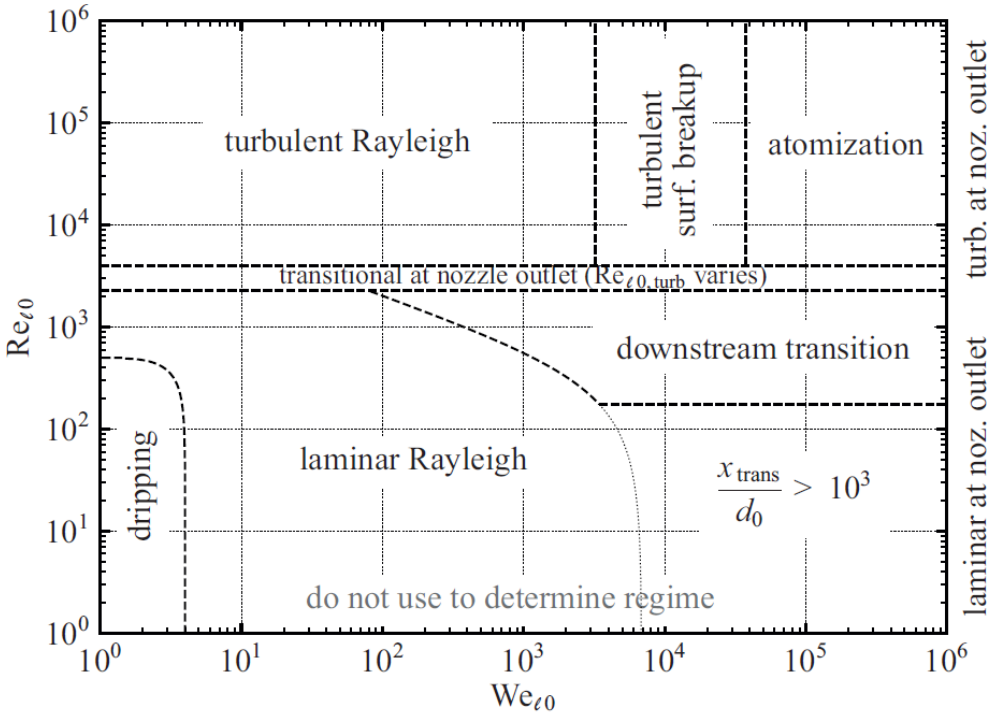

Figure 2.13. A schematic of the regime diagram generated by Trettel showing all the different modes of breakup ***[58].***

It should be noted that the regime diagram presented in Figure 2.13 above is specific to the liquid under investigation, the ambient fluid properties, and the nozzle geometry. Therefore, it

cannot be used as a general regime diagram. In order to determine the boundaries between the different regimes for a specific experimental set up, the quantitative approach outlined by Trettel must be used.

Dripping and Transition to Laminar Rayleigh:

The transition from dripping to jetting can be classified using a critical Weber number (Wecrit). Trettel outlines that this is best done using the empirical equation proposed by Clanet and Lasheras **[61]**:

$$We_{crit} = 4\frac{Bo_{outer}}{Bo}[1 + KBoBo_{outer} - ((1 + KBoBo_{outer})^2 - 1)^{0.5}]^2 \quad 2.9$$

Where 'K' is a constant that is equal to approximately 0.4. The terms Bo and Bo_{outer} are the Bond numbers taking into account the inside and outside nozzle diameters respectively, i.e.,

$$Bo = \frac{\rho g {d_0}^2}{\gamma} \qquad Bo_{outer} = \frac{\rho g d_{outer}^2}{\gamma} \quad 2.10$$

Laminar Rayleigh and Transition to Turbulence at the Nozzle:

The laminar Rayleigh regime is predicted accurately using Rayleigh and Weber's original theories outlined in Section 2.1.1. As such Equation 2.3 can be used to predict the breakup length, and the droplet diameter can be predicted using Rayleigh's approach ($d_d = 1.89d_0$). The transition to turbulence at the nozzle exit is defined by a critical Reynolds number (Recrit) and is a function of the nozzle geometry (i.e., the nozzle aspect ratio). Therefore, the empirical equation by Van de Sande and Smith (Equation 2.7) is satisfactory to determine the critical Reynolds number.

Transition to the Downstream Transition Regime:

Trettel explains that the downstream transition regime is governed by a semi-turbulent flow. Therefore, while the jet is not fully turbulent at the nozzle exit, it undergoes a transition to

turbulence downstream after a specific length, known as the transition length or simply x_{trans}, which is defined as:

$$x_{trans} = \frac{Re_{trans}\mu}{\rho v_0} \tag{2.11}$$

Where Re_{trans} is the transition Reynolds number. According to Trettel, Retrans can be calculated using the critical Reynolds number, the Weber number and the term $\ln(r_0/\eta_0)$ as shown below:

$$Re_{trans} = ln\left(\frac{r_0}{\eta_0}\right)(3We + Re_{crit}We^{0.5}) \tag{2.12}$$

If the transition length is greater than the breakup length in the laminar Rayleigh regime (i.e., x_{trans} > LBU), then the jet will follow the downstream transition breakup.

The other regimes presented in Figure 2.13 will not be discussed here as they are beyond the scope of this study. However, they can be found in Trettel's work **[58]**. It should also be noted that while the work done by Trettel is quite spectacularly organized and provides a new way of jet characterization. It will not be exclusively relied upon. Both the conventional approach (i.e., Ohnesorge's classification) as well as Trettell's approach will be used in this study where necessary.

2.1.4.2 Externally Manipulated Jets and Droplet Production

The idea of manipulating a liquid jet before or after it exits the nozzle has been under investigation since the mid-20th Century. Following the early experimental investigations of jet breakup in the Rayleigh regime, researchers found the average droplet diameter and the fastest growing disturbance to agree reasonably well with Rayleigh's linear analysis. However, in all cases satellite droplets were present between the two main large droplets which could only be explained as a result of the non-linear effects in jet breakup. Therefore, several studies were organized to either study these non-linear effects or to try and overcome them in order to produce droplets of uniform size and shape.

Crane et. al. decided to investigate the effect of mechanical vibrations on jet breakup characteristics using a highly flexible electronically driven vibrator placed at the nozzle exit capable of vibrating at frequencies of 50 – 5000 Hz **[62]**. The purpose of this was to study the possibility of initiation of unstable combustion in diesel engines while operating under low velocity in the laminar region. Crane et. al. undertook their experiments using water flowing through nozzles with an orifice diameter of 1.2 mm and an aspect ratio of 0.5 to avoid any hydraulic flip or cavitation effects. From their experiments they made significant observations regarding drop production. They found that the drop production frequency was equal to the applied vibration frequency, the inter drop spacing was remarkably constant after breakup, and the jet velocity was accurately measured through the multiplication of the wavelength (inter-drop spacing) and the applied frequency. This clearly indicates that applying a vibration to the jet would lead to regularity in breakup. However, Crane et. al. also observed that in fact the wavelength measured during their experiments deviated from Rayleigh's prediction with an error of approximately 15%. They also observed that the jet would have contracted by a factor of approximately 0.8 before breakup and increasing the applied frequency would decrease the breakup length due to the growth of disturbances of shorter wavelengths.

A similar study was conducted by Donnelly and Glaberson on the stability of a vertical liquid jet under an imposed audio frequency **[63]**. Experiments were conducted using distilled water and glycerin – water mixtures with orifice diameters of 0.075 – 0.635 mm, and an imposed frequency of 40 – 2000 Hz. The purpose of this study was to determine jet stability with respect to the growth of perturbations of different wavelengths (i.e., different wavenumbers) with respect to time. Acoustic disturbances were applied to the jet via a loudspeaker placed near the orifice, or for more viscous jets a direct contact method to the liquid flow was used. The appearance of the jets with applied disturbances of wavenumbers ranging from 0.148 to 1.07 are shown below in Figure 2.14.

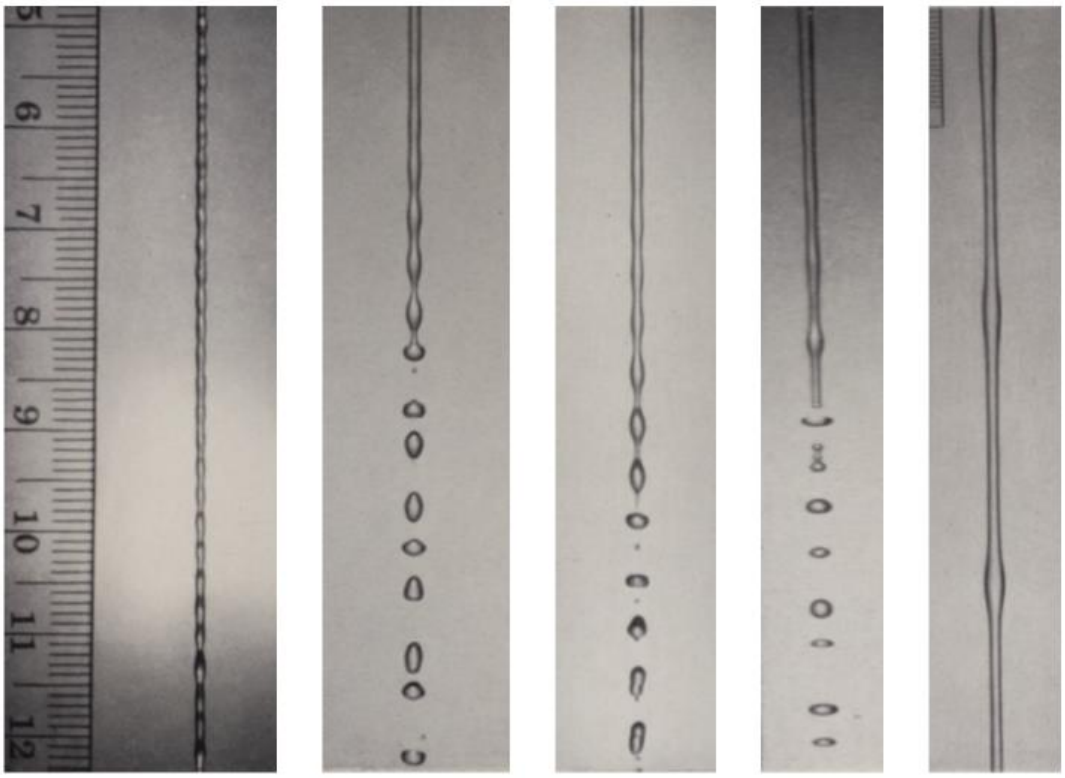

Figure 2.14. The appearance of a jet with a disturbance of wavenumbers k = 1.04 to 0.148 applied onto them ***[63]***

It can be noted from Figure 2.14 that applied disturbances with wavenumbers closer to that predicted by Rayleigh (k = 0.697) lead to more regular breakup, and disturbances of wavenumbers k > 1 do not grow leading to a continuous stable jet. It can also be noted that following along with the theory, disturbances of small wavenumbers (i.e., large wavelengths) would cause the jet to extend for a much longer distance before breakup. From Figure 2.14, Donnelly and Glaberson noted that the maximum amplification of disturbances took place at wavenumbers of approximately 0.7 and went on to state that no non-linear effects were recorded with an applied frequency. These remarks are however highly debatable and have been questioned by several researchers, as it can be noted from Figure 2.14 that at a wavenumber of 0.678 satellite droplets are still being created and so non-linear effects have not completely vanished but rather have been reduced.

Following this Goedde and Yuen also organized a study to determine the stability of liquid jets with imposed disturbances **[64]**. The aim of this study was to find out in what manner nonlinear effects influence the growth of surface waves, the breakup of the liquid jet, and the behavior of droplet production. Goedde and Yuen worked with short nozzles with orifice diameters of 1 – 2 mm, and low velocity (3 – 5 m/s) laminar jets to avoid any cavitation, turbulence, or aerodynamic effects. Axisymmetric disturbances were imposed on the liquid jet via an oscillating voltage of 0.3 – 1 kV on a metal plate with a hole through which the jet flowed. The alternating electrostatic force would thus produce deformations on the jet surface of the prescribed frequency. Experiments were conducted with water and glycerin – water solutions, and from the same photograph of the emitted liquid jet the neck and the neighboring swell were recorded. According to Rayleigh's linearized analysis the exponential growth rate of an instability is a constant. Goedde and Yuen found that the exponential growth rate of the neck and the swell are in fact not constant but rather the exponential growth rate of the difference between the neck and the swell is a constant. Initially the neck grows faster than the swell but later when the non-linear effects become important the swell grows faster than the neck. This analysis disagrees with Rayleigh's linearized theory but goes to show that non-linear effects are present even in the Rayleigh breakup mode. As the average exponential growth rate is a constant the non-linear effects tend to cancel out, pushing the jet to obey Rayleigh's linearized theory, however due to the different growth rates of the swell and the neck the point of drop detachment is always away from the center of the neck. This phenomenon discovered by Goedde and Yuen would then in fact explain why the droplet production and the growth of optimal disturbances follow Rayleigh's linearized theory, but also why satellite droplets are produced with respect to the non-linear effects.

Paul Haas carried out a similar study, which was focused more on the production of droplets rather than quantifying the nonlinear effects on jet break up **[65]**. In this study Haas worked with ethylene glycol using offices of 0.185 – 0.49 mm in diameter. The jet velocity ranged from 4.6 – 11.8 m/s, producing droplets of 0.43 – 1.1 mm in diameter. In order to achieve a controlled breakup, Haas applied an external vibration to the liquid jet as it was pumped from the reservoir through the nozzle. This was done by attaching a variable frequency oscillator externally along the feed line. This device would produce a mechanical vibration of 2 – 20,000 Hz, similar to an audio system except without the diaphragm to produce sound. Haas observed that without any applied vibration the droplet production would be very irregular, and only when a vibration of

0.67 – 1.5 times the natural frequency of jet breakup was applied would there be a very regular breakup. The natural frequency (f_{res}) was observed to be relation of the jet velocity (v_0) and the orifice diameter (d_0) as $f_{res} = 0.2v_0/d_0$, which is similar to that predicted by Merrington and Richardson. From the experimental results Haas found that the droplet diameter would be anywhere between 2.46 and $1.55d_0$ and the distance between the drops being anywhere between 5 to 1.9 d_0. While the results for the droplet sizes agree well with Rayleigh's prediction of $1.89d_0$, the droplet spacing shows that the wavelengths of the unstable disturbances are below the critical value described by Plateau and Rayleigh. This confusion can be cleared up by analyzing Haas's results further and characterizing his breakup. It becomes evident that this study was operated in both the Rayleigh and first wind regime, with some data points falling even in the second wind regime following Figure 2.10. While this was not the intention set out by Haas, this study shows that by applying vibrations of the correct frequency and amplitude, the jet breakup can be controlled in both the Rayleigh and first wind regime, and possibly the second wind induced regime as well.

Building on the works of previous researchers, Ruiz organized a study to investigate the wavelength of the disturbances formed on the surface of the liquid jet onto which external mechanical vibrations were applied **[66]**. Donnelly and Glaberson had already shown that when external vibrations of the appropriate frequency are applied to the jet the non-linear effects are diminished and uniform drops are produced. Ruiz however points out that this study was concerned with determining the drop size and spacing between drops, and as such the observed disturbances had already grown sufficiently in size and hence had incorporated several nonlinear effects on the jet surface. Ruiz therefore created a study to observe the small disturbance on the surface of the jet onto which mechanical vibrations of small amplitude have been applied. The difference between this study and the previous ones of Donnelly and Glaberson, and Goedde and Yuen, was that Ruiz used a new laser-based technique rather than the traditional photographic imaging, and hence could record the wavelengths of the small disturbances on the jet surface which were not visible by imaging. In this study Ruiz conducted experiments using water flowing through a nozzle with a large orifice diameter of 6.25 mm and an aspect ratio of 1. The jet was mechanically excited (acoustic excitation) through the use of a large loudspeaker. Two laser beams, the first placed close to the nozzle exit and the second slightly further down were used to detect the jet diameter and any disturbances on the surface of the jet. From his study Ruiz found that contrary to what is predicted

by Rayleigh's linear theory and the observation of previous researchers the most unstable disturbance for a mechanically excited jet producing uniform droplets does not have a wave number of $k = 0.697$, but rather the maximum point of instability lies in a location where by $0.3 < k < 0.5$. This goes to show that for mechanically excited the optimally unstable disturbances may have a wavelength larger than that predicted by Rayleigh. Furthermore, the experimental setup and equipment used may also have an effect, as the disturbances produced externally may not have mirror effects on the jet, or may even in fact have an impact in reducing the non-linear effects but in the process pushing the optimal unstable disturbance to a lower wavenumber.

More recently studies carried out by Shimasaki and Taniguchi, and by Sudesna Roy, have shown how externally disturbed jets can be used to produce metal droplets for industrial applications and to study solidification **[67]**. Shimasaki and Taniguchi proposed an electromagnetic pinch method to produce silicon particles for spherical silicon solar cells **[68]**. In their approach an intermittent electromagnetic pinch force is applied to a jet of liquid metal. This will generate disturbances of equal interval on the surface of the jet. As the disturbances grow downstream, the jet breaks into uniform droplets. In order to test this method, they conducted experiments using gallium, with an orifice of 1 mm diameter and a jet velocity of 1.4 m/s. The liquid jet was allowed to flow through a set of induction coils through which electromagnetic disturbances of frequencies ranging from 200 – 1000 Hz could be supplied onto the flowing jet. Shimasaki and Taniguchi found that when no electromagnetic force was applied the jet did not breakup at regular intervals. As the frequency was increased the breakup became more regular but satellite droplets were still produced. At the optimal frequency the breakup became very regular and very few satellite droplets were produced. If the frequency was increased even further the breakup changed back to being very irregular with the formation of several satellite droplets. Figure 2.15 below is a representation of their results at different applied frequencies.

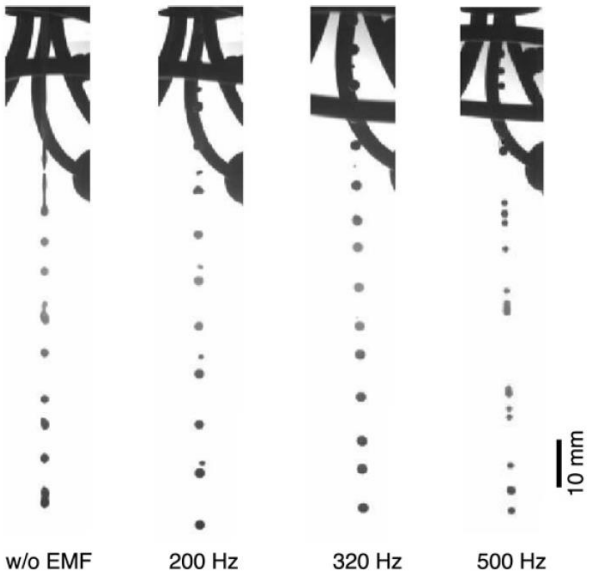

*Figure 2.15. Photographs of gallium droplet formation by applying an intermittent electromagnetic force of different frequencies **[68]**.*

Sudesna Roy carried out a study to produce mono-sized metal droplets in order to study their solidification pattern **[69]**. The droplets were produced using the uniform droplet spray process (UDS) patented by Chun and Parsow **[10]**. The UDS is a modification of the original method patented by Bienvenu, which consists of 2 specific parts that help produce uniform droplets **[9]**. The first is a vibrating orifice that provides disturbances into the bulk liquid as it exists the nozzle. The second is an annular electrode placed close to the orifice exit that provides an electric field around the droplets as they fall and solidify. This is to ensure that the droplets disperse as they fall due to the fact that they are equally spaced. Furthermore, the applied frequency required to generate mono-dispersed droplets must be changed to accommodate the decreasing metal head in the crucible. In the UDS system, Chun and Parsow replaced the vibrating orifice with a piezoelectric transducer placed within the bulk liquid, very close to the orifice exit. This would provide vibrations into the liquid just before it exits the orifice. This arrangement allows better control of the frequency of vibration, which can quickly be changed as the exit velocity of the liquid stream changes, but would present challenges at high temperature operations.

There exists a wide range of applications whereby liquid jets are broken down into desired drops from ink jet printing to fuel combustion. However, controlling the jet break up and droplet sizes produced is not very simple due to the spontaneous nature of jet breakup and formation of

satellite droplets resulting in a bimodal distribution which several applications do not want to accommodate. Eggers points out that one of the most versatile methods to achieve regular jet break up is by external forcing, using an external flow, or by applying an external field, or a combination of both. This would allow the jet diameter and the droplet sizes produced to be controlled to a very high degree of accuracy as seen in the works of Shimasaki and Taniguchi, and Sudesna Roy which were highlighted earlier.

2.2 Electrically Charged Jets, and Electrohydrodynamic Atomisation

The review on electro-spraying, will be divided into 4 subsections, organised in a similar fashion to the review on continuous jet breakup presented in Section 2.1. This will start off with a discussion of the initial developments in electro-spraying, which include fundamental theories and early experimental investigations on charged liquids. Following this the second subsection will cover the different attempts at characterising and classifying the different modes of electro-spraying. The cone-jet mode of electrohydrodynamic atomisation will be discussed next, and finally the last subsection will very briefly introduce modern attempts at numerical models of electro-spraying in the cone-jet mode.

2.2.1 Fundamentals of Charged Droplets and Electrical Discharges

While atomisation dates back to the ancient Roman times, electro-hydrodynamic atomisation was first observed by William Gilbert in the 17th century. He discovered that a water drop would deform when sufficient charge is applied to it. During his studies he observed that a droplet resting on a flat surface to which an excess charge was applied would change shape from hemispherical to conical as the charge was increased. While this phenomenon was studied through the ages, it was not until Lord Rayleigh's maximum charge theory (established in the late 19th century) did we start to truly understand what happens to a droplet under excessive electric stress.

After theoretically predicting the deformation of a free-falling liquid cylinder, Lord Rayleigh applied a similar approach to theoretically estimate the maximum charge a liquid droplet

could carry before it disintegrates. Rayleigh discovered that for a free-falling jet, disturbances are generated on the surface of a jet and propagate along the liquid cylinder. At the point whereby the wavelength is greater than the circumference of the liquid cylinder they would cause the cylinder to become unstable. To overcome this instability the cylinder would disintegrate into droplets of a radius greater than that of the cylinder in order to conserve the surface energy balance between the liquid cylinder and individual droplets **[14]**. From this Rayleigh predicted when an electric imbalance is applied to a liquid cylinder the disturbances generated must be again of a similar nature.

Following this and after applying a balance of the forces on a pendant drop, Rayleigh derived the maximum charge limit after which any excess charge would lead to the disintegration of the droplet. This was the foundation of modern day electro-spraying and while these theories were developed by Rayleigh over a hundred years ago there still exist several fundamental unanswered questions regarding EHDA. According to Rayleigh's theory of instability the maximum charge (q_r) a liquid drop of radius (r_d) can hold before becoming unstable is related to its surface tension γ, density ρ and the permittivity of free space (ε_0) as follows **[70]**:

$$q_r = 8\pi(\gamma\varepsilon_0)^{\frac{1}{2}} r_d^{\frac{3}{2}} \tag{2.13}$$

While Rayleigh laid the foundation of EHDA and developed the fundamental theories, the physical observation and experimental work was pioneered by Zeleny in the early 20th century, and because of these works there exist several applications today in the field of electro-spraying. Zeleny set out to determine the discharges from liquid points under different voltages and electric fields, and so subjected water menisci hanging from a capillary tube to strong electric fields. He observed that at high electric field strengths the menisci would become electrically stressed and would oscillate to overcome the excess energy applied to it and would eventually become very unstable and shatter into several smaller drops **[71]**. Zeleny later specifically studied the meniscus oscillation and observed that when the voltage is increased, instead of a steady hemispherical shape the meniscus deforms into a conical shape with some liquid extending out from the apex of the cone. He also noted several other unstable shapes the meniscus would take if the electric field was further increased or if the flow rate was changed, becoming the first person to classify the different spraying modes of EHDA. These unstable menisci are shown below in Figure 2.16. Zeleny also observed the electrical discharge from the liquid meniscus at increased electric field strengths and

noted that when they occur, these electrical discharges lead to a decrease in the field strength around the pendant drop and so the drop instability would cease or decrease until the field strength increased again **[72]**.

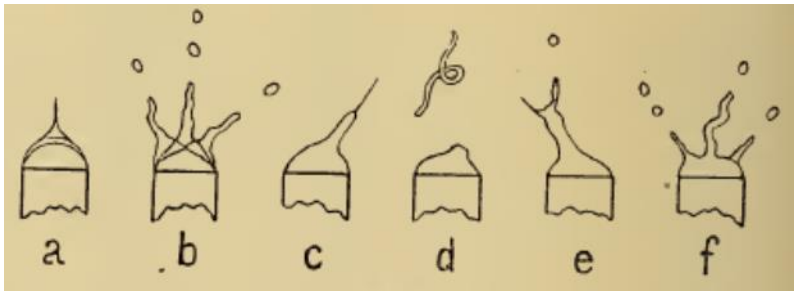

*Figure 2.16. The different forms of unstable menisci as the electric field is increased from capillary a through to f **[71]**.*

Following these major breakthroughs, the next two decades did not show much progress in the field of electro-spraying. Several researchers continued trying to understand the breakup mechanisms of electrified liquid droplets through rigorous experimentation. Wilson and Taylor carried out experiments with charged soap bubbles and determined the pressure difference between the capillary and electric stress that would cause the bubble to burst **[73]**. Nolan on the other hand doubted whether these results from Wilson and Taylor's soap bubble experiment could be extrapolated for liquid drops due to geometric and physical property differences **[74]**. He therefore, conducted several experiments on the breaking of falling water drops, and found that for smaller drops the Wilson and Taylor prediction was valid. However, it was not valid for larger drops (i.e. grater than 2 cm) therefore concluding that the physical properties of the drop (which at the time were commonly ignored) do in fact play an important role during electro-spraying and a simple relation between the electric field and size of the drop could not be applied to all systems. Macky carried out similar experiments on soap bubbles as done by Wilson and Taylor. He observed that after a critical increase in the electric field the conical shape of the soap bubble starts elongating exponentially and liquid is emitted from its apex in a vey fine jet **[75]**. Figure 2.17 shows the soap bubbles observed by Macky as the electric field was increased from zero to the critical value for filament ejection from the conical apex.

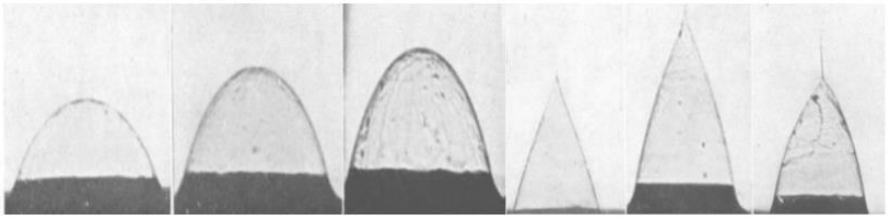

Figure 2.17. Soap bubble meniscus deformation from hemispherical to conical as the electric field applied to it is increased from left to right ***[75].***

Macky further continued his study but now on the deformation of falling water drops in an electric field. He observed that the falling drops were elongated and changed from spherical to a prolate spheroid shape with pointed ends. At both these ends filaments of liquid was drawn out from which small water droplets were ejected. This is shown in Figure 2.18 below. Macky observed no significant changes in the electric field required for such deformation when the polarity of the voltage was changed. However, he did note that the discharges occurred at a slightly lower electric field strengths in negative fields which resulted in the more unstable brush discharges as opposed to corona discharges in positive fields **[76]**. During discharges the current is supplied into the atmosphere around the droplet and is carried by the gas. On this topic from a later study Zeleny concluded that under stable conical spraying operations the current is carried entirely by the droplets, but if ionisation is also present the atmosphere around the drop would also carry some charge from the system **[77]**.

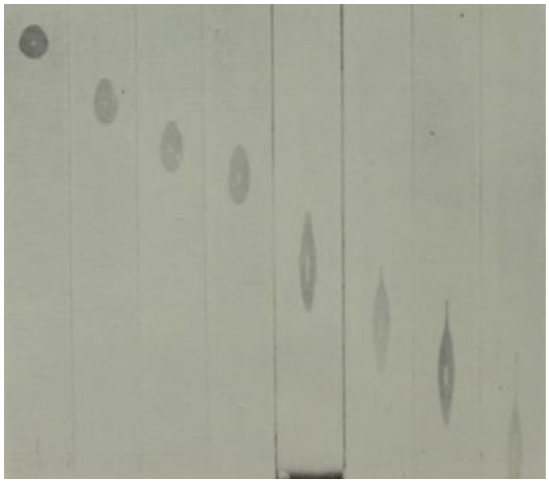

Figure 2.18. Water droplet deformation from spherical to a prolate spheroid as it falls through a strong electric field ***[76]***

English continued the study on discharges from a water drop and tried to analyse them from both positive and negative water drops of different diameters **[78]**. He observed the change in spraying modes from a dripping mode to a fan like spray mode at higher voltages to a region of instability with an even further increase in voltage as had been earlier classified by Zeleny. English noted that for a negatively charged droplet the onset of discharge was at a lower voltage, verifying Macky's results.

Vonnegut and Neubauer conducted several experiments in hopes to produce mono-dispersed droplets of 100 micrometres using an AC or DC positive electrostatic field **[79]**. They also measured the charge of the droplets and observed that the droplets in a DC field were all similarly charged but in an AC field droplets had no net charge, as half the droplets had one sign charge and the other half had the opposite sign charge. They too, however, just as previous researchers, could not quantify experimentally the total charge in the system due to ionisation such as corona discharges into the atmosphere around the droplets. Neubauer and Vonnegut took this study further and tried to vary the electrical conductivity of the liquids between 10-5 to 10-2 S/m **[80]**. From their analysis they concluded that there exists some upper limit of electrical conductivity beyond which atomisation is not possible.

Drozin conducted similar studies to test the dispersibility of different liquids by applying an increasing voltage to the pendant drop of a liquid with specific properties being ejected from a capillary. While not generating any explicit numbers, Drozin found that only polar liquids can be dispersed **[81]**. The different modes of dispersion observed by Drozin are shown below in Figure 2.19. The results of Vonnegut and Neubauer, and Drozin may seem to lack much substance considering the major developments in electro-spraying today. However, it should be noted that these early studies were the first to show the importance of both the liquid properties and electrode geometries in EHDA, as several studies in the past had only focussed on the applied voltage and droplet size as the governing factors.

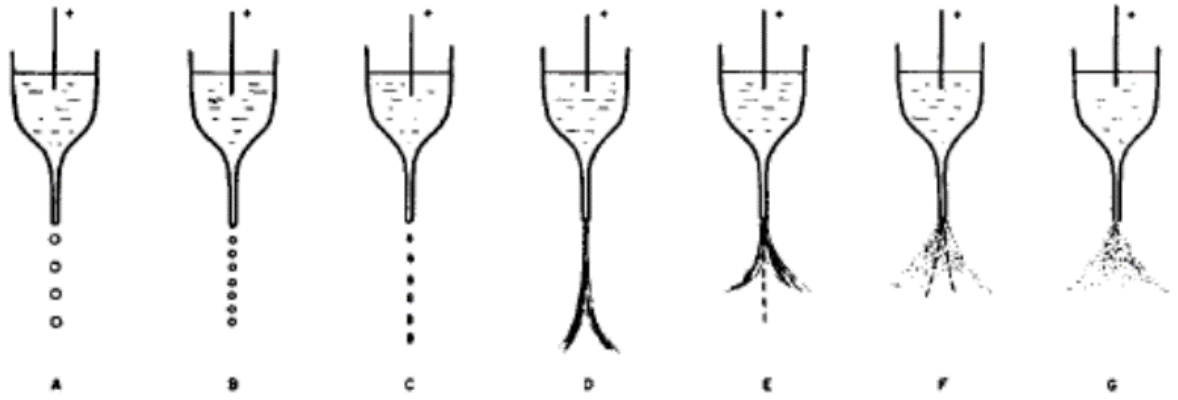

Figure 2.19. Stages of dispersion observed as the applied voltage is increased from A to G ***[81]***

Continuing his work on electrically stressed soap bubbles, Taylor extended this study to also include the breakup of glycerine and glycerine-water drops **[82]**. To study the effects of geometric parameters, he placed the capillary tube (that was positively charged) face up towards a curved counter electrode, thereby negating the forces of gravity on the pendant drop. Through his work, Taylor produced what can be regarded as the greatest qualitative results in the field of EHDA. As he correctly predicted the voltage and the electric field required to disintegrate a hemispherical pendant drop droplet into a conical shape. He also proved that his mathematical approximation of the conical half angle of 49.3° aligned perfectly with what he observed experimentally. Finally, he also went on to observe that smaller droplets would not be produced directly from a larger pendant drop, but in fact a filament would be extended from the apex of the conical meniscus, which in turn would then break into finer droplets, several magnitudes in size smaller than the radius of the original drop. The observation made by Taylor on the deformation of a droplet with an increased voltage is presented in Figure 2.20 below.

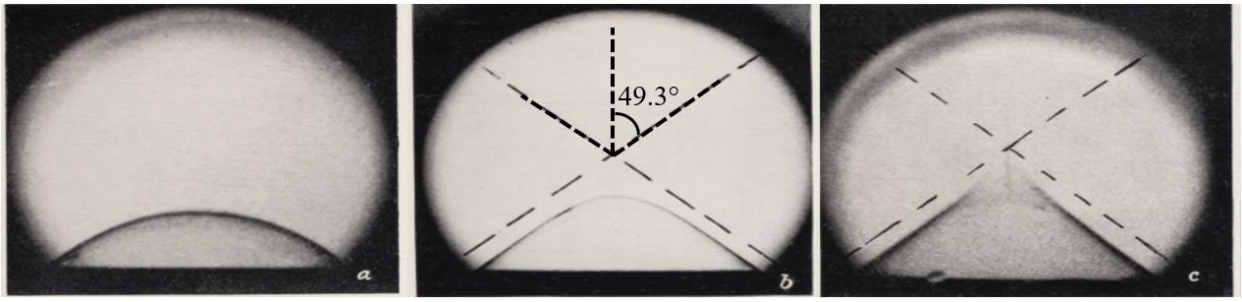

Figure 2.20. The effects due to the electric stress on a hemispherical droplet leading to its deformation into a conical shape as the voltage applied on it is increased from left to right (a to c) ***[82]****.*

However, there were a few drawbacks to Taylor's mathematical predictions as he was assuming the liquid had to be a perfect electrical conductor and any conical menisci that deviated from his calculation of 49.3° would be unstable. This was later debated on by several researchers and proved otherwise. Taylor also concluded that the voltage required to distort the pendant drop was related only to the liquid surface tension and the electrode geometry. However, it was later proven that several other factors also played a major role such as the liquid's density, viscosity, and electrical conductivity, as well as the atmospheric conditions.

2.2.2 Characterisation and Classification of the Different Modes of Electro-spraying

Taylor's work established the physics behind the deformation of a conical meniscus and hanging pendant drop, however the size of the ejected droplets and the number of droplets emitted was still an unknown. Furthermore, there did not exist any commonly agreed upon classification modes of electro-spraying. Hendricks tried to calculate the maximum charge to mass ratio of the dispersed droplets in order to predict the average size and number of droplets produced during different spraying modes in order to develop a uniform theory for EHDA **[83, 84]**. After applying the Rayleigh maximum charge equation to the continuity equation, he related the charge to mass ratio of droplets to their diameter, density, and surface tension. This prediction was known as the 'minimum energy state solution' for electrostatic atomisation that unified all EHDA spraying modes but was then later regarded as inaccurate as researchers found that there are several other factors such as droplet evaporation and gas ionisation that also carried the charge and were not

properly accounted for. Schweizer and Hanson conducted similar experiments to those done by Hendricks, to study the charge to mass ratio after the pendant drop is dispersed into smaller droplets **[85]**. They observed that the charge to mass ratio was in fact more aligned with Rayleigh's maximum charge limit rather than the minimum energy state solution. This may be because of a much lower atmospheric ionisation as weaker electric fields were used in their study. Krohn also objected the minimum energy state solution **[86]**. He showed that after analysing data from several previous researchers, their charge to mass ratio was in fact higher than that predicted by this theory. But the analysis was also slightly lower than the Rayleigh instability limit. This could be due to the low-level ionisation that goes unnoticed and so he concluded that the minimum energy state solution was an unsuitable hypothesis. Similar conclusions were also drawn by Bollini et. al. as they tried to electro-spray molten tin and bismuth **[87]**. They did observe that an increase in voltage led to an increase in droplet frequency and a decrease in droplet size. However, when analysing their charge to mass ratios they did conclude that their values were below the Rayleigh limit but much higher than the minimum energy state solution.

Following these inaccuracies in predicting the charge to mass ratio, several studies were done focussing on better understanding the physical mechanisms for stable electrostatic atomisation. The failure of the minimum energy state solution showed that having one single theory that ties all the EHDA spraying modes was an unrealistic and unreliable approach. Different modes of spraying were stable for a small range of applied voltages after which a transition in the spray mode took place as the voltage was increased. During the transition phase the spray was unstable, and the droplets produced had a wide size distribution and uneven geometry. Special attention was given to the cone-jet atomisation as it had been observed to be very stable and led to uniform spraying of mono-dispersed micrometre sized droplets. Hayati et. al. conducted several studies in this regard. They observed through experimentation the shape of the conical meniscus and the process of jet formation for liquids of varying physical properties being atomised in different gaseous environments **[88]**. They noted that the equilibrium conical shape observed and predicted by Taylor (49.3°) was different from the angles of 18° – 58° they observed while electro-spraying, and furthermore, these were highly dependant on the flow rate, applied voltage and the specific liquid properties **[89]**. Figure 2.21 below shows the dependence of the applied voltage to the shape of the conical meniscus and the emitted jet as recorded by Hayati et. al. during their study.

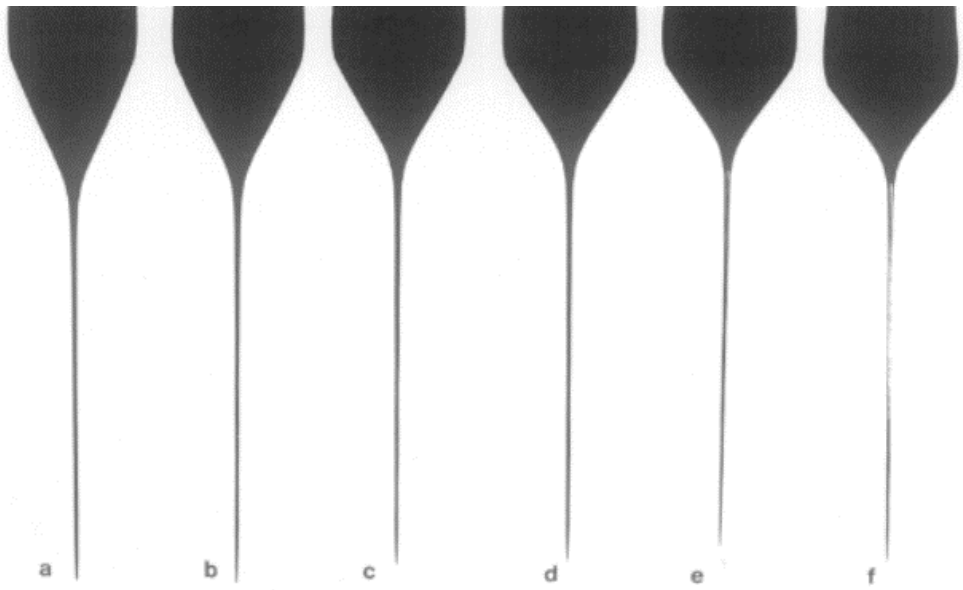

Figure 2.21. Variation of the conical meniscus and emitted liquid jet as the applied voltage is increased from figure a-f ***[89]***

From Figure 2.21, it can be noted that as the voltage is increased the conical angle increases and the jet produced decreases very slightly in diameter due to the increased electrical stresses on the liquid. Hayati et. al. also showed that several other factors such as the charge to mass ratio, droplet size, and droplet size distribution were heavily dependant on the operating and physical parameters during each experiment. They also tried to finalise their electro-spraying quantification through a mathematical model whereby they argued against the perfect conductor assumption made by Taylor and several other researchers **[90]**. In their study they presented a model claiming only semi-conductors could be atomised through electro-spraying, and while no definite values were stated, they claimed there exists an upper electrical conductivity limit of the liquid, beyond which a stable conical meniscus would not form.

Smith also conducted similar experiments by varying the liquid properties to better understand their effect on atomisation **[91]**. He showed that the conical meniscus was in fact not an equipotential surface and there existed both radial and tangential electric fields on its surface. This meant that within the conical meniscus there exist convection currents of the liquid in the radial and axial direction and the flow does not have a flat profile. Furthermore, from his mathematical model he concluded that there should exist no upper limit for conductivity as the conical meniscus can always be stabilised provided the correct operating conditions are applied.

Cloupeau and Foch also conducted a similar study with liquids of varying properties to better understand and finalise the debate on whether there existed an upper limit of electrical conductivity for electrostatic atomisation **[92]**. While all their experiments were conducted with liquids having an electrical conductivity in the range of 10^{-9} to 10^{-2} S/m (i.e., they never studied high conductivity liquids), they never found a limit for electrostatic atomisation in the studied range. Along similar lines, Mahoney et al. tried to apply EHDA in the cone jet mode to produce metal powders. Their system was constructed to accomplish atomisation of a continuously fed wire that was charged to a high voltage. The wire would be melted at the tip and due to the electrohydrodynamic instability the liquid melt would be sprayed into smaller droplets. While their results did show that micron and submicron sized powders could be created, Mahoney et. al. never explored any electro-spraying phenomena and their relation to different physical, operating, or geometric parameters. However, this study did show that even liquids with very high conductivity (i.e., liquid metals) could be atomised **[8]**.

While these studies showed great improvements and understanding of a specific mode of electro-spraying, i.e., the cone-jet mode, Cloupeau and Foch battled another major obstacle in trying to understand EHDA. They aimed to unify the different modes of spraying, not through a single mathematical theory such as the minimum energy state theory, but rather through a unified qualitative and quantitative approach. They undertook this task and after extensive analysis of the different physical and operating parameters they developed one of the best classifications of electrohydrodynamic atomisation spray modes **[93, 94, 95]**. This classification was based on the appearance and deformation of the meniscus and liquid jet after being electrically stressed. The different forms of electro-spraying range from dripping and micro-dripping modes whereby droplets similar in size to the capillary are produced, to cone-jet and ramified jet modes that produce micron size droplets in a spray form. This showed that for a certain liquid there exists a specified range of operating conditions for each electro-spraying mode and therefore one unified theory to explain and predict all atomisation modes would be very difficult to obtain and would have several inaccuracies. Shriyaeya and Grigor'ev also proposed a different mechanism of classification of the different modes of electro-spraying as compared to that of Cloupeau and Foch **[96, 97]**. They proposed a time related mechanism that accounted for the operating and geometric parameters, as well as the different physical properties of the liquid. The time related mechanism includes the generation of relaxation times for all the different stresses incurred on the liquid when

electro-spraying (inertia, viscous, surface tension, and electrical stresses). As the mode of spraying changes from one form to another, the dominant stresses would also change, for example in the dripping mode the electrical stresses and surface tension would be dominant, but in the cone-jet mode the inertia would become important as well. As such the relaxation times would also change, and so Shriyaeya and Grigor'ev proposed that the different relaxation times could be used to classify the specific modes of electrospraying.

Jaworek and Krupa extended these studies and tried to unify both methods of classification **[98, 99]**. After rigorous experimentation and observation with varying liquid properties and a wide range of operating conditions, they classified up to ten different modes of atomisation. These ranged from pulsating modes (such as dripping and micro-dripping modes) during which fragments of liquid are ejected from the capillary nozzle at regular intervals, to continuous jet disintegration modes (such as the cone-jet and ramified jet modes) during which a continuous length of liquid is disintegrated into droplets. Understanding and determining these modes of operation are very valuable as EHDA is a very volatile field with respect to the operating, geometric and physical parameters, which if not appropriately assessed would lead to irregularities in the droplet/spray production. The details about the different atomisation spray modes can be found in the works of Jaworek and Krupa **[98, 99]**. For this study the primary focus is based on the cone jet mode of EHDA due to its uniformity and high level of control in droplet sizes.

2.2.3 The Cone-Jet Mode of Electrohydrodynamic Atomization

This is the most extensively studied mode of EHDA and it is widely applied in several industries. The term cone-jet was coined by Cloupeau and Foch due to its physical appearance. It is also called the Taylor cone mode of electro-spraying as it includes the formation of an electrically stressed conical meniscus that was first accurately studied by Taylor. In this mode the existing liquid meniscus changes shape from hemispherical to an inverted cone shape due to the electrical stresses applied to it. From its apex a thin jet (in many previous studies also called a filament) is ejected that is a several orders of magnitude smaller than the base of the cone. The schematic below represents a stable cone jet mode.

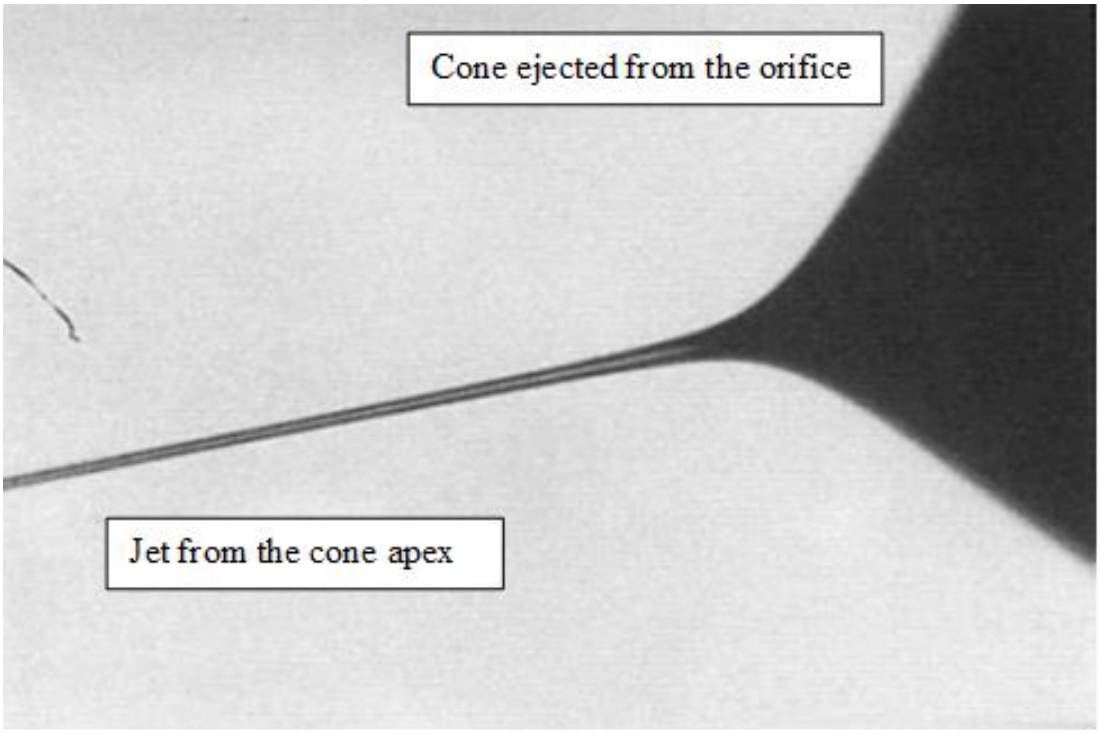

*Figure 2.22. The cone and jet shape as shown by De La Mora and Loscartles **[102]***

The jet which is ejected from the conical meniscus breaks up into droplets due to growing surface instabilities. This breakup can be of three different forms depending on the flow rate and the surface charge on the jet. At low surface charges (low electric stresses) the jet will breakup due to varicose instabilities. As the surface charge and flow rate are increased the instabilities will change to a kink form and then to a ramified jet mode with even further increases. These different breakup modes are described below by Hartmann et. al. in a simple drawing shown below in Figure 2.23 **[100]**.

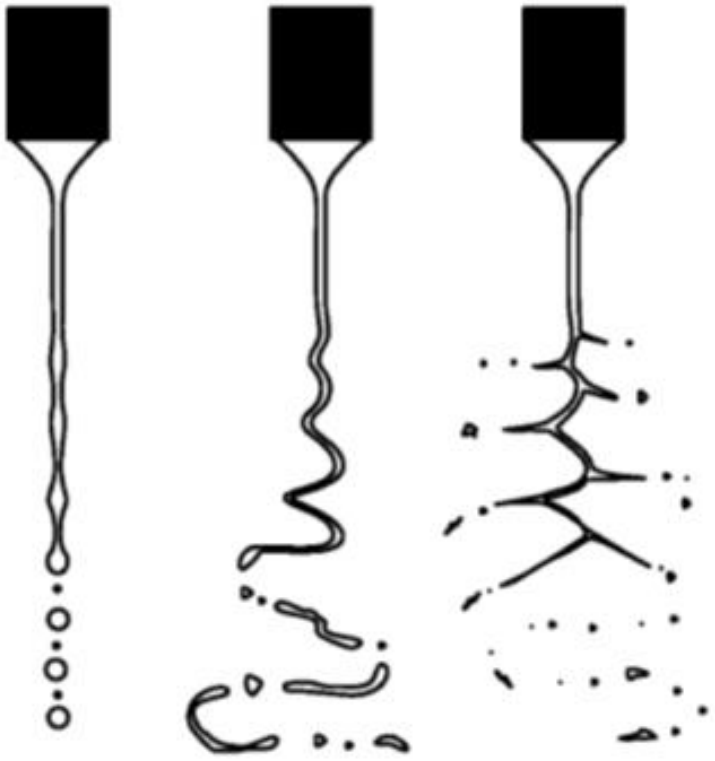

*Figure 2.23. The jet breakup modes due to varicose, kink, and ramified jet instability from left to right **[100]**.*

The varicose instability involves similar breakup to that of a free-falling Rayleigh jet whereby standing waves are formed on the jet and at every nodal point liquid is pinched off to balance the surface energy, forming droplets of uniform size. The kink instability and the ramified jet instability are much more irregular due to a high charge to volume ratio and a higher flow rate. Therefore, the jet rapidly and randomly oscillates to balance the extra supplied energy causing it to break into a series of non-uniform ligaments and droplets. An even higher charge to volume ratio would cause the jet to branch out into multiple smaller jets and break into a shower like spray. This is very important in the paint industry but produces droplets of a wide range of sizes from a few micrometres to a few hundred micrometres. In this study the focus will be solely on the varicose mode of the cone jet, due to its high level of stability (easiest to predict and control) as well as the narrow range of particle size distribution.

2.2.4 Modern Electrohydrodynamic Atomisation Studies and Applications

Following the classification of the different modes of EHDA a lot of focus was placed on understanding and quantifying these modes through numerical and analytical mathematical models. These models were developed to better understand the shapes of the menisci, the sizes of the droplets produced and the effects of the operating conditions, geometric arrangement, and physical properties of the liquids on the different modes of EHDA. In developing these models most of the focus has always been placed on the cone-jet mode of electro-spraying due to its high stability. Fernandez De la Mora pioneered some of this work and presented a numerical model to better understand the conical meniscus and why several studies had shown cone angles that deviated from the Taylor angle (of 49.3°) **[101]**. While obeying Taylor's basic laws and boundary conditions, De la Mora observed that in his experiments the stable cone angle when spraying was less than that of Taylor's prediction and resided in the range of 32° – 46°. De la Mora concluded that this was because the cone and spray were charged and these were modifying the field around the meniscus, causing the meniscus to reduce to a lower angle but still remain stable. De la Mora and Loscartles continued this work but made a few modifications by including the surface charge of the cone and jet to study their effects on the meniscus **[102]**. Through their studies and after extensive experimentation they found several scaling laws for the flow rate, current emitted and the jet diameter. These scaling laws have been continually modified and adjusted by several researchers over the past 25 years to incorporate a wider range of liquids or to adjust for different geometric and operating conditions. The details of the different scaling laws and their applications have been outlined in review papers by Xie et. al., and by Jaworek, and are considered quite accurate for both small and large scale applications **[7, 103]**.

However, since the turn of the century, the focus on electro-spraying and EHDA has moved more towards the industrial application of this process rather than model development. EHDA is now commonly used in the paint and ink-jet printing industry, as well as in fuel injection engines, food processing, drug development and delivery, and also to generate nanoparticles for mass spectrometry **[104, 105, 106, 107, 108]**.

2.3 Summary

In this chapter, two droplet production processes, the continuous liquid jet break up and electrohydrodynamic atomization have been reviewed. Focus was placed primarily on low velocity laminar jets when discussing continuous jet disintegration, and on the con-jet mode when discussing EHDA. The different theoretical advancements, and applications of these processes with regards to droplet production have also been noted and reviewed.

Liquid jets when manipulated with vibrations of appropriate frequencies can disintegrate in a very orderly fashion, producing droplets of uniform size and shape. While this phenomenon has been tried and tested by several researchers, generating smaller droplets (< 100 μm) becomes quite challenging. This is because smaller orifices are needed, which in turn would require very high overhead pressures and vibration frequencies, making the overall system quite difficult to control and operate.

In the field of EHDA it was noted that if a jet is appropriately charged, it would reduce significantly in diameter before break up. However, for a jet to undergo such a process the flow must be kept very low (~ 10 μL/s), and a significant voltage must be applied. This makes EHDA an impractical approach in trying to generate droplets for industrial applications.

Therefore, a new atomization approach has been proposed. This will be a two step (two physics) approach, combining the knowledge of vibrated jet breakup and EHDA. In the first step, a system will be designed and developed such that it can generate uniform droplets due to applied disturbances in the bulk liquid. In the second step, the knowledge gained from EHDA will be applied. As such the atomization process will also have in place a system that can charge the jet as it exits the office. This will push the jet to reduce in diameter. With both these systems in place droplets of smaller sizes can be created.

Chapter 3: Mathematical Models

This chapter will cover the mathematical models used and developed in this study. Empirical equations and correlations developed from previous studies will also be mentioned. In this chapter only the varicose breakup mode will be discussed. This Chapter will be divided into five (5) sections. The first section will briefly introduce the different forces involved in jet breakup and their dependance on the different physical and experimental parameters. The linearized analytical approach developed by Rayleigh will be covered next. The third and fourth sections will focus on the equations of the length of the jet before breakup, and the exit velocity of the jet, respectively. Finally, the last section will focus on the Bernoulli – Electrostatic approach in order to determine the relative importance of forces acting on the jet from the moment it exits the nozzle, to the point of breakup.

3.1 Forces Acting on a Liquid Jet

There are five forces of interest acting on the jet. These include: the inertial, viscous, gravitational, surface tension, and electrostatic forces. These forces vary in magnitude depending on the liquid properties and the experimental conditions.

a) Inertial Force

The force of inertia is a result of the momentum of the fluid, and it is usually expressed by the velocity and the density of the material. For example, following Newton's laws of motion the inertial force ($F_{inertia}$) can be represented using the mass of the body (m) and its acceleration (a), as shown in Equation 3.1 below. The mass and acceleration are simply the derivatives of the density and velocity of the system, respectively.

$$F_{inertia} = ma \tag{3.1}$$

In the Rayleigh regime the inertial forces are one of the dominant factors governing jet breakup. An increase in the inertial forces would lead to an increase in the breakup length as discussed in Chapter 2. However, if the velocity of the jet is increased beyond a certain critical value, then the

flow may transition to a turbulent regime with increased aerodynamic effects, and thus the breakup will change from the varicose mode to a more chaotic type.

b) Viscous Force

The viscous force is dictated by the liquid viscosity and the rate at which the fluid velocity changes in space. The viscosity of a liquid determines the resistance to flow, as it is a result of friction (the amount of shear) between layers of fluid. The magnitude of the viscous force ($F_{viscous}$) for a fluid flowing over a 2D plate is presented in Equation 3.2 below. The force is directly proportional to the viscosity (μ), liquid velocity (v_0), and the area along which the fluid flows (A), and it is indirectly proportional to the separation distance between the topmost and bottommost liquid layers (l).

$$F_{viscous} = \mu A \frac{v_0}{l} \tag{3.2}$$

The viscous forces have an effect on the velocity of the jet formed as it exits the orifice (as will be discussed in Section 3.4). They also play a part on the breakup of the jet and the propagation of disturbances along its surface. In the Rayleigh regime, the viscous forces have an effect of damping out small wavelength disturbances along the jet. As such only perturbations of larger wavelengths will be allowed to grow and lead to jet breakup. The jet would therefore extend much further downstream before disintegrating.

c) Gravity

The gravitational force is simply a law of attraction between all matter. While the force of gravity is a governing factor in the dripping regime, it has little effect in the breakup of continuous jets. This will be addressed in a later topic in this thesis.

d) Surface Tension Force

This is the cohesive force in fluids that pulls the liquid molecules into one another in order to minimize the surface area[3]. It is governed by the surface tension coefficient of the fluid and the length along which the force is acting. The effect of the surface tension force is much better represented through the surface energy pressure balance derived by Young and Laplace in the early 19th Century as shown in Equation 3.3 below **[109]**:

$$P_{st} = \gamma\left(\frac{1}{R_1} + \frac{1}{R_2}\right) \tag{3.3}$$

The terms R_1 and R_2 are the principle radii of curvature in the radial and axial directions respectively. For spherical objects such as liquid droplets, these curvatures are identical. However, that is not the case for a liquid cylinder (i.e., an unperturbed jet) as shown Figure 3.1 below:

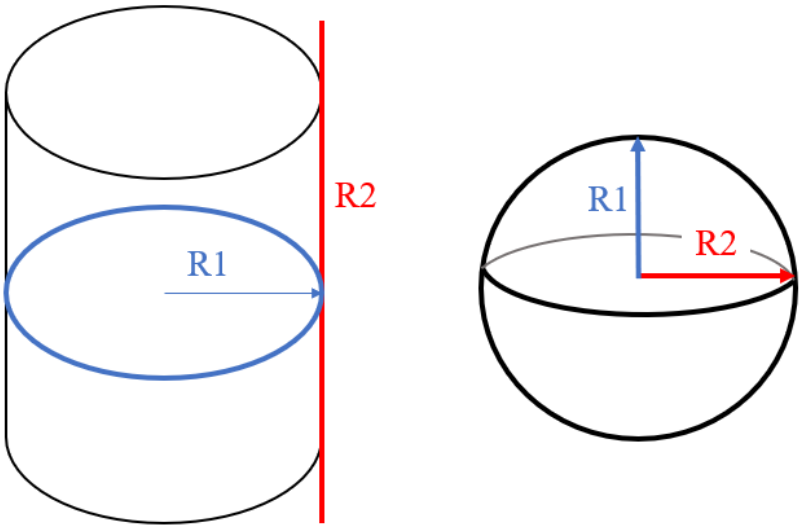

Figure 3.1. Curvatures R1 and R2 for a cylinder and a sphere of radius r_0

From Figure 3.1 it can be noted that for a straight cylinder the axial radius of curvature (R_2) is much greater than the radial radius of curvature (R_1). Equation 3.3 can thus be modified to a simpler form as:

[3] It is important to note that throughout this study, unless otherwise specified, surface tension refers to the gas – liquid surface tension.

$$R_1 = r_0 \tag{3.4}$$

$$R_2 \to \infty \tag{3.5}$$

Therefore,

$$P_{st} = \frac{\gamma}{r_0} \tag{3.6}$$

e) Electrostatic Force

An Electrostatic force arises from the electrical charges carried by materials. The intensity of this forces is determined by the strength of the electric field (i.e., the charge density and distance between charged materials) **[[110]]**. This study deals with a particularly difficult case of electroquasistatics, as a flowing jet is stressed into a Taylor cone of a much smaller diameter due to the constant electric field created around it. The simplest way to account for this would be through the classical electrodynamic model put forth by Landau and Lifshitz, which states that the electric stress on a liquid can be given by the Maxwell stress tensor **[[111]]**. Similar conclusions have been independently derived by Melcher and Warren, and have also been used in modelling electrodynamic jet formation by Benignos, and Munoz **[112, 113, 114]**.

The Maxwell stress tensor (σ^e_{ij}) as outlined by Castellanos for a linear, homogeneous, and isotropic medium, is shown in Equation 3.7 **[115]**:

$$\sigma_{ij}^e = \varepsilon_0 E_i E_j - \frac{1}{2} E_k E_k \delta_{ij} \tag{3.7}$$

Whereby ε_0, is the electrical permittivity of free space, E_i is the electric field in the respective direction, and δ_{ij} is the Kronecker-delta function. This can further be broken down into a normal component of the electric stress (σ_n^e) and a tangential component (τ_n^e) as shown below:

$$\sigma_n^e = \frac{\varepsilon_0}{2}\left(E_n^{o\,2} - E_n^{i\,2}\right) + \frac{\varepsilon_0}{2} E_t^2 \tag{3.8}$$

$$\tau_n^e = \varepsilon_0 E_t \tag{3.9}$$

Where E_n^o represents the outer normal electric field, E_n^i the inner normal electric field, and E_t the tangential electric field on the surface. However, Taylor's hypothesis was that the liquid is an equipotential surface and a perfect conductor. Therefore, there ceases to exist an internal electric field and tangential electric field, i.e.:

$$E_n^i = E_t = 0 \tag{3.10}$$

It follows, that only the normal electric field plays a part in stressing the liquid. Thus, the pressure due to the electric stress on the liquid can be given as:

$$P_E = \frac{1}{2}\varepsilon_0 E_n^2 \tag{3.11}$$

In electro-spraying, the pressure balance between the surface tension and electrostatic forces can now be given as:

$$P_{EHDA} = \frac{\gamma}{r_0} - \frac{1}{2}\varepsilon_0 E_n^2 \tag{3.12}$$

3.1.1 Quantifying the Forces Acting on a Liquid Jet

The impact different forces have on a liquid jet are very dependent on the thermophysical properties of the jet, as well as on the experimental parameters. Good insight into electrostatically assisted atomization can be achieved by assessing the relative importance of forces acting on a stream. Therefore, dimensionless numbers that represent the forces in fluid mechanics and electro-spraying will be introduced. The 6 dimensionless numbers used in this study are shown in Table 3.1:

Table 3.3. List of dimensionless numbers used in this study

Dimensionless number	Abbreviation	Equation	Force Ratio
Reynolds	Re	$\rho v_0 d_0 / \mu$	$Inertial / Viscous$
Weber	We	$\rho v_0^2 d_0 / \gamma$	$Inertial / Surface\ tesnion$
Ohnesorge	Oh	$\mu / \sqrt{\rho \gamma d_0}$	$Viscous / Inertial * Surface\ tension$
Froude	Fr	$v_0^2 / g d_0$	$Inertial / Gravity$
Bond	Bo	$\rho g d_0^2 / \gamma$	$Gravity / Surface\ Tension$
Electrical Bond	Es	$\varepsilon_0 E_n^2 d_0 / \gamma$	$Electrostatic / Surface\ Tension$

3.2 Plateau – Rayleigh Instabilities

The Plateau – Rayleigh instability describes the process whereby a continuous cylindrical column of liquid breaks up into droplets, as presented in Figure 3.2 below.

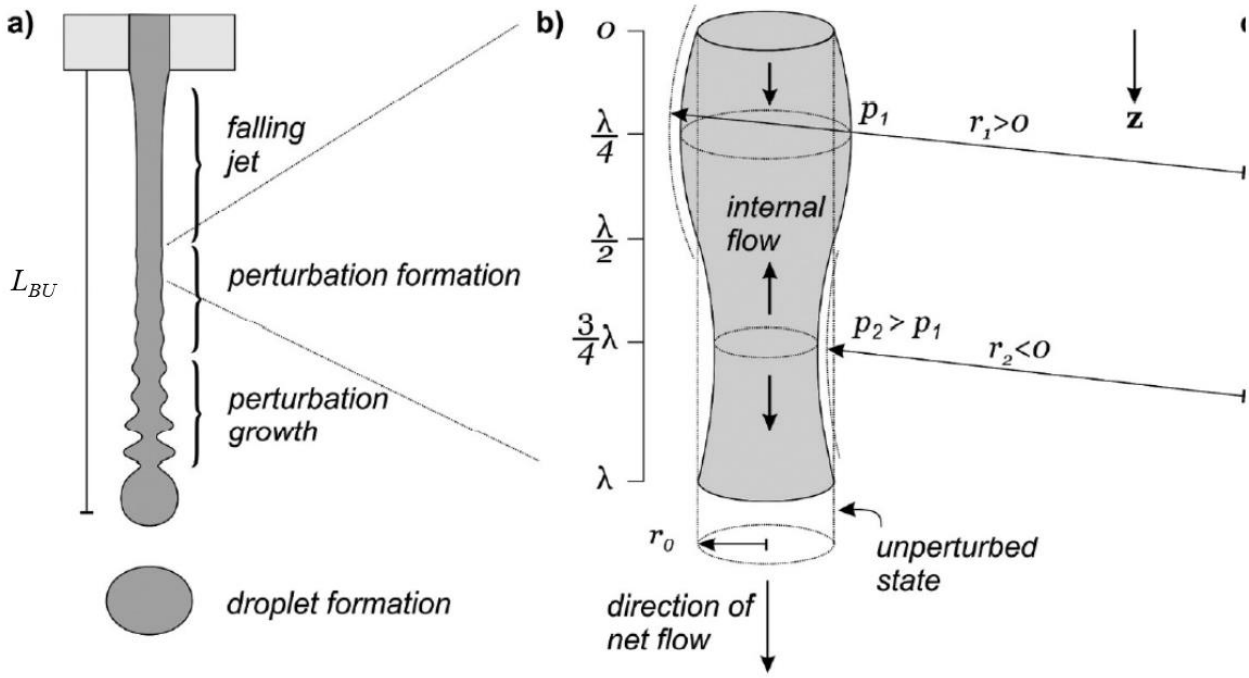

Figure 3.2. Schematic of the Plateau-Rayleigh instability on a liquid jet. a) Formation and growth of the perturbation zones, leading to jet breakup and droplet formation. b) Details of the perturbations on the jet that lead to Young-Laplace pressure gradients due to the jet curvatures ***[116]****.*

This hypothesis was originally derived by Plateau and later built on and proven analytically by Rayleigh. Here unstable disturbances of specific wavelengths grow in amplitude along the jet until which a droplet is pinched off. The general description of the Rayleigh breakup has been discussed in Section 2.1.1. Rayleigh's analytical approach on jet breakup will be presented. It shows the fastest growing disturbance as well as the droplet sizes produced from a mathematical standpoint. It is important to note that in this analysis the liquid is assumed to be inviscid and aerodynamic effects are completely ignored. The only forces considered are the surface tension and the inertial effects.

In an equilibrium state, the liquid jet would be an infinitely long cylinder of radius r_0. However, as perturbations grow along the surface, Rayleigh hypothesized that the radius of the jet would be related to the amplitude of the disturbance (η, where $\eta << r_0$), the growth rate of the instability (ω, which is also called the angular frequency), the wavenumber (k), and the distance in the axial direction (z). Therefore, the evolution of the radius of the jet is given by:

$$r_j = r_j(r,z,t) = r_0 + \eta e^{\omega t + ikz} \tag{3.13}$$

Rayleigh hypothesized that a perturbation in the radius would also lead to similar perturbations in the velocity of the jet in both the radial (v_r) and axial (v_z) directions, as well as in the pressure inside the jet (p_j). These are shown below as:

$$v_r = v_r(r,z,t) = v_{r,0} e^{\omega t + ikz} \tag{3.14}$$

$$v_z = v_z(r,z,t) = v_{z,0} e^{\omega t + ikz} \tag{3.15}$$

$$p_j = p_j(r,z,t) = p_{j,0} e^{\omega t + ikz} \tag{3.16}$$

Having defined the different parameters, the Navier – Stokes Equation can now be applied in order to understand the motion of the liquid.

$$\rho \frac{D\vec{v}}{Dt} = -\Delta P + \rho g + \mu \nabla^2 \vec{v} \tag{3.17}$$

In Rayleigh's linearized approach the liquid is assumed to be inviscid and so the viscous effects can be neglected. The body force (i.e., gravity) is also assumed to be negligible and can also be eliminated. The reason for this will be discussed further in Chapter 4. Finally, the system is assumed to be symmetric around the azimuthal axis. This reduces the Navier – Stokes Equation (Equation 3.17) to a simple Euler Equation which can be written in the radial and axial directions as:

$$radial: \quad \frac{\partial v_r}{\partial t} + v_r \frac{\partial v_r}{\partial r} + v_z \frac{\partial v_z}{\partial r} = -\frac{1}{\rho} \frac{\partial p_j}{\partial r} \tag{3.18}$$

$$axial: \quad \frac{\partial v_z}{\partial t} + v_r \frac{\partial v_r}{\partial z} + v_z \frac{\partial v_z}{\partial z} = -\frac{1}{\rho} \frac{\partial p_j}{\partial z} \tag{3.19}$$

Substituting the appropriate derivations of Equations 3.14 – 3.16 into Equations 3.18 and 3.19 gives:

$$radial: \quad e^{\omega t + ikz}\left(v_{r,0}\omega + v_{r,0}\frac{dv_{r,0}}{dr}e^{\omega t + ikz} + v_{z,0}\frac{dv_{z,0}}{dr}e^{\omega t + ikz}\right) = -\frac{1}{\rho}\frac{dp_{j,0}}{dr}e^{\omega t + ikz} \tag{3.20}$$

$$axial: \quad e^{\omega t + ikz}\left(v_{z,0}\omega + ikv_{r,0}^2 e^{\omega t + ikz} + ikv_{z,0}^2 e^{\omega t + ikz}\right) = -\frac{1}{\rho} ikp_{j,0} e^{\omega t + ikz} \tag{3.21}$$

Following Rayleigh's linearized approach, the perturbations are assumed to be small and therefore all the terms that contain the expression $(\exp(\eta\omega t+ikz))^2$ can be neglected. The equations in the radial and axial directions can thus be written as:

$$radial: \quad v_{r,0}\omega = -\frac{1}{\rho}\frac{dp_{j,0}}{dr} \tag{3.22}$$

$$axial: \quad v_{z,0}\omega = -\frac{1}{\rho}ikp_{j,0} \tag{3.23}$$

Equations 3.22 and 3.23 show that the velocity in the radial and axial directions are both related to the pressure of the jet. From this a correlation between the axial and radial velocities can be developed, by first applying the derivative d/dr on both sides of Equation 3.23, and then replacing the pressure term in Equation 3.22 with the axial velocity.

$$v_{r,0} = \frac{1}{ik}\frac{dv_{z,0}}{dr} \tag{3.24}$$

Having developed this correlation, the mass conservation equation can be introduced to better understand the relation of the different velocity components with respect to the different coordinate axes.

$$\frac{1}{\rho}\frac{\partial\rho}{\partial t} + \frac{1}{r}\frac{\partial}{\partial}(rv_r) + \frac{1}{r}\frac{\partial v_\theta}{\partial\theta} + \frac{\partial}{\partial z}v_z = 0 \tag{3.25}$$

The liquid jet is assumed to be incompressible and symmetric around the azimuthal axis and as such the first and third terms from Equation 3.25 can be ignored. Equation 3.25 reduces to:

$$\frac{\partial v_r}{\partial r} + \frac{v_r}{r} + \frac{\partial v_z}{\partial z} = 0 \tag{3.26}$$

Following a similar methodology as before, and applying the appropriate derivations of Equations 3.14 – 3.16 into Equation 3.26, along with the derivative d/dr on both sides of Equation 3.26 yields:

$$\frac{d^2v_{r,0}}{dr^2} - \frac{v_{r,0}}{r^2} + \frac{1}{r}\frac{dv_{r,0}}{dr} + ik\frac{\partial v_{z,0}}{\partial r} = 0 \tag{3.27}$$

Equation 3.23 can now be placed into Equation 3.27 to give a second order homogenous ordinary differential equation:

$$\frac{d^2v_{r,0}}{dr^2} - \frac{v_{r,0}}{r^2} + \frac{1}{r}\frac{dv_{r,0}}{dr} - k^2v_{r,0} = 0 \tag{3.28}$$

This can be further simplified and be written as:

$$r^2 \frac{d^2 v_{r,0}}{dr^2} + r \frac{dv_{r,0}}{dr} - (1 + (kr)^2) v_{r,0} = 0 \tag{3.29}$$

Equation 3.29 is a modified Bessel function of the first order and has the solution:

$$v_{r,0} = c_1 I_1(kr_0) \tag{3.30}$$

Where c_1 is an integration constant and $I_1(kr_0)$ is a sinusoidal series expansion. Two boundary conditions are needed to solve for the constant c_1.

3.2.1 Boundary Condition 1, Kinematic Relation

The first boundary condition dictates that the rate of change of the initial jet diameter is equal to the initial velocity in the radial direction, i.e.:

$$\frac{\partial r_0}{\partial t} = v_{r,0} e^{\omega t + ikz} \tag{3.31}$$

The variable r_0 can be substituted using Equation 3.13. Solving for the derivative on the left hand side of Equation 3.31 would give:

$$\frac{dr_0}{dt} = \eta \omega e^{\omega t + ikz} \tag{3.32}$$

This would therefore entail that:

$$v_{r,0} = \eta \omega \tag{3.33}$$

From Equation 3.30 the constant c_1 can therefore be written as:

$$c_1 = \frac{\eta \omega}{I_1(kr_0)} \tag{3.34}$$

An equation for the pressure in the jet can now be derived. This is done by first substituting Equations 3.33 and 3.34 into Equation 3.22 to get the initial pressure change in the radial direction:

$$\frac{dp_{j,0}}{dr} = -\rho \omega c_1 I_1(kr_0) \tag{3.35}$$

As Equation 3.35 contains the solution of a modified Bessel function, the recurrence relationship (i.e., integrating Equation 3.35) can be used to solve for the initial pressure in the jet. The constant c_1 can then be substituted for from Equation 3.34 giving:

$$p_{j,0} = -\frac{\eta\rho\omega^2}{k}\frac{I_0(kr_0)}{I_1(kr_0)} \tag{3.36}$$

The pressure of the jet originally presented in Equation 3.16 can now be expressed as:

$$p_j = -\frac{\eta\rho\omega^2}{k}\frac{I_0(kr_0)}{I_1(kr_0)}e^{\omega t+ikz} \tag{3.37}$$

3.2.2 Boundary Condition 2, Pressure due to Surface Curvature

The second boundary condition is obtained by equating the internal and external pressures on the jet surface using the Young – Laplace equation as shown below.

$$p_j = \gamma\left(\left(\frac{1}{r_1}-\frac{1}{r_2}\right)_{perturbed} - \left(\frac{1}{r_1}-\frac{1}{r_2}\right)_{unperturbed}\right) \tag{3.38}$$

Where $r_{1,unperturbed} = r_0$, and $r_{2,unperturbed} = \infty$ from Equation 3.3. As $\eta << r_0$ then the perturbed radius, $r_{1,perturbed}$ can be written as:

$$\frac{1}{r_{1,perturbed}} = \frac{1}{r_0+\eta e^{\omega t+ikz}} \approx \frac{1}{r_0} - \frac{\eta e^{\omega t+ikz}}{r_0} \tag{3.39}$$

The second perturbed radius is found through the curvature of the jet:

$$\frac{1}{r_{2,perturbed}} = -\frac{d^2r(z,t)}{dz^2} = k^2\eta e^{\omega t+ikz} \tag{3.40}$$

Equations 3.39 and 3.40 can be placed in Equation 3.38 and the pressure in the jet can be given as:

$$p_j = -\frac{\gamma\eta}{r_0^2}(1-k^2r_0^2)e^{\omega t+ikz} \tag{3.41}$$

3.2.3 Solution

Using the two boundary conditions, two different correlations for the pressure of the jet have been developed presented in Equations 3.37 and 3.41. These correlations can therefore be equated to give the final solution to the problem, known as the dispersion relation for the Plateau – Rayleigh instability, as presented below.

$$\frac{\rho r_0^2 \omega^2}{\gamma} = kr_0(1-(kr_0)^2)\frac{I_1(kr_0)}{I_0(kr_0)} \tag{3.42}$$

The dispersion relation for the Plateau – Rayleigh instability contains two solutions of the modified Bessel function and as such it is not very easy to interpret. A much better way is by plotting the left-hand side of the function (which contains the growth rate and other fixed parameters) against the wavenumber. This plot is shown in Figure 3.3 below.

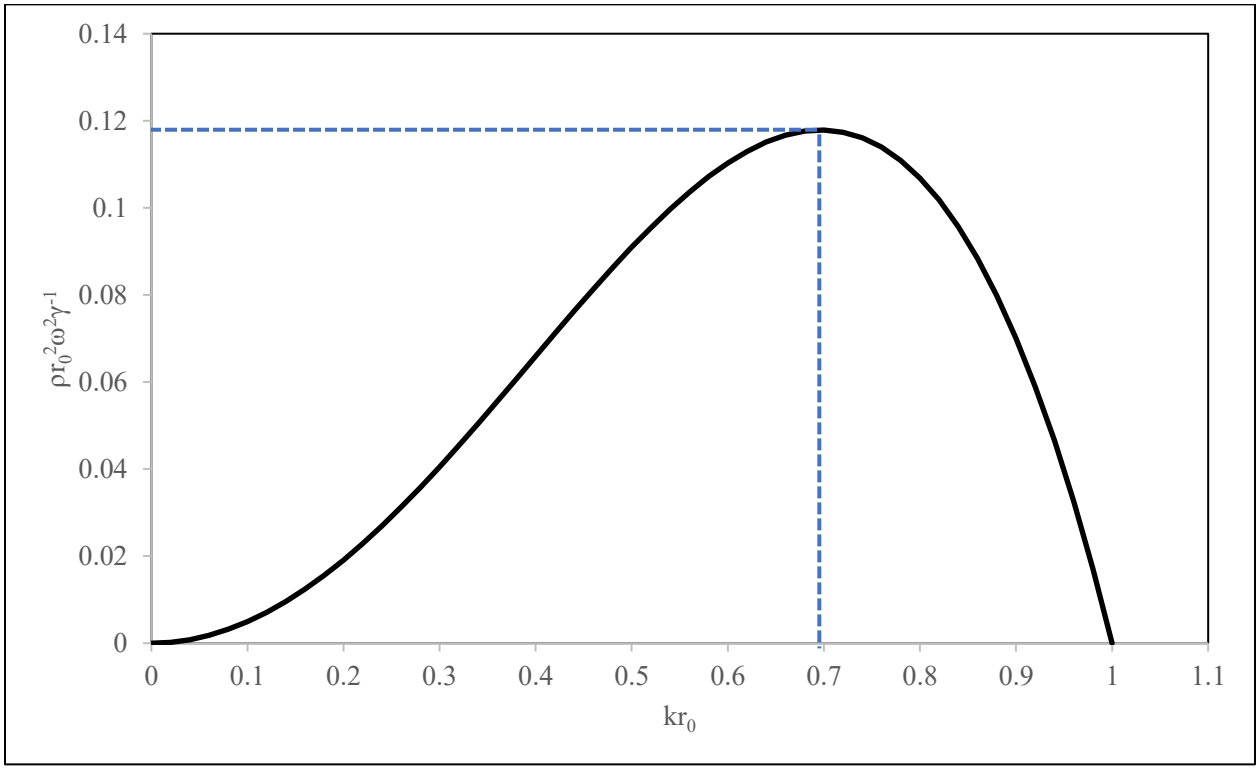

Figure 3.3. The dispersion relation for the Plateau-Rayleigh instability. The curve has a maximum at 0.697 and 0.118 in the x and y coordinates respectively

It can immediately be noted from Figure 3.3 and Equation 3.42 above, that the unstable modes of vibration are only possible if $kr_0 < 1$. This concurs with the critical wavelength proposed by Plateau and Rayleigh.

$$kr(r,z,t) = \frac{2\pi r_0}{\lambda} \tag{3.43}$$

$$\lambda_{crit} = 2\pi r_0 \tag{3.44}$$

From Figure 3.3, the function reaches its maximum at $kr_0 = 0.697$. Therefore, the fastest growing wavelength (the optimal wavelength) can be described as:

$$\lambda_{opt} = 9.01 r_0 \tag{3.45}$$

Following Equation 3.45 and considering the jet to be a continuous cylinder, a mass balance can be used to determine the droplet diameter as:

$$d_d = 1.89 d_0 \tag{3.46}$$

While Equation 3.46 is strictly for an inviscid jet, it does give very reasonable results for low viscosity liquids such as water and some oils, as has been shown by Tyler, Teng et. al., and Donnelly and Glaberson **[21, 117, 63]**. However, for more viscous liquids, Teng et. al. observed that the equation from Weber's theory (presented below) is better at predicting the droplet diameter.

$$\frac{d_d}{d_0} = \left(\frac{3\sqrt{2}}{2} \pi \sqrt{1 + 3Oh} \right)^{\frac{1}{3}} \tag{3.47}$$

3.3 Length of Breakup

To solve for the continuous length of a jet until its breakup, Weber first assumed that axisymmetric perturbations can be written as a function of the growth rate, the initial amplitude of the disturbance, and the time taken for the disturbance to grow **[18]**. If the disturbance grows at the maximum growth rate (ω_{max}) as shown in Figure 3.3, then after a time t_{BU} (the breakup time), the perturbation would have grown to a size equal to the jet radius. Thus, under these conditions the disturbance amplitude can be written as:

$$\eta(r, z, t) = r_0 = \eta_0 e^{\omega_{max} t_{BU}} \tag{3.48}$$

From Figure 3.3 the maximum growth rate is when the wavenumber (x – coordinate) is $kr_0 = 0.697$ and the y – coordinate is 0.118. For a given liquid the physical properties and the initial jet diameter are considered constant and as such the maximum growth rate can be easily determined.

$$\omega_{max} = 0.344 \sqrt{\frac{\gamma}{\rho r_0^3}} \tag{3.49}$$

Equation 3.49 above is of course excluding any viscous effects following the linear analysis developed by Rayleigh (presented in Section 3.2 above). A much more accurate way would be to follow the analysis of Weber, whereby he included the viscous effects and found that:

$$\omega_{max} = 0.97 \frac{1}{1 + 3Oh} \sqrt{\frac{\gamma}{\rho r_0^3}} \tag{3.50}$$

From Equation 3.48 the breakup time can be written as:

$$t_{BU} = ln\left(\frac{r_0}{\eta_0}\right) \frac{1}{\omega_{max}} \tag{3.51}$$

A simple relation can then be used to determine the breakup length:

$$L_{BU} = t_{BU} v_0 \tag{3.52}$$

Substituting for the breakup time using Equations 3.50 and 3.51, the length of breakup can then be determined as a function of the initial disturbance, orifice size, and the physical properties of the liquid[4]:

$$\frac{L_{BU}}{d_0} = ln\left(\frac{r_0}{\eta_0}\right)\left(We^{\frac{1}{2}} + 3\frac{We}{Re}\right) \tag{3.53}$$

According to Weber the term $\ln(r_0/\eta_0)$ can be assumed to be a constant with a value of 12. Several other researchers have suggested slightly different values, such as Grant and Middlemann who claim it should be around 13.4 with a dependance on the Ohnesorge number **[26]**. Meister and Scheele suggested values between 11 – 16, while Trettel used a value of 8.5 in his recent analysis **[118, 58]**. For this study, the original suggestion of 12 by Weber will be used, as Sterling and Sleicher presented good correlations using Weber's approach for the Rayleigh regime **[27]**.

[4] The Length of breakup (L_{BU}) is an approximation obtained from Weber's analysis, and is therefore an empirical relation rather than an analytical one.

3.4 The Velocity Equation

From section 3.3 it is clear that the velocity of the jet is directly related to the length of breakup, and as such it is important to be able to easily predict this velocity. To do so the different variables involved in developing this analysis must be defined. This is done through the schematic of a draining crucible, shown in Figure 3.4 below.

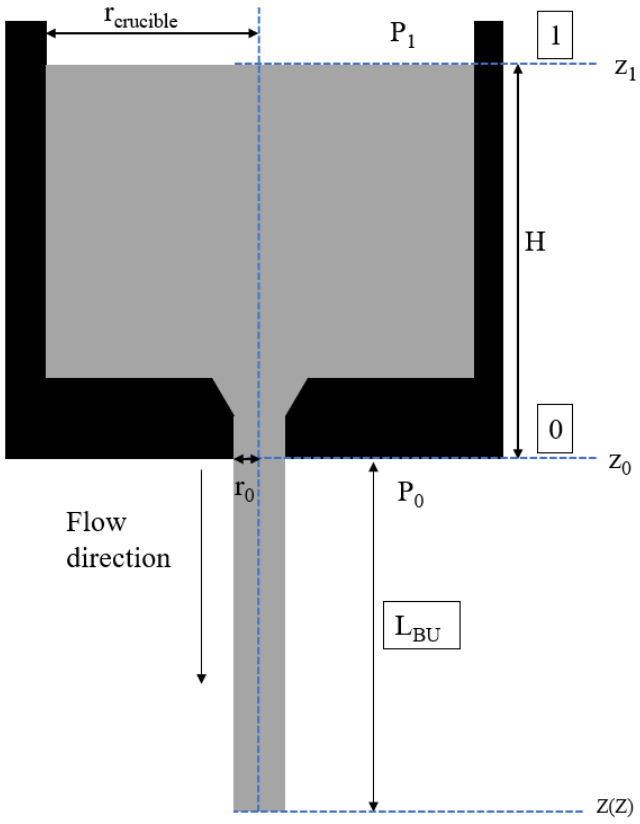

Figure 3.4. Schematic of a fluid flowing through the orifice of a crucible

The Bernoulli energy balance can then be applied as follows:

$$\frac{1}{2}\rho v_0^2 + P_0 + \rho g z_0 = \frac{1}{2}\rho v_1^2 + P_1 + \rho g z_1 \tag{3.54}$$

In equation 3.54, the subscripts 0 and 1 are used to define the parameters at locations 0 and 1 in Figure 3.4. It should also be noted that the radius of the crucible is much larger than the radius of the orifice ($r_{crucible} >> r_0$), and so the first term on the right-hand side of Equation 3.54 can be considered as negligible. Following Figure 3.4 the difference in the axial locations z_1 and z_2 can

simply be noted as the head of the liquid H, and the difference in pressure between P_1 and P_0 can simply be written as the external overhead pressure ΔP. Putting all this together Equation 3.54 can be used to solve for the jet velocity as shown below:

$$v_0 = \sqrt{2\left(gH + \frac{\Delta P}{\rho}\right)} \tag{3.55}$$

Although the formulation presented above is clearly organized and would give a good approximation, it is incomplete. It does not consider the surface tension, nor the viscosity of the liquid, and also ignores any of the effects related to nozzle geometry (such as the aspect ratio or the chamfer angle). Therefore, in this study the methodology formulated by Steven Roach will be used. This is presented in Equation 3.56 **[[119]]**.

$$v_0 = C_D \sqrt{2g\left(H + \frac{1}{\rho g}\left(\Delta P - \frac{\gamma}{r_0}\right)\right)} \tag{3.56}$$

Equation 3.56 considers the surface tension through the use of the Young – Laplace formulation presented in Equation 3.6. It also considers the viscosity of the liquid by introducing a dimensionless discharge coefficient 'C_D'. The discharge coefficient is a function of the Reynolds number and the nozzle geometry, and can have a value between 0.2 – 0.9 as noted from previous studies **[120, 121, 20]**. This will be further elaborated on when discussing the experimental results in Chapter 4.

3.5 Bernoulli – Electrostatic Energy Balance

When a liquid jet exits the orifice at a velocity v_0, it has a certain amount of inertial force acting on it, keeping it compact. However, as it falls the jet also experiences other forces, i.e., gravity, surface tension, viscous, and electrostatic forces. As such the jet is accelerated and therefore changes in diameter.

Since the droplet diameter is related to the jet diameter (Equations 3.46 and 3.47) it is vital to understand how the jet changes in size with respect to the different forces acting on it. The Bernoulli energy balance can therefore be applied, as follows:

$$\frac{1}{2}\rho v_0^2 + p_0 + \rho g z_0 = \frac{1}{2}\rho v^2(z) + p(z) + \rho g z(z) \tag{3.57}$$

The pressures acting on the jet are due to the surface tension and the electric field around the jet. They can be expressed through the use of the Young – Laplace formulation (Equation 3.6) and the EHDA pressure balance (Equation 3.12), such that:

$$p_0 = \frac{\gamma}{r_0} \tag{3.58}$$

$$p(z) = \frac{\gamma}{r(z)} - \frac{1}{2}\varepsilon_0 E_n^2(r,z) \tag{3.59}$$

Replacing these pressure descriptions into Equation 3.57 and simplifying it yields:

$$\frac{1}{2}\rho v_0^2 + \rho g z_0 + \frac{\gamma}{r_0}\left(1 - \frac{r_0}{r(z)}\right) + \frac{1}{2}\varepsilon_0 E_n^2(r,z) = \frac{1}{2}\rho v^2(z) + \rho g z(z) \tag{3.60}$$

And,

$$\frac{1}{2}\rho v_0^2 - \frac{1}{2}\rho v^2(z) + \frac{\gamma}{r_0}\left(1 - \frac{r_0}{r(z)}\right) + \frac{1}{2}\varepsilon_0 E_n^2(r,z) = \rho g z(z) - \rho g z_0 \tag{3.61}$$

The difference in the axial locations z_0 and z(z) can simply be noted as the length of breakup of the jet, L_{BU}.

$$\frac{1}{2}\rho v_0^2 - \frac{1}{2}\rho v^2(z) + \frac{\gamma}{r_0}\left(1 - \frac{r_0}{r(z)}\right) + \frac{1}{2}\varepsilon_0 E_n^2(r,z) = -\rho g L_{BU} \tag{3.62}$$

Equation 3.62 can then be simplified further to give a relation between the velocity at the location z (i.e., where $z = L_{BU}$), and the velocity at the exit.

$$\left(\frac{v(z)}{v_0}\right)^2 - 1 = \frac{2}{\rho v_0^2}\left(\frac{\gamma}{r_0}\left(1 - \frac{r_0}{r(z)}\right) + \frac{1}{2}\varepsilon_0 E_n^2(r,z) + \rho g L_{BU}\right) \tag{3.63}$$

And,

$$\frac{v(L_{BU})}{v_0} = \left(1 + \frac{2gL_{BU}}{v_0^2} + \frac{2\gamma}{\rho v_0^2 r_0}\left(1 - \frac{r_0}{r(L_{BU})}\right) + \frac{\varepsilon_0 E_n^2(r,z)}{\rho v_0^2}\right)^{\frac{1}{2}} \tag{3.64}$$

The dimensionless numbers presented in Table 1 can be used to replace the individual parameters in order to give an easier interpretation of Equation 3.64.

$$\frac{v(L_{BU})}{v_0} = \left(1 + \frac{1}{Fr}\frac{L_{BU}}{r_0} + \frac{4}{We}\left(1 - \frac{r_0}{r(L_{BU})}\right) + \frac{Es}{We}\right)^{\frac{1}{2}} \tag{3.65}$$

While Equation 3.65 above gives a very clear representation of whether the jet will experience any form of acceleration with respect to the different forces in play, in this study it may be simpler to view this effect with respect to the radius of the jet. This can be done by using a simple mass balance of the volumetric flow rate (Q), as presented in Equation 3.66.

$$Q = \pi r_0^2 v_0 = \pi r^2(L_{BU}) v(L_{BU}) \tag{3.66}$$

$$\frac{v(L_{BU})}{v_0} = \left(\frac{r_0}{r(L_{BU})}\right)^2 \tag{3.67}$$

Replacing Equation 3.67 into Equation 3.65 gives:

$$\left(\frac{r_0}{r(L_{BU})}\right)^4 = 1 + \frac{1}{Fr}\frac{L_{BU}}{r_0} + \frac{4}{We}\left(1 - \frac{r_0}{r(L_{BU})}\right) + \frac{Es}{We} \tag{3.68}$$

Equation 3.68 will be used to assess the relative contributions of the surface tension, gravity, or electrostatic forces on the jet diameter. If the inertial forces are very high relative to the other forces mentioned, the last three terms of Equation 3.68 can be considered as negligible and the radius of the jet will not change significantly by the time it breaks up.

3.6 Summary

This chapter covered the mathematical models governing jet formation and break up. Focus was placed on just laminar jets in the Rayleigh regime. The Plateau – Rayleigh instability was reviewed and derived, showing the wavelength of the fastest growing disturbance (Equation 3.43 – 3.47). The equation to predict the length of the jet (derived by Webber) was reviewed (Equation 3.53). From the Bernoulli energy balance the equation for the velocity of the jet was derived (Equation 3.56). Finally, a Bernoulli – Electrostatic model was introduced that would predict the jet diameter with respect to the different forces acting on it (Equation 3.68).

In the following chapters the following model will be used to better understand and quantify the atomization process developed in this study. Equations 3.43 – 3.47 will be used to calculate the velocity of the jet during operation. From this, Equation 3.53 will be applied to predict the length

of breakup, and Equation 3.58 can then be used to determine the radius of the jet at break up. Finally, the droplet sizes can be calculated using Equations 3.43 – 3.47. The droplet size and size distribution will then be evaluated and compared to the predicted values. The effect of the frequency and the applied electric field will then be quantified and analyzed in more detail.

Chapter 4: Experimental Set-up and Procedure

4.1 Introduction

The focus of this chapter is on the experimental setup and the procedure of atomization. The entire setup consists of a variety of different components. These can be characterized into 5 different groups:

1. The crucible and nozzle system,
2. The mechanical vibration unit,
3. The electrostatic system,
4. The heating and melting system,
5. The optics and visualization unit,

All the above-mentioned components of apparatus are housed inside a stainless-steel atomization tower, except the power generator for the melting system. The generator provides alternating electric current needed to melt the alloys. The generator is connected to the heating and melting system (an induction coil) using water cooled cables. The five (5) mentioned components and the tower itself will be discussed in the following sections.

4.2 Crucible and Nozzle System

Two different configurations of the crucible-nozzle system were employed in this study. The first was used when working with low temperature liquids such as water and ethylene glycol. The second was used when working with larger orifice sizes (generally when the orifice diameter, d_0, was larger than 0.75 mm). Either a ceramic, graphite or 3D printed PLA crucible was used. During these experiments no external overhead pressure was applied, and the liquid was simply allowed to flow through the orifice due to the hydrodynamic pressure applied by the liquid head. When working with smaller orifice sizes or liquid metals, a steel crucible was employed that would allow a constant external overhead pressure to be maintained in the system. The nozzle design in all the mentioned crucibles was also varied to have a study with a wider scope and to determine if there was any significant effect due to the nozzle geometry.

4.2.1 The 3D Printed PLA Crucible

Figures 4.1 a) – d) are images of the PLA crucibles used in this study. Figure 4.1 e) is a schematic of these crucibles. The fused deposition modelling (FDM) technology was used to print these crucibles using the Creality ender 5 pro 3D printer with a precision of +/- 0.1 mm, and the OVERTURE PLA of 1.75 mm in diameter was used.

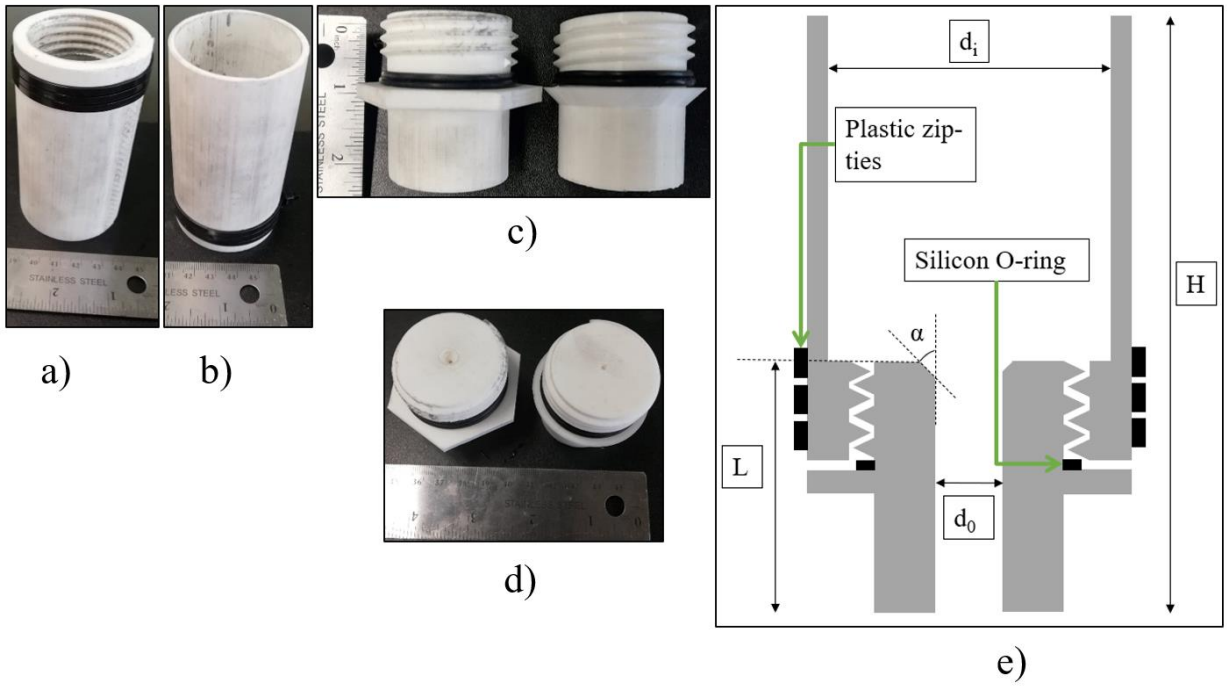

Figure 4.1. a) and b) The top section of the 3D printed PLA crucibles. c) and d) The bottom nozzle sections of the crucible. e) The schematic of the entire PLA crucible used in this study

As can be seen from Figure 4.1 e) there are five main distinctive features used to define these crucibles. The maximum height (H), the nozzle wall thickness (L), the orifice diameter (d_o), the crucible inner diameter (d_i), and the chamfer angle (α). It can also be noted that these crucibles were constructed having two different sections: the top crucible section and the nozzle section. The nozzles were printed in such a way that they would screw into the crucible and could thus be changed when needed without having to print a new top section of the crucible. A silicon o-ring was used on the nozzle to ensure better sealing and to prevent any leakage of liquid. Plastic zip-ties were also used to re-enforce the bottom section of the crucible and to prevent the crucible from cracking or deforming due to shear stress when screwing in the nozzles. These crucibles employed both a straight and a chamfered nozzle design, α, of 0° and 30° respectively. They also had much

longer nozzle lengths of 5 cm. The crucibles had a maximum height of 12 cm (including the nozzle length), an inner diameter of 5 cm, and an orifice size of 2 mm in diameter.

4.2.2 The Ceramic and Graphite Crucibles

Figures 4.2 a) and b) show the ceramic (alumina) and graphite crucibles used in this study respectively. Figure 4.2 c) is a schematic representation of these crucibles.

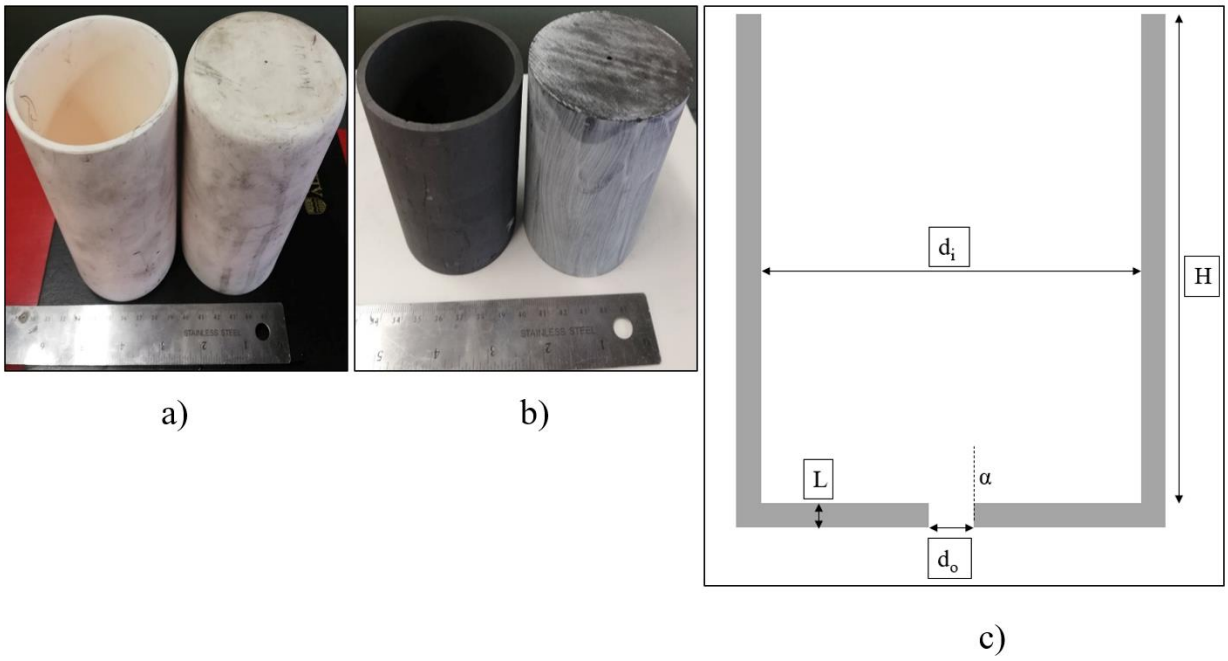

Figure 4.2. a) The alumina crucibles, b) the graphite crucibles, c) the schematic of the alumina and graphite crucibles used in this study

The ceramic crucibles shown in Figure 4.2 a) were obtained from AdValue Technology. The graphite crucibles shown in Figure 4.2 b) were obtained from The Graphite Store and were manufactured by Graphatek LLC. Both the alumina and the graphite crucibles had straight drilled nozzle orifices (with no chamfer) on their bottom bases. The base therefore met the orifice at an angle of $\alpha = 0°$. The length of the nozzle wall, L, was equal to the thickness of the crucible, 3.5 mm for the alumina crucibles, and 4 mm for the graphite crucibles. The alumina crucibles had a maximum height, H, of 14 cm and an inner diameter, d_i, of 6.5 cm, and had orifices of 0.75 and 1 mm in diameter. The graphite crucibles had a maximum height, H, of 9 cm and an inner diameter, d_i, of 5.5 cm, and had orifices of 1.5 and 2 mm in diameter.

4.2.3 The Steel Crucible

When trying to atomize metals or when working with smaller orifice diameters (d_0<0.75 mm), the hydrodynamic pressure due to the head of the liquid is not be enough to overcome its surface tension. An overhead pressure is needed to push the liquid through the orifice to form a continuous stable jet. A new crucible design was therefore manufactured at the University of Alberta. Figures 4.3 a) and b) present the images of the pressurized steel crucible. Figure 4.3 c) is an image of some of the nozzles used with this crucible. Figure 4.3 d) is a schematic of this crucible and nozzle system.

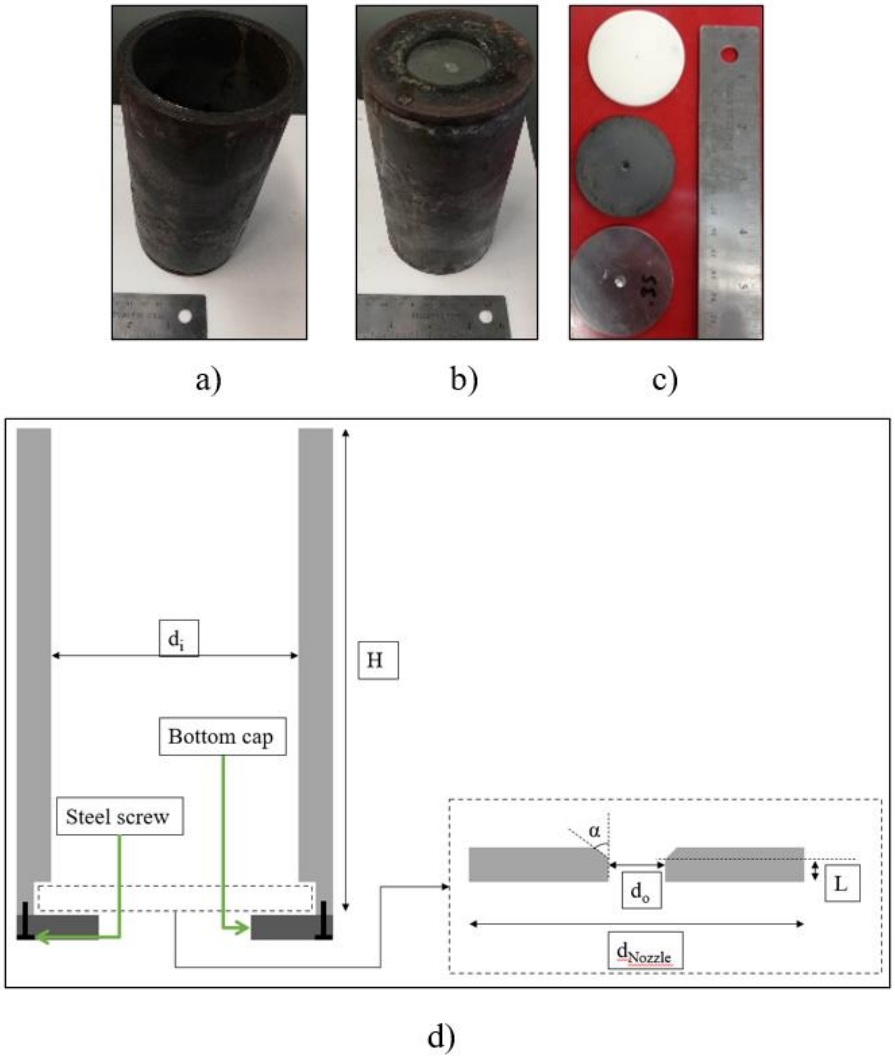

Figure 4.3. a) and b) The top and bottom views respectively of the steel crucible, c) the alumina, graphite and steel nozzle plates that can be mounted and dismounted from the crucible, and d) the schematic of the entire steel crucible-nozzle system.

The steel crucible was manufactured with an internal diameter of 7 cm and a maximum height of 15 cm. As shown in Figure 4.3 d), this crucible was manufactured without a fixed nozzle plate. Instead, nozzle plates of a diameter d_{Nozzle} = 4 cm made of steel, graphite or alumina (presented in Figure 4.3 c)) could easily be installed and replaced for different experiments. This was done by undoing the steel screws to remove the bottom cap. The appropriate nozzle plate was then fitted tightly into position before carefully re-attaching the cap. This crucible was used with nozzle plates having orifice diameters between 0.45 – 0.05 mm. All the nozzle plates in the system had chamfered orifices with an angle of $\alpha = 30°$ and had nozzle a length of 0.37 mm.

A summary of the different crucibles and nozzle systems are represented in Table 4.1 below

Table 4.1. Summary of the crucible nozzle system used in this study

Crucible Type	Max. liquid head [H] (cm)	Max. external overhead pressure (kPa)	Nozzle shape [α]	Nozzle material	Orifice sizes [d_0] (mm)	Nozzle length [L] (mm)
Steel	14	103	30°	Graphite, Alumina, Steel	0.05 – 0.45	0.37
Graphite	9	0	0°	Graphite	1.5 – 2	4
Alumina	14	0	0°	Alumina	0.75 – 1	3.5
PLA	12	0	0° and 30°	PLA	2	50

4.3 Mechanical Vibration Unit

The vibration unit consisted of three different parts displayed in Figure 4.4 below:

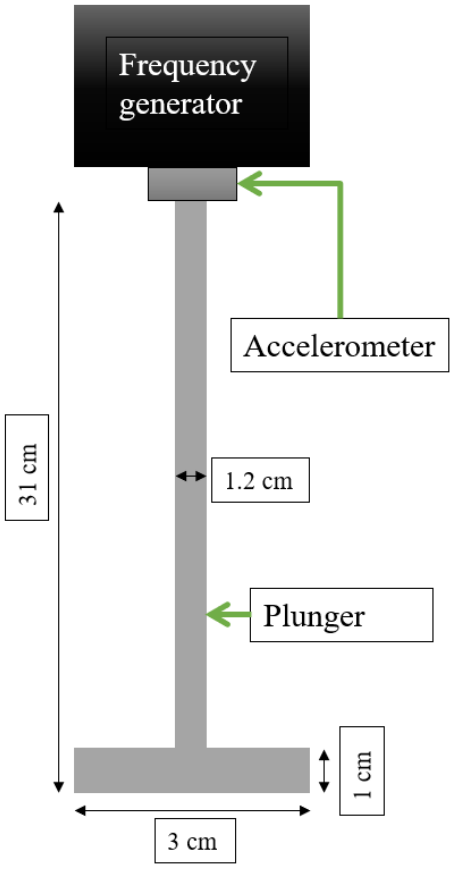

Figure 4.4. The schematic of the frequency generation unit

A frequency generator was used to produce mechanical sine waves with frequencies ranging between 10 – 20,000 Hz with an accuracy of 1 Hz.

An accelerometer manufactured by Dytran Instruments Inc. (impedance head model 5860B) provides feedback of the frequency and amplitude of vibration provided by the frequency generator. The accelerometer is physically connected to the frequency generator. Both the frequency generator and accelerometer are then also connected to the same function generator whereby the frequency and amplitude can be input, and the generated wave function of vibration can be viewed.

The third part of this unit is a 31 cm long ceramic plunger that is attached to the bottom of the accelerometer. The rod of the plunger was 1.2 cm in diameter with its bottom disk having a

diameter of 3 cm. The purpose of the ceramic plunger was to transmit the mechanical vibration generated by the frequency generator to the bulk liquid in the crucible. The plunger was always situated in the crucible such that the bottom surface of its disk was at an optimal distance ($d_{plunger}$) from the bottom of the crucible.

4.4 The Electrostatic System

The electrostatic system must be setup with two electrodes between which an electric field can be created. In this study the first electrode was a negatively charged copper ring. The images and schematic of the entire negative electrode system are shown in Figure 4.5 below:

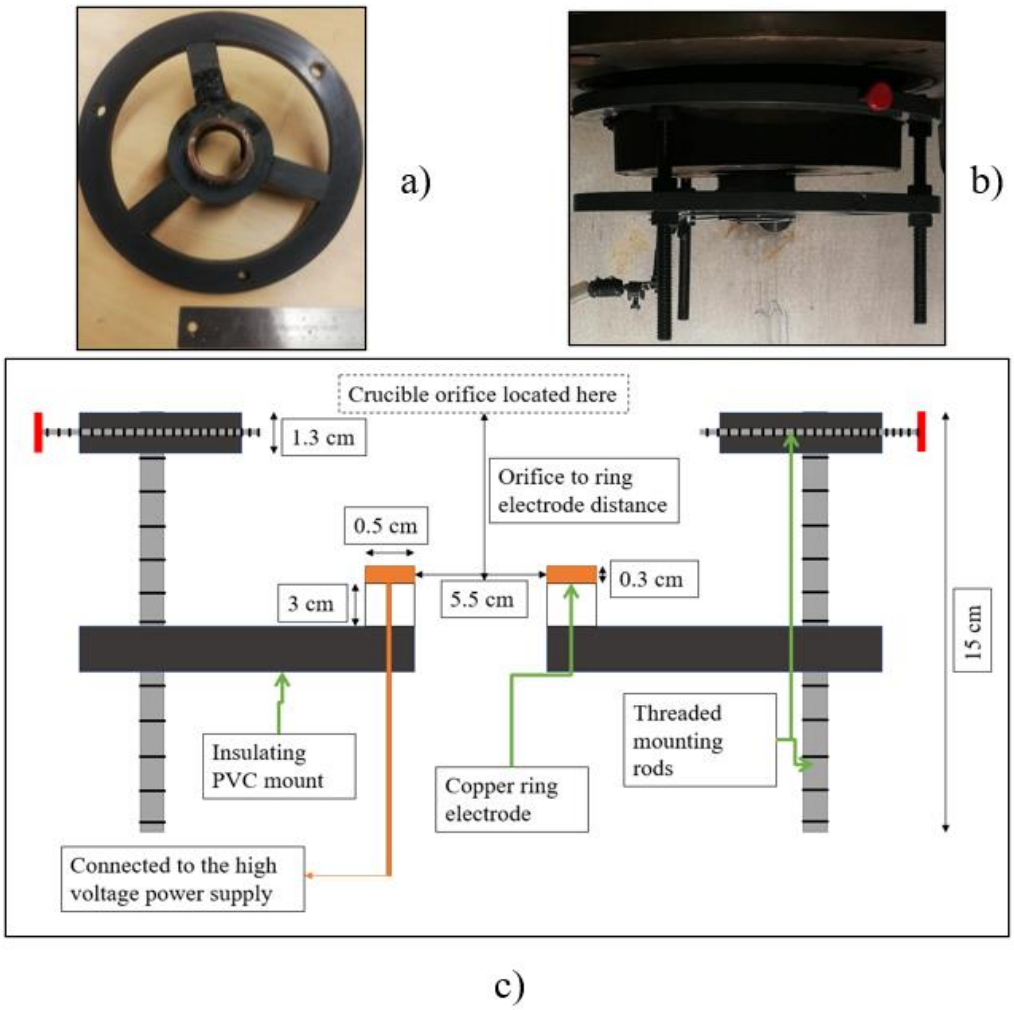

Figure 4.5. a) and b) The images of the ring electrode used in this study placed on a large PVC mounted c) The schematic of the negative ring electrode system used in this study

It can be noted from Figure 4.5 c) that the ring electrode was designed such that it had an outer diameter of 6 cm and an inner diameter of 5.5 cm. It was placed on a PVC mount underneath the crucible which in turn had threaded rods such that the electrode could be moved closer or farther away from the orifice of the crucible.

The second electrode in most electrohydrodynamic atomisation studies was chosen to be the ground rather than an electrode of opposite polarity. This is to ensure a more stable system with a lower build up of excess charge at the orifice or on the liquid which could easily lead to brush or corona discharges, or even in extreme cases continuous low energy arcing. In this study the bulk liquid was grounded and so acted as the second electrode. An electric field was therefore created between the crucible orifice and the ring electrode.

The ring electrode was connected to a high voltage power supply, i.e., the Spellman High Voltage SL10. This is a 10-Watt power supply capable of delivering up to +/-100 kV. A grounding cable was also run from the power supply to the metal crucible housing the bulk liquid, or directly into the liquid if the crucible was made of graphite, alumina or PLA.

4.5 The Furnace

When working with metals they had to be heated past their melting point to ensure they were in a liquid state and could thus be atomised. In order to achieve this, induction heating was implemented. A seven-turn induction coil made of copper with an outer tube diameter of 6.35 mm (0.25 inches) was used. The coil had an inner diameter of 15 cm allowing the steel crucible to be comfortably housed within it. The induction coil was securely fastened within the atomisation chamber and was connected to the induction furnace power supply via water cooled power cables to ensure sufficient cooling while operating under high-power loads. The induction furnace used was the VIP Inductotherm which is capable of delivering up to 20 kW of power at a frequency of 10 kHz allowing the crucible to reach a temperature of up to 1800 K. A schematic representation showing the steel crucible system, the frequency generator, the electrostatic system, and the heating and melting system is shown in Figure 4.6 below:

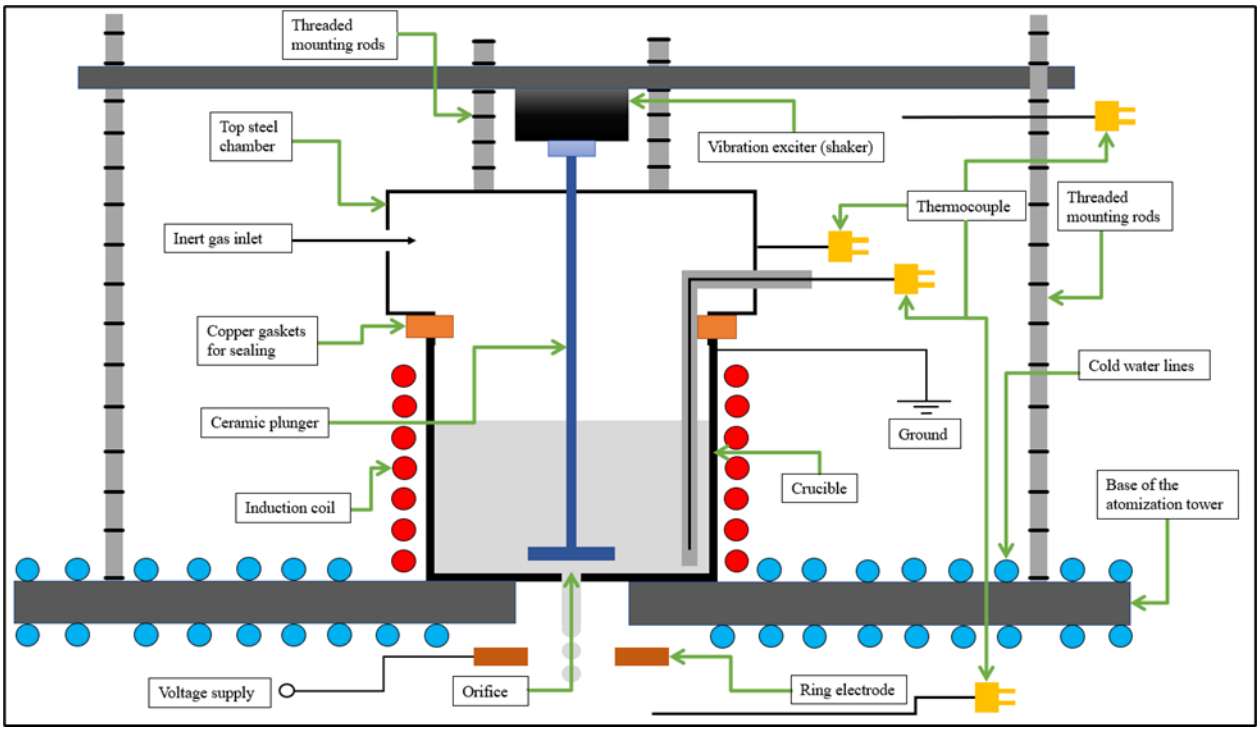

Figure 4.6. Schematic representation of the crucible system, mechanical vibration unit, electrostatic system, and the heating and cooling system.

From Figure 4.6 it can be seen that the melt is seated within the induction coils. The grounding cable ensures that the liquid jet exiting the orifice is electrically neutral as it enters the negative electric field below. A top steel chamber mounted on threaded steel rods and placed on copper gaskets is used to seal the entire crucible area and to ensure a positive gauge pressure can be maintained. The frequency generation unit is also mounted on threaded rods connected to the base of the atomisation tower, which allow the plunger to move closer or further away from the orifice. It is important to note that the shaker sits outside the pressurised crucible system and so much further away from the crucible and induction coils (i.e., the hot area of the setup) to prevent it from any heat damage. However, the plunger is allowed to enter the crucible to ensure the vibration generated by the frequency generator is transmitted to the liquid melt before it exits the orifice. Four K-type thermocouples are used to monitor the temperature. One thermocouple was placed within the melt inside the crucible. The second one was placed on the outer wall of the sealing steel chamber, closer to the shaker. The remaining two were placed in the surrounding air in the top and the bottom compartments of the atomisation tower, i.e., next to shaker and close to the ring electrode respectively. In order to ensure that no extra and unwanted heat was circulated around

the system and onto other equipment, cold water was constantly run within the tower through 6.35 mm diameter copper tubing. The water was supplied from the main cold-water line in the laboratory at a temperature between 15 – 20 °C. This water was then passed through a chiller which ensured the temperature was further reduced to 13°C before being fed into the tower. The returning water was again fed to the chiller and recirculated back into the tower at 13°C.

4.6 Shadowgraph

In order to capture the images of the falling droplets a shadowgraph technique (also known as the backlighting technique) was employed. Shadowgraphy is a shadow imaging method that makes use of high magnification for visualising particles down to the micron scale. A schematic of the system is shown below in Figure 4.7.

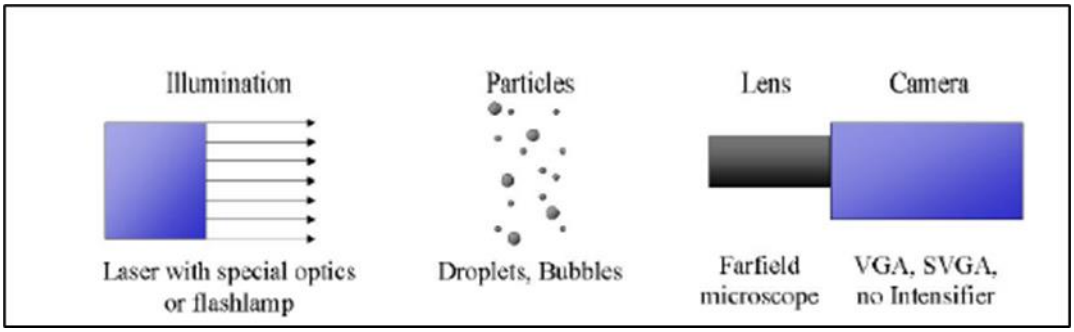

Figure 4.7. A general view of the shadowgraph system

The shadow imaging technique is based on high resolution imaging with a pulsed backlight illumination. In this study a double frame Imager Intense Camera from LaVision Corporate was used. This is a 12-bit CCD camera with a resolution of 1376 x 1040 pixels and a frequency of 3.3 – 10Hz. It has a maximum depth of field of 6.7 mm. This camera captures two images during each frame with a time difference between the photos being 30 μs. As shown in Figure 4.7, the camera was connected to a farfield microscope lens. The lens used in this study was the Basic 12x Zoom Lens, manufactured by Navitar Incorporated. The lens was capable of delivering a 12x(0.58 – 7x) magnification with a numerical aperture of 0.004 – 0.55. After calibration, the field of view was set at 15.6-by-11.8 mm in the x and y axis respectively with a magnification of 12.6 pixels per millimeter. The backlight illumination was provided by a double pulsed Nd:YAG laser. This was the ULTRA CFR laser from Big Sky Laser Technologies Incorporated capable of operating at a

frequency of 0 – 15 Hz. The laser provided 6 ns illumination pulses of 45 mJ at a wavelength of 523 nm (i.e., visible green light). The pulse width was calibrated to be the same as that of the camera at 30 μs, in order to record two images during each frame. From the laser head an optical fibre cable carrying the laser light was run to a diffuser of a length of 10.4 cm. The diffuser is a housing with a fluorescence lens at its exit and is used to spread the light and provide illumination over a larger area. The diameter of the fluorescence lens (6 cm in this study) is used to determine the focal point and in turn to calibrate the camera. As shown in Figure 4.8 below, the camera, laser head and diffuser were mounted on a translation stage that had three degrees of freedom. The translation stages used in this study were the ISEL Linear Motion Units manufactured by Isel Automations. The configurations used were the Isel models LES 4, 5 and 6 for the x, y and z axis respectively and worked with an accuracy of 0.02 mm. The camera, laser and translation stages were all configured with an internal trigger using the DaVis 7.2 software by LaVision.

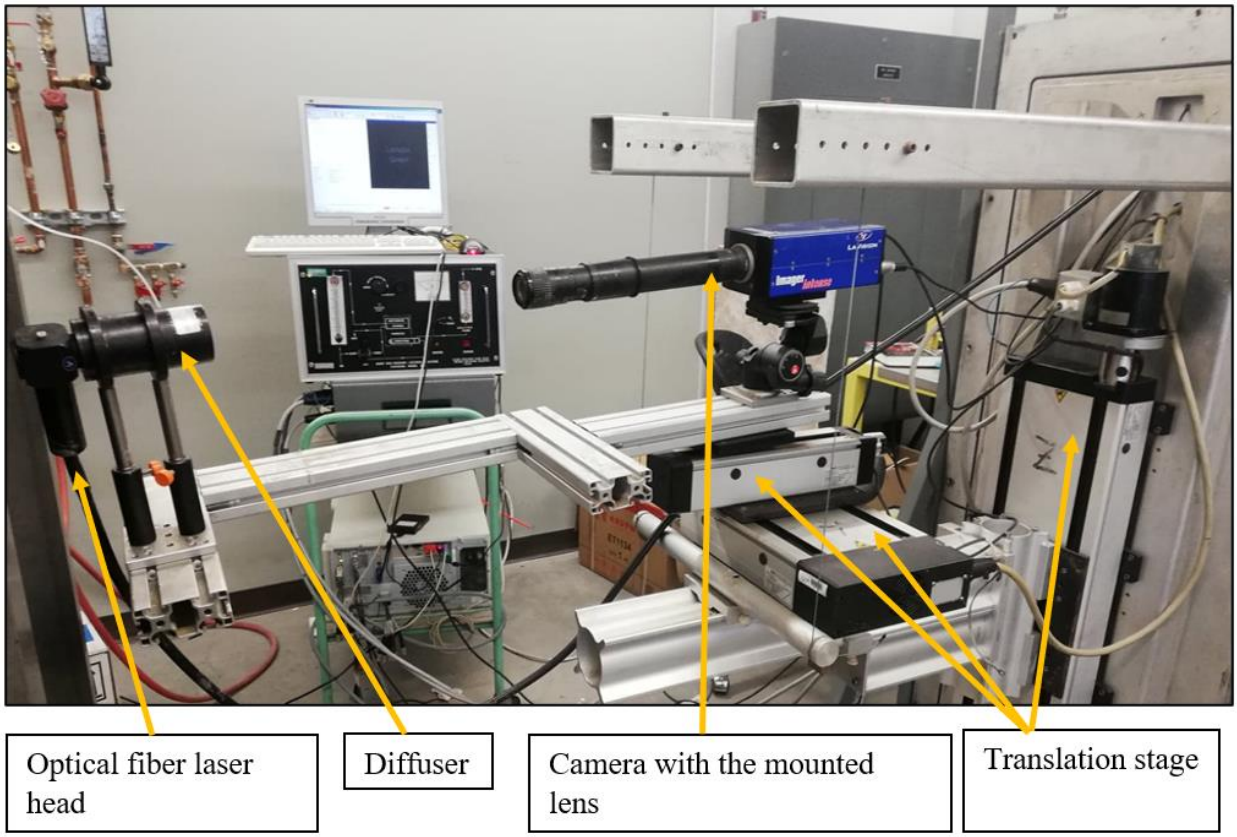

Figure 4.8. The optics and visualisation equipment in the atomisation tower.

After recording the images of the falling droplets, they were analysed for their size and their velocity. A two-step segmentation algorithm built into the DaVis 7.2 software was applied to measure the droplet sizes. In the first segment the droplets are located in what is called a "bounding box". In this step an inverted image is obtained whereby the shadow image of the droplet is subtracted from a reference image (an image representing the illumination without any particles). This is shown below in Figure 4.9.

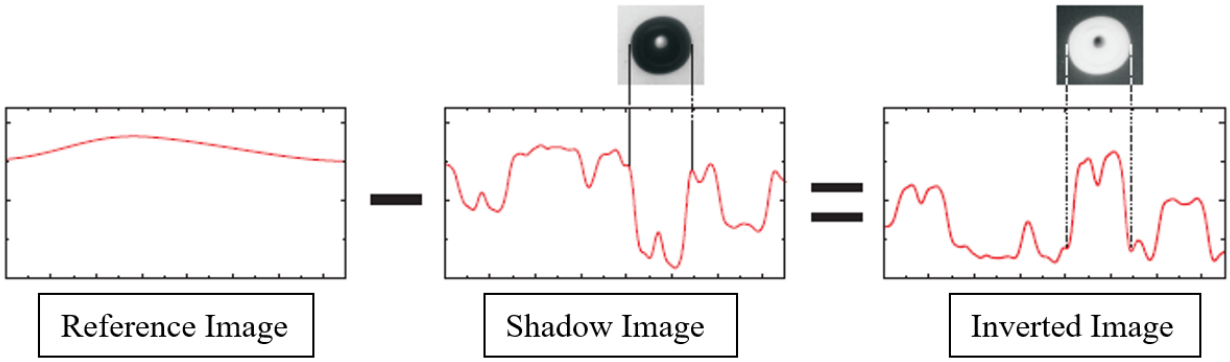

Figure 4.9. Inverting the shadow image using the reference image.

Following this, a global threshold defined by the user is used to detect the particles. The global threshold is relative to the maximum and minimum intensity of the inverted image. The DaVis 7.2 sizing algorithm finds all areas with an intensity above the global threshold and marks these areas with a bounding box. This is represented in Figure 4.10 below. Only areas above the global threshold are considered for the next steps of calculation. These would be the areas marked #1, 2, 3 and 4 in Figure 4.9. Any peaks of intensity lower than the global threshold will be ignored and will be detected as noise by the algorithm.

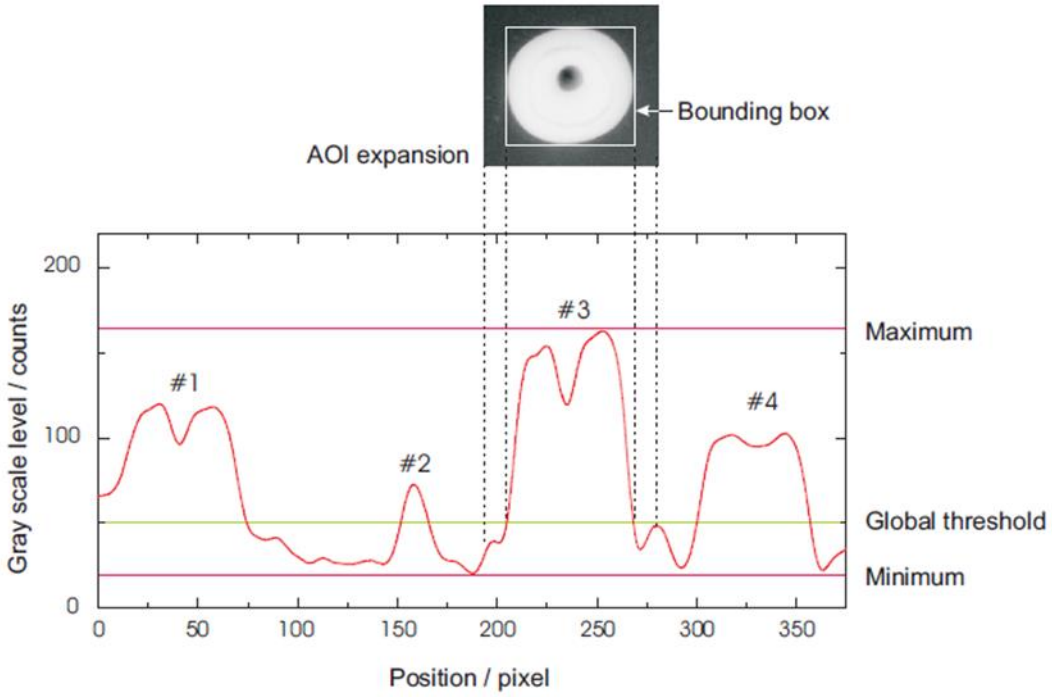

Figure 4.10. Thresholds for the first segmentation.

During the second segment of analysis, the areas of the images which are above the global threshold are cut off and analysed individually. Figure 4.11 represents the second segmentation analysis of particle #3 in Figure 4.10. User defined high-level and low-level grey scale counts are used to determine the size of the particles. The algorithm then counts the number of pixels above the high-level scale and the low-level scale. From this the particle area and diameter are computed assuming the particle to be a circle. It is important to note that if high values of the high-level scale, and low values of the low-level scale are selected then unfocussed particles will also be selected which could lead to errors in the particle size calculations. For this study the global threshold, high-level scale, and low-level scale values were selected as 40%, 60% and 40%, respectively.

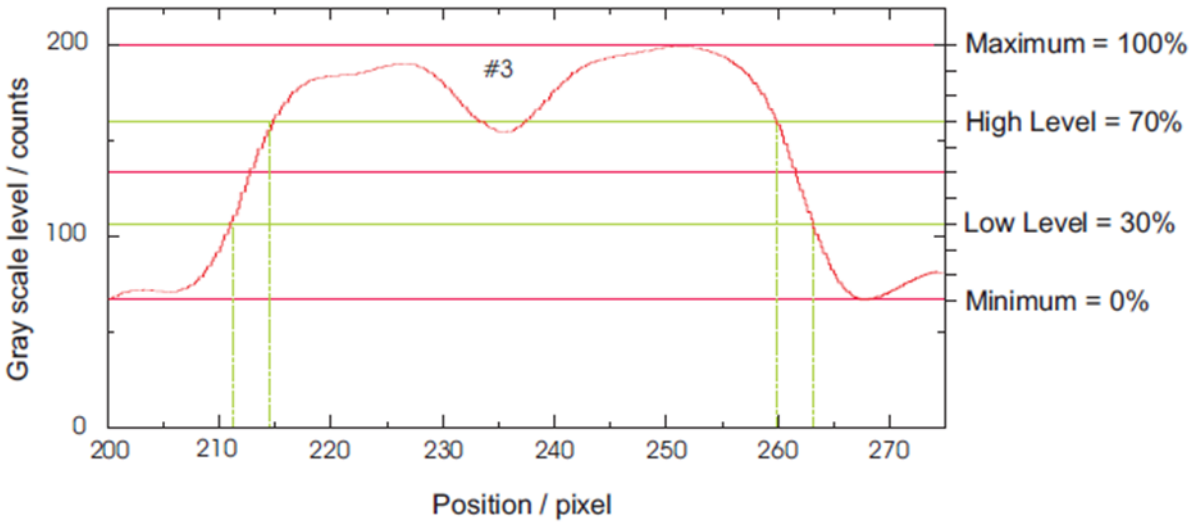

Figure 4.11. Example of the thresholds for the second segmentation.

In order to calculate the velocity of the droplets, the algorithm first calculates the size and location of every droplet from each frame and stores the information in two separate lists. After completing the sizing of all source images, the velocity calculation algorithm is initiated. This algorithm has two main conditions: the droplet size and the time shift of the droplet in the two separate frames. The shift of the particle identifies the location of the particle after the given delay between the two frames from which the velocity of the particle can be calculated. The velocity is only accepted if the diameter deviation between the two frames was within a given range, which in this study was chosen as +/-5%.

The DaVis 7.2 software finally displays the results of the droplet diameters as a histogram with respect to the relative frequency, and the velocity with respect to the droplet diameter in the form of a scatter plot. Several other forms of output are also available, but these were the two used in this study. The algorithm also calculates the statistical results of the detected particles. These include the average droplet diameter (D10), the Sauter mean diameter (D32), and the median diameter (DV50). An example of this is shown in Table 4.2.

Table 4.2. An example of the compiled statistical data for a run with water as the working liquid.

Material	Water
Orifice Diameter (mm)	0.275
Applied Frequency (Hz)	1000
Applied Voltage (kV)	2
Applied external overhead pressure (Pa)	2550
Average Droplet Diameter (D10) (mm)	0.587
Sauter Mean Diameter (D32) (mm)	0.589
Median Diameter (DV50) (mm)	0.574

4.7 Atomisation Chamber

The atomisation chamber consisted of two compartments: a lower rectangular compartment of 0.55m (Width) x 1.5m (Height) x 1.52m (Depth), and an upper cylindrical compartment of 0.75m (Height) x 0.58 m (Diameter). The chamber when closed and ready for an experimental run is shown in Figure 4.12 below.

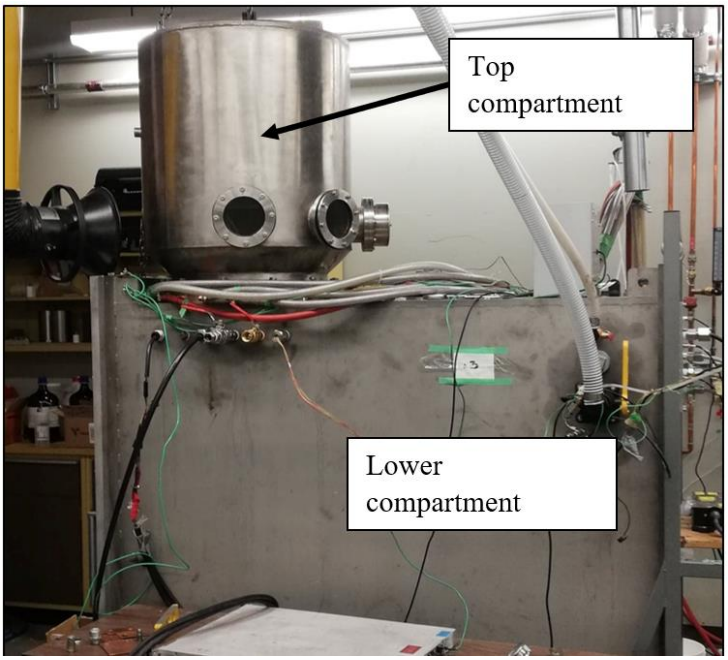

Figure 4.12. The atomisation chamber showing both compartments when closed.

The atomisation chamber is made of 19.1 mm (0.75 inch) thick stainless steel and houses the camera, laser head and translation stage, as well as the negatively charged ring electrode in the bottom compartment. While the crucible system, induction coils and vibration unit sit in the top compartment. All the electrical connections into the two compartments are fitted using stainless steel vacuum feedthroughs, ensuring the chamber can be safely operated under a high vacuum of up to 0.0013 Pa (10^{-5} torr), and could also be pressurised up to 101 kPa (15 psi). To enable these pressure conditions both gas feed lines and a vacuum line are connected to the chamber. To pressurise the system, gas is fed via 6.35 mm diameter tubing from pressurised gas cylinders. To depressurise the system, an Edwards EDS 300 vacuum pump is used allowing the chamber to attain a minimum pressure of 0.5 Pa (0.004 torr). Cold water at a temperature of 13°C is also constantly cycled through the chamber via 6.35 mm diameter tubing to cool the surfaces of the chamber and to prevent heat from spreading to and damaging vital equipment such as the camera and the lens, the frequency generator, the ring electrode along with its mount, and several electrical connections inside the chamber. A stainless-steel collecting vessel of a diameter of 30 cm and a height of 40 cm was filled with 4 litres of mineral oil and placed at the bottom of the lower compartment directly underneath the orifice to collect the solidified metal droplets.

4.8 Atomization Procedure

In this study the atomisation process includes up to five independent variables and three dependant variables. The independent variables include the applied frequency, the orifice diameter, the applied voltage, the applied over head pressure, and the liquid temperature. The dependant variables include the droplet diameter, the jet velocity, and the jet wavelength.

Collecting the average values of the droplet diameter during different runs and correlating the values to the independent variables was one of the primary objectives, and it is a major theme to be discussed in the Results and Discussion Chapter. The droplet diameter data was collected using the shadowgraph system as discussed in Section 4.6. When working with metals any droplets collected in an oil bath that had sufficiently solidified into powders were also cleaned, dried and sieved before being stored for future analysis.

Several other variables do exist in such a study that were not included in the scope of this project due to the limited time frame but should be avenues of any future studies related to this project. Some of these include: the electrode shape and geometry, the orifice to electrode distance, the electrode polarity, and the plunger shape.

Therefore, when starting an experimental run depending on the liquid to be atomised the correct crucible was selected. The chosen orifice diameter and the respective plunger to orifice diameter was then noted and fixed. The ring electrode was kept fixed at a distance 1.5 cm below the orifice and was connected to the negative polarity of the high voltage power supply while the bulk liquid was grounded and kept at zero volts. When working with metals both compartments of the atomisation chamber were shut after ensuring the thermocouples were in place and the camera and the laser were turned on and working. The entire atomisation tower was flushed empty using the vacuum pump to a gauge pressure 0.67 Pa (500 mtorr) and then filled with Argon or Helium to a gauge pressure of 13,800 Pa (2 psig). Several cycles of this were done until an oxygen level of less than 10 ppm was recorded using an oxygen analyser. In this project the oxygen analyser used was the Model 2D Oxygen Monitor manufactured by Centorr Vacuum Industries. After achieving the desired oxygen level of 10 ppm, the atomisation tower was kept at a positive gauge pressure of 13,800 Pa (2 psi) for the remainder of the experiment. Once the atomisation conditions had been satisfied (i.e., the required oxygen level had been met, and the liquid was at the desired temperature) the vibration of the frequency generator was initiated and the experiment was begun. The droplets were recorded and several sets of images (between 70 – 250 in each set) were taken for the entire run.

4.9 Summary

The apparatus and atomisation process described above were used to study the effect of the operating parameters such as the applied frequency, applied voltage, nozzle diameter, liquid flow rate, and their correlation to the average droplet size, size distribution, jet breakup regime, jet wavelength and production throughput. The results to these studies will be described in the next chapter.

Chapter 5: Results and Discussion

The results from the experiments conducted during this study will be analyzed and discussed in this chapter. This chapter will be divided into 4 sections. In section 5.1 the experimental results will be outlined and discussed with respect to the jet formation in the Rayleigh regime. Section 5.2 will focus on jet breakup and the effect of the applied vibration. In Section 5.3 the effect of the applied voltage will be discussed. The Bernoulli – Electrostatic model and its application will be reviewed in Section 5.4. In this chapter the shadowgraph images and histograms obtained during the experiments will be referred to. This information is located in Appendix A of this thesis.

5.1 Jet Formation in the Rayleigh Regime

In this section the experimental conditions regarding jet formation will be outlined and discussed. This is to ensure that during all experiments the jet is operating in the Rayleigh Regime as outlined by Figure 2.11. The jet breakup will thus be due to axisymmetric disturbances. The Rayleigh breakup has been discussed in great detail in Chapters 2 and 3.

5.1.1 Material Selection

Experiments in this study were conducted using three different materials. These are presented in Table 5.1 below, along with their respective thermophysical properties.

Table 5.1. List of materials used in this study, along with their density, viscosity and surface tension at the noted temperature

Material [Reference]	Operating Temperature (°C)	Density (kgm^{-3})	Viscosity (Pa s)	Surface Tension (Nm^{-1})
Water **[122]**	20	1000	0.001	0.073
Ethylene Glycol **[123]**	20	1100	0.02	0.049
Tin (99.9% purity) **[124]**	400	7000	0.0013	0.553

The values of the thermophysical properties in Table 5.1 were obtained from different engineering handbooks and material property databases, as referenced next to each material in the table. The

water used in this study was tap water obtained from the main water supply line to the laboratory. The ethylene glycol and tin were purchased from the Fisher Scientific Company.

The materials presented in Table 5.1 were chosen as our experimental liquids because they are easily available, affordable, and easy to work with and handle (i.e., quite unreactive with reasonably low melting points). These liquids also cover a wide range of property values, with the density varying by a factor of seven, and the surface tension and viscosity each varying by one order of magnitude between the different liquids. Thus, when generating correlations, a wider range of values are accounted for. Hence the correlations can be easily extrapolated for different materials.

It is important to note that in Table 5.1, the operating temperature of the fluids is listed. This is because all three thermophysical properties (density, viscosity, and surface tension) are functions of temperature. An increase in the operating temperature would lead to a decrease in these property values, and therefore would affect the breakup of the liquid jet. The operating temperature of water and ethylene glycol was kept at 20 °C, i.e., the laboratory room temperature. Tin on the other hand has a melting point of 231 °C **[3].** However, an operating temperature of 400 °C was chosen, to ensure the liquid jet had enough time to break into spherical droplets, and to avoid the material from solidifying before this happens.

5.1.2 Experimental Conditions

Several experiments were conducted using the materials mentioned in Table 5.1. The experimental parameters were varied and noted, as shown in Table 5.2.

Table 5.2. List of experiments conducted, and the experimental parameters during each run. The abbreviations S, A, G, P in the 6th column stand for the steel, graphite, alumina and PLA crucibles, respectively

Material	Orifice diameter (mm)	Liquid head (cm)	Overhead pressure (Pa)	Flow rate (ml/min)	Crucible, Figure number	Velocity (m/s)	Jet breakup length (mm)	C_D
Water	0.07	5	6206	0.5	S, 4.3	2.25	2	0.74
	0.1	5	6760	1.2	S, 4.3	2.75	4	0.81
	0.275	5	2551	6.3	S, 4.3	1.78	12	0.79
	0.35	5	2620	10.5	S, 4.3	1.82	17	0.78
	0.45	5	2896	18.3	S, 4.3	1.92	26	0.77
	0.75	13	0	32	A, 4.1	1.21	35	0.82
	1	7.5	0	40	A, 4.1	0.85	38	0.78
	1	6.5	0	37.5	A, 4.1	0.80	36	0.80
	1	5.5	0	34	A, 4.1	0.72	32	0.81
	1.5	6.5	0	87.5	G, 4.1	0.83	68	0.79
	1.5	7.5	0	95	G, 4.1	0.90	74	0.79
	2	5.5	0	150	G, 4.1	0.80	101	0.82
	2	7.5	0	185	G, 4.1	0.98	124	0.85
	2	9.5	0	200	G, 4.1	1.06	134	0.81
	2	5.5	0	110	P, 4.2	0.58	74	0.60
	2	7.5	0	125	P, 4.2	0.66	84	0.58
	2	9.5	0	150	P, 4.2	0.80	101	0.61
	2	5.5	0	113	P, 4.2	0.60	76	0.62
	2	7.5	0	124	P, 4.2	0.66	83	0.57
	2	9.5	0	145	P, 4.2	0.77	97	0.59
Ethylene Glycol	0.1	5	10753	1.4	S, 4.3	2.97	8	0.67
	0.275	5	5654	8.1	S, 4.3	2.25	28	0.69
	0.45	5	3034	16.1	S, 4.3	1.69	41	0.68
	2	5.5	0	120	G, 4.1	0.64	111	0.64
	2	7.5	0	135	G, 4.1	0.72	126	0.61
	2	9.5	0	160	G, 4.1	0.85	151	0.64
Tin	0.35	5	18616	11.2	S, 4.3	1.93	17	0.83
	0.45	5	14410	16.3	S, 4.3	1.71	22	0.81

From Table 5.2 it can be noted that the orifice diameter was varied from 0.07 – 2 mm in diameter, and depending on this, the correct crucible and nozzle configuration was chosen. The steel crucible was used for orifices of less than 0.75 mm in diameter, as an overhead pressure was necessary to create a liquid jet.

The flow rate noted in Table 5.2 was measured by collecting the volume of the drained liquid in a measuring cylinder for 2 minutes. This was repeated 3 times, and an average was taken and recorded. When working with metals, the mass of the solidified material was collected and weighed. The mass flow rate was then converted to the volumetric flow rate using the density recorded in Table 5.1. The velocity of the jet was then calculated through a mass balance presented in Equation 3.66. Following this, the length of breakup was calculated using Weber's Equation, as presented in Section 3.3, Equation 3.53. Finally, the discharge coefficient was calculated using Equation 3.56.

From Table 5.2 it can be seen that for every given material as the orifice size decreases, generally the velocity and the overhead pressure (where applied) increase. Following the works of Young – Laplace presented in Chapter 3 (Equations 3.3 – 3.6), a decrease in the orifice size would lead to an increase in the surface energy. If the hydrodynamic pressure of the head of the liquid is not sufficient to overcome these surface forces, then an external pressure must be applied in order to form a jet. Therefore, as noted in Table 5.2 a decrease in the office size requires higher pressures for operation due to the increased surface energy. Furthermore, as noted in Chapter 2, a jet can only be formed if the inertial forces overcome the cohesive surface tension forces. Hence, as the orifice size decreases, the jet velocity (i.e., the inertial force) increases. This is in accordance with the description of the inertial forces presented in Section 3.1.

The data presented in Table 5.2 show that the discharge coefficient is dependent on the liquid and the nozzle system used. The discharge coefficient is higher when working with water and tin, as compared to ethylene glycol. This is because of the viscosity of the different materials. From Table 5.1 it is seen that Tin and water both have very similar viscosity values at the given operating temperatures. Ethylene glycol on the other hand has a much higher viscosity. Therefore, the viscous forces resisting the formation of the jet are much higher when using ethylene glycol,

resulting in a lower discharge coefficient. The discharge coefficient is also dependent on the nozzle system, particularly the aspect ratio of the nozzles. As presented in Table 4.1, all the nozzle systems used in this study have a very small aspect ratio ($L/d_0 < 4$), except the PLA crucibles which have an aspect ratio of $L/d_0 = 50$. Following this, it can be seen from Table 5.2, when working with water and a 2 mm orifice diameter, the discharge coefficient changes significantly when the crucible is changed from graphite to PLA. This is due to the increase in the aspect ratio. As reviewed in Section 2.1.2.3, an increase in the aspect ratio would lead to increased friction between the walls of the nozzle and the surface of the liquid jet, generating greater resistance against the flow. This slows down the flow of the liquid, as the kinetic energy of the liquid is consumed to overcome the frictional forces, and thus the discharge coefficient reduces significantly. A reduction in the velocity of the jet has very significant effects on the jet breakup length, the jet diameter, and the droplet diameter. This will all be discussed in detail in the following sections of this chapter.

5.2 Jet Breakup, Droplet Production, and the Effect of an Applied Vibration

This project is based on jet breakup in the laminar Rayleigh regime. The experimental parameters presented in Table 5.2 must therefore be checked to ensure that the jet is operating in the desired regime. This is done primarily through the Ohnesorge plot, as outlined in Chapter 2, Section 2.1.3.2 **[52]**. In addition to this, the breakup classification methods proposed by Trettel (reviewed in Section 2.14) will also be used in this study **[58]**.

5.2.1 Jet Breakup Classification

The Ohnesorge plot is widely used by engineers and scientists to determine and predict the jet break up. It is a simple and quick method of liquid jet breakup classification. The experimental data collected in this study was therefore plotted in the Ohnesorge plot and shown in Figure 5.1.

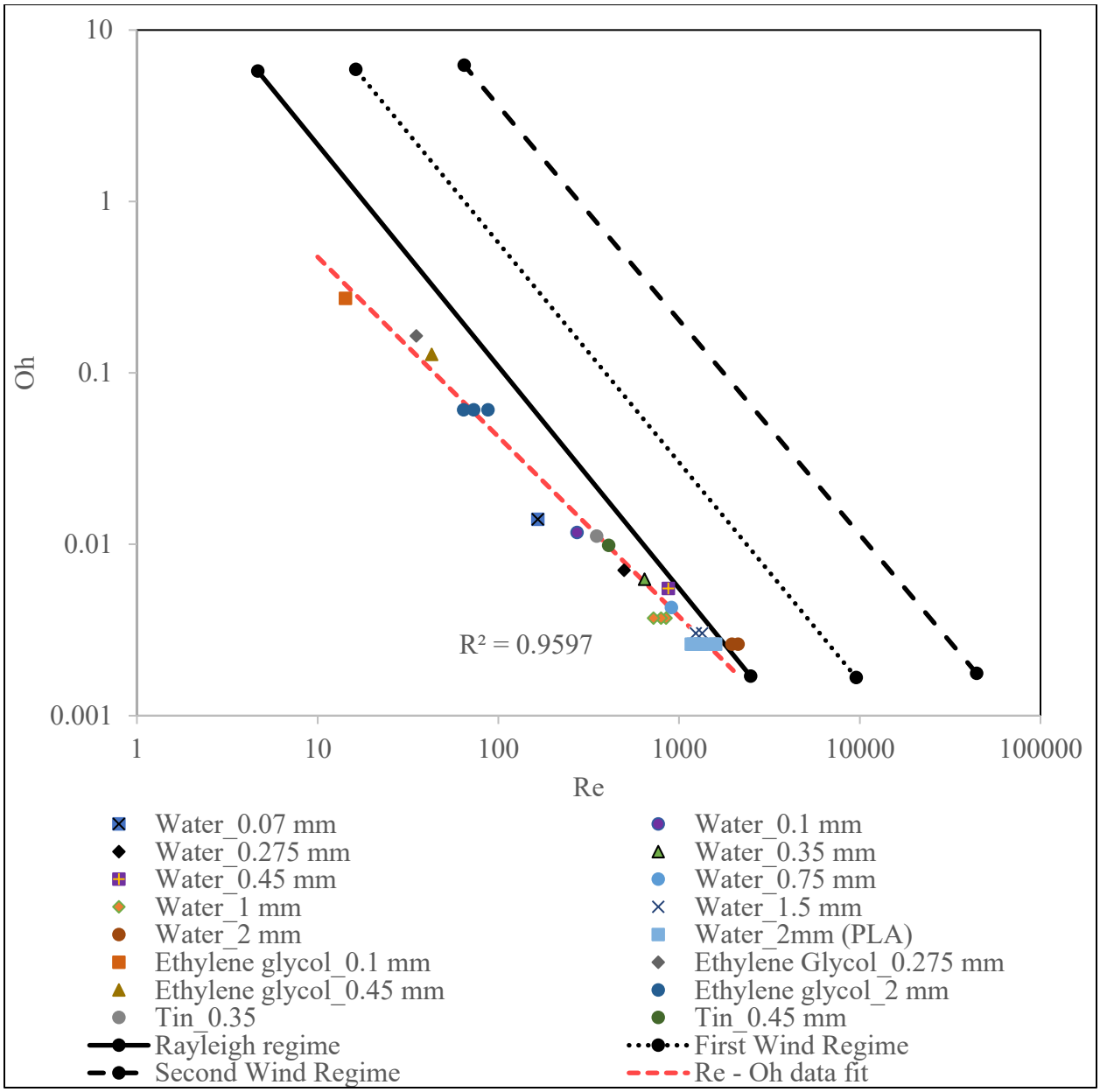

Figure 5.1. The experimental data (presented in Table 5.2) presented on an Ohnesorge plot, along with the line of best fit, labelled the 'Re - Oh data fit'

In Figure 5.1 the different regimes are presented by the black oblique lines crossing the plot. The area prior to the left of the solid oblique line is the Rayleigh Regime, and the area after the oblique line on the far right is the atomization regime. The First Wind and Second Wind Regimes lie respectively between the Rayleigh and atomization regimes.

Most of the data plotted in Figure 5.1 lies, almost parallel to the Rayleigh regime limit. A simple correlation between the Reynolds and the Ohnesorge number can be created. This is shown in Figure 5.1 through the line labeled as the 'Re - Oh data fit'. Taking all data into consideration, this fit gives a least r-squared value of approximately 0.96, and an average error of 16.3%. It is presented in Equation 5.1 below.

$$Oh = 5.31(Re^{-1.05}) \tag{5.1}$$

Following the definition of the Reynolds and Ohnesorge numbers presented in Table 3.1, Equation 5.1 can be recognized for the operation velocity to be the subject of the formula. This is presented in Equation 5.2.

$$v = \left(5.31(\mu^{0.05})\left(\frac{1}{\rho^{0.55}}\right)(\gamma^{0.5})\left(\frac{1}{{d_0}^{0.55}}\right)\right)^{0.95} \tag{5.2}$$

From Equation 5.2, the velocity of the jet is a function of the liquid properties (density, viscosity, and surface tension), and the orifice diameter. The surface tension and the viscosity are directly proportional to the jet velocity, and hence an increase in these parameters will lead to an increase in the velocity. Following the definitions of the Reynolds number (inertial force/viscous force), and the Weber number (inertial force/surface tension), an increase in the viscosity or surface tension would mean that the inertial forces must be increased for a jet to form. Hence, the direct proportionality of the velocity towards the surface tension and viscosity. The viscosity has little effect on the jet velocity, showing that for a jet to be created in the Rayleigh regime, the main force opposing this under these experimental conditions is the surface tension and not the viscosity.

The density and orifice diameter are inversely proportional to the jet velocity, and so an increase in either one, or both of these parameters will lead to a decrease in the velocity. The increase in the density leads to higher inertial forces following Equation 3.1 (Newton's second law of motion). Therefore, to balance the inertial force present in the system the operation velocity must be reduced. A larger orifice diameter reduces the effects of the surface tension and viscous forces that oppose the creation of the jet, and so larger orifice sizes lead to reduced velocities, as lower inertial forces are required.

Equation 5.1 is of great importance in this project. This is because objective of this study is to operate in the Rayleigh regime and to obtain uniform jet breakup. The Rayleigh regime has the bounds We > 8 and Weg < 0.4, as presented in Table 2.1. This gives a very wide area of operation. However, from Figure 5.1 it can be seen, that in fact the area of operation is best fit to a particular region with the correlation presented in Equation 5.1. Therefore, rather than just assuming and guessing an optimal velocity for the jet using the bounds by Lin and Reitz, and Ranz (Table 2.1), the correlation in Equation 5.1 can be used to easily approximate the velocity of operation, using just the liquid thermophysical properties and the orifice diameter.

While the Ohnesorge plot presented in Figure 5.1 is a quick and simple method to determine the jet breakup regime, it does have several drawbacks. The three most significant drawbacks with regards to this project are:

1 The Ohnesorge plot is completely qualitative, and the regimes are constructed based on jet observation from different experiments by several researchers **[52, 53, 54]**. Many of these experiments were conducted using a very specific set of equipment, and so if the geometric parameters are changed, one may observe that the data does not fit in the correct regime.

2 The Ohnesorge plot ignores the dripping regime. The Rayleigh regime is seen to be very large (as shown in Figure 5.1), stretching several orders of magnitude in both the Reynolds and Ohnesorge axes. However, this is not necessarily true. If the Reynolds number is reduced significantly such that the inertial forces cannot overcome the viscous and surface tension forces, then a jet will not be able to form. Rather the liquid will exit the orifice in a dripping fashion. To overcome this hurdle, the bounds suggested by Ranz, and Lin and Reitz, presented in Table 3.1 are often used to determine the dripping regime **[56, 57]**. However, these bounds in themselves have several drawbacks as discussed in detail in Chapter 2.

3 The Ohnesorge plot ignores any nozzle effects and so effects such as turbulence and cavitation cannot be accounted for. Nozzle geometry also has an effect of reducing the flow rate due to an increased aspect ratio, as was seen in Table 5.2. This effect is also ignored in the Ohnesorge plot.

In order to ensure that the jets produced in this study are operating in the laminar Rayleigh regime, each of these drawbacks has to be accounted for.

5.2.1.1 Accounting for the Qualitative Nature of the Ohnesorge Plot

It can be noted in Figure 5.1, most of the data points collected in this study lie in the Rayleigh Regime, very close to the transition line to the First Wind Regime. Some data points do lie just beyond the Rayleigh regime. However, this should not be of too much concern, as the Ohnesorge plot is constructed using averaged qualitative data from several experiments. The bounds for the different regimes are therefore lines of best fit, and as such data points lying on or close to the transition lines can often be assumed to be in the desired regime, provided another proof of break up is presented. For this study the proof lies in the photographs and histograms of the droplets obtained during the experiments[5]. An example of the water droplets produced at 3 different times with an orifice of 0.35 mm, along with the size distribution histogram is presented in Figure 5.2 below. For further references, similar images for the other experiments mentioned in Table 5.2 are presented in Appendix A.

[5] The quantitative approach outlined by Trettel (reviewed in Chapter 2) will also be used as an added approach to ensure that the droplets are on the Rayleigh regime.

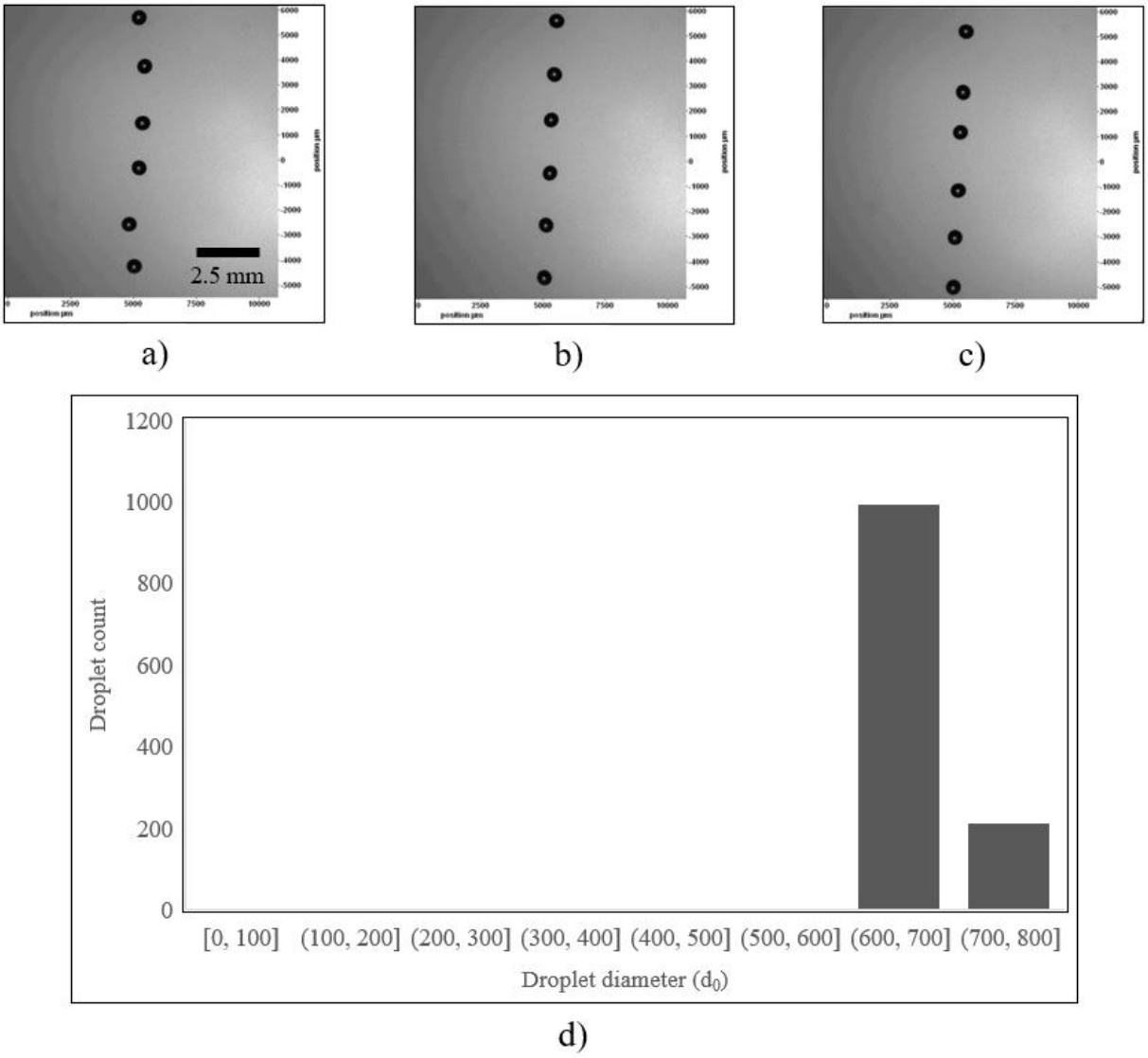

Figure 5.2. Images of water droplets from a 0.35 mm orifice at times 5, 10, and 15 seconds presented in a), b), and c) respectively. The histogram showing the droplet size distribution, presented in d).

From the images of the droplets captured by the shadowgraph camera, the droplets can be seen to breakup in a very orderly fashion and are all larger in size as compared to the orifice diameter (d_0 = 0.35 mm). From the histogram detailing the droplet sizes, it is clear that most of the droplets are of similar size, with no satellites being produced. This therefore demonstrates that the jet is not breaking up in the First Wind regime, whereby the droplets produced are of comparable size to the orifice diameter, as reviewed in Section 2.13.

5.2.1.2 Accounting for the absence of the Dripping Regime

The second hurdle to account for is to ensure that the droplets are not produced via dripping at the office. This is done through the assessment of the Weber number. Following the work of Trettel, and Clanet and Lasheras, a jet is described to be flowing continuously if it has a Weber number is greater than a critical Weber number ($We > We_{crit}$), as presented in Equation 2.9 and discussed in Section 2.14 **[58, 61]**. The critical Weber number is a function of a constant K (which is approximately equal to 0.4), and the Bond number for the inner and outer nozzle diameters. In this project wetting at the orifice is ignored, and so the Bond number for the outer nozzle diameter is taken to be equal to that of the inner diameter. The calculated critical Weber number therefore has a value of approximately 4 for all experimental parameters in this study ($We_{crit} = 4$). If all data points have a Weber number greater than the critical value, then conventionally a simple graphical representation of the Reynolds number versus the Weber number (showing $We > We_{crit}$ for all Re) would be enough to satisfactorily conclude that the jet is continuous and not in the dripping regime. However, a better method would be to follow the works of Trettel, as this gives an insight into the transition into the 'downstream regime' as well[6].

In his work, Trettel explains that as a laminar jet exits an orifice it transitions into a semi turbulent profile if it extends far enough without breaking into droplets **[58]**. In this, Trettel is explaining that if the velocity of the jet is large enough, then the jet will extend further downstream, and in the process transition from laminar to semi-turbulent. This semi-turbulent profile is responsible for the transition from a Rayleigh regime to a 'downstream transition regime'[7]. Trettel defined the transition length as presented in Equation 2.11. If the jet breakup length (calculated using Equation 3.53) is larger than the transition length (Equation 2.11), then the jet moves into the downstream transition regime. Therefore, a better format of displaying the conventional Reynolds versus Weber number plot, would instead be to display it in the form of a transition length to breakup length ratio versus the Weber number, as the 'downstream transition', 'Rayleigh' and the 'dripping' regimes can all be represented in the same plot. This is shown in Figure 5.3.

[6] Trettel renamed the first wind regime as the downstream transition regime. This has been reviewed in Section 2.14.

[7] This should not be confused with a turbulent jet existing the orifice. In the case mentioned in the text, the jet exits as laminar but transitions to a semi-turbulent profile, which in turn causes it to transition to the downstream transition regime.

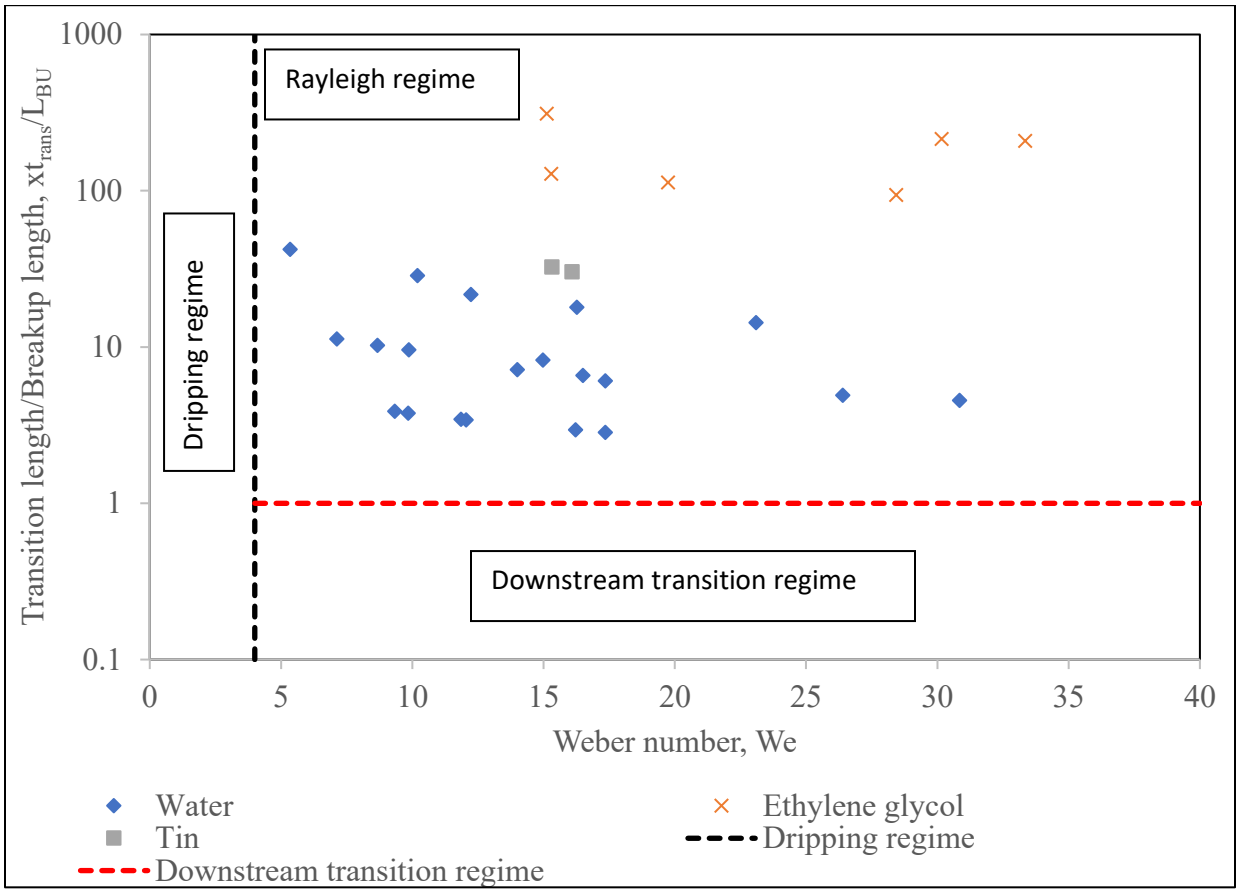

Figure 5.3. A plot showing the Rayleigh, downstream transition, and dripping regimes, with respect to the Weber number, for all experimental data presented in Table 5.2

From Figure 5.3 it can firstly be noted that none of the data points lie in the dripping regime, as the Weber number is always greater than the critical Weber number. It can also be seen from Figure 5.3, the transition length is much greater than the calculated break up length, and so none of the data points lie in the downstream transition regime. This further clears the confusion regarding the data points lying on or just beyond the transition line from the Rayleigh to the First Wind regime as shown in Figure 5.1.

While there does not seem to be any trend regarding the relation of the jet length ratio to the Weber number in Figure 5.3, it is clear that ethylene glycol has a much higher transition to breakup length ratio, as compared to water and tin. This is due to the much higher viscosity of ethylene glycol, as noted in Table 5.1.

5.2.1.3 Accounting for the Onset of Turbulence at the Orifice Exit

Having concluded that the jet is operating in the Rayleigh regime, the next step would be to account for the onset of turbulence as the jet exits the orifice. From the works of Trettel (reviewed in Section 2.14), a jet can operate in the Rayleigh regime but also be turbulent at the same time. Turbulence is due to the nozzle geometry and the inertial forces of the liquid exiting the orifice. Therefore, as outlined in Equation 2.7 (from the works of Van de Sande and Smith), if the Reynolds number (i.e., the inertial force) is greater than the critical Reynolds number for a given nozzle aspect ratio, then the jet exiting the office will be turbulent **[40]**. The ratio of the critical to experimental Reynolds number for the different materials and orifice sizes is shown in Figure 5.4 below.

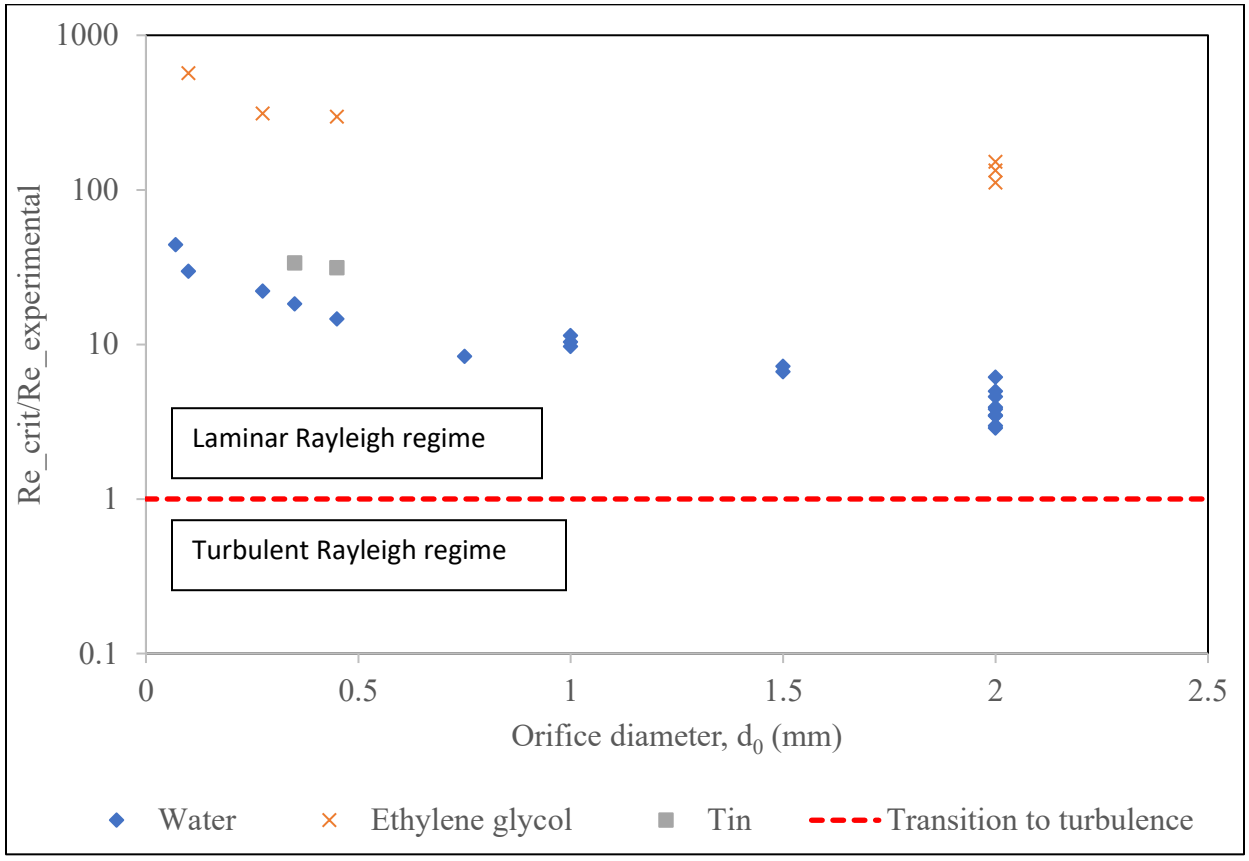

Figure 5.4. The transition to turbulence using the ratio of the critical to experimental Reynolds number

In Figure 5.4 the critical Reynolds number is greater than the experimental Reynolds number for all cases, and therefore, the jet is operating in the laminar Rayleigh regime. In Figure 5.4 it can also be seen that the ratio of the Reynolds number is approximately 2 orders of magnitude higher for ethylene glycol than for the other materials. This is because of the significantly higher viscosity of ethylene glycol. Since the Reynolds number is a ratio of the inertial to viscous forces, ethylene glycol jets have much lower Reynolds numbers, and therefore these jets must be operated at much higher velocities in order to enter the turbulent regime, as compared to water and tin.

From Figure 5.4 it can also be noted that the ratio of the critical to experimental Reynolds number is much higher for smaller orifice sizes. This again can be explained from the definition of the Reynolds number as presented in Table 2.1. In this particular case the Reynolds number is a function of two dependent variables for a fixed liquid, i.e., the velocity of the jet and the orifice diameter. When reviewing Table 5.2 it was seen that the velocity of the jet generally increases with a decreasing office size. This would have an increasing effect on the Reynolds number. However, following the same pattern, on the other hand as the orifice size decreases the Reynolds number should reduce in magnitude. In this study, the decrease in the orifice size is of a much greater magnitude than the increase in the velocity. Therefore, the Reynolds number decreases with the orifice diameter. Hence, the increase in the ratio of the critical to experimental Reynolds number with a decrease in the office size as shown in Figure 5.4. Following these observations, two conclusions can be made regarding the transition to turbulence while operating in the Rayleigh regime. Firstly, it can be noted that a liquid of higher viscosity operates much more easily in the laminar regime. Secondly, as the orifice size reduces in diameter, a much higher velocity is required to transition the jet from laminar to turbulent.

After analyzing the results presented in Table 5.2 and Figures 5.1 – 5.4, it can be concluded that the jet is operating in the desired laminar Rayleigh regime. The next items to discuss are therefore the jet breakup and droplet production.

5.2.2 Jet Diameter and the Result of an Applied Vibration on Droplet Production

In order to best understand the breakup of the liquid jet into droplets, both the jet diameter and the applied frequency must be assessed.

5.2.2.1 Effects of an Applied Vibration, and Determining the Optimal Frequency

During each experimental run the droplets produced with, and without an applied vibration were recorded using the shadowgraphy system. The frequency of vibration was altered until an optimal frequency was attained. For every run the jet diameter was also calculated following the Bernoulli energy balance presented in Equations 3.68. The results of the optimal vibration frequency, droplet diameters, and calculated jet diameter are presented in Table 5.3.

Table 5.5. The calculated jet diameter, and measured droplet diameters with and without the applied optimal frequency

Material	Orifice diameter (mm)	Velocity (m/s)	Jet diameter (mm)	Optimal vibration frequency (Hz)	Average droplet diameter with applied vibration (mm)	Average droplet diameter without applied vibration (mm)
Water	0.07	2.25	0.07	1100	0.42	0.39
	0.1	2.75	0.10	1500	0.29	0.29
	0.275	1.78	0.27	1000	0.60	0.66
	0.35	1.82	0.34	900	0.68	0.589
	0.45	1.92	0.43	780	0.72	0.58
	0.75	1.21	0.68	340	1.35	0.65
	1	0.85	0.84	250	1.68	1.50
	1	0.80	0.84	250	1.62	1.52
	1	0.72	0.83	250	1.55	1.68
	1.5	0.83	1.15	250	1.90	1.28
	1.5	0.90	1.16	250	1.98	1.50
	2	0.80	1.41	200	2.92	1.79
	2	0.98	1.46	200	3.12	1.66
	2	1.06	1.48	200	3.21	1.59
	2	0.58	1.33	200	2.55	1.75
	2	0.66	1.36	200	2.71	1.81
	2	0.80	1.41	200	2.88	2.02
	2	0.60	1.34	200	2.61	1.68
	2	0.66	1.36	200	2.69	1.62
	2	0.77	1.40	200	2.71	1.55
Ethylene Glycol	0.1	2.97	0.10	1400	0.28	0.41
	0.275	2.25	0.27	800	0.72	0.57
	0.45	1.69	0.42	700	0.78	0.90
	2	0.64	1.22	200	2.51	1.75
	2	0.72	1.25	200	2.66	1.38
	2	0.85	1.30	200	2.81	2.29
Tin	0.35	1.93	0.34	1000	0.78	0.64
	0.45	1.71	0.43	900	0.74	0.71

From Table 5.3 it can be noted, as the orifice size decreases the calculated jet diameter also decreases, becoming almost equal to the orifice at the smallest diameters. It can also be noted that as the orifice size decreases, the optimal vibration frequency increases. Both these observations are related to the increase in the jet velocity at lower orifice sizes. As the jet velocity increases the

inertial forces increase which prevent the surface tension and viscous forces in having an effect in decreasing the jet diameter[8]. With regards to the optimal vibration, as the velocity increases the disturbances on the jet propagate much faster downstream, and so the frequency of the applied vibration must be increased as well.

The droplet diameters measured with, and without an applied vibration, are very different from each other, even though the rest of the operating conditions are the same, as presented in Table 5.3. For better illustration, the droplet sizes produced with and without an applied vibration are shown in Figures 5.5 and 5.6 respectively.

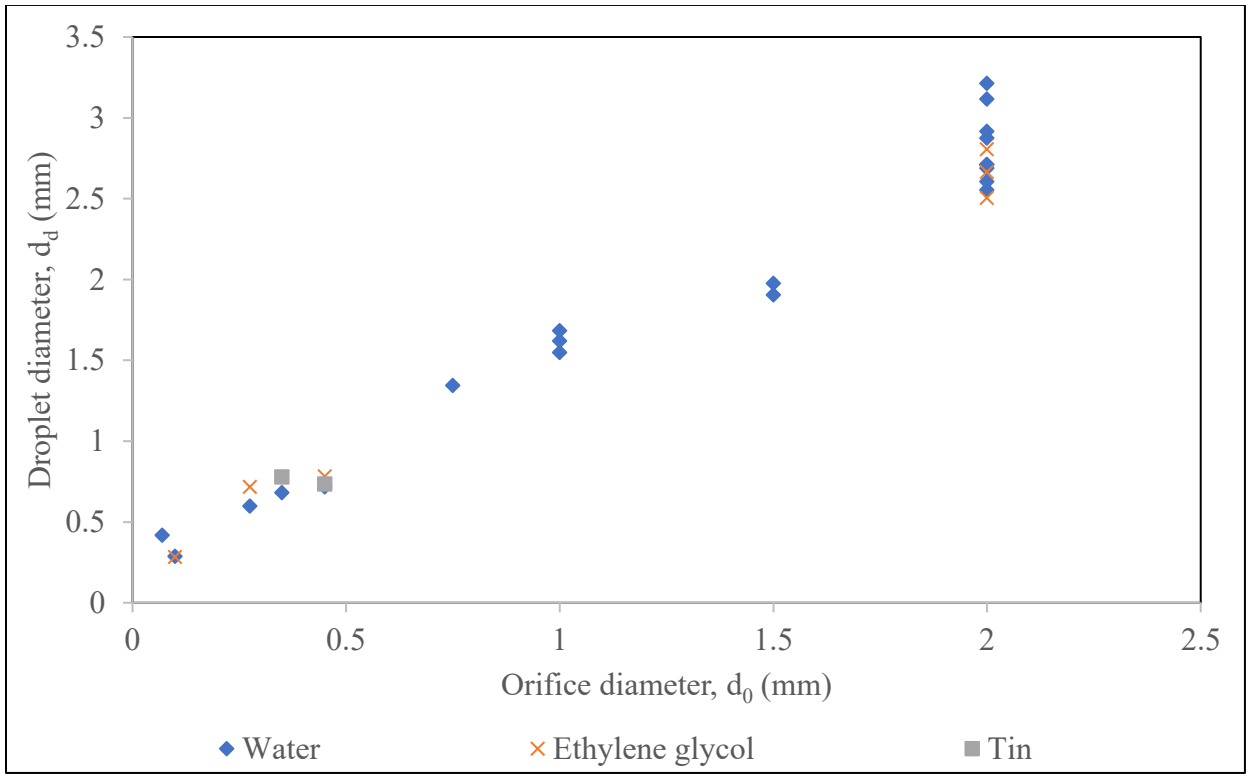

Figure 5.5. The measured droplet diameters when a vibration of optimal frequency was applied to the liquid

[8] This is covered in more detail in Section 5.2.2.2 below.

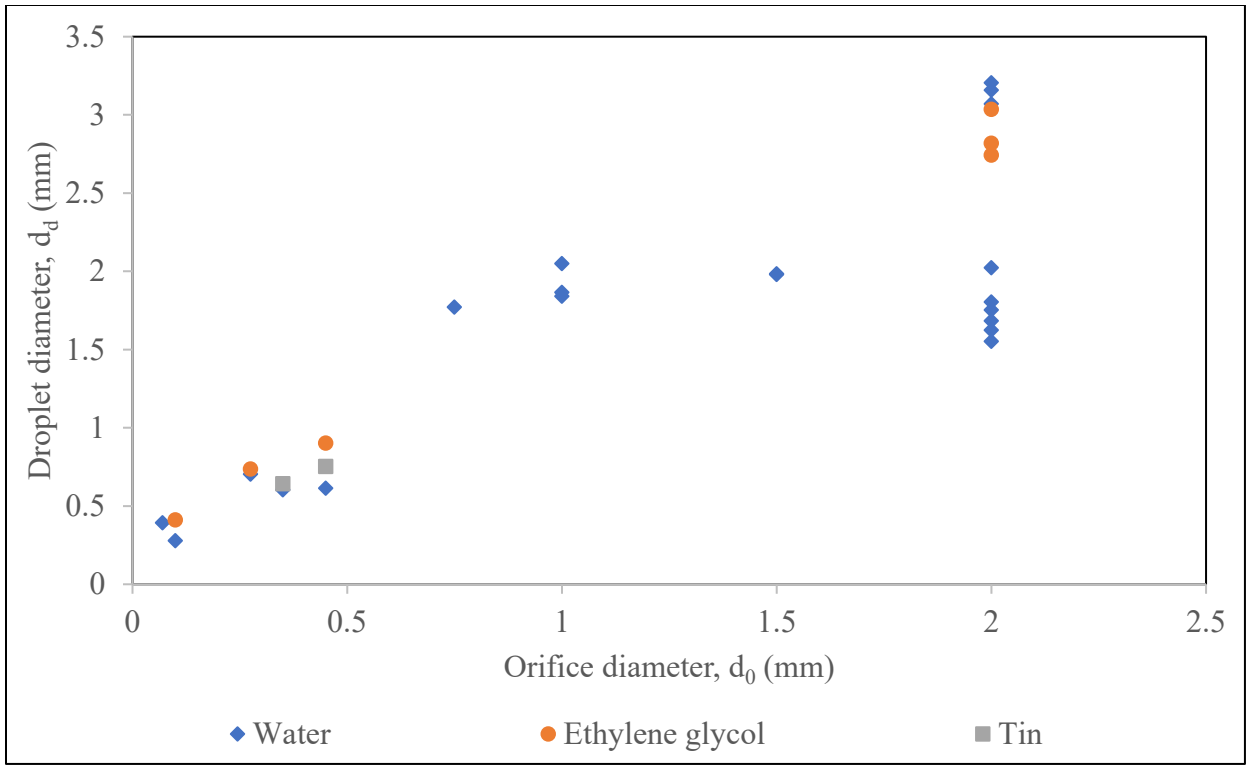

Figure 5.6. The measured droplet diameters when a vibration of optimal frequency was not applied to the liquid

Figures 5.5 and 5.6 illustrate that applying a vibration to the bulk liquid affects the droplet production. In order to assess this difference, the droplet sizes and size distributions must be compared. In Figure 5.5 it can be observed that the droplet diameters produced with an applied vibration follow a consistent trend; as the orifice diameter decreases, the droplet diameter also decreases. This is however not true for the droplets produced without an applied vibration, as shown in Figure 5.6. Therefore, the added vibrations make the droplet production much more consistent and predictable. From Table 5.3 it can be argued that the droplets produced without the added vibrations are smaller in several cases. In order to understand why this is so, the droplet size distributions must be compared. Figure 5.7 below shows the percentage of the droplets within a 20% range of the average droplet diameter, with respect to the different orifice diameters.

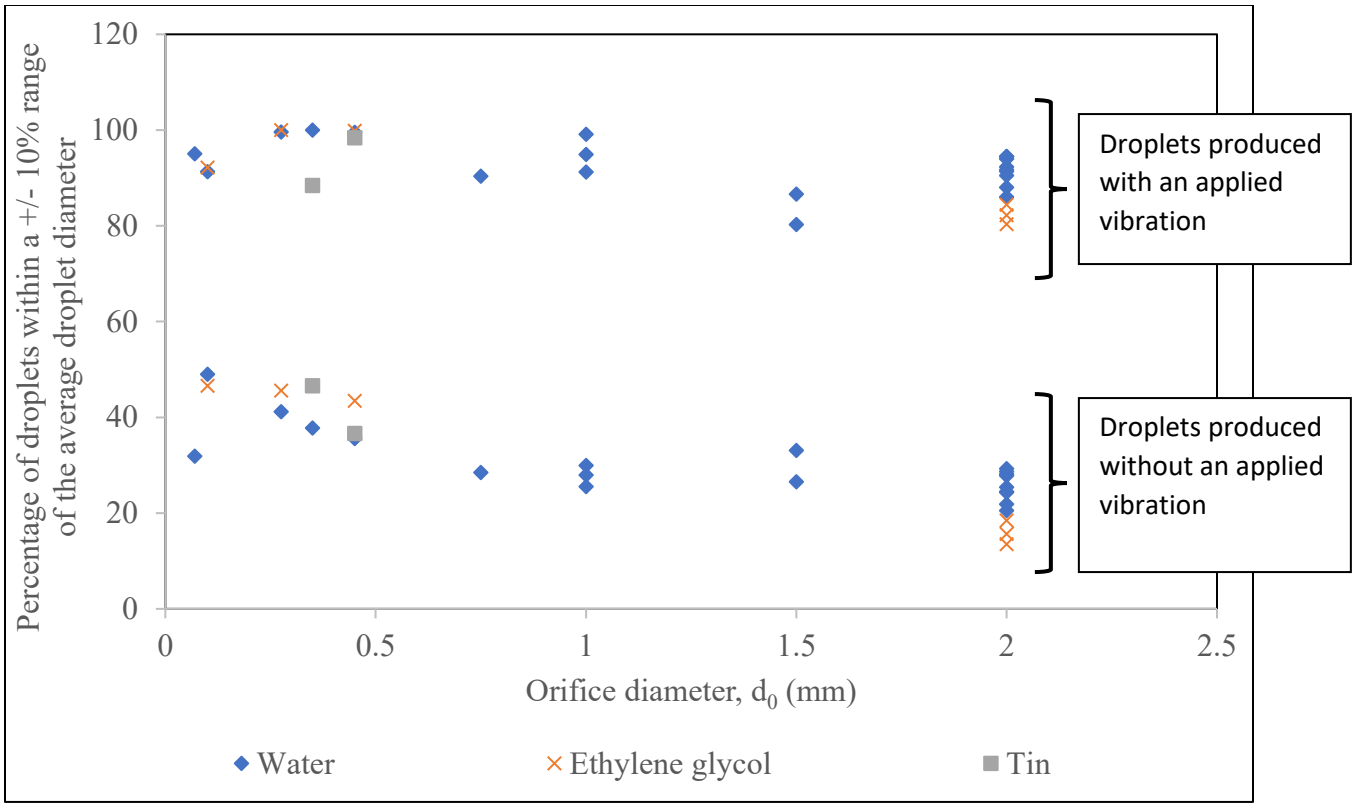

Figure 5.7. The size distribution of the droplets produced at different orifice sizes, presented as a percentage of the total number of droplets within a 20% range of the average measured droplet size

In Figure 5.7 when a vibration is applied a much higher percentage of droplets lie within a 20% range of the average diameter. This goes to show that the droplets produced with an applied frequency have a much narrower size distribution. Therefore, the question from earlier can be answered, regarding why the droplets produced without an applied frequency were smaller in diameter in some cases. It is because they have a much larger size distribution with very many satellites being produced. The satellites have a very small diameter and therefore the average droplet diameter is much lower without an applied frequency[9]. Figure 5.7 also answers the questions regarding the optimal frequency of vibration and how it was chosen. As mentioned earlier, in this study the frequency was altered during each run until a specific "optimal frequency" was obtained. This optimal frequency was picked such that, of the droplets produced, at least 80% of them lied within a 20% range of the average droplet diameter, as presented in Figure 5.7.

[9] For further reference the size distribution histograms for every run with and without an applied optimal frequency are presented in Appendix A.

5.2.2.2 Determining the Jet Diameter for Different Experimental Conditions

Having measured the droplet diameters for all runs, it is important to relate these values to those predicted using the Rayleigh and Weber equations. The Rayleigh equation predicts that the droplets produced will have a value dependent only on the orifice diameter, as shown in Equation 3.46. Weber's equation goes a step further, and takes into account the thermophysical properties of the liquids, via the Ohnesorge number. The Weber correlation is displayed in Equation 3.47. The Rayleigh and Weber equations were used to predicted the droplet diameter for every experimental run. From this, the error between the measured and predicted droplet diameter was noted and is presented in Table 5.4 below.

Table 5.4. The errors when using the Rayleigh and Weber equations to predict the droplet diameters produced for every run in this study

Material	Orifice size (mm)	Jet velocity (m/s)	With an applied frequency		Without an applied frequency	
			Error from Rayleigh's Equation (%)	Error from Weber's Equation (%)	Error from Rayleigh's Equation (%)	Error from Weber's Equation (%)
Water	0.07	2.25	215.9	194.6	197.8	111.1
	0.1	2.75	51.9	41.7	47.1	37.3
	0.275	1.78	15.1	7.6	35.4	0.2
	0.35	1.82	2.9	3.7	8.8	33.0
	0.45	1.92	15.7	21.1	27.9	47.4
	0.75	1.21	5.1	11.1	25.0	2.7
	1	0.85	11.0	16.6	1.3	19.7
	1	0.8	14.3	19.7	2.5	20.1
	1	0.72	18.1	23.3	8.4	10.1
	1.5	0.83	32.8	37.0	30.2	43.0
	1.5	0.9	30.3	34.7	30.0	43.4
	2	0.8	22.8	27.6	18.8	33.4
	2	0.98	17.6	22.7	16.5	33.2
	2	1.06	15.0	20.3	15.2	32.9
	2	0.58	32.4	36.7	53.6	53.4
	2	0.66	28.4	32.8	52.2	52.0
	2	0.8	23.9	28.7	46.5	46.2
	2	0.6	31.1	35.4	55.4	55.3
	2	0.66	28.9	33.3	57.0	56.9
	2	0.77	28.3	32.7	58.9	58.7
Ethylene Glycol	0.1	2.97	49.7	27.2	118.0	85.3
	0.275	2.25	37.8	21.0	41.8	0.8
	0.45	1.69	7.9	18.1	6.2	21.3
	2	0.64	33.7	39.5	19.7	31.9
	2	0.72	29.5	35.7	27.4	39.3
	2	0.85	25.8	32.2	25.4	38.9
Tin	0.1	1.93	17.6	9.8	2.8	9.2
	0.45	1.71	13.6	19.3	11.3	34.0
Average error			23.7	25.5	30.6	34.7

From Table 5.4 it can immediately be noted that the errors for the droplets produced using an orifice of 0.07 mm are much larger than any of the other errors shown. This is due to the wetting

of the liquid jet at the orifice exit, causing the jet to increase in size and produce droplets of much larger diameters. The effects of wetting will not be considered in this project. However, for the sake of consistency and having identified an obvious outlier, the error for the droplets from the 0.07 mm orifice were excluded when calculating the average error.

As noted in Table 5.4, very significant errors were recorded for both, the Rayleigh and the Webber equation, with each correlation averaging an error of greater than 20%. This shows that neither the Rayleigh nor the Webber correlation is good enough to predict the droplet diameter. The reason for this is because neither equation takes into account the velocity of the jet. In Table 5.2 it was very clear that along with the orifice diameter and the thermophysical properties, the liquid head, overhead pressure, and the nozzle aspect ratio all played a part in dictating the velocity of the jet. Then in turn the velocity of the jet determines the jet breakup length and the jet diameter at breakup. Therefore, using correlations such as those presented by Webber and Rayleigh are not accurate, except for inviscid linear systems.

The jet velocity must be accounted for in order to find a correlation capable of predicting the droplet diameters. This is done through the use of the jet diameter and length of breakup Equations. As mentioned earlier, and reviewed in detail in chapter 3, the length of breakup is given by Equation 3.53, and the jet diameter at break up is given by Equation 3.68. These equations are functions of the inertial, viscous, and surface tension forces. When reviewing Equation 3.68 it was clear that a jet will only reduce in diameter if the inertial forces are not very high with respect to the other forces acting on the jet. In order to best analyze this, the ratio of the jet diameter to the orifice diameter, with respect to the Froude number is shown in Figure 5.8 below.

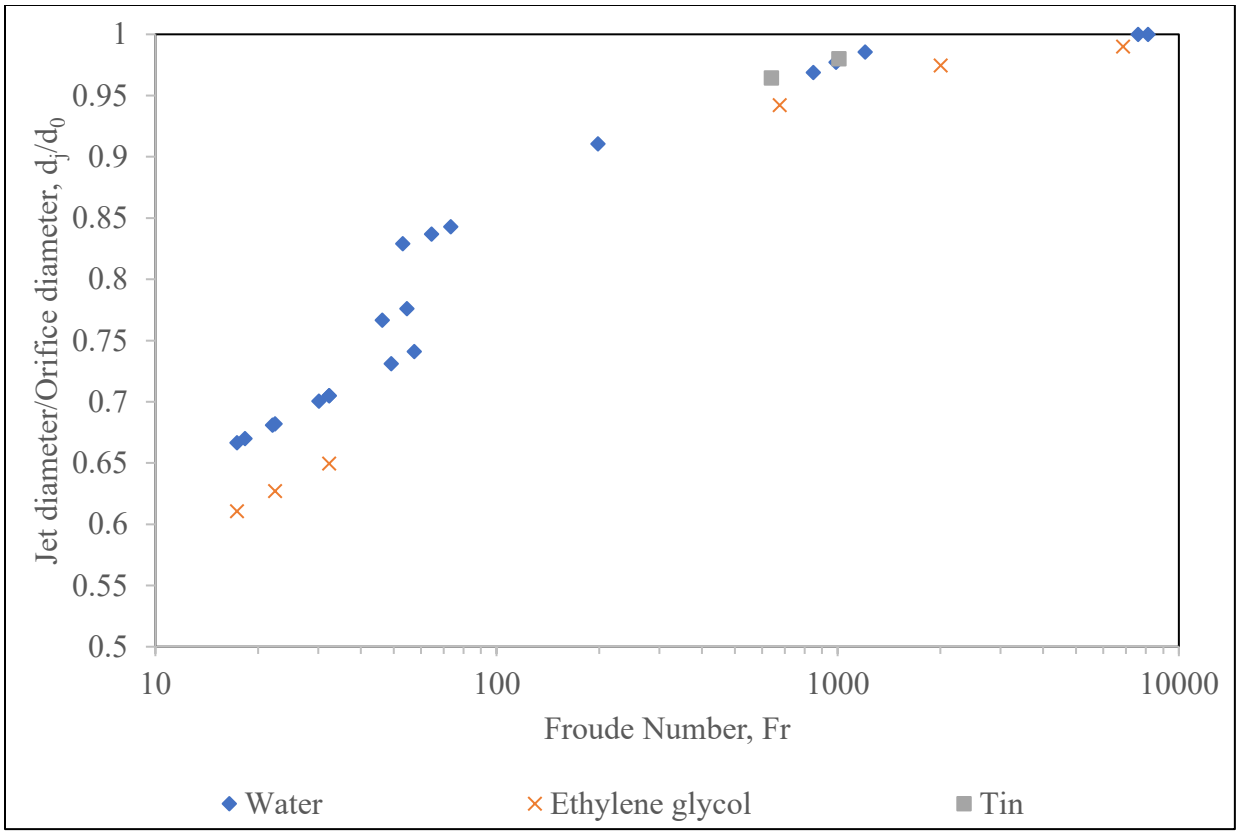

Figure 5.8. A comparison of the ratio of the jet diameter to orifice diameter with respect to the Froude number (i.e., the inertial forces).

Figure 5.8 shows that as the Froude number increases, the ratio of the jet diameter to the orifice diameter approaches unity. This is due to the significantly increased inertial forces with respect to the other forces present along the jet at smaller diameters. From Table 2.1, the Froude number is a ratio of the inertial to gravitational forces. The acceleration due to gravity is always a constant, therefore, the increase in the Froude number is due to the increased inertial forces at smaller orifice diameters. When the inertial forces are so much greater than the other forces (viscous and surface tension), the jet does not reduce in diameter and stays approximately the same size as the orifice. At low Froude numbers the jet diameter reduces to almost 60% of the orifice diameter, as presented in Figure 5.8. This occurs at larger orifice sizes and for more viscous liquids (such as ethylene glycol), due to the increased viscous forces.

In Figure 5.8 there appears to be somewhat of a discontinuity at the lower Froude numbers (Fr < 60). The data points show an almost step wise increase in the ratio of the jet diameter to the orifice

diameter. These data points are obtained from the 2 mm, and 1.5 mm orifice diameters. When operating with these diameters, the head of the liquid in the crucible was very similar to that when operating with the 1 mm diameter orifice, as shown in Tables 5.2 and 5.4. Therefore, the velocity of the jet is higher for the 2 mm orifices. Thus, the jet diameter does not reduce as much as it could have if the head was kept slightly lower, and therefore it appears as though there is a discontinuity in the data. However, this should not be of much concern as the jet is operating in the laminar Rayleigh regime for all runs (as discussed in Section 5.2.1), and the purpose of Figure 5.8 is simply to show that as the inertial forces increase (i.e., as the Froude numbers increase), the jet diameter reduces less in size and eventually becomes equal to the orifice diameter at very high Froude numbers.

5.2.2.3 Developing a Correlation for the Droplet Diameter

Having calculated the jet diameter at the breakup point, the next step was to determine if it correlated better to the droplet diameters than the Rayleigh and Webber Equations presented earlier in Table 5.4. Figure 5.9 below shows the ratio of the droplet to jet diameter, plotted against the calculated jet diameters.

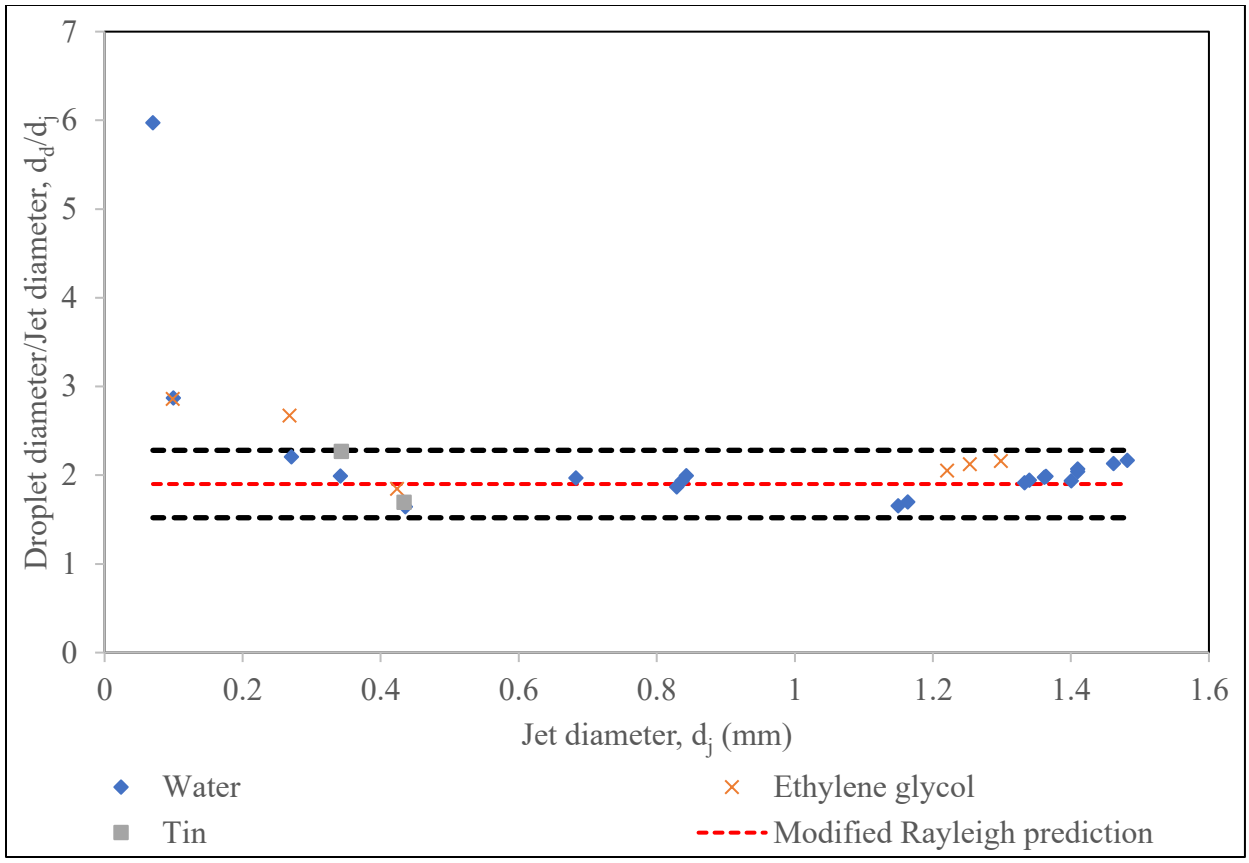

Figure 5.9. A correlation between the droplet diameters produced with an applied frequency and the calculated jet diameter, along with the modified Rayleigh prediction

In Figure 5.9 only the droplets produced with an applied frequency are presented. A modified Rayleigh prediction is presented as a straight line running horizontally across the graph, such that the droplet diameter is equal to 1.89 times the jet diameter ($d_d = 1.89dj$). This is similar to that presented in Equation 3.46, except that the jet diameter is used instead of the orifice diameter. Two parallel lines to the modified Rayleigh prediction are used to denote a 20% error. From Figure 5.9 it can be noted that all the data points, except the first two, lie within the 20% error range of the modified Rayleigh prediction. The data that lies above the 20% error line is due to the wetting at the smaller orifices. As stated before when discussing Table 5.4, the wetting at the orifice leads to larger droplet sizes, and so much larger errors when compared to the predicted values.

When calculating the average error in Figure 5.9, the value from the smallest orifice diameter (d0 = 0.07mm) was not included due to the very obvious effect of wetting. This is similar to the approach used when calculating the average error in Table 5.4, when using the conventional

Webber and Rayleigh correlations. However, as opposed to the results presented in Table 5.4, whereby the average error was noted as 23.7 % and 25.5 % for the Rayleigh and Weber equations respectively, the average error when using the modified Rayleigh equation is much lower, with a value of 10.7 %. The modified Rayleigh approach is therefore much better at predicting the droplet sizes as compared to the traditional correlations presented in Table 5.4. However, this approach is only valid for scenarios with no wetting at the orifice, and where the droplets produced are of uniform size. Both these conditions must be satisfied. As this project does not take wetting into consideration it will not be discussed any further. However, in order to test the second condition, a similar graph to Figure 5.9 has been created, except the data points are of the average droplet sizes produced without any applied vibration. This is presented in Figure 5.10 below.

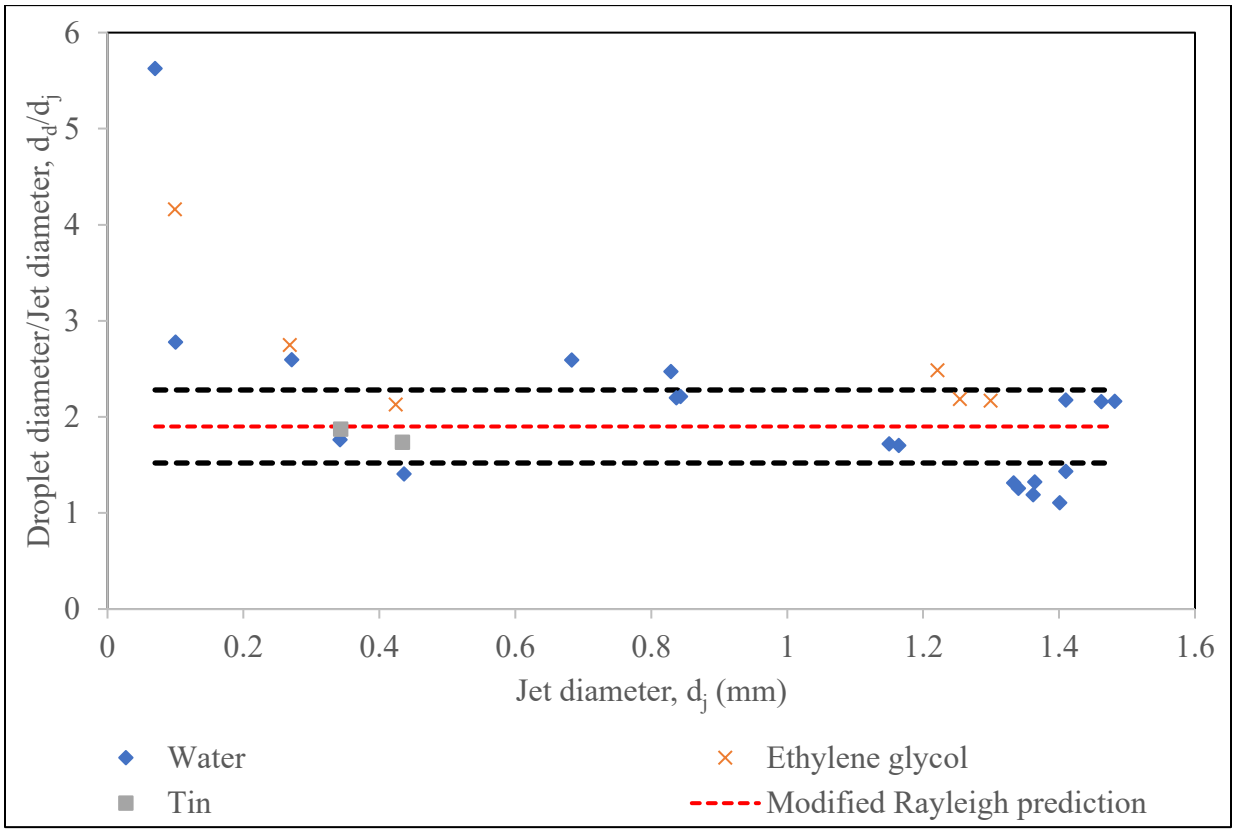

Figure 5.10. A correlation between the droplet diameters produced without an applied frequency and the calculated jet diameter, along with the modified Rayleigh prediction

As concluded earlier in Section 5.2.2.1, the droplets produced without an applied vibration have a very large size distribution (i.e., they are non-uniform in size). Therefore, unlike Figure 5.9, the

data points in Figure 5.10 are scattered across the graph, and do not lie in any distinct region. Comparing the modified Rayleigh prediction to the experimental data presented in Figure 5.10 gives an error of 25.7 %. This therefore goes to show that the modified Rayleigh approach is only valid for cases whereby the droplets are uniform in size.

5.2.2.4 Quantifying the Effect of an Applied Frequency

Having identified the optimal vibration frequency during several experiments, an empirical correlation for this data was developed. This was done by generating a scaling law using the Buckingham Pi method, and a least squares linear regression. The Buckingham Pi method was used to generate a dimensionless number, called the dimensionless frequency (F), presented in Equation 5.3 below.

$$F = \frac{d_d f_a}{v} \tag{5.3}$$

The dimensionless frequency (F) is a function of three variables of interest: the droplet diameter (d_d), the optimal frequency (fa), and the jet velocity (v). In this study there are several other variables, such as the liquid thermophysical properties, the applied overhead pressure, the liquid head during each experiment, and the nozzle geometry. However, these variables can all in fact be accounted for by the jet velocity, as presented in Equation 5.2. Thus, the dimensionless frequency was generated using just three variables, making it simple and concise.

Following this, a scaling law was designed. It is presented in Equation 5.4.

$$F = A(Re^{a1} We^{b1} Oh^{c1} Fr^{d1} Bo^{e1}) \tag{5.4}$$

Equation 5.4 is in the form of a power law, whereby A, and a1 – e1 are the constants of regression. Fitting the data and creating a correlation was done by translating Equation 5.4 into a linear logarithmic Equation as presented below.

$$\log(F) = \log(A) + a1 \log(Re) + b1 \log(We) + c1 \log(Oh) + d1 \log(Fr) + e1 \log(Bo) \tag{5.5}$$

This allows any simple regression tool (such as the 'LINEST' function in Microsoft Excel, or the 'fitlm' function in MATLAB) to be used to find the values of the constants A, and a1 – e1. In Equations 5.5 all five dimensionless numbers (Re, We, Oh, Bo and Fr) commonly used in fluid mechanics have been included. However, after running the linear regression several times, it was found that the most functional approach was to just include the Froude number alone on the right-hand side of Equation 5.5. This is because of the simplicity of the Froude number and the variables it accounts for. Unlike the other dimensionless numbers mentioned above, the Froude number does not include any of the thermophysical properties of the liquids, but does include the jet velocity. As discussed in Section 5.1, the velocity of the jet is a function of the thermophysical properties, and it dictates jet breakup and droplet formation. While the We, Re and Bo numbers do include the jet velocity, they also include the thermophysical properties, and each of these numbers leaves out one of the three properties. The Re number does not account for the surface tension forces, the We and Bo number do not account for the viscous forces. As such, the We, Re and Bo numbers are biased, and therefore do not give an accurate representation of the different forces, leading to inaccurate regressions. The Oh number includes all three thermophysical properties, but fails to include the jet velocity, and so is widely inaccurate.

Thus, using just the Froude number, the best fit for the experimental data in Equation 5.6 was found to be as follows:

$$F = \frac{1.69}{Fr^{0.25}} \tag{5.6}$$

Figure 5.11 below is a representation of the experimental data, along with the relation presented in Equation 5.6.

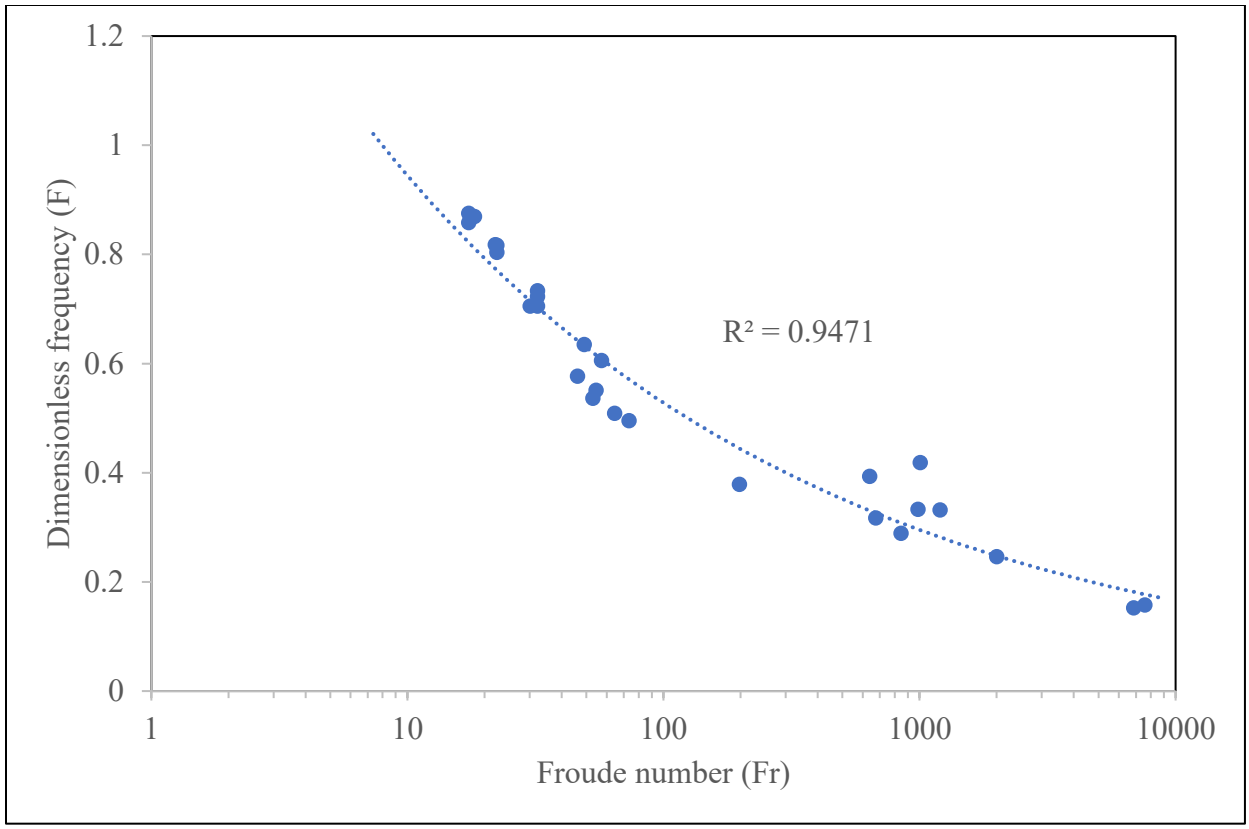

Figure 5.11. The dimensionless frequency (F) plotted against the Froude number (Fr). Both, the experimental data and the correlation in Equation 5.6 are presented here

Figure 5.11 shows that the relation presented in Equation 5.6 fits well with the experimental data, with an R^2 value of approximately 0.95. Equation 5.6 has a maximum error of 28.7 % when compared to the experimental data. However, both the average and median errors are less than 10%, with values of 8.3 % for the average error, and 6.7 % for the median error. These results outline that a successful atomization procedure operating in the Rayleigh regime (through the application of an induced vibration) has been designed, tested, and quantified. It is capable of producing droplets of uniform size, and acceptable correlations for the droplet diameter and applied frequency have been created.

Following this, the next part of this study was to determine the effect of an applied voltage on the droplet production.

5.3 Effects of an Applied Voltage on Droplet production

From several studies conducted on EHDA (as discussed in Section 2.2), a liquid meniscus/jet will be stressed into a conical shape if it is charged, or placed in a region of high electric charge. A jet with a diameter much smaller than the orifice diameter will then be ejected from the apex of the cone. More on the cone-jet mode of electrospraying and EHDA is covered in Chapter 2.

In this study, after successfully identifying the optimal frequency, and producing uniformly sized droplets, an electric field was then introduced around the jet as it exits the orifice. The purpose of this was to observe the effect of the applied electric field on the droplet sizes produced. Table 5.5 below shows the range of the applied voltage.

Table 5.5. The different voltages applied to the ring electrode for different experimental conditions

Material	Orifice diameter (mm)	Crucible, Reference Figure	Applied frequency (Hz)	Applied voltage (kV)
Water	0.07	Steel, Figure 4.3	1100	2, 5, 7
	0.275	Steel, Figure 4.3	1000	2, 5, 7
	0.35	Steel, Figure 4.3	900	2, 5, 7
	0.45	Steel, Figure 4.3	780	2, 5, 7
	0.75	Alumina, Figure 4.1	340	2, 5, 7
	1	Alumina, Figure 4.1	250	2, 5, 7
	1.5	Graphite, Figure 4.1	250	2, 5, 7
	2	Graphite, Figure 4.1	200	2, 5, 7
Ethylene Glycol	0.275	Steel, Figure 4.3	800	2, 5, 7
	0.45	Steel, Figure 4.3	700	2, 5, 7
	2	Graphite, Figure 4.1	200	2, 5, 7
Tin	0.35	Steel, Figure 4.3	1000	1, 2, 3
	0.45	Steel, Figure 4.3	900	1, 2, 3

As displayed in Table 5.5, experiments were conducted following the same conditions as outlined before in Table 5.2. The optimal frequency for uniform droplet production was applied for each run. The applied voltage was varied from a low, to a medium, to a high voltage value. These values are 2, 5, and 7 kV respectively when using water and ethylene glycol. When using tin, the low, medium, and high voltage values were changed to 1, 2, and 3 kV respectively. The maximum

values (i.e., the high voltage values) of 7 and 3 kV were chosen, as any further increase led to an electric discharge from the ring electrode. When working with tin the maximum voltage was reduced from 7 to 3 kV because the atmosphere was changed from air to helium. The dielectric strength of air is much higher than that of helium, and so a lower voltage is required to cause an electric discharge in a helium atmosphere **[125]**.

For every experimental run the average droplet diameter was measured and compared do the droplet size without any applied voltage (i.e., as presented in Table 5.3). This data for the low, medium and high voltages is presented in Figures 5.12, 5.13, and 5.14 respectively.

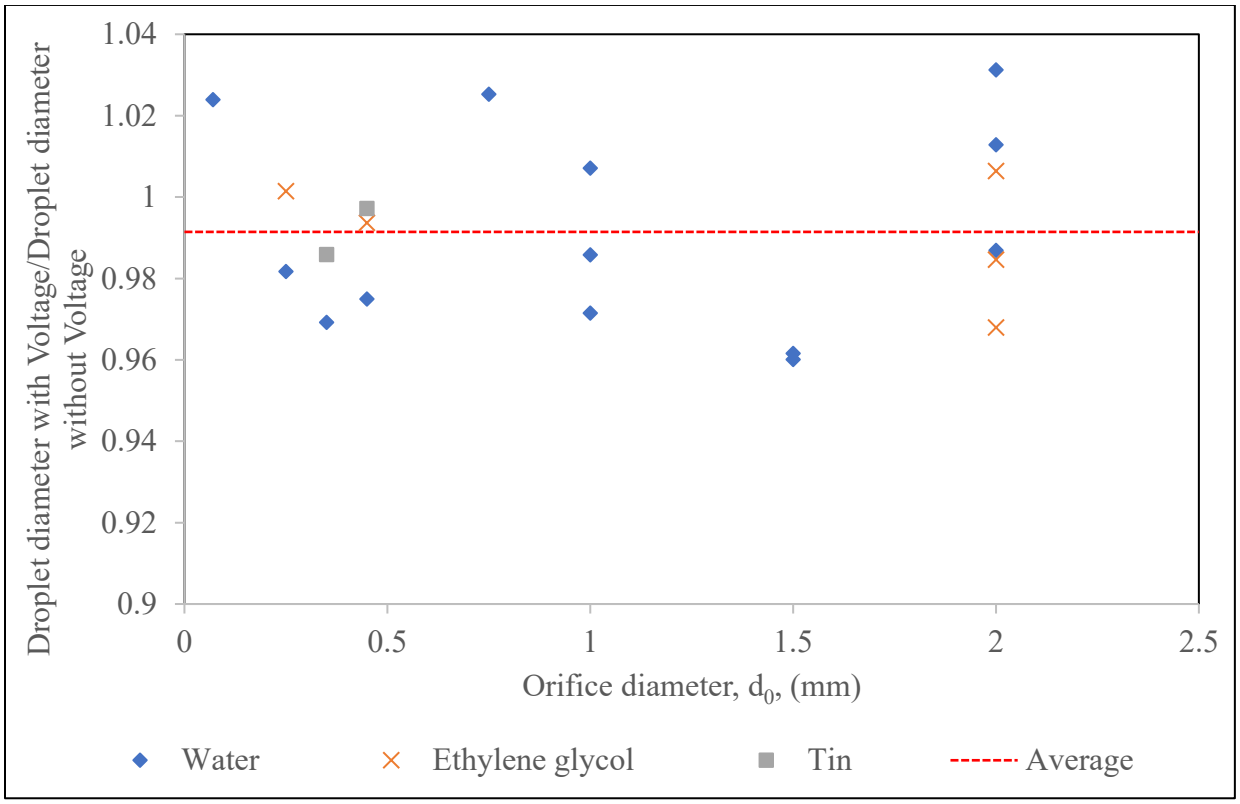

Figure 5.12. The ratio of the droplet diameters produced with and without any applied voltage, with respect to the orifice diameter. The voltage applied was the 'low' value of 2kV when working with water and ethylene glycol, and 1 kV when working with tin. The average value for the droplet diameter ratio (y-axis) is 0.99.

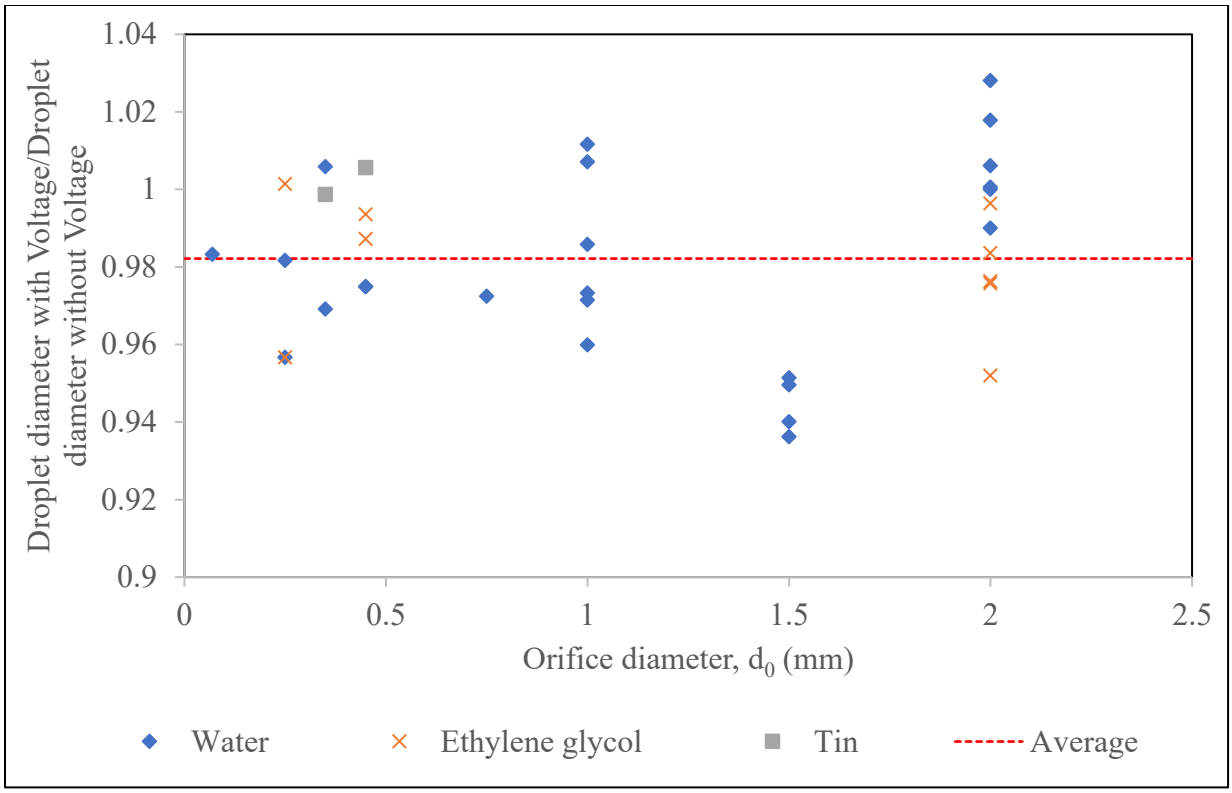

Figure 5.13. The ratio of the droplet diameters produced with and without any applied voltage, with respect to the orifice diameter. The voltage applied was the 'medium' value of 5kV when working with water and ethylene glycol, and 2 kV when working with tin. The average value for the droplet diameter ratio (y-axis) is 0.98.

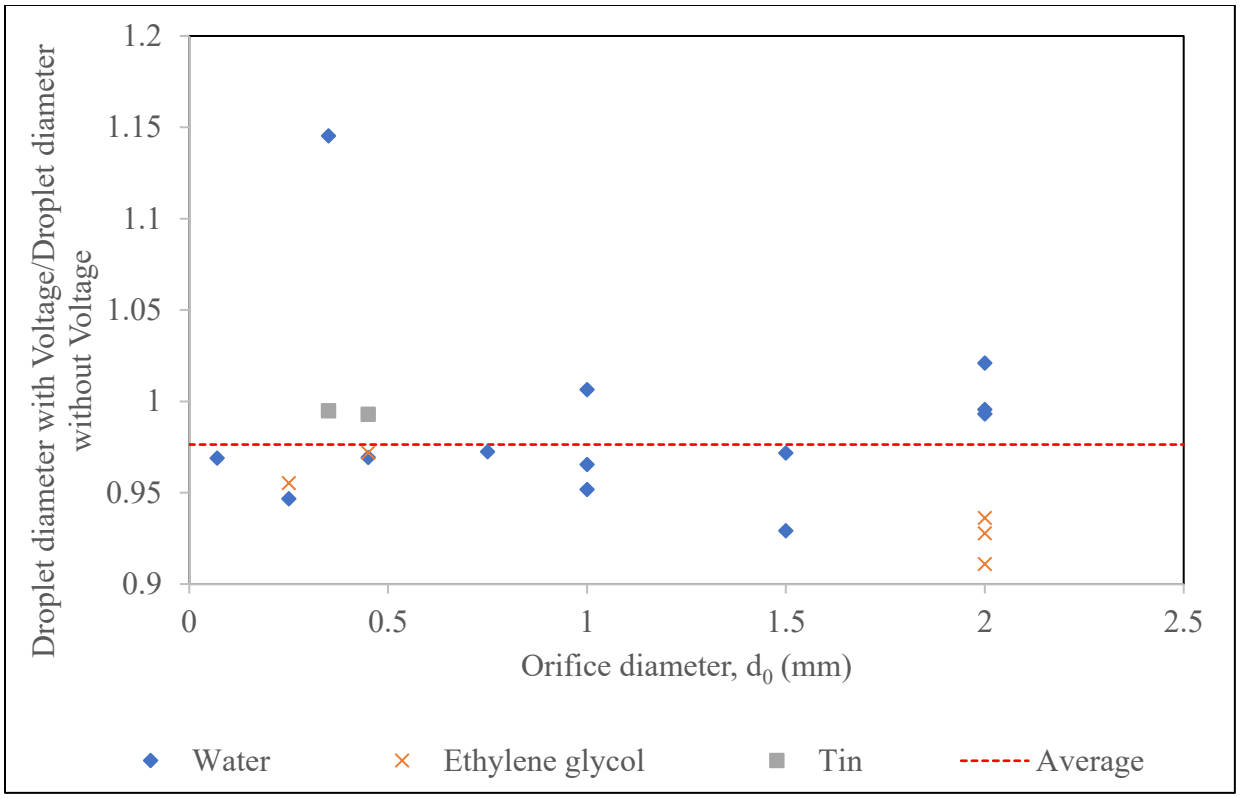

Figure 5.14. The ratio of the droplet diameters produced with and without any applied voltage, with respect to the orifice diameter. The voltage applied was the 'high' value of 7kV when working with water and ethylene glycol, and 3 kV when working with tin. The average value for the droplet diameter ratio (y-axis) is 0.975.

In Figures 5.12 – 5.14 a horizontal dashed line is used to represent the average of the ratio of the droplet diameters produced with and without an applied voltage. As the voltage is increased from a low to medium to high voltage, the average decreases from 0.99 to 0.98 to 0.975, respectively. Thus, the introduction of a voltage (i.e., electric stress) has an effect on reducing the average droplet diameters, albeit the effect is not very significant.

From Figures 5.12 – 5.14 it can be observed that at the larger orifice diameters (i.e., 2 mm), the introduction of an electric field has a much higher effect in reducing the droplet diameters of ethylene glycol than of water. This is because the velocity of the jet of ethylene glycol is lower than that of water, as presented in Table 5.2. Thus, the inertial forces on the jet of ethylene glycol would be lower, and the applied electric stresses would have a much greater effect in stressing the liquid. The opposite of this can be seen at orifice diameters of 0.275 mm, whereby the ethylene

glycol jet has a greater velocity than the water jet (as presented in Table 5.2). Thus, the effect of the electric field is lower in ethylene glycol than in water. At the orifice diameters of 0.45 mm the velocity of the water jet is higher than that of ethylene glycol. However, the effect of the electric field is seen to be greater on the water. This may be due to the errors created by the effects of wetting. It can also be noted in Figures 5.12 – 5.14, the voltage has a very little effect on the droplet diameters of metals. This again is due to the much higher inertial forces that oppose the constriction of the jet. In the Figures above it can be seen that for some data points the ratio of the droplets with and without an applied voltage is sometimes greater than 1. This is due to the wetting at the orifice, leading to larger jet diameters and thus larger droplet sizes.

5.4 The Bernoulli – Electrostatic Model

In the previous section, an increase in the applied voltage was seen to have an effect in reducing the droplet sizes produced. However, to best understand the effect of the electric field on a liquid jet, a Bernoulli – Electrostatic model was created. This model is based on the Bernoulli energy balance, the Young – Laplace surface energy formulation, and the electrostatic pressure balance on a Taylor cone. It is presented in Equation 5.7 below. The detailed derivation, and explanation of this Equation can be found in Section 3.5, Equations 3.57 – 3.68.

$$\left(\frac{r_0}{r(L_{BU})}\right)^4 = 1 + \frac{1}{Fr}\frac{L_{BU}}{r_0} + \frac{4}{We}\left(1 - \frac{r_0}{r(L_{BU})}\right) + \frac{Es}{We} \tag{5.7}$$

In Equation 5.7 the ratio of the orifice to the jet radius (i.e., the left-hand side of the equation) increases if the inertial forces are reduced, or if the electric, surface tension, gravitational, or viscous stresses are increased. For a given material operating in the Rayleigh regime little can be done regarding the viscous and surface tension forces, as these are inherently dependent on the thermophysical properties of the material. However, the gravitational and electric stresses are externally applied to the system. The gravitational forces cannot be increased under normal conditions. Therefore, the easiest way to manipulate Equation 5.7 is through the electric stresses. If the electric field is increased significantly, the value on the right-hand side will increase. Therefore, the jet will be constricted into a smaller diameter. However, it is important to note that the electric field can only be increased to a point such that the dielectric strength of the surrounding atmosphere is not exceeded. If in fact the dielectric strength is exceeded, then discharges (in the

form of corona and brush) due to gas ionization, will take place at the electrode, leading to an unstable system. Following Paschen's Law, the dielectric strength can be increased by manipulating the pressure of the atmosphere **[126, 127]**. Electrical breakdown will be discussed in more detail in Section 5.4.2.

5.4.1 Application of the Bernoulli – Electrostatic Model

The Bernoulli – Electrostatic model presented in Equation 5.7 is very simple and straightforward to follow, with no rigorous mathematical manipulation required. However, attention must be drawn to the last term of the equation, as it contains the electrostatic bond number (Es). This dimensionless number is presented in Table 2.1. It is a function of the orifice diameter, surface tension, electrical permittivity of the atmosphere, and the electric field created. The electric field in turn is a function of the applied voltage, the electrode shape, and the inter electrode spacing, making it very difficult to calculate analytically for most geometries. A numerical modeling approach is recommended instead. For example, using a computational software such as Comsol Multiphysics is a better approach in approximating the electric field.

The Bernoulli – Electrostatic model was tested using 10 different liquids (5 metals and 5 nonmetals). This was done in order to determine the operating conditions necessary to reduce the droplet size using the electrostatic force once a laminar jet is broken up into monodispersed droplets. The thermophysical properties of these materials at specific temperatures are noted in Table 5.6 below.

Table 5.6. List of materials with their thermophysical properties at the noted temperatures. These materials were used to test the Bernoulli - Electrostatic equation

Material, Reference	Temperature (°C)	Density (kg/m^3)	Viscosity (Pas)	Surface tension (N/m)
Water [**1**]	20	1000	0.001	0.073
Ethylene Glycol [**2**]	20	1100	0.02	0.049
Gasoline **[128]**	20	755	0.0003	0.0212
Ethanol **[129]**	20	792	0.0013	0.022
Oil **[130]**	20	910	0.05	0.035
Tin [**3**]	500	7000	0.0013	0.553
Zinc **[3]**	420	6570	0.00385	0.785
Aluminium **[131]**	700	2357	0.0012	0.868
Copper **[132]**	1085	8953	0.00336	1.3
Bismuth **[133]**	544	10068	0.0025	0.388

With the given thermophysical properties, the operation velocity can be calculated using the Re – Oh data fit presented in Equation 5.1. From this the inertial forces acting on the jet can be calculated using the Froude number. Knowing the Froude number gives a good insight on the final jet diameter, as it is a balance between the inertial force and the gravitational force (which is a constant). Therefore, as shown in Equation 5.7, if the Froude number increases the second term on the right hand-side (of Equation 5.7) becomes negligible and the jet does not reduce in size as it travels from the orifice to the breakup point. Figure 5.15 below presents the Froude number of the different materials flowing through orifice sizes ranging from 0.025 – 0.5 mm.

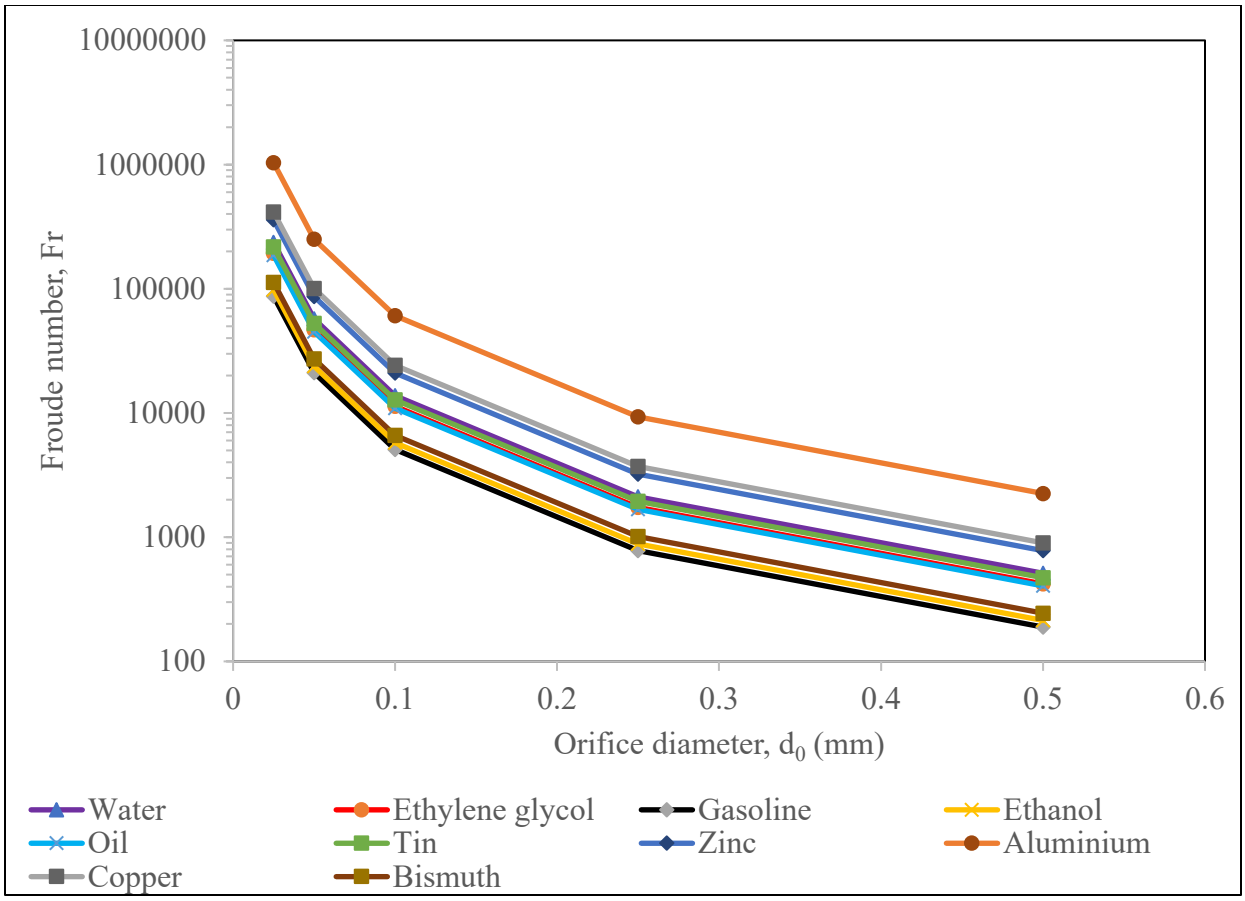

Figure 5.15. The Froude number at different orifice diameters for the materials presented in Table 5.6.

From Figure 5.15 the Froude number is seen to increase exponentially for all materials as the orifice is reduced in size. This shows that at the smaller orifice diameters, the second term on the right hand-side of Equation 5.7 becomes negligible and the jet will not reduce significantly in size as it stretches from the orifice to the breakup point. The exponential increase of the Froude number is due to the increase in the operational velocity of the jet at smaller orifice diameters. From Equation 5.2, the velocity is seen to be inversely related to the orifice diameter, and so a decrease in the orifice size would lead to an increase in the operational velocity (and the Froude number), as higher inertial forces are required for the jet to continue operating in the Rayleigh regime. If in fact the velocity is not increased then the jet will shift to the dripping regime, as shown in Figure 5.3.

From Figure 5.15, it can also be noted that Aluminium has the highest Froude number (inertial forces) for all orifice diameters. This is because of its relatively high surface tension, and relatively low density as compared to the other materials presented in Table 5.6. Therefore, following

Equation 5.2, Aluminium should be operated at the highest velocity for all orifice sizes in order to remain in the Rayleigh regime. Similarly, gasoline and ethanol have very low surface tension values and therefore operate at much lower velocities, hence the lower Froude numbers at all orifice diameters. Bismuth has a lower surface tension than all the nonmetals mentioned. However, it also has the highest density. Therefore, from Equation 5.2, the operation velocity is reduced, and as such the Froude number is lower for Bismuth as compared to all other materials except gasoline and ethanol.

Having calculated the operational velocity for all the materials at different orifice sizes, the length of breakup can be calculated next using Equation 3.53. The Bernoulli – Electrostatic model can then be applied. This can be done in two ways. Either the electric field or the jet radius can be taken as a dependent variable.

5.4.1.1 Using the Bernoulli – Electrostatic Model for the Applied Electric Field

When using the Bernoulli – Electrostatic model, it is sometimes more beneficial to have the electric field as a dependent variable in order to determine the strength of the field required for different materials and orifice sizes. In doing this, the radius of the jet must be fixed to a specific fraction of the orifice radius. Figure 5.16 below shows the electric field required to reduce the jet to 90% of the orifice diameter at break up, for all the materials mentioned in Table 5.6.

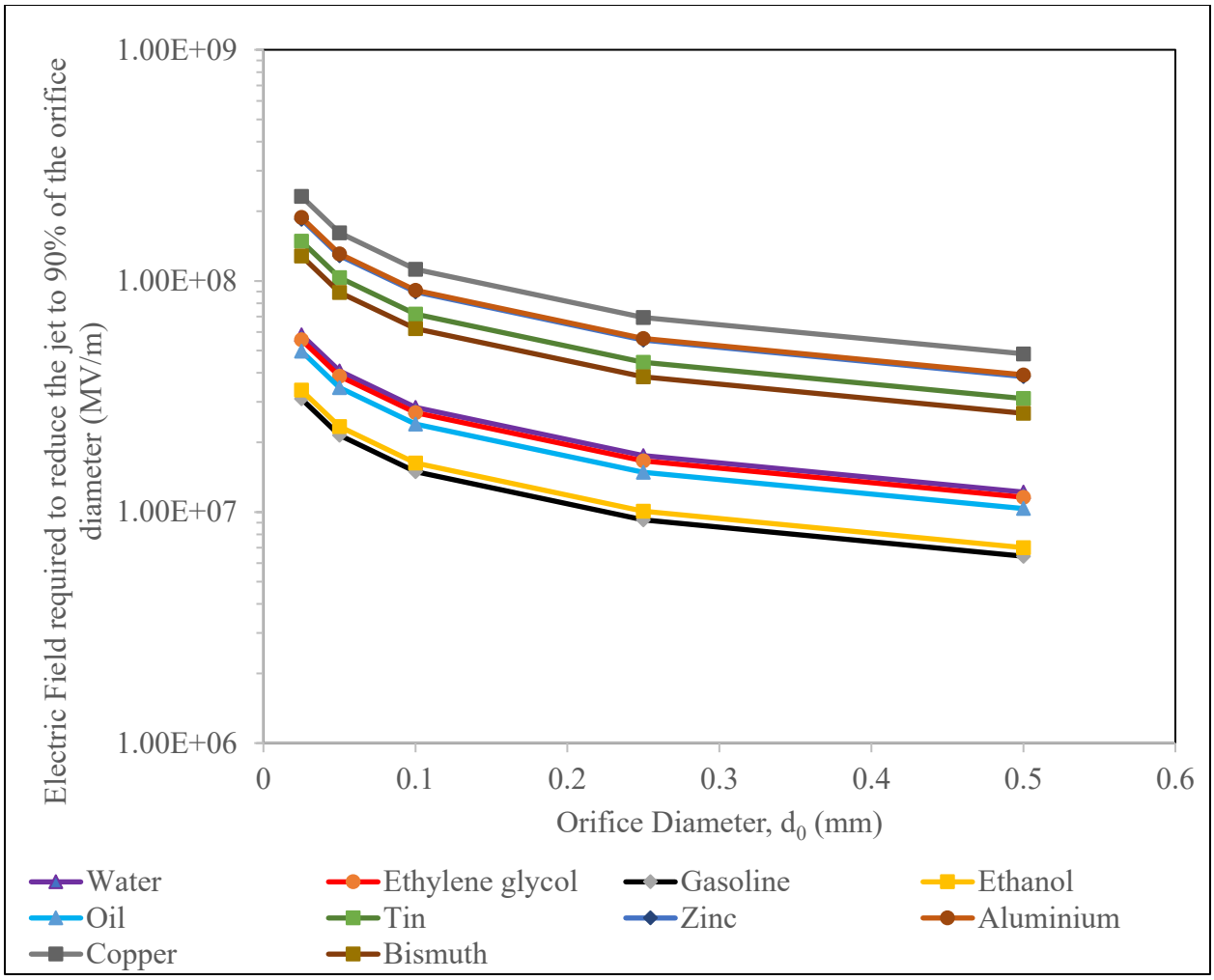

Figure 5.16. The Electric field required to reduce the jet diameter of the different materials by 10% as compared to the orifice size. The electric field was calculated using Equation 5.7

It can be seen from Figure 5.16, as the office size decreases, the electric field increases exponentially. This is because of the much higher forces of inertia at the lower orifice sizes as seen in Figure 5.15. The data in Figure 5.16 can be divided into two distinct groups. Group 1 consists of all the metals, and group 2 consists of all the nonmetals. There is a clear disparity between the two groups in the electric field required to reduce the jet diameter.

This is primarily due to the higher densities of the metals, and the Froude numbers recorded in Figure 5.15. In the Bernoulli – Electrostatic model (Equation 5.7), the last term is a function of the electric field divided by the density (i.e., the electric stress to inertial force ratio). Therefore, as the density of the metals is much higher, a larger electric field is required to have an impact on the

right hand-side of Equation 5.7. From a physical perspective, this means that the jet is operating with a much higher inertial force, and as such a stronger electric field is required to constrict the jet into a smaller diameter. The Froude and Weber numbers also play a part in dictating the jet diameter, as noted in Equation 5.7. An increase in the Froude number would lead to a decrease on the right hand-side of Equation 5.7, and thus less constriction of the jet diameter. Similarly, if the Weber number is increased (i.e., surface tension is decreased) then the jet will constrict to a much higher degree. This explains why Bismuth, which has the highest density, but lowest surface tension and Froude number, requires the lowest electric field for constriction. Aluminium on the other hand has the highest Froude number, and relatively high surface tension, but a lower density, and as such requires an intermediate electric field amongst the metals to reduce in jet diameter.

In Figure 5.16, a division is also present between the nonmetals. The electric field required to reduce the jet diameter is much lower for ethanol and gasoline as compared to the other nonmetals. This follows the same explanation as that presented above for the division between the metals and nonmetals. Ethanol and gasoline have a lower surface tension and density as compared to the other nonmetals, which promotes a greater reduction in jet diameter. However, the main factor for this division is due to the Froude number. From Figure 5.15, it can be seen that the Froude number is much lower for ethanol and gasoline, and so the inertial forces resisting the jet reduction are lower for these two liquids.

5.4.1.2 Using the Bernoulli – Electrostatic Model for the Jet Diameter

In Section 5.4.1.2 the Bernoulli – Electrostatic model was used to determine the electric field required to reduce the jet diameter for a range of different orifice sizes. The Bernoulli – Electrostatic model can also be used to calculate the effect of the electric field in reducing the jet diameter at a fixed orifice. In doing so the applied electric field is fixed at a given value, and the jet diameter at breakup is taken as the dependent variable and solved for using Equation 5.7.

To better illustrate this, the electric field can be calculated as function of the applied voltage. As mentioned earlier in this study, the applied electric field is a function of the applied voltage and electrode geometry. Therefore, for illustration purposes the ring electrode shown in Figure 4.5 is replaced with two parallel plates as shown in Figure 5.17.

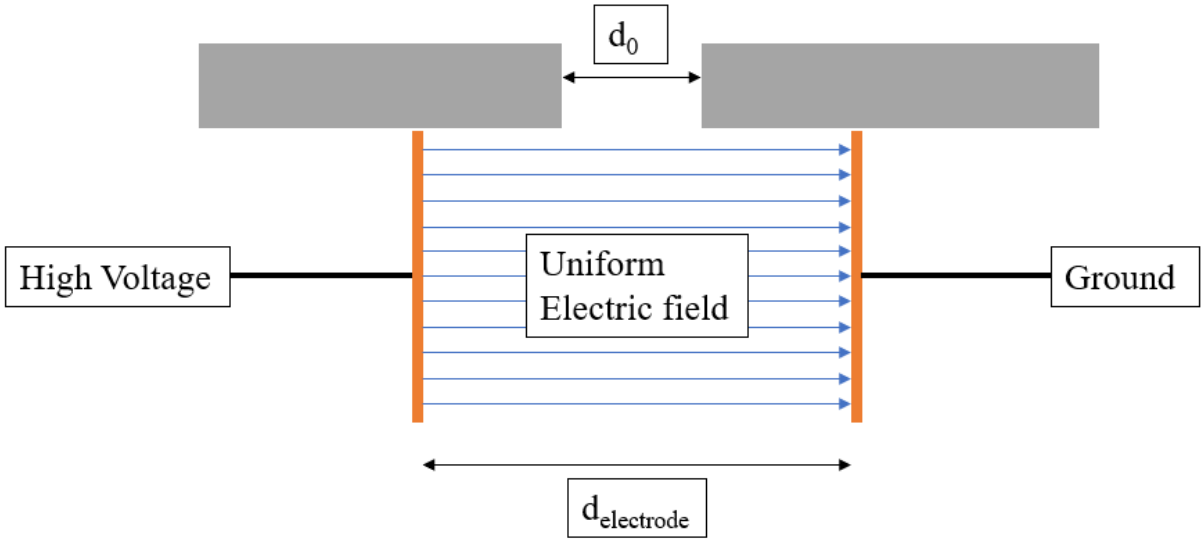

Figure 5.17. The use of parallel plate electrodes to create a region of uniform electric field strength

Two parallel plates as shown in Figure 5.17 are used to make the process of calculating the electric much simpler. Each of the two plates is taken as an electrode. One of them is charged with a high voltage, and the other is kept as a ground. Thus, a uniform electric field (E) is created between the plates. The field strength is calculated as a function of the applied voltage (V) and the distance between the plates ($d_{electrode}$). For the purpose of illustration, the distance between the plates can be fixed at 1 mm. Thus, using Faraday's law, the electric field created between the two plates can be calculated using Equation 5.8 **[134]**.

$$E = \frac{V}{d_{electrode}} \tag{5.8}$$

To determine the effect of the applied voltage on the jet diameter, the Bernoulli – Electrostatic model is applied. The orifice diameter in this case is taken as a fixed value of 0.1 mm, and the five metals listed in Table 5.6 are used as the working liquids. The applied voltage was varied from 0 – 100 kV, and the jet diameter was calculated. The results are presented in Table 5.7.

Table 5.7. The effect of applied voltages in reducing the jet diameter to orifice diameter ratio for 5 different metals

Material	Jet diameter/Orifice diameter, d_j/d_0, at different applied voltages					
	0 kV	20 kV	40kV	60 kV	80 kV	100 kV
Tin	1	0.99	0.96	0.93	0.89	0.84
Zinc	1	0.99	0.98	0.95	0.92	0.89
Aluminium	1	0.99	0.98	0.95	0.92	0.89
Copper	1	1	0.98	0.97	0.94	0.92
Bismuth	1	0.99	0.95	0.91	0.86	0.81

The jet diameter presented in Table 5.7 does not reduce in size when no voltage (0 kV) is applied, as no electric field is created between the plates. As the voltage is increased to 40 kV the jet is observed to reduce slightly in size due to the increased electric stresses. If the voltage is increased even further to 100 kV, the jet will reduce significantly in size, due to the very high electric stresses, with the copper jet reducing by 8%, and the bismuth jet reducing by 19%. From the modified Rayleigh correlation presented in Section 5.2.2.3, the droplet sizes will reduce linearly with the jet diameter. Hence the droplets of copper and bismuth produced at 100 kV will be 8% and 19% smaller respectively, than those produced without any applied voltage.

It should be noted however, that with the application of a 100 kV, an electric field of 100 MV/m is created. This is a very strong electric field and reaching this value requires special conditions in order to avoid any electrical discharges.

5.4.2 Electrical Breakdown in Gaseous Atmospheres

For a stable electric field to exist between two electrodes (e.g., between the two parallel plates shown in Figure 5.17), the gaseous atmosphere between these electrodes must behave as a dielectric medium (i.e., must prevent electrical conduction) **[134]**. If the electrical field strength is exceeded beyond the dielectric strength of the gas, then electrical breakdown will take place between the two electrodes, as the gas has stopped behaving as a dielectric, and is in fact accommodating the transfer of current from a region of high voltage to a region of low voltage.

Electrical breakdown takes place by the process of ionization due to very high voltages. Ionization is the process whereby the electric field provides enough energy to dislodge an electron from an atom of the gas. The electron is then accelerated by the electric field and moves a certain distance called the "mean free path"[10]. If in this distance the electron collides with another gas atom, it provides enough energy to dislodge another electron, which in turn is again accelerated by the electric field. If the field strength is strong enough there is a rapid multiplication of electrons which permits electrical conduction, and thus electrical breakdown of the dielectric material **[134]**. This is accompanied by a glow (such as a corona or brush discharge) at sufficiently high voltages, and a persistent electrical arc between electrodes at even higher voltages **[135]**.

The maximum voltage for electrical breakdown (V_{br}) is dependent on the gas pressure, electrode geometries, electrode spacing (i.e., inter-electrode distance), and the type of gas used. The parallel plate electrode configuration shown in Figure 5.17 presents the lowest probability of electrical breakdown, as the field created is very uniform with no regions of charge concentration **[136]**. The type of gas used also dictates the electrical breakdown voltage, as different gases have different dielectric strengths, as shown in Table 5.8 **[137]**.

*Table 5.8. The dielectric strength of different gases **[137]***

Material	Dielectric Strength (MV/m)
Air	3
Nitrogen	3.1
Helium	0.47
Argon	0.56
Carbon-dioxide	2.73
Sulphur hexafluoride	7.75

From Table 5.8 it can be seen that different gases will be able to sustain different strengths of the electric field before breaking down. It can also be noted that the maximum fields for all gases are much lower than the 100 MV/m required to decrease the jet diameter, as presented in Table 5.7.

[10] The "mean free path" is the average distance a particle such as an electron/photon travels before colliding with another particle.

However, much higher field strengths can be achieved for the gases listed in Table 5.8. This is done by changing the pressure of the gas. According to the electrical breakdown law of Friedrich Paschen, the maximum voltage that leads to electrical breakdown is a function of the product of the gas pressure and the electrode spacing for different gases (i.e., $V_{br} \propto P_{gas}d_{electrode}$) **[138]**.

a) If the pressure of the gas is increased, the mean free path of the electrons decreases, and thus the number of collisions with other atoms increases. However, the electrons do not get enough time to be accelerated by the electric field before colliding into another atom, and so the collisions that take place are of much lower energy. Thus, more electrons cannot be released and so the electrical breakdown does not take place. The breakdown voltage (Vbr), therefore increases with the increase in the gas pressure, allowing stronger electric fields.
b) If the pressure of the gas is decreased to a vacuum, then the number of gas atoms decreases. The mean free path of the electrons increases. However, due to the lower number of atoms, the electrons lose their energy by the time they collide with other atoms. Thus, more electrons cannot be released, and so the electrical breakdown does not take place. The breakdown voltage (Vbr), therefore increases with the decrease in the gas pressure, allowing stronger electric fields.

For example, under an ultra-high vacuum of 10 μtorr gauge pressure, Mahoney et. al., achieved a voltage of 30 kV between electrodes spaced at 10 mm **[8]**. Rossener et. al., on the hand showed that a voltage of up to 300 kV can be achieved with an interelectrode spacing of 4.5 mm if the gas pressure is increased to 2.4 MPa **[138]**. Therefore, with the correct manipulation of the gas pressure between the electrodes a stronger electric field can be reached and sustained without any electrical breakdown.

5.4.3 Overview on Designing an Electrostatically Assisted Atomization Process Operating in the Rayleigh Regime

The work done in this study can now be put together and an electrostatically assisted atomization process focused on jet breakup in the Rayleigh regime can be designed. First a material must be selected. Copper is one of the metals commonly used in the additive manufacturing and so it will be considered as the working liquid in this design process. From Figure 5.16 it is also clear that

copper requires the strongest electric field to have an effect on the jet diameter, and therefore using copper in the design process gives a good indication of one of the limits of this design. The orifice diameter must be decided on next. In additive manufacturing, powder sizes range from 20 to 120 microns in size **[5]**. Therefore, orifice sizes ranging from 25 to 200 microns will be selected. Following this, the operation velocity and the overhead pressure required can be calculated using Equations 5.2 and 3.56, respectively. The jet breakup length can then be calculated using Equation 3.53. Following this, the Bernoulli – Electrostatic model can be used to determine the effect of an applied voltage in reducing the jet diameter. In this particular case the electrode geometry described in Figure 5.17 will be used with an electrode spacing of 1 mm ($d_{electrode}$ = 1mm). The applied voltage will be set to 100 kV, as that is the maximum achievable with the power supply available in the AMPL laboratory[11]. The electric field can then be calculated using Equation 5.8. Finally, the jet diameter can be calculated using the Bernoulli – Electrostatic equation (Equation 5.7), and the droplet diameter can be calculated using the modified Rayleigh equation as presented in Section 5.2.2.3. To ensure uniform droplet production the required vibration frequency can be calculated using the correlation presented in Equation 5.6. Table 5.9 below is a summary of the experimental parameters as well as the calculated droplet diameter along with the required vibration frequency for this design process.

Table 5.9. A summary of the different parameters in this design process

Material: Copper					
Applied voltage: 100 kV					
Orifice diameter (mm)	Jet Velocity (m/s)	Overhead Pressure (kPa)	Droplet diameter with 100 kV (μm)	Droplet diameter with 0 kV (μm)	Vibration frequency (Hz)
0.025	10.1	817	45	47	14830
0.05	7.0	391	91	95	7340
0.1	4.9	188	174	189	3800
0.2	3.4	89	325	378	2010

[11] It should be noted that a 100 kV powers supply is not technologically novel. Power supplies capable of providing much higher voltages of > 500 kV can easily be found, purchased, and installed. However, for this design process a 100 kV is selected as it gives a good reference of the effect of a "high voltage". Higher voltages also come with other drawbacks such as the need for a higher vacuum (more on this is discussed below).

From Table 5.9 it can be seen that applying a voltage of 100 kV does not have a very significant effect in reducing the size of the droplets produced, especially at the smaller orifice sizes of 0.025 and 0.05 mm. To have a more pronounced effect the voltage must be increased. But before that, two factors must be accounted for. First the atmospheric conditions for the electric field to be stable with the application of 100 kV must be discussed. Secondly, the tower size must be considered as well, as it needs to be large enough to ensure the droplets have enough time to solidify as they fall.

As mentioned in Section 5.4.2 the breakdown voltage in a gas can be increased by manipulating the pressure of the gas. Either a high vacuum, or a high-pressure atmosphere must be created. Considering the size of an atomization chamber is around 1450 liters (as presented in Section 4.7), creating a high-pressure environment for such a large volume can be both expensive and dangerous. Therefore, a high vacuum environment is a much more reasonable approach. Following the works of Rabinowitz, the breakdown voltage in air with an inter-electrode spacing of 1 mm can be increased to approximately 105 kV if the pressure is reduced to 10 µtorr **[139]**. Rabinowitz found that decreasing the pressure further to 1 ntorr had little effect in increasing the breakdown voltage. Therefore, an atmosphere of 10 µtorr would be required to operate at the desired 100 kV as noted in Table 5.9. This can be achieved through the use of kinetic gas transfer pumps, for example, a diffusion pump or a turbomolecular vacuum pump[12].

When designing the atomization unit, the solidification time and the distance for the droplet to change into a powder must be considered. In this design, the tower is operated under a high vacuum, and therefore, the droplet will lose energy and solidify via thermal radiation. A solidification model for this approach has been described by Mahoney et. al., and is shown in Equation 5.9 **[8]**.

$$t_s = \frac{\rho d_d H_f}{6\varepsilon\sigma(T_m)^4} \tag{5.9}$$

In Equation 5.9, the solidification time (t_s) is related directly to the material density (ρ), the droplet diameter (d_d), and the heat of fusion (H_f). The solidification time is inversely related to the material

[12] Pressures of 7.5 mtorr – 0.75 µtorr are defined as a high vacuum, and are commonly used in industrial processes. These vacuum levels can be easily attained through the use of a diffusion pump or a turbomolecular vacuum pump.

emissivity (ε), the Stephan – Boltzmann constant (σ), and the material melting temperature raised to the fourth power (T_m^4). The values of these parameters specific to copper are as follows:

- Density (ρ) = 8953 kg/m^3 **[132]**
- Heat of fusion (H_f) = 204 J/g **[140]**
- Emissivity (ε) = 0.3 **[141]**
- Melting temperature (T_m) = 1085 °C **[132]**

From this the solidification time can be calculated using Equation 5.9. The solidification distance can then be calculated by multiplying the droplet velocity by the solidification time. The results of the solidification distances for the different droplet diameters are shown in Table 5.10.

*Table 5.10. Solidification times and distances for copper droplets of different sizes in a vacuum, following the solidification equation presented by Mahoney et. al. **[8]**.*

Material: Copper		
Applied voltage: 100 kV		
Droplet diameter (μm)	Solidification time (s)	Solidification distance (m)
45	0.24	2.4
91	0.48	3.38
174	0.91	4.47
325	1.71	5.8

From Table 5.10 it can be noted that the solidification distances range from approximately 2 – 6 meters for three different droplet sizes. As the droplet size reduces, the solidification distance and the solidification time is decreasing following Equation 5.9. Therefore, with that in mind, the atomization tower must be large enough to accommodate complete solidification of the desired droplet sizes produced.

Having presented a simple design for the "electrostatically assisted atomization process in the Rayleigh regime", its advantages and drawbacks must be discussed in order to understand the feasibility of such a process. This process does present several benefits over the conventional

atomization processes discussed in Chapter 1 (i.e., gas, water, plasma, and rotary electrode atomization). The advantages include:

1. This approach will be much cheaper to operate than gas and plasma atomization as a consistent supply of expensive inert gas is not required.
2. Monodispersed droplets with very few satellites are created as opposed to water, gas and rotary electrode atomization techniques.
3. The powder produced will not have any porosities since no secondary fluid is required, as compared to water and gas atomization.

The drawbacks of this approach include:

1. The size of the powders created are much larger than those required in additive manufacturing, unless orifices of very small diameters are used. However, using a smaller orifice e.g., a 0.025 mm orifice will demand a high overhead pressure of 817 kPa (as presented in Table 5.9). Therefore, the crucible system must be constructed appropriately to effectively handle such pressures.
2. Applying a high voltage requires the atmosphere in the atomization unit to be altered to a high vacuum. This can be achieved using kinetic gas transfer pumps such as a diffusion pump or a turbomolecular vacuum pump. However, these pumps can be expensive and therefore a large capital investment is required in setting up the system.
3. Since the atmosphere in the unit is a vacuum, the solidification distance is very large as solidification takes place via thermal radiation. Therefore, the atomization unit must also be big enough, which can be quite expensive to construct.

After assessing the "electrostatically assisted atomization process", it can be noted that it does have an effect in reducing the droplet diameter by 4.3% and 14% for orifice sizes of 0.025 and 0.2 mm, respectively. However, this reduction in size is not significant enough, especially at smaller orifice sizes. Furthermore, with the drawbacks mentioned above, this process does not show much promise in producing metal powders for AM. However, in designing and studying this process, a better method to produce monodispersed droplets would be to operate with smaller orifice sizes (e.g., 0.025 – 0.05 mm), and apply the optimal vibration frequencies using the correlation presented in Equation 5.6. With this, droplets of uniform size with low porosities can be created.

Furthermore, it would not require a constant supply of inert gas (i.e., low operation cost), and neither will it require expensive pumps or a large atomization unit (i.e., low capital costs).

5.5 Summary

This chapter focused on developing an understanding on the jet characteristics due to an applied vibration, and an applied electric field. The experiments conducted through the course of this study were analyzed, and the correlations between different parameters were discussed. In this chapter, the jet formation was first assessed in order to ensure the operation was in the laminar Rayleigh regime. This was done through the qualitative Ohnesorge plot, and the quantitative approach outlined by Trettel. From these analyses it was found that the jet was operating in the desired regime, and furthermore a correlation for the operation was developed in the form of a 'Re – Oh data fit' (Equation 5.1).

Following this, the effect of the applied vibration was analyzed. It was found that the droplet size distribution reduced with the application of a vibration of "optimal frequency". The droplet sizes measured were then compared to the predicted values using Rayleigh and Weber equations. Neither of these equations gave satisfactory predictions, each averaging an error of 30% or higher. Therefore, a modified Rayleigh correlation that takes into account both the jet breakup length and the jet diameter, was used. This correlation was found to be much more accurate, with an average error of 8.5 %, when compared to the measured values. Following this, the applied vibration was quantified using the Buckingham Pi method and a least squares linear regression. The dimensionless frequency was related to the Froude number. This relation showed to have an acceptable average error of 9.8% and a median error of 8.8%.

The effect of the applied voltage on droplet sizes was also analyzed in this chapter. Three different voltages were applied during every experiment (i.e., a low, medium, and high voltage). It was found that applying an increasing voltage led to a decrease in the measured droplet sizes, albeit this effect was not very pronounced. Therefore, to better understand the effects of the electric field on a liquid jet, a Bernoulli – Electrostatic model was presented and analyzed. Two simple theoretical tests were carried out with different liquids using this model. First the electric field

required to constrict the jet of each material at different orifices was calculated. It was found that as the orifice size decreased, the electric field required increased exponentially. In the second test the orifice size was fixed at 0.1 mm, and the jet diameter was calculated at different applied voltages. It was found that increasing the voltage substantially, led to a larger reduction in the liquid jet diameter.

A simple design was then presented on the “electrostatically assisted atomization process in the Rayleigh regime”. It was found that a high vacuum was necessary to sustain the required electric field. It was also seen that the atomization unit must be constructed to be large enough to allow the solidification of the droplets via thermal radiation. Following this, the benefits and drawbacks of the described atomization process were noted, and compared to the conventional atomization processes (gas, water, plasma, and rotary electrode atomization). It was concluded that the electrostatically assisted atomization process does not show much promise in producing powders of small sizes, as the electric field does not have a significant effect in reducing the size of the droplets produced. A better approach would be to instead operate using small orifices in the Rayleigh regime, and an apply a vibration in the melt to produce monodispersed droplets.

Chapter 6: Conclusion and Future Work

The objective of this thesis was to investigate an atomization technique, combining the principles of EHDA, and jet breakup in the Rayleigh regime. In order to do so, a system was designed, constructed, and tested by the AMPL group at the University of Alberta. Several experiments were conducted using water, ethylene glycol, and tin, with office sizes ranging from 0.07 – 2 mm in diameter. A vibration of specific frequency was applied to the bulk liquid, and an electric field was created at the orifice exit. The objective of the applied vibration was to ensure that the liquid jet disintegrated into monodisperse droplets. The purpose of the electric field was to induce electrical stresses on the liquid jet, and as such produce droplets of smaller sizes. The flow of the work conducted during this study was divided into four major sections. The first section was focused on ensuring that the experiments conducted were all in the desired Rayleigh regime. The second section was to determine and quantify the effect of the applied vibration. The third section was focused on understanding the effect of the applied voltage (i.e., the electric field generated around the jet). The fourth section was focused on applying and analyzing the Bernoulli – Electrostatic model.

6.1 Conclusion

The major findings and conclusions from this study are as follows:

- All experiments were conducted in the desired laminar Rayleigh regime. A Reynolds – Ohnesorge correlation was then generated using the experimental data. From this correlation the operation velocity can be determined using the liquid thermophysical properties, and the orifice diameter.
- Applying a vibration of optimal frequency facilitated the production of monodispersed droplets. The optimal frequency was chosen such that 80% of the droplets produced were within a 10% range of the average droplet size measured.
- The conventional Rayleigh and Weber theories were found to have very large errors (of 23.7% and 25.5% respectively) when predicting the droplet diameters. This was because neither of these theories accounted for the jet velocity. Therefore, a modified Rayleigh approach was used that accounted for the jet velocity through the use of the jet breakup

length, and the jet diameter at break up. The modified Rayleigh approach was significantly better at predicting the droplet diameters with an average error of 10.7%.

- A correlation for the optimal vibration frequency was developed in the form of a power law. The Buckingham Pi method was used to generate a dimensionless frequency (F), which was then related to the Froude number (Fr). This relation fitted well with the experimental data, showing a least R-squared value of 0.95, and a median and average error of 8.5% and 7.2% respectively.
- The effect of the applied electric field was determined by applying three different levels of voltages to the electrode at the orifice exit. The droplet diameters measured were seen to decrease in size with an increase in the voltage, albeit this effect was not very significant.
- The Bernoulli – Electrostatic model was tested to determine the effect of the electrical stresses on the jet diameter. This model shows that increasing the applied voltage (i.e., the electric field strength) leads to a reduction in the jet diameter, and the electric field strength required to constrict the jet diameter increases as the orifice diameter decreases.
- A simple design was outlined on the electrostatically assisted atomization process in the Rayleigh regime. It was found that applying a high voltage 100 kV required the atmosphere in the atomization unit to be altered to a vacuum of 10 μtorr in order to avoid electrical discharges. This would require a high capital cost in creating the atomization process, as a diffusion pump or a turbomolecular vacuum pump is required to achieve a high vacuum. However, the advantage of using this process would be the lower operation costs as no inert gas is required to break up the liquid stream, as compared to conventional atomization techniques.
- Furthermore, the electrostatically assisted atomization process does present several other advantages over conventional atomization techniques, such as, monodispersed powder production with low occurrence of satellites, and powders with low porosities as no secondary fluid is needed for atomization. However, it fails to have an effect in significantly reducing the droplet diameters, especially when using smaller orifice sizes. For example, with an orifice size of 0.025 mm a copper droplet will only reduce by 4.3% in diameter, even with the application of a high voltage of 100 kV. Therefore, this process cannot be recommended for powder production for AM.

6.2 Future Work

In the previous section it was concluded that the electrostatically assisted atomization process was not an efficient method to produce metal powders for AM. However, for the future work a better approach to producing monodispersed metal droplets would be to operate in the Rayleigh regime using smaller orifice sizes (e.g., 0.025 – 0.05 mm). The optimal vibration frequency can then be applied using the correlation presented in this study, to ensure monodispersed droplets are produced. This process could be carried out with different metals and the powders created can be analyzed and compared to those produced using conventional atomization techniques.

List of References

[1] Akhtar, S., Saad, M., Misbah, M. R., & Sati, M. C. (2018). Recent advancements in powder metallurgy: A review. *Materials Today: Proceedings*, *5*(9), 18649-18655.

[2] Ford, S., & Despeisse, M. (2016). Additive manufacturing and sustainability: an exploratory study of the advantages and challenges. *Journal of cleaner Production*, *137*, 1573-1587.

[3] Attaran, M. (2017). The rise of 3-D printing: The advantages of additive manufacturing over traditional manufacturing. *Business Horizons*, *60*(5), 677-688.

[4] Frazier, W. E. (2014). Metal additive manufacturing: a review. *Journal of Materials Engineering and performance*, *23*(6), 1917-1928.

[5] Moghimian, P., Poirié, T., Habibnejad-Korayem, M., Zavala, J. A., Kroeger, J., Marion, F., & Larouche, F. (2021). Metal Powders in Additive Manufacturing: A Review on Reusability and Recyclability of Common Titanium, Nickel and Aluminum Alloys. *Additive Manufacturing*, 102017.

[6] Henein, H., Uhlenwinkel, V., & Fritsching, U. (Eds.). (2017). *Metal sprays and spray deposition* (pp. 1-563). Berlin: Springer.

[7] Xie, J., Jiang, J., Davoodi, P., Srinivasan, M. P., & Wang, C. H. (2015). Electrohydrodynamic atomization: A two-decade effort to produce and process micro-/nanoparticulate materials. *Chemical engineering science*, *125*, 32-57.

[8] Mahoney, J. F., Perel, J., & Vickers, K. E. (1981). *U.S. Patent No. 4,264,641*. Washington, DC: U.S. Patent and Trademark Office.

[9] Bienvenu, G. (1984). *U.S. Patent No. 4,428,894*. Washington, DC: U.S. Patent and Trademark Office.

[10] Chun, Jung-Hoon, and Christian H. Passow. "Production of charged uniformly sized metal droplets." U.S. Patent 5,266,098, issued November 30, 1993.

[11] Kuroki, Y., Kawasaki, A., & Watanabe, R. (1991). Preparation of monosized metal powders by pulsated orifice injection. *Journal of the Japan Society of Powder and Powder Metallurgy*, *38*(6), 700-706.

[12] Eggers, J., & Villermaux, E. (2008). Physics of liquid jets. *Reports on progress in physics*, *71*(3), 036601.

[13] Eggers, J. (2006). A brief history of drop formation. In *Nonsmooth Mechanics and Analysis* (pp. 163-172). Springer, Boston, MA.

[14] Eggers, J. (1997). Nonlinear dynamics and breakup of free-surface flows. *Reviews of modern physics*, *69*(3), 865.

[15] Rayleigh, L. (1879). On the capillary phenomena of jets. *Proc. R. Soc. London*, *29*(196-199), 71-97.

[16] Rayleigh, L. (1878). On the instability of jets. *Proceedings of the London mathematical society*, *1*(1), 4-13.

[17] Rayleigh, L. (1892). XVI. On the instability of a cylinder of viscous liquid under capillary force. *The London, Edinburgh, and Dublin Philosophical Magazine and Journal of Science*, *34*(207), 145-154.

[18] Weber, C. (2019). Breakup of a liquid jet. *UT Faculty/Researcher Works*.

[19] Schweitzer, P. H. (1937). Mechanism of disintegration of liquid jets. *Journal of Applied Physics*, *8*(8), 513-521.

[20] Lefebvre, A. H., & McDonell, V. G. (2017). *Atomization and sprays*. CRC press.

[21] Tyler, E. (1933). XL. Instability of liquid jets. *The London, Edinburgh, and Dublin Philosophical Magazine and Journal of Science*, *16*(105), 504-518.

[22] Haenlein, A. (1932). Disintegration of a liquid jet.

[23] Miesse, C. C. (1955). Correlation of experimental data on the disintegration of liquid jets. *Industrial & Engineering Chemistry*, *47*(9), 1690-1701.

[24] Leroux, S., Dumouchel, C., & Ledoux, M. (1996). The stability curve of Newtonian liquid jets. *Atomization and sprays*, *6*(6).

[25] Fenn III, R. W., & Middleman, S. (1969). Newtonian jet stability: the role of air resistance. *AIChE Journal*, *15*(3), 379-383.

[26] Grant, R. P., & Middleman, S. (1966). Newtonian jet stability. *AIChE Journal*, *12*(4), 669-678.

[27] Sterling, A. M., & Sleicher, C. A. (1975). The instability of capillary jets. *Journal of Fluid Mechanics*, *68*(3), 477-495.

[28] Phinney, R. E. (1972). Stability of a laminar viscous jet–The influence of the initial disturbance level. *AIChE Journal*, *18*(2), 432-434.

[29] Phinney, R. E., & Humphries, W. (1970). *Stability of a viscous jet-Newtonian liquids*. NAVAL ORDNANCE LAB WHITE OAK MD.

[30] Giffen, E., & Muraszew, A. The atomization of liquid fuels 1953.

[31] Sallam, K. A., Dai, Z., & Faeth, G. M. (2002). Liquid breakup at the surface of turbulent round liquid jets in still gases. *International Journal of Multiphase Flow*, *28*(3), 427-449.

[32] Wu, P. K., Miranda, R. F., & Faeth, G. M. (1995). Effects of initial flow conditions on primary breakup of nonturbulent and turbulent round liquid jets. *Atomization and sprays*, *5*(2).

[33] A. Mansour and N. Chigier, (1994) Effect of turbulence on the stability of liquid jets and the resulting droplet size distribution, *Atomization and Sprays*, *4(5), 583-604*.

[34] Rupe, J. H. (1962). On the dynamic characteristics of free-liquid jets and a partial correlation with orifice geometry. Technical Report 32-207, Jet Propulsion Laboratory, Pasadena, CA.

[35] Malot, H., & Dumouchel, C. (2001). EXPERIMENTAL INVESTIGATION OF THE DROP SIZE DISTRIBUTION OF SPRAYS PRODUCED BY A LOWVELOCITY NEWTONIAN CYLINDRICAL LIQUID JET. *Atomization and Sprays*, *11*(3).

[36] McCarthy, M. J., & Molloy, N. A. (1974). Review of stability of liquid jets and the influence of nozzle design. *The Chemical Engineering Journal*, *7*(1), 1-20.

[37] Birouk, M., & Lekic, N. (2009). Liquid jet breakup in quiescent atmosphere: A review. *Atomization and Sprays*, *19*(6).

[38] Hiroyasu, H. (1991). Break-up length of a liquid jet and internal flow in a nozzle. In *Proc. 5th. ICLASS* (pp. 275-282).

[39] Arai, M., Shimizu, M., & Hiroyasu, H. (1985, July). Break-up length and spray angle of high speed jet. In *Proceedings of the 3rd International Conference on Liquid Atomization and Spray Systems* (Vol. 1, pp. 1-10).

[40] Van de Sande, E., & Smith, J. M. (1976). Jet break-up and air entrainment by low velocity turbulent water jets. *Chemical Engineering Science*, *31*(3), 219-224.

[41] Yeh, C. L. (2002). Numerical study of inlet and geometry effects on discharge coefficients for liquid jet emanating from a plain-orifice atomizer. *Journal of Mechanics*, *18*(3), 153-161.

[42] Marmottant, P., & Villermaux, E. (2004). On spray formation. *Journal of fluid mechanics*, *498*, 73-111.

[43] Reitz, R. D., & Bracco, F. V. (1982). Mechanism of atomization of a liquid jet. *The physics of Fluids*, *25*(10), 1730-1742.

[44] Ramamurthi, K., & Patnaik, R. (2002). Two-step start transients with long feedlines discharging liquid through sharp-edged cylindrical nozzles. *Atomization and Sprays*, *12*(1-3).

[45] Smith, S. W. J., & Moss, H. (1917). Experiments with mercury jets. *Proceedings of the Royal Society of London. Series A, Containing Papers of a Mathematical and Physical Character*, *93*(652), 373-393.

[46] Bravo, L., & Kweon, C. B. (2014). *A review on liquid spray models for diesel engine computational analysis*. ARMY RESEARCH LAB ABERDEEN PROVING GROUND MD.

[47] Tate, T. (1864). XXX. On the magnitude of a drop of liquid formed under different circumstances. *The London, Edinburgh, and Dublin Philosophical Magazine and Journal of Science*, *27*(181), 176-180.

[48] Tamada, S., & Shibaoka, Y. (1966). *Atomization—A Survey and Critique of the Literature*. Stanford Research Report. University of Stanford, 1966 (6): 1066.

[49] Lowke, J. J. (1997). Simple model for the transition current from globular to spray transfer in gas metal arc welding.

[50] Bracco, F. V. (1985). Modeling of engine sprays. *SAE transactions*, 144-167.

[51] He, L., & Ruiz, F. (1995). Effect of cavitation on flow and turbulence in plain orifices for high-speed atomization. *Atomization and sprays*, *5*(6).

[52] Ohnesorge, W. V. (2019). The formation of drops by nozzles and the breakup of liquid jets. *UT Faculty/Researcher Works*.

[53] Miesse, C. C. (1955). Correlation of experimental data on the disintegration of liquid jets. *Industrial & Engineering Chemistry*, *47*(9), 1690-1701.

[54] Reitz, R. D. (1978). *Atomization and other breakup regimes of a liquid jet*. Princeton University.

[55] Dumouchel, C. (2008). On the experimental investigation on primary atomization of liquid streams. *Experiments in fluids*, *45*(3), 371-422.

[56] Ranz, W. E. (William E. (1956). *On sprays and spraying; a survey of spray technology for research and development engineers*. University Park, Pa.

[57] Lin, S. P., & Reitz, R. D. (1998). Drop and spray formation from a liquid jet. *Annual review of fluid mechanics*, *30*(1), 85-105.

[58] Trettel, B. (2020). Reevaluating the jet breakup regime diagram. *Atomization and Sprays*, *30*(7).

[59] Sterling, A. M., & Abbott, W. T. (1981). Mechanisms of Water Jet Instability. In *Proceedings of the First U S. WATER JET CONFERENCE* (pp. 7-9).

[60] Asset, G. M., & Bales, P. D. (1951). *HYDRAULIC JETS AT LOW REYNOLDS NUMBER AND CONSTANT WEBER NUMBER.(Medical Laboratories Research Report No. 64)* (No. NP-3466). Chemical Corps.

[61] Clanet, C., & Lasheras, J. C. (1999). Transition from dripping to jetting. *Journal of fluid mechanics*, *383*, 307-326.

[62] Crane, L., Birch, S., & McCormack, P. D. (1964). The effect of mechanical vibration on the break-up of a cylindrical water jet in air. *British Journal of Applied Physics*, *15*(6), 743.

[63] Donnelly, R. J., & Glaberson, W. (1966). Experiments on the capillary instability of a liquid jet. *Proceedings of the Royal Society of London. Series A. Mathematical and Physical Sciences*, *290*(1423), 547-556.

[64] Goedde, E. F., & Yuen, M. C. (1970). Experiments on liquid jet instability. *Journal of Fluid Mechanics*, *40*(3), 495-511.

[65] Haas, P. A. (1992). Formation of uniform liquid drops by application of vibration to laminar jets. *Industrial & engineering chemistry research*, *31*(3), 959-967.

[66] Ruiz, F. (2002). Small Waves on the Jet" Intact Length:" Results Using a New Experimental Technique. *Atomization and Sprays*, *12*(5&6).

[67] Bojarevics, V., Taniguchi, S., & Pericleous, K. (2006). Droplet generation with modulated AC electromagnetic field at nozzle exit. In *Proc. 5th Int. Symp. on Electromagnetic Processing of Materials (EPM2006)* (pp. 23-27).

[68] Shimasaki, S. I., & Taniguchi, S. (2011). Formation of uniformly sized metal droplets from a capillary jet by electromagnetic force. *Applied Mathematical Modelling*, *35*(4), 1571-1580.

[69] Roy, S. (2009). Mono-Size Droplet Production by the Uniform-Droplet Spray Process-with Applications to ASTM F75 and Ailicon.

[70] Rayleigh, L. (1882). XX. On the equilibrium of liquid conducting masses charged with electricity. *The London, Edinburgh, and Dublin Philosophical Magazine and Journal of Science*, *14*(87), 184-186.

[71] Zeleny, J. (1914). The electrical discharge from liquid points, and a hydrostatic method of measuring the electric intensity at their surfaces. *Physical Review*, *3*(2), 69.

[72] Zeleny, J. (1915). On the condition of instability of electrified drops, with applications to electrical discharge from liquid points. In *Proc. Camb. Phil. Soc.* (Vol. 18, pp. 71-83).

[73] Wilson, C. T. R., & Taylor, G. I. (1925, July). The bursting of soap-bubbles in a uniform electric field. In *Mathematical proceedings of the Cambridge philosophical society* (Vol. 22, No. 5, pp. 728-730). Cambridge University Press.

[74] Nolan, J. J. (1924, January). The breaking of water-drops by electric fields. In *Proceedings of the Royal Irish Academy. Section A: Mathematical and Physical Sciences* (Vol. 37, pp. 28-39). Royal Irish Academy.

[75] Macky, W. A. (1930, July). The deformation of soap bubbles in electric fields. In *Mathematical Proceedings of the Cambridge Philosophical Society* (Vol. 26, No. 3, pp. 421-428). Cambridge University Press.

[76] Macky, W. A. (1931). Some investigations on the deformation and breaking of water drops in strong electric fields. *Proceedings of the Royal Society of London. Series A, Containing Papers of a Mathematical and Physical Character*, *133*(822), 565-587.

[77] Zeleny, J. (1935). The role of surface instability in electrical discharges from drops of alcohol and water in air at atmospheric pressure. *Journal of the Franklin Institute*, *219*(6), 659-675.

[78] English, W. N. (1948). Corona from a water drop. *Physical Review*, *74*(2), 179.

[79] Vonnegut, B., & Neubauer, R. L. (1952). Production of monodisperse liquid particles by electrical atomization. *Journal of colloid science*, *7*(6), 616-622.

[80] Neubauer, R. L., & Vonnegut, B. (1953). Supplement to "production of monodisperse liquid particles by electrical atomization". *Journal of Colloid Science*, *8*(5), 551-552.

[81] Drozin, V. G. (1955). The electrical dispersion of liquids as aerosols. *Journal of colloid science*, *10*(2), 158-164.

[82] Taylor, G. I. (1964). Disintegration of water drops in an electric field. *Proceedings of the Royal Society of London. Series A. Mathematical and Physical Sciences*, *280*(1382), 383-397.

[83] Hendricks Jr, C. D. (1962). Charged droplet experiments. *Journal of Colloid Science*, *17*(3), 249-259.

[84] Hogan, J. J., & Hendricks, C. D. (1965). Investigation of the charge-to-mass ratio of electrically sprayed liquid particles. *Aiaa Journal*, *3*(2), 296-301.

[85] Schweizer, J. W., & Hanson, D. N. (1971). Stability limit of charged drops. *Journal of Colloid and Interface Science*, *35*(3), 417-423.

[86] Krohn, V. E. (1973). Evidence that the minimum-energy state is not accessible to a system of droplets produced by electrohydrodynamic spraying. *Applied Physics Letters*, *23*(5), 220-221.

[87] Bollini, R., Sample, S. B., Seigal, S. D., & Boarman, J. W. (1975). Production of monodisperse charged metal particles by harmonic electrical spraying. *Journal of Colloid and Interface Science*, *51*(2), 272-277.

[88] Hayati, I., Bailey, A. I., & Tadros, T. F. (1986). Mechanism of stable jet formation in electrohydrodynamic atomization. *Nature*, *319*(6048), 41-43.

[89] Hayati, I., Bailey, A. I., & Tadros, T. F. (1987). Investigations into the mechanisms of electrohydrodynamic spraying of liquids: I. Effect of electric field and the environment on pendant drops and factors affecting the formation of stable jets and atomization. *Journal of Colloid and Interface Science*, *117*(1), 205-221.

[90] Hayati, I., Bailey, A. L., & Tadros, T. F. (1987). Investigations into the mechanism of electrohydrodynamic spraying of liquids: II. Mechanism of stable jet formation and electrical forces acting on a liquid cone. *Journal of colloid and interface science*, *117*(1), 222-230.

[91] Smith, D. P. (1986). The electrohydrodynamic atomization of liquids. *IEEE transactions on industry applications*, (3), 527-535.

[92] Cloupeau, M., & Prunet-Foch, B. (1989). Electrostatic spraying of liquids in cone-jet mode. *Journal of electrostatics*, *22*(2), 135-159.

[93] Cloupeau, M., & Prunet-Foch, B. (1990). Electrostatic spraying of liquids: Main functioning modes. *Journal of electrostatics*, *25*(2), 165-184.

[94] Cloupeau, M., & Prunet-Foch, B. (1994). Electrohydrodynamic spraying functioning modes: a critical review. *Journal of Aerosol Science*, *25*(6), 1021-1036.

[95] Cloupeau, M. (1994). Recipes for use of EHD spraying in cone-jet mode and notes on corona discharge effects. *Journal of Aerosol Science*, *25*(6), 1143-1157.

[96] Grigor'ev, A. I., & Shiryaeva, S. O. (1994). Capillary instabilities of charged drops and electrical dispersion of liquids. *Fluid dynamics*, *29*(3), 305-318.

[97] Shiryaeva, S. O., & Grigor'ev, A. I. (1995). The semiphenomenological classification of the modes of electrostatic dispersion of liquids. *Journal of ELECTROSTATICS*, *34*(1), 51-59.

[98] Jaworek, A., & Krupa, A. (1999). Classification of the modes of EHD spraying. *Journal of Aerosol Science*, *30*(7), 873-893.

[99] Jaworek, A., & Krupa, A. (1999). Jet and drops formation in electrohydrodynamic spraying of liquids. A systematic approach. *Experiments in fluids*, *27*(1), 43-52.

[100] Hartman, R. P. A., Brunner, D. J., Camelot, D. M. A., Marijnissen, J. C. M., & Scarlett, B. (2000). Jet break-up in electrohydrodynamic atomization in the cone-jet mode. *Journal of aerosol science*, *31*(1), 65-95.

[101] De La Mora, J. F. (1992). The effect of charge emission from electrified liquid cones. *Journal of Fluid Mechanics*, *243*, 561-574.

[102] De La Mora, J. F., & Loscertales, I. G. (1994). The current emitted by highly conducting Taylor cones. *Journal of Fluid Mechanics*, *260*, 155-184.

[103] Jaworek, A. (2007). Micro-and nanoparticle production by electrospraying. *Powder technology*, *176*(1), 18-35.

[104] Wilm, M. S., & Mann, M. (1994). Electrospray and Taylor-Cone theory, Dole's beam of macromolecules at last?. *International Journal of Mass Spectrometry and Ion Processes*, *136*(2-3), 167-180.

[105] Gómez-Estaca, J., Balaguer, M. P., Gavara, R., & Hernandez-Munoz, P. (2012). Formation of zein nanoparticles by electrohydrodynamic atomization: Effect of the main processing variables and suitability for encapsulating the food coloring and active ingredient curcumin. *Food Hydrocolloids*, *28*(1), 82-91.

[106] Gomez, A., Bingham, D., De Juan, L., & Tang, K. (1998). Production of protein nanoparticles by electrospray drying. *Journal of Aerosol Science*, *29*(5-6), 561-574.

[107] Gomez, A., & Tang, K. (1994). Charge and fission of droplets in electrostatic sprays. *Physics of Fluids*, *6*(1), 404-414.

[108] Li, S. W., Jayasinghe, S. N., & Edirisinghe, M. J. (2006). Aspirin particle formation by electric-field-assisted release of droplets. *Chemical engineering science*, *61*(10), 3091-3097.

[109] van Heugten, W. G. N. (2015). Shape and stability in liquid threads and jets: a link to droplet formation.

[110] Young, H. D., Freedman, R. A., & Ford, A. L. (2013). University Physics with Modern Physics Technology Update. Pearson Education.

[111] Landau, L. D., Bell, J. S., Kearsley, M. J., Pitaevskii, L. P., Lifshitz, E. M., & Sykes, J. B. (2013). Electrodynamics of continuous media (Vol. 8). elsevier.

[112] Melcher, J. R., & Warren, E. P. (1971). Electrohydrodynamics of a current-carrying semi-insulating jet. *Journal of Fluid Mechanics*, *47*(1), 127-143.

[113] Carretero Benignos, J. A. (2005). *Numerical Simulation of a single emitter colloid thruster in pure droplet cone-jet mode* (Doctoral dissertation, Massachusetts Institute of Technology).

[114] Munoz, C. N. (2015). *Computational Modelling of Electrohydrodynamic Atomization* (Doctoral dissertation, The University of Manchester (United Kingdom)).

[115] Castellanos, A. (Ed.). (1998). *Electrohydrodynamics* (Vol. 380). Springer Science & Business Media.

[116] Rapp, B. E. (2016). *Microfluidics: modeling, mechanics and mathematics*. William Andrew.

[117] Teng, H., Kinoshita, C. M., & Masutani, S. M. (1995). Prediction of droplet size from the breakup of cylindrical liquid jets. *International journal of multiphase flow*, *21*(1), 129-136.

[118] Meister, B. J., & Scheele, G. F. (1969). Prediction of jet length in immiscible liquid systems. *AIChE Journal*, *15*(5), 689-699.

[119] Roach, J. R. (2001). *Determination of the physical properties of melts* (Mater's thesis, University of Alberta (Canada)).

[120] Lichtarowicz, A., Duggins, R. K., & Markland, E. (1965). Discharge coefficients for incompressible non-cavitating flow through long orifices. *Journal of mechanical engineering science*, *7*(2), 210-219.

[121] Roach, S. J., & Henein, H. (2005). A new method to dynamically measure the surface tension, viscosity, and density of melts. *Metallurgical and Materials Transactions B*, *36*(5), 667-676.

[122] *Table 41. Physical Properties of Heavy water, D2O and Water, H2O.* (2021) Retrieved from https://app.knovel.com/hotlink/itble/rcid:kpHLDE0002/id:kt00XRBRC3/handbook-laboratory-distillation/table-41-physical-properties

[123] *Table 2.1. Physicochemical Properties of Solvents Commonly Used for Extraction at Atmospheric Pressure and 20°C.* (2021) Retrieved from https://app.knovel.com/hotlink/itble/rcid:kpLPE00001/id:kt01212QM2/liquid-phase-extraction/table-2-1-physicochemical

[124] *Table A5. Properties of Metals or Metal Melts.* (2021) Retrieved from https://app.knovel.com/hotlink/itble/rcid:kpHRMDPTE4/id:kt01213351/handbook-refractory-materials/table-a5-properties-metals

[125] Bozhko, I. V., Glazkov, N. I., Troitskii, S. R., & Fal'Kovskii, N. I. (1982). Breakdown voltages of inert gases at temperatures of 300–2000° K. *Journal of Applied Mechanics and Technical Physics*, *23*(1), 15-21.

[126] Naidu, M. S. (2013). *High voltage engineering*. Tata McGraw-Hill Education.

[127] Khalifa, M. (1990). High-voltage engineering.

[128] *Table 1. Primary Fuels.* (2021) Retrieved from https://app.knovel.com/hotlink/itble/rcid:kpJPC00001/id:kt011KIJI1/joint-propulsion-conference/table-1-primary-fuels

[129] *Table 1. Physical Properties of Water and the Propellants Studied.* (2021) Retrieved from https://app.knovel.com/hotlink/itble/rcid:kpAIAASA0A/id:kt011K7KNP/52nd-aiaa-sae-asee-joint/table-1-physical-properties

[130] *Table 4.3. Comparison of Some Bulk Physicochemical Properties of a Liquid Oil (Triolein) and Water at 20°C.* (2021) Retrieved from https://app.knovel.com/hotlink/itble/rcid:kpFFCE001G/id:kt00XRFTS4/fennemas-food-chemistry/table-4-3-comparison

[131] *Table 1. Summary of the Important Physical Properties of High-Purity (≥99.95% Al) Aluminum.* (2021) Retrieved from https://app.knovel.com/hotlink/itble/rcid:kpCAAA0001/id:kt00XRBWT5/corrosion-aluminum-aluminum/table-1-summary-important

[132] *Table 39. Physical Properties of Pure Copper.* (2021) Retrieved from https://app.knovel.com/hotlink/itble/rcid:kpMEHVMEM5/id:kt01211O73/mechanical-engineers/table-39-physical-properties

[133] *Table 3.11. Basic Thermophysical Properties of Mercury, Hg, Lead, Pb, Bismuth, Bi, Gallium, Ga, Indium, In.* (2021) Retrieved from https://app.knovel.com/hotlink/itble/rcid:kpTPMNEAT1/id:kt01214EN2/thermophysical-properties/table-3-11-basic-thermophysica

[134] Sadiku, M. N. (2001). *Elements of electromagnetics* (Vol. 428). New York: Oxford university press.

[135] Levitin, G., Reinhardt, K., & Hess, D. (2012). Plasma cleaning for electronic, photonic, biological, and archeological applications. *Ch*, *2*, 55.

[136] Denissov, D., Rebholz, H., Köhler, W., & Tenbohlen, S. (2005, August). Dielectric strength of different gases in GIS. In *14th Int. Symposium on High Voltage Engineering*.

[137] Berger, L. "Dielectric strength of insulating materials." *Carbon* 1, no. 2006 (2006): 2.

[138] Hopf, A., Rossner, M., Berger, F., & Prucker, U. (2015, June). Dielectric strength of alternative insulation gases at high pressure in the homogeneous electric field. In *2015 IEEE Electrical Insulation Conference (EIC)* (pp. 131-136). IEEE.

[139] Rabinowitz, M. (1965). Electrical breakdown in vacuum: New experimental and theoretical observations. *Vacuum*, *15*(2), 59-66.

[140] T*able 70. Enthalpy of Fusion - Miscellaneous Materials.* (2021).Retrieved from https://app.knovel.com/hotlink/itble/rcid:kpYCPDCECD/id:kt00BKANX1/yaws-critical-property/table-70-enthalpy-fusion

[141] Krishnan, S., & Nordine, P. C. (1993, November). Optical properties and emissivities of liquid metals and alloys. In *NASA. Lewis Research Center, Workshop on the Thermophysical Properties of Molten Materials*.

Appendix A

This section contains the shadowgraph images and the droplet size distribution plots for the experiments listed in Tables 5.2 and 5.8. Each Figure contains three shadowgraph images taken at 3 different times, labelled a), b) and c), and a shadowgraph plot labelled d) located below the shadowgraph images. Two figures are presented for each run. In the first figure the optimal frequency noted in Table 5.8 was applied. In the second figure no vibration frequency was applied. The purpose of these figures is to demonstrate the effect of the applied vibration frequency on droplet production.

A1 Experiments Using Water, with Orifice Sizes of 0.07 – 2 mm

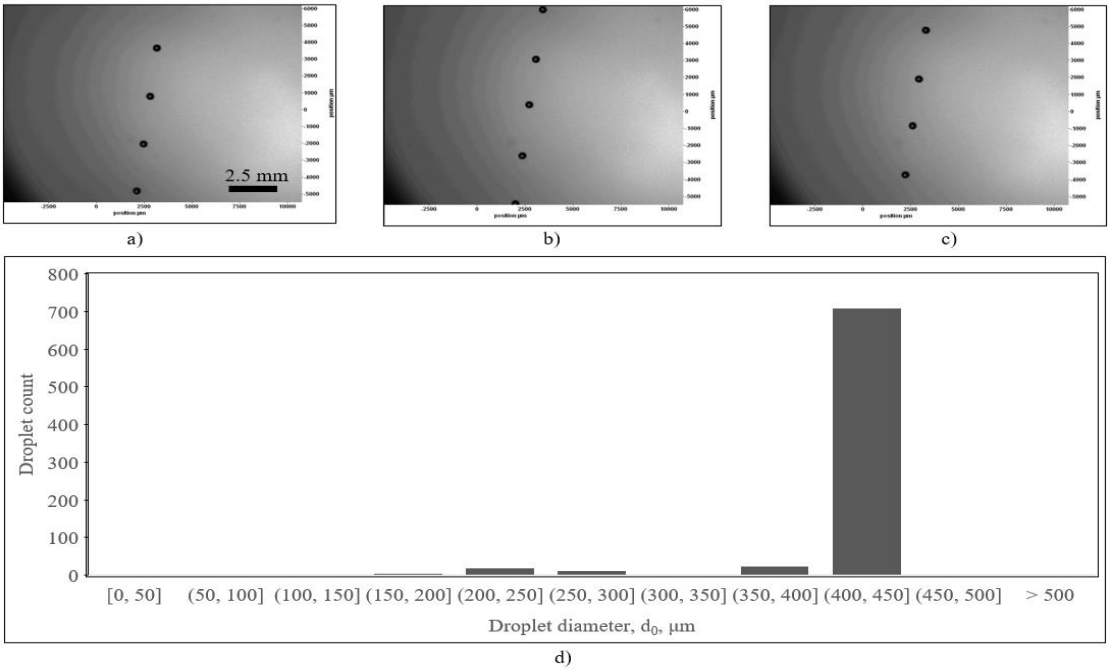

Figure A1. Images of water droplets from a 0.07 mm orifice with an applied frequency of 1100Hz, presented in a), b), and c). The histogram showing the droplet size distribution, presented in d).

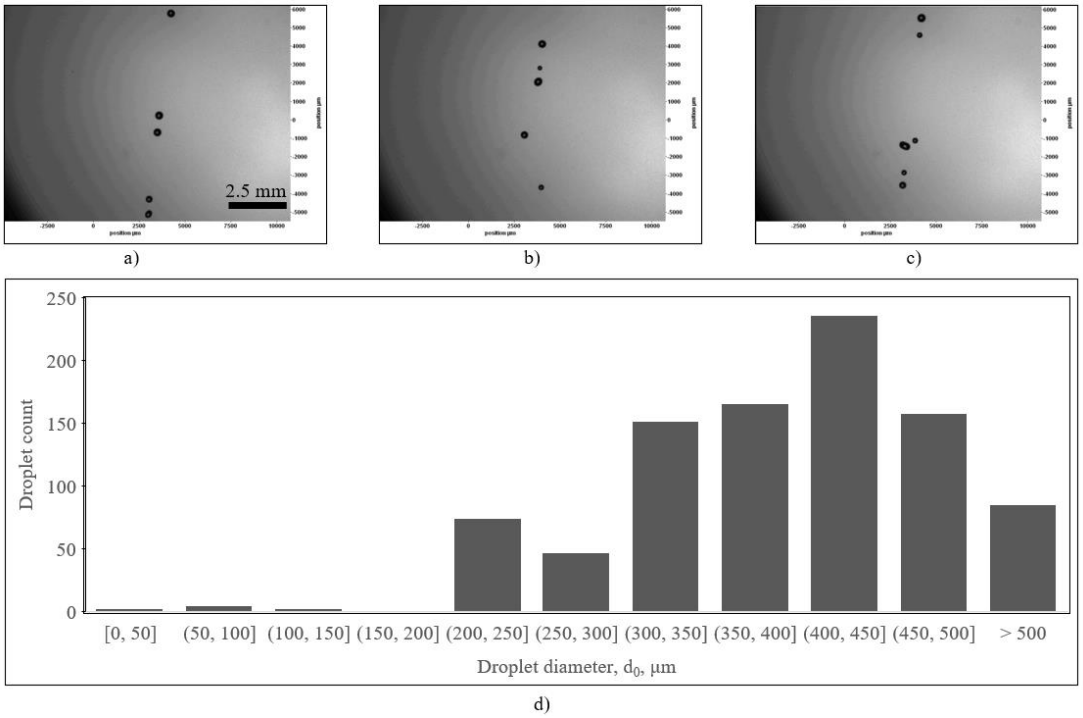

Figure A2. Images of water droplets from a 0.07 mm orifice without an applied frequency, presented in a), b), and c). The histogram showing the droplet size distribution, presented in d).

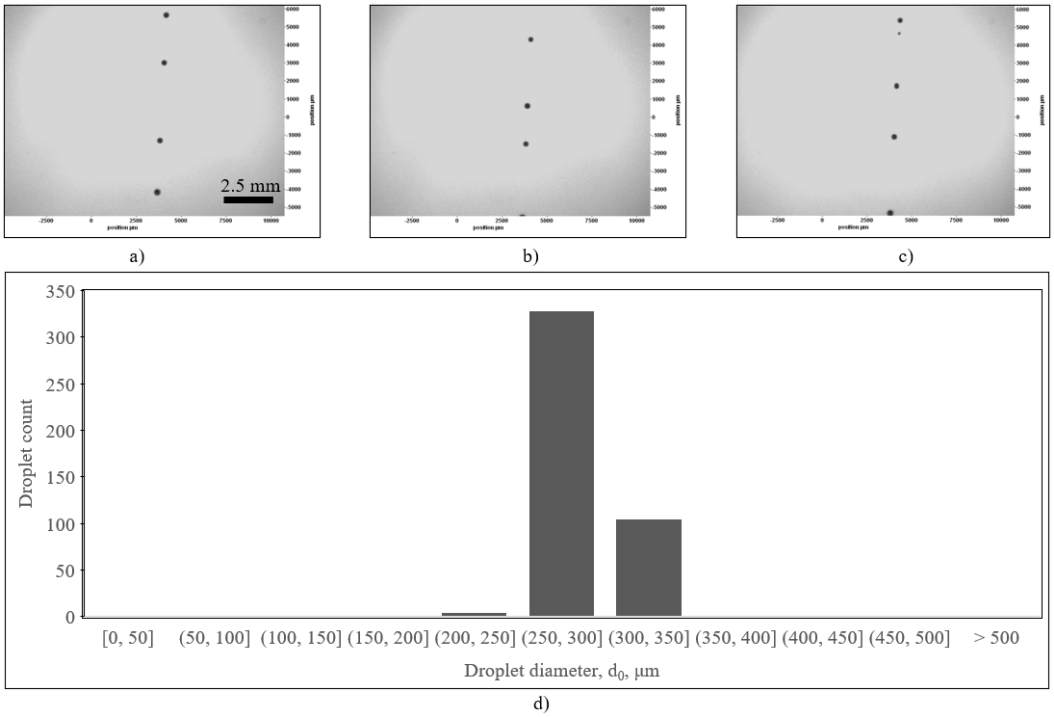

Figure A3. Images of water droplets from a 0.1 mm orifice with an applied frequency of 1500 Hz, presented in a), b), and c). The histogram showing the droplet size distribution, presented in d).

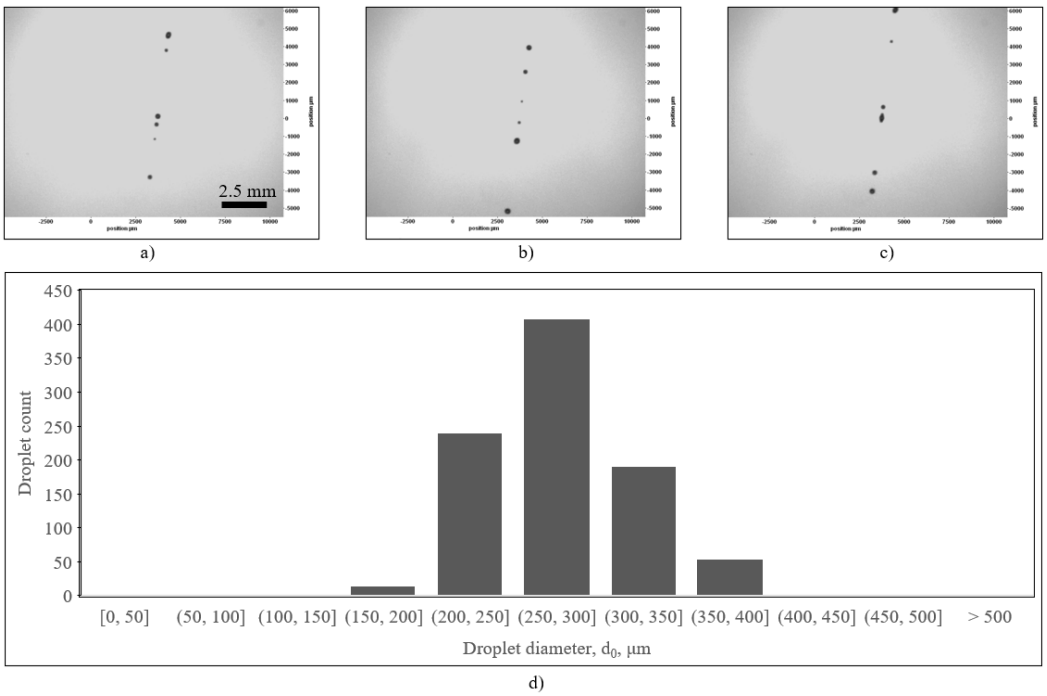

Figure A4. Images of water droplets from a 0.1 mm orifice without an applied frequency, presented in a), b), and c). The histogram showing the droplet size distribution, presented in d).

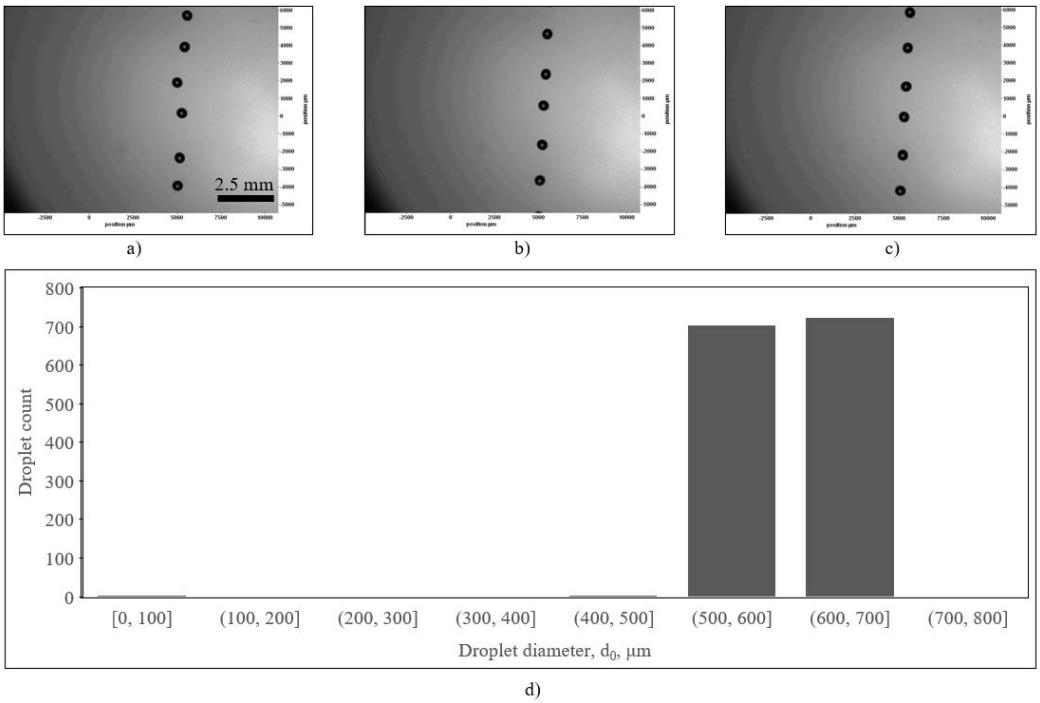

Figure A5. Figure 3. Images of water droplets from a 0.275 mm orifice with an applied frequency of 1000 Hz, presented in a), b), and c). The histogram showing the droplet size distribution, presented in d).

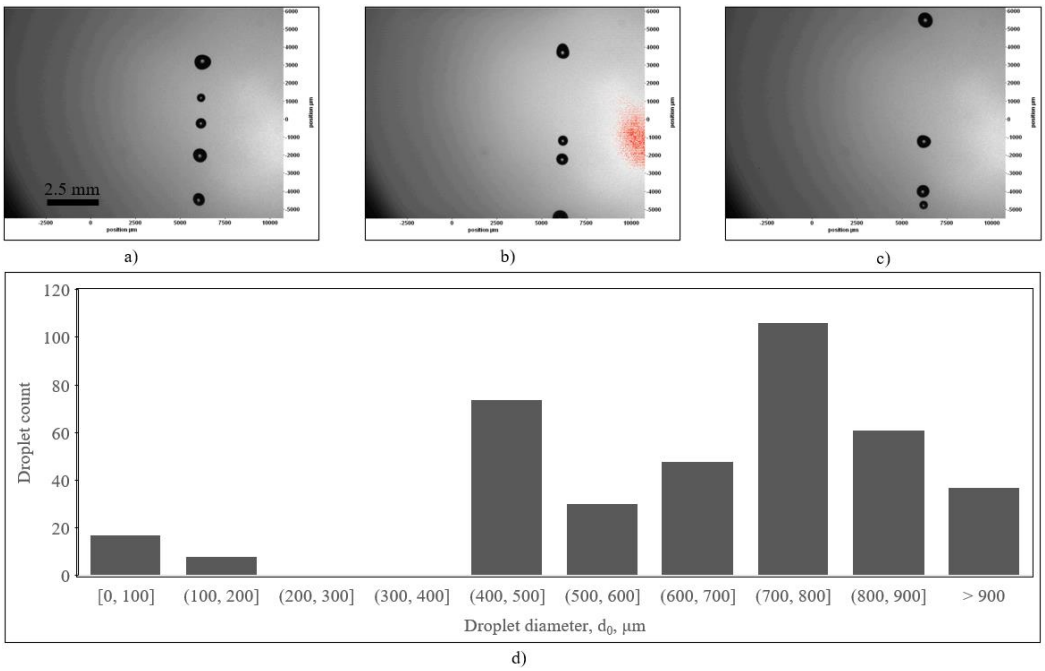

Figure A6. Images of water droplets from a 0.275 mm orifice without an applied frequency, presented in a), b), and c). The histogram showing the droplet size distribution, presented in d).

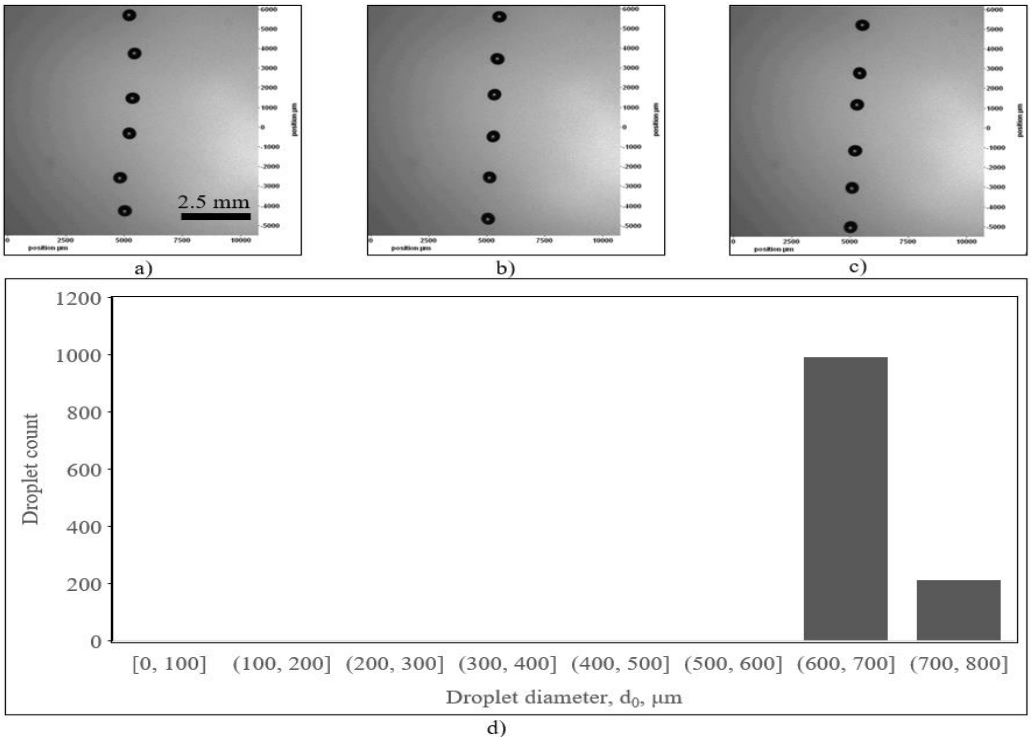

Figure A7. Images of water droplets from a 0.35 mm orifice with an applied frequency of 900 Hz, presented in a), b), and c). The histogram showing the droplet size distribution, presented in d).

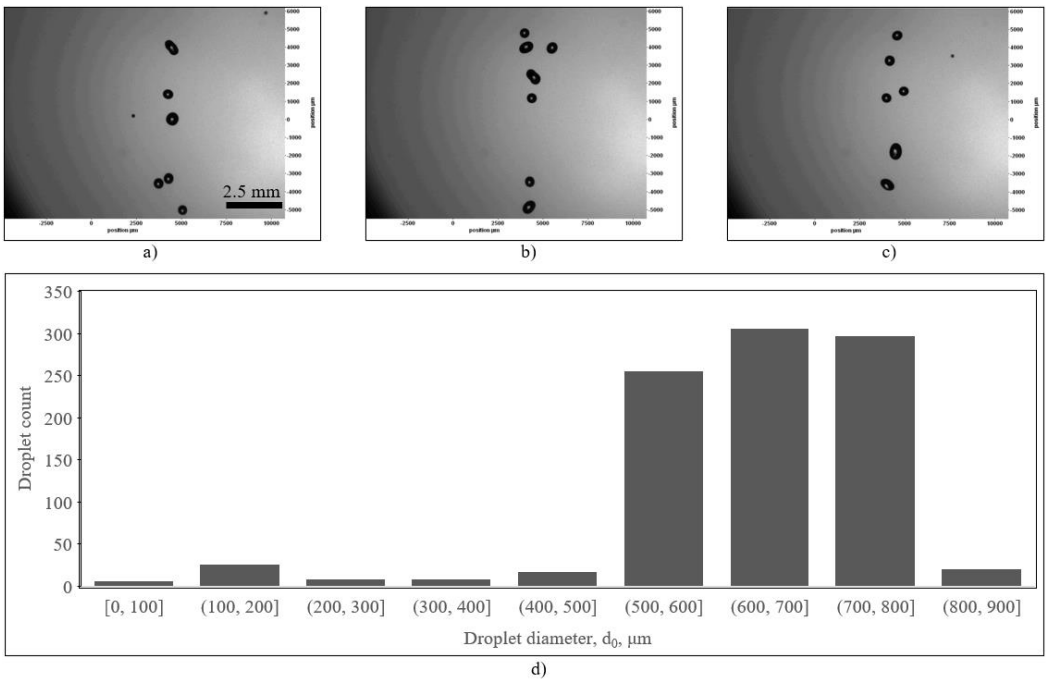

Figure A8. Images of water droplets from a 0.35 mm orifice without an applied frequency, presented in a), b), and c). The histogram showing the droplet size distribution, presented in d).

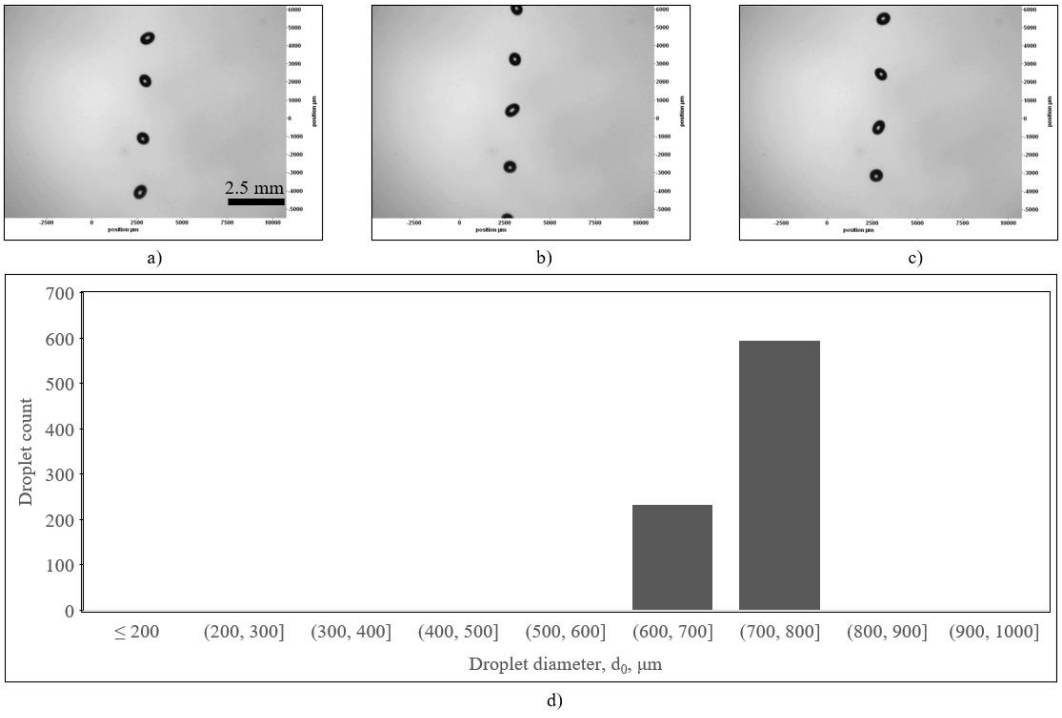

Figure A9. Images of water droplets from a 0.45 mm orifice with an applied frequency of 780 Hz, presented in a), b), and c). The histogram showing the droplet size distribution, presented in d).

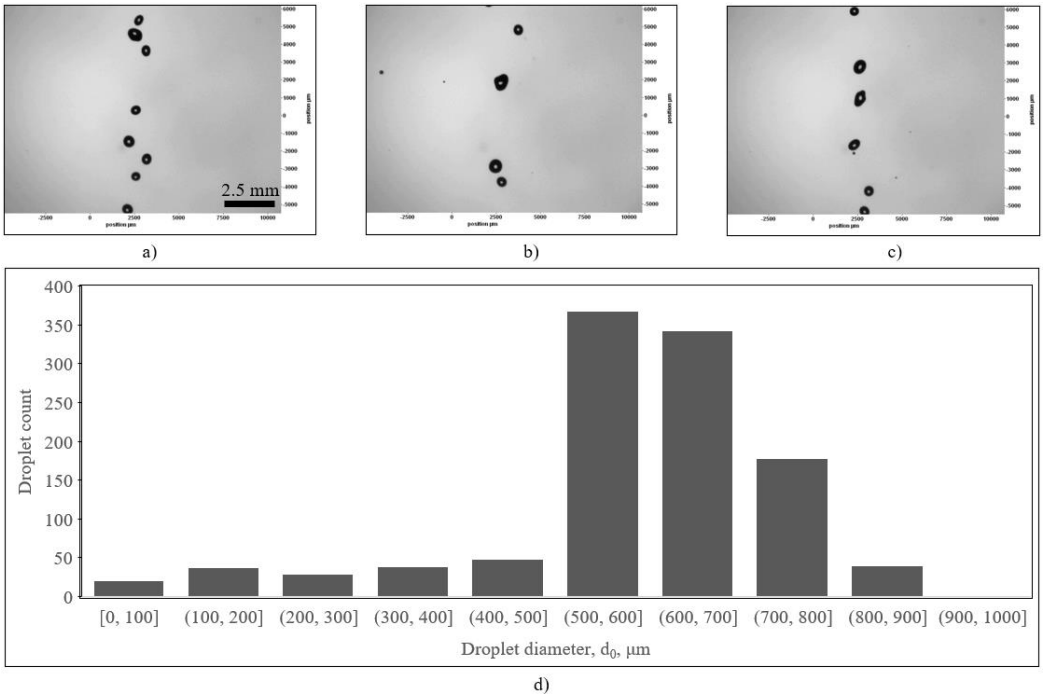

Figure A10. Images of water droplets from a 0.45 mm orifice without an applied frequency, presented in a), b), and c). The histogram showing the droplet size distribution, presented in d).

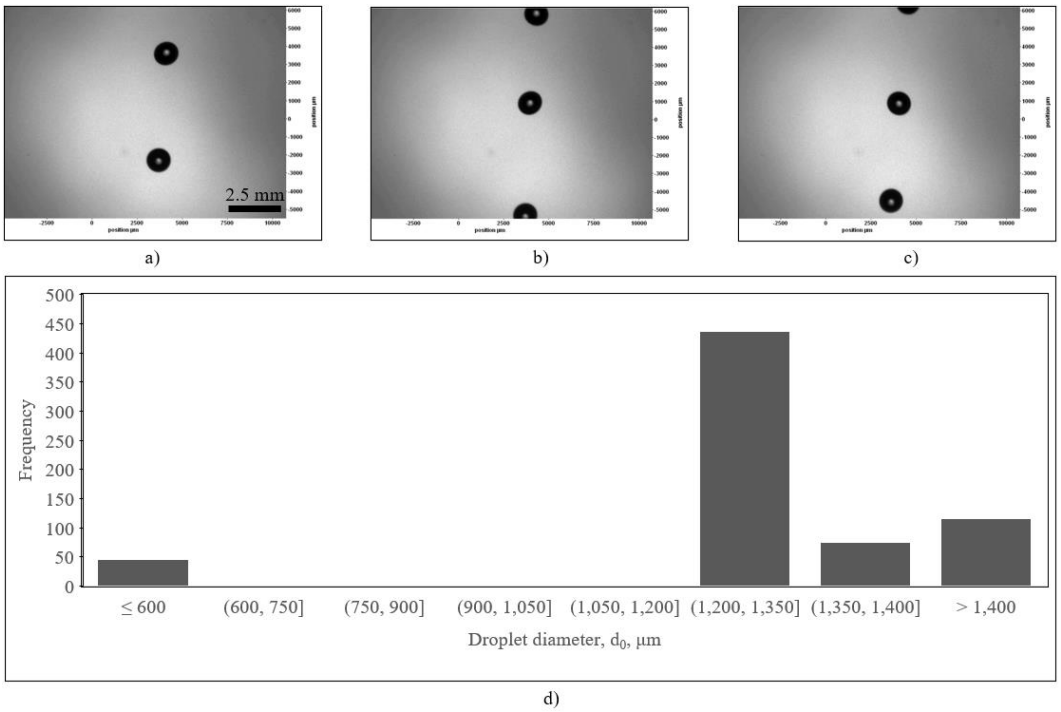

Figure A11. Images of water droplets from a 0.75 mm orifice with an applied frequency of 340 Hz, presented in a), b), and c). The histogram showing the droplet size distribution, presented in d).

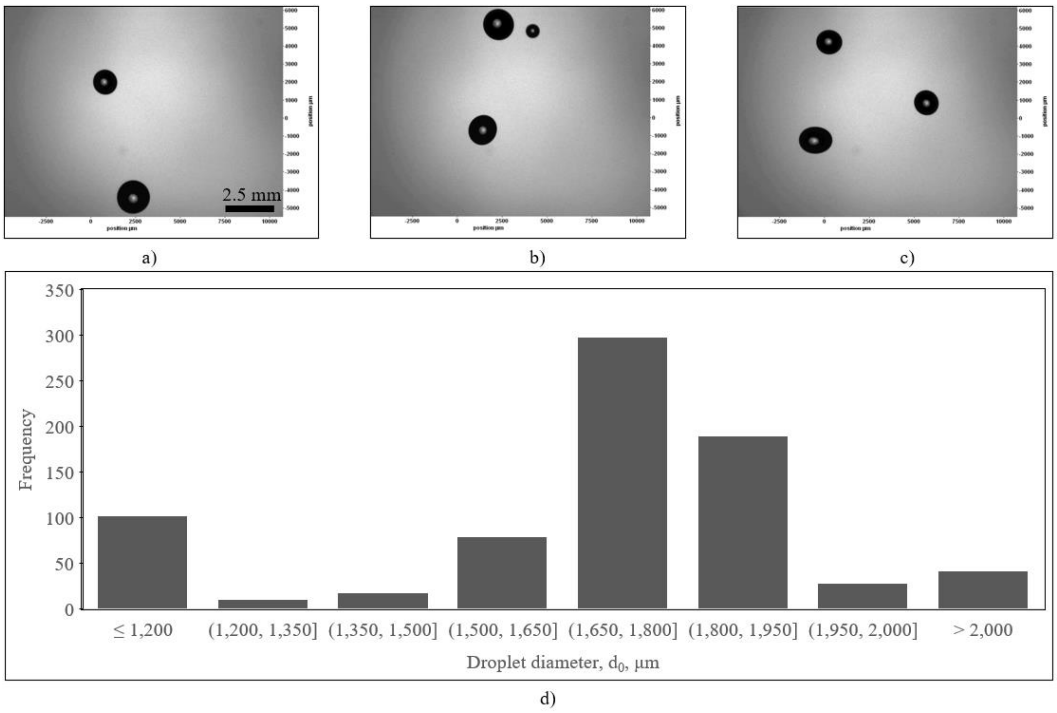

Figure A12. Images of water droplets from a 0.75 mm orifice without an applied frequency, presented in a), b), and c). The histogram showing the droplet size distribution, presented in d).

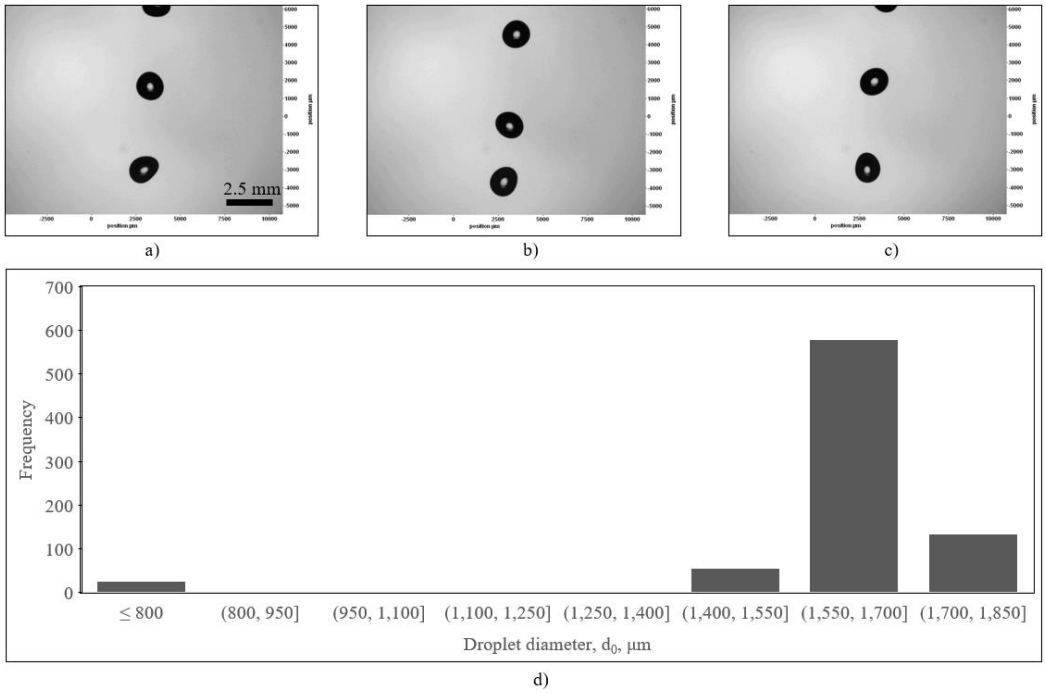

Figure A13. Images of water droplets from a 1 mm orifice with a head of 5.5 cm and an applied frequency of 250 Hz, presented in a), b), and c). The histogram showing the droplet size distribution, presented in d).

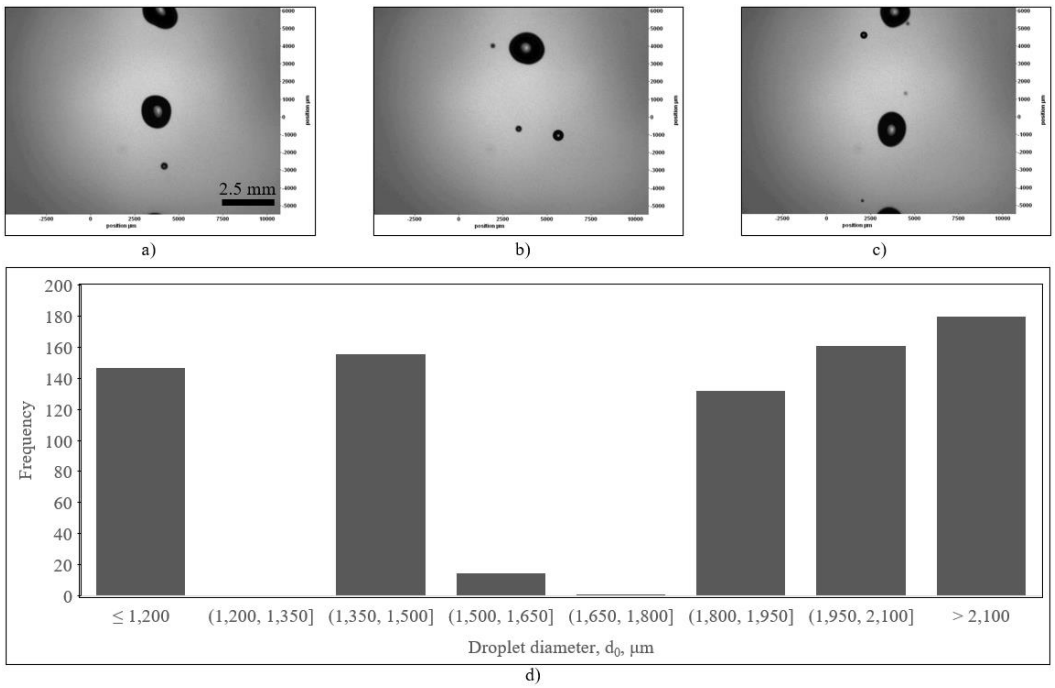

Figure A14. Images of water droplets from a 1 mm orifice with a head of 5.5 cm and without an applied frequency, presented in a), b), and c). The histogram showing the droplet size distribution, presented in d).

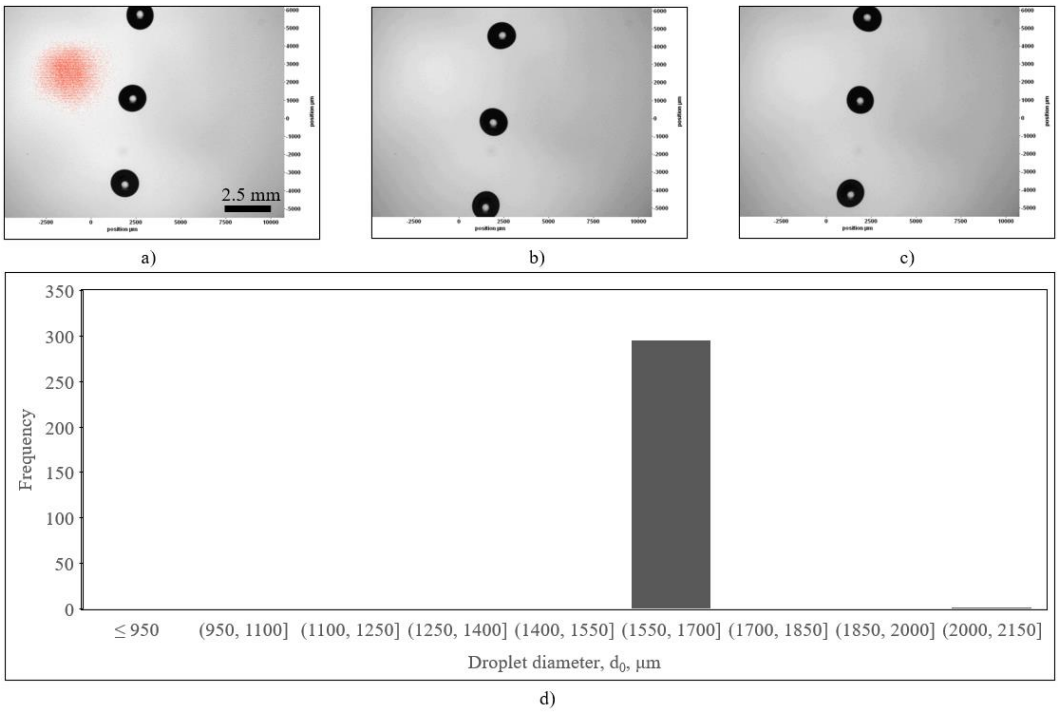

Figure A15. Images of water droplets from a 1 mm orifice with a head of 6.5 cm and an applied frequency of 250 Hz, presented in a), b), and c). The histogram showing the droplet size distribution, presented in d).

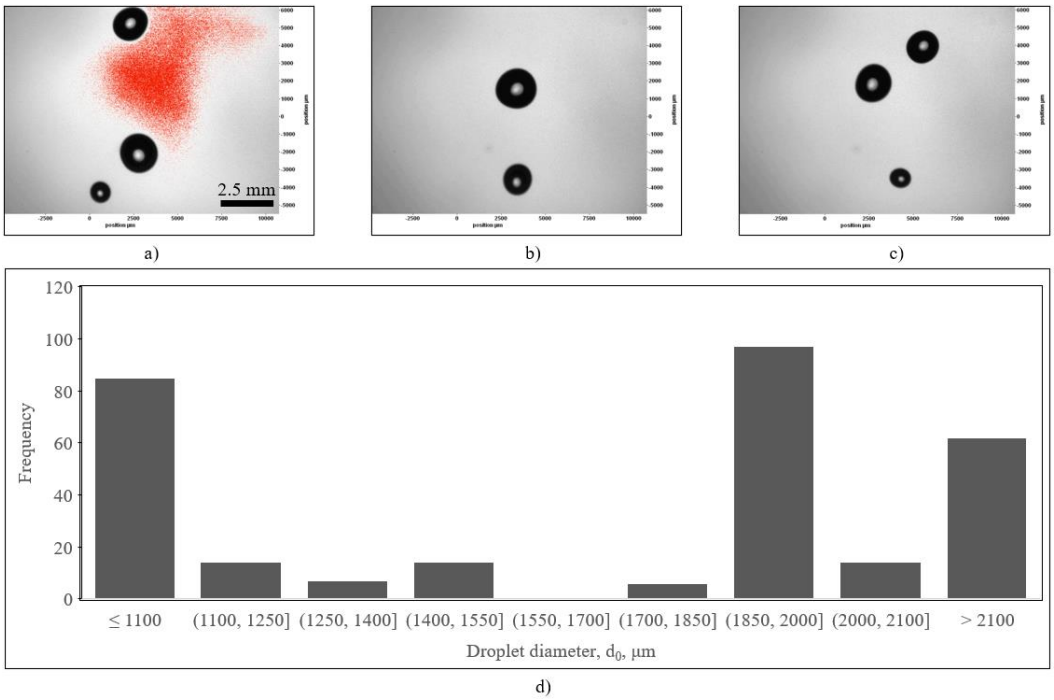

Figure A16. Images of water droplets from a 1 mm orifice with a head of 6.5 cm and without an applied frequency, presented in a), b), c). The histogram showing the droplet size distribution, presented in d).

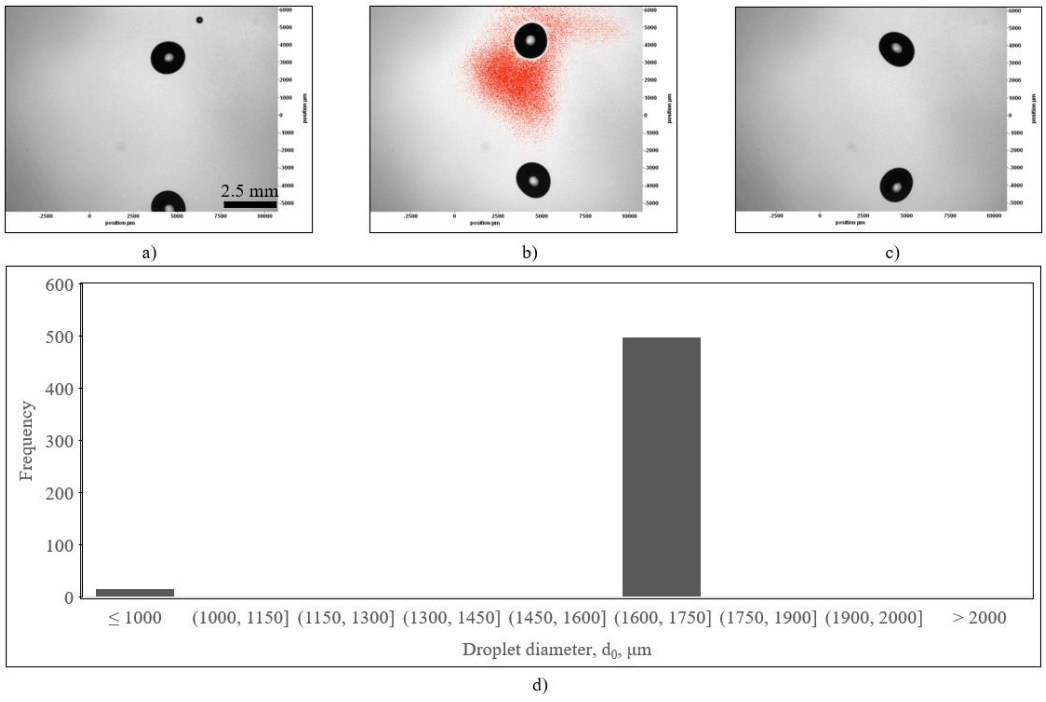

Figure A17. Images of water droplets from a 1 mm orifice with a head of 7.5 cm and an applied frequency of 250 Hz, presented in a), b), c). The histogram showing the droplet size distribution, presented in d).

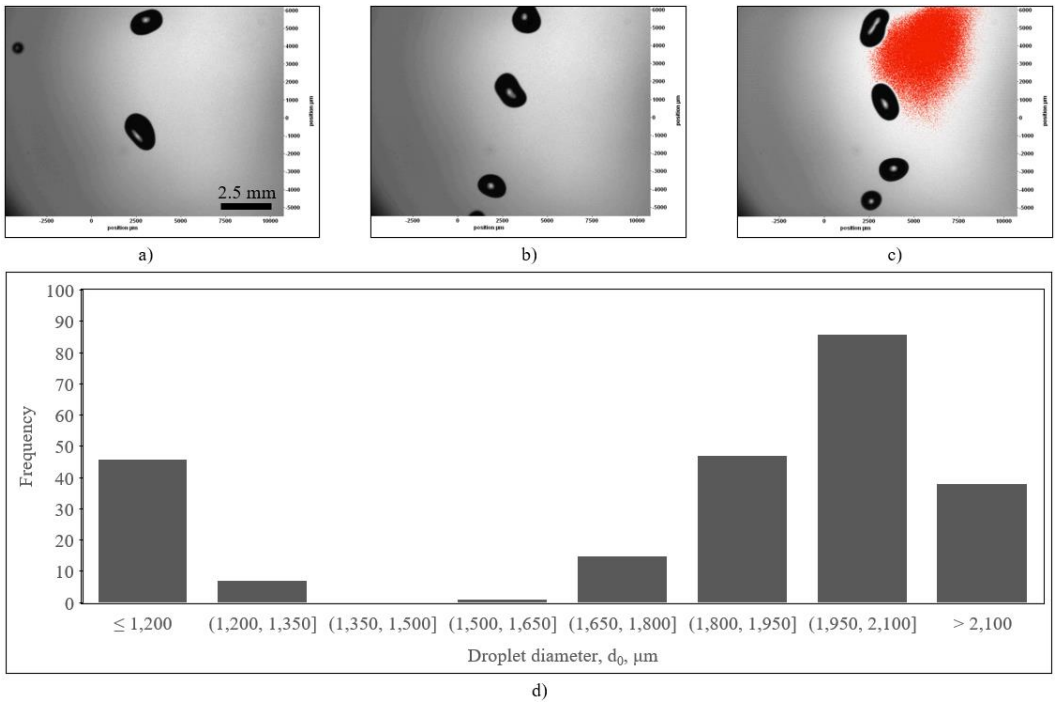

Figure A18. Images of water droplets from a 1 mm orifice with a head of 7.5 cm and without an applied frequency, presented in a), b), c). The histogram showing the droplet size distribution, presented in d).

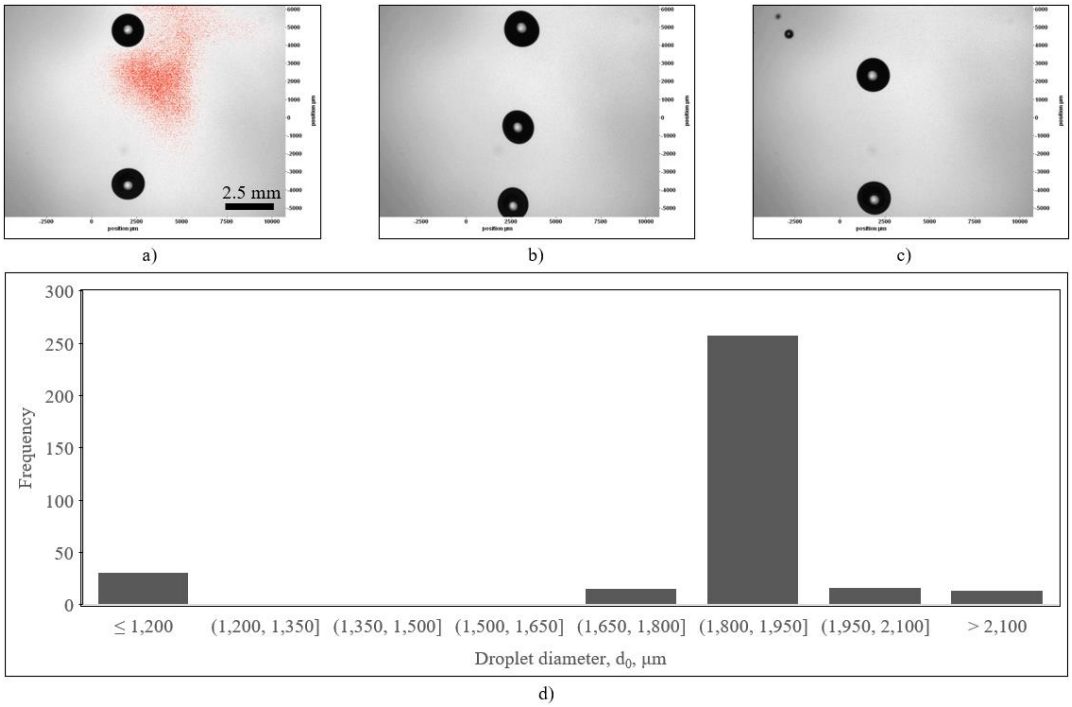

Figure A19. Images of water droplets from a 1.5 mm orifice with a head of 6.5 cm and an applied frequency of 250 Hz, presented in a), b), c). The histogram showing the droplet size distribution, presented in d).

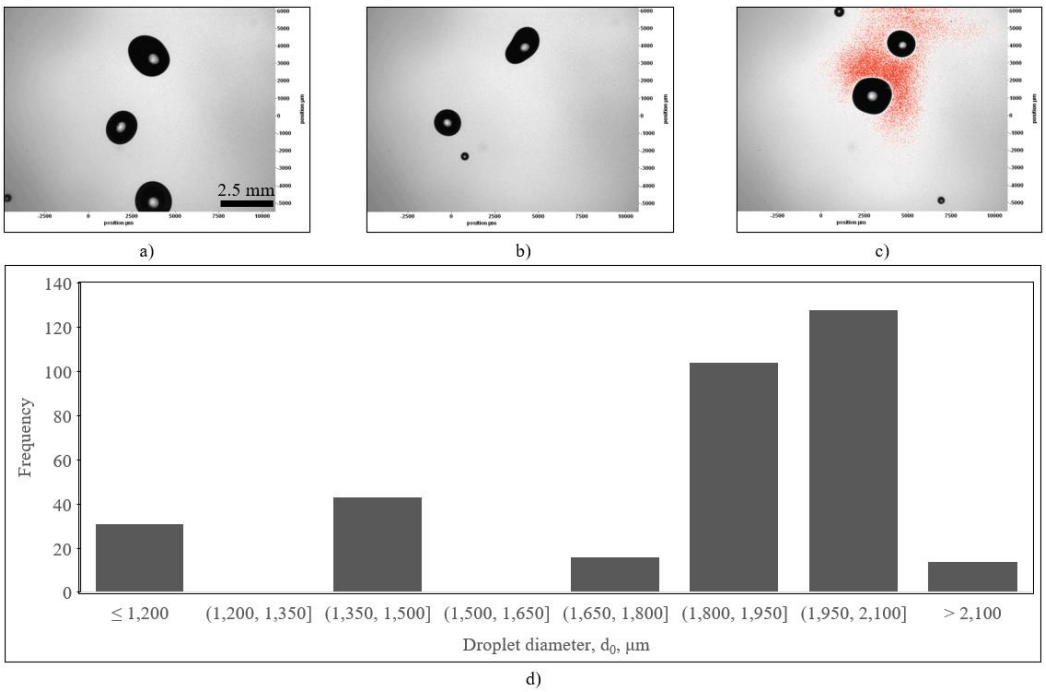

Figure A20. Images of water droplets from a 1.5 mm orifice with a head of 6.5 cm and without an applied frequency, presented in a), b), c). The histogram showing the droplet size distribution, presented in d).

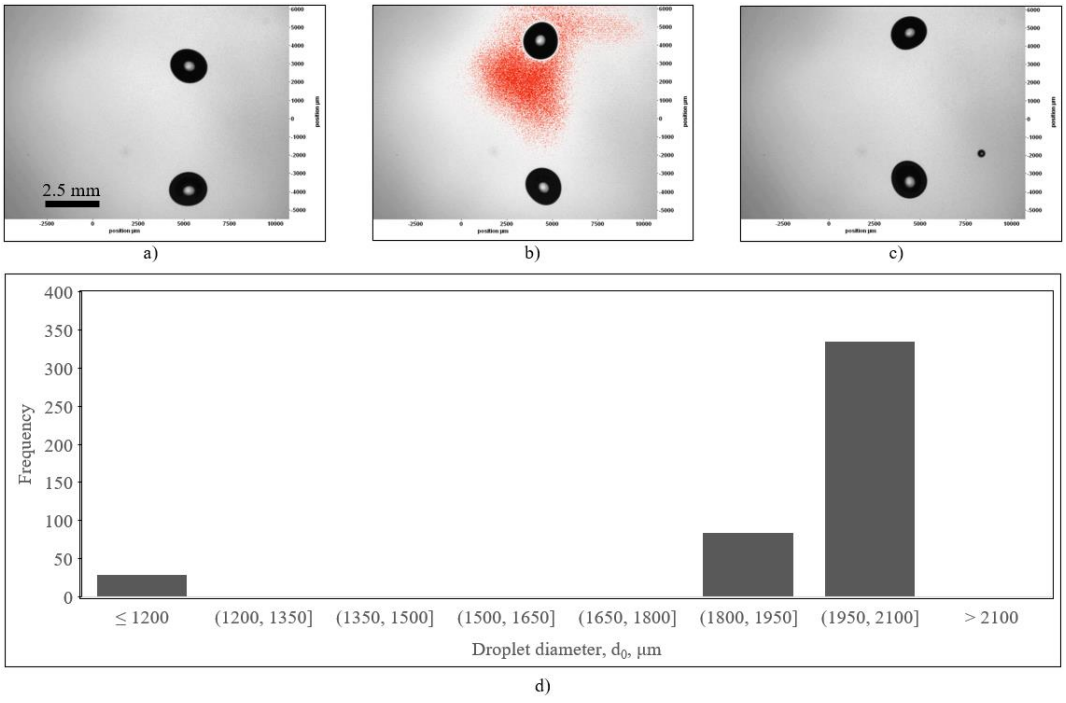

Figure A21. Images of water droplets from a 1.5 mm orifice with a head of 7.5 cm and an applied frequency of 250 Hz, presented in a), b), c). The histogram showing the droplet size distribution, presented in d).

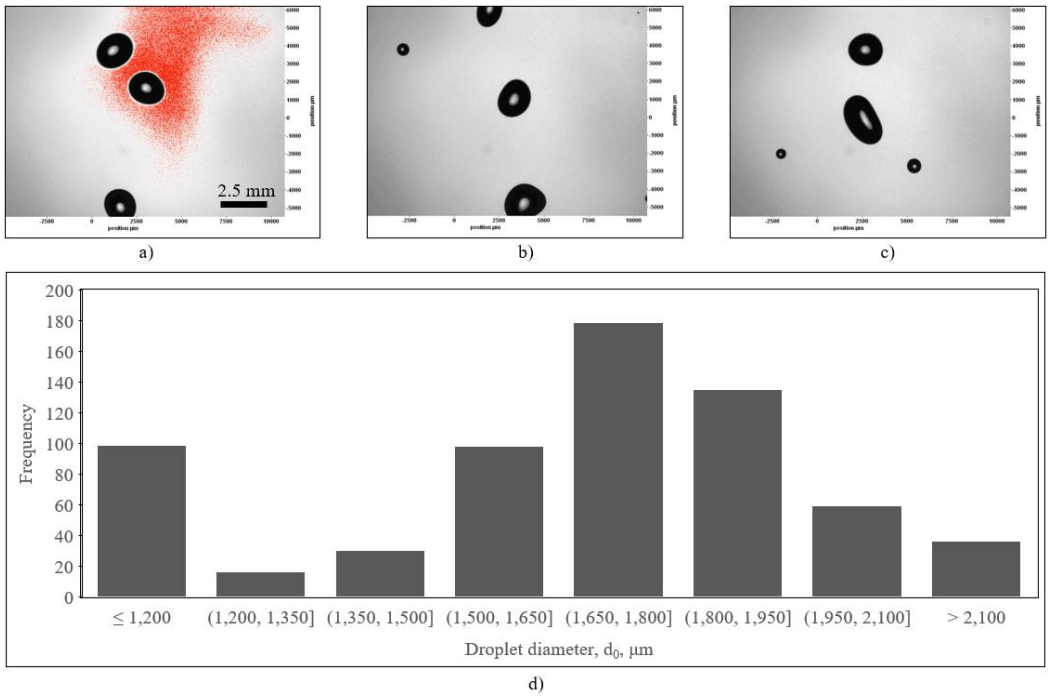

Figure A22. Images of water droplets from a 1.5 mm orifice with a head of 7.5 cm and without an applied frequency, presented in a), b), c). The histogram showing the droplet size distribution, presented in d).

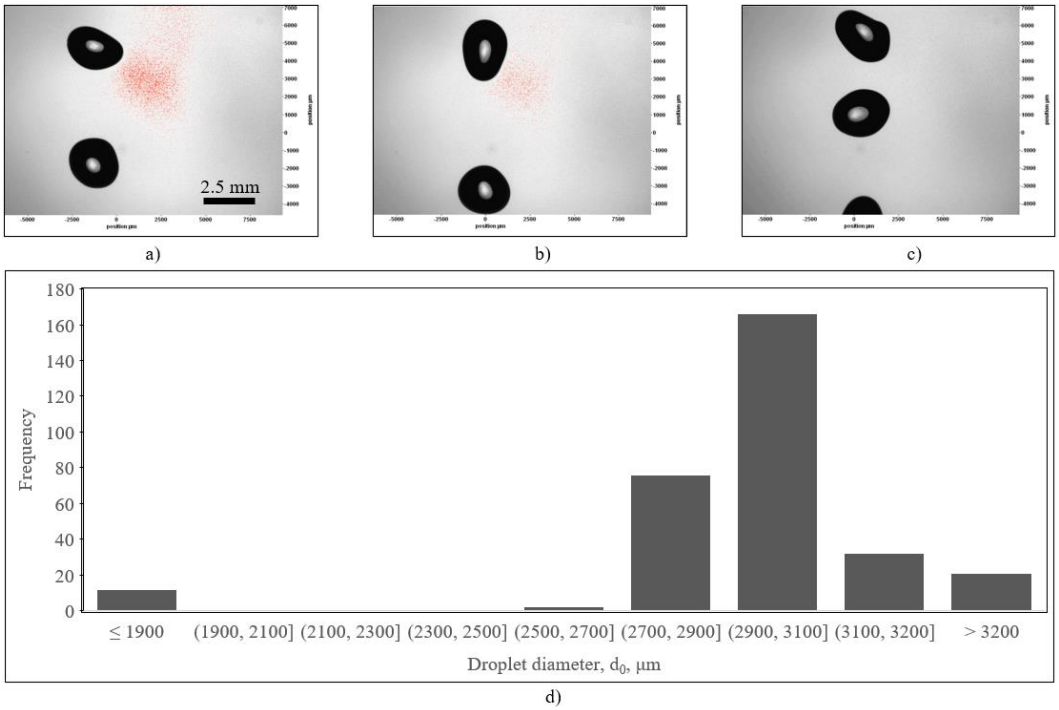

Figure A23. Images of water droplets from a 2 mm orifice with a head of 5.5 cm and an applied frequency of 200 Hz, presented in a), b), c). The histogram showing the droplet size distribution, presented in d).

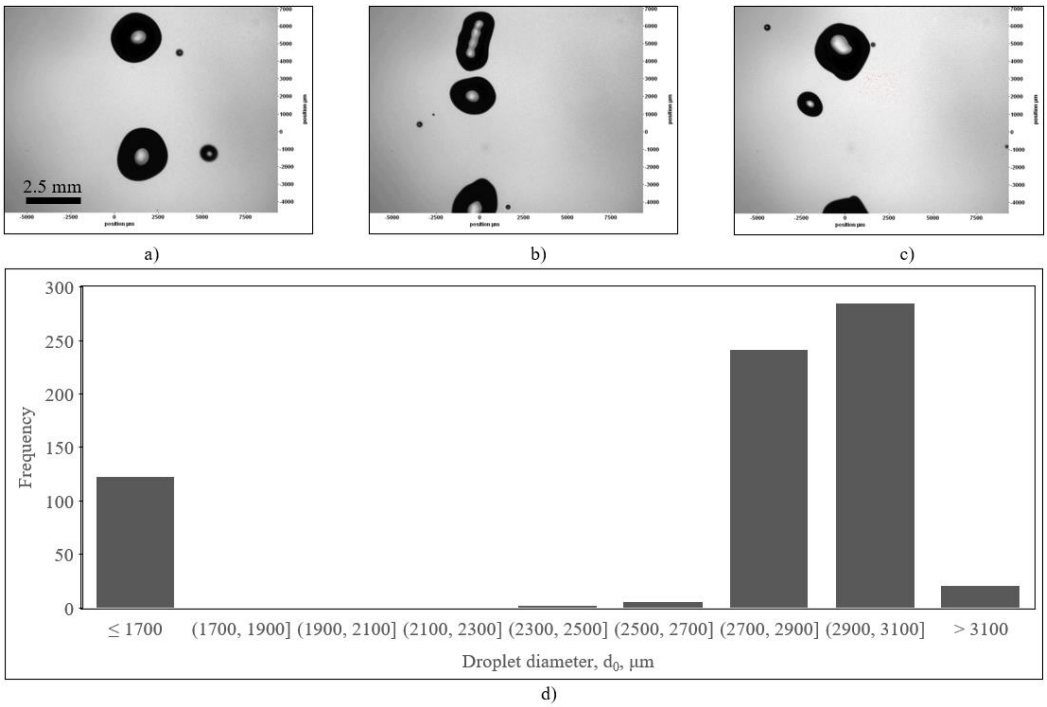

Figure A24. Images of water droplets from a 2 mm orifice with a head of 5.5 cm and without an applied frequency, presented in a), b), c). The histogram showing the droplet size distribution, presented in d).

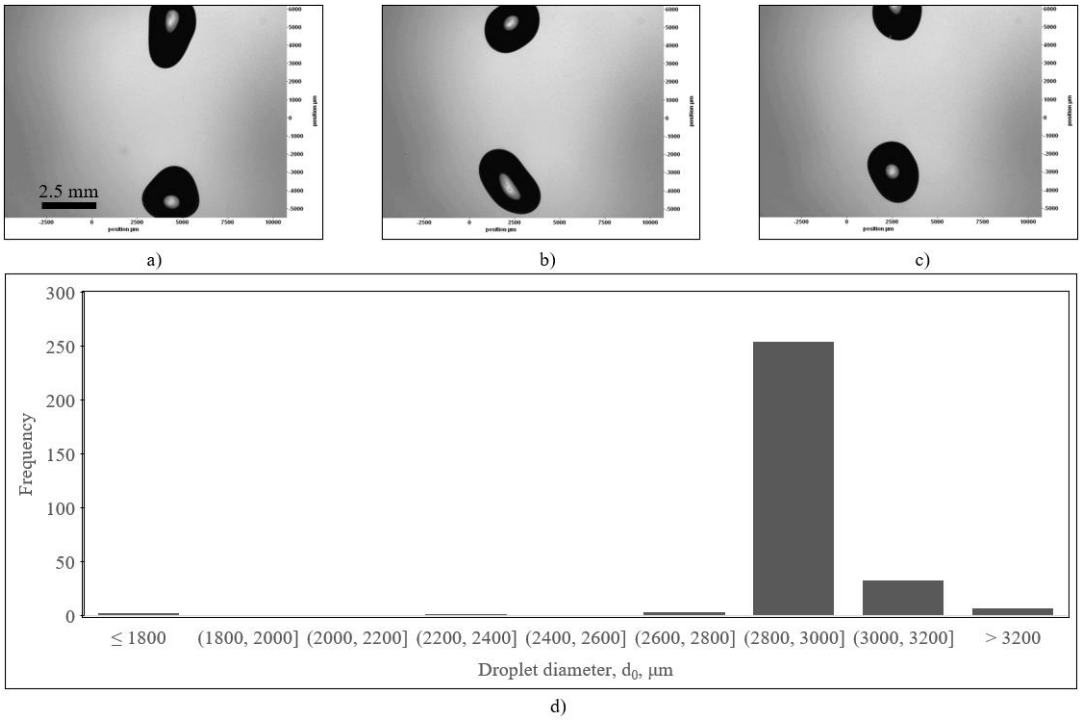

Figure A25. Images of water droplets from a 2 mm orifice with a head of 7.5 cm and an applied frequency of 200 Hz, presented in a), b), c). The histogram showing the droplet size distribution, presented in d).

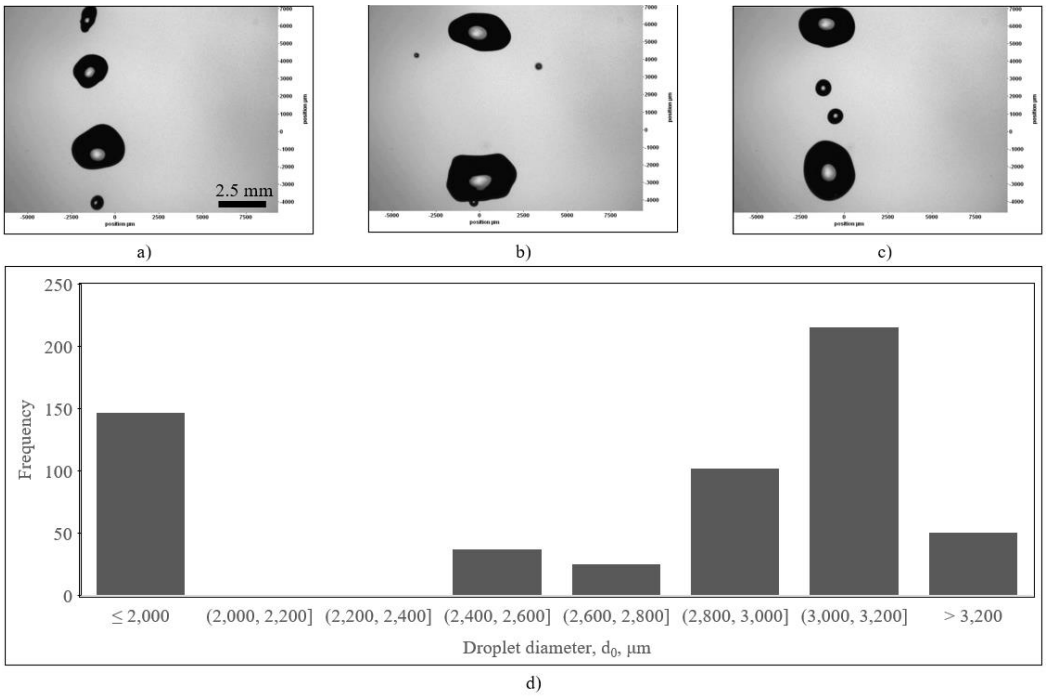

Figure A26. Images of water droplets from a 2 mm orifice with a head of 7.5 cm and without an applied frequency, presented in a), b), c). The histogram showing the droplet size distribution, presented in d).

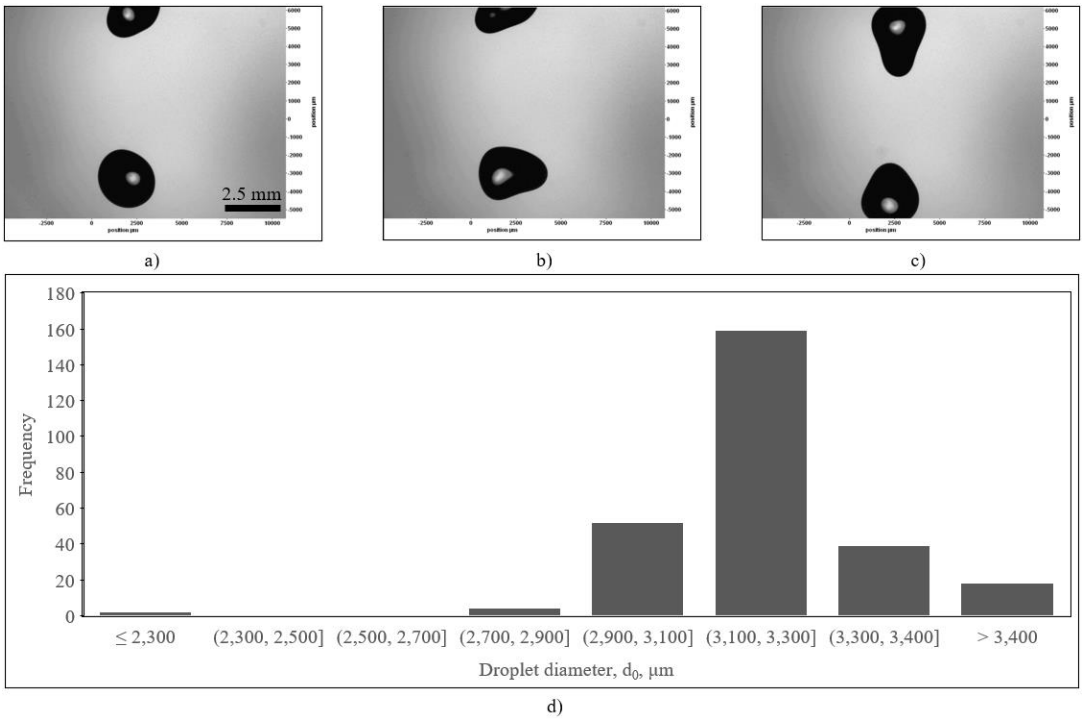

Figure A27. Images of water droplets from a 2 mm orifice with a head of 9.5 cm and an applied frequency of 200 Hz, presented in a), b), c). The histogram showing the droplet size distribution, presented in d).

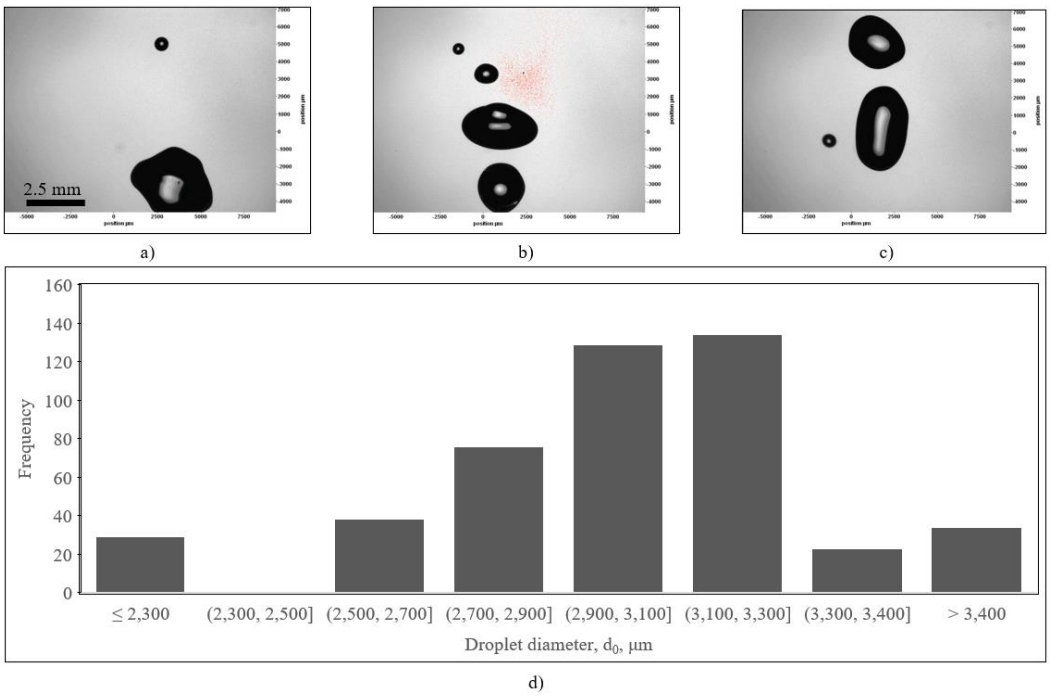

Figure A28. Images of water droplets from a 2 mm orifice with a head of 9.5 cm and without an applied frequency, presented in a), b), c). The histogram showing the droplet size distribution, presented in d).

A2 Experiments Using Ethylene Glycol, with Orifice Sizes of 0.07 – 2 mm

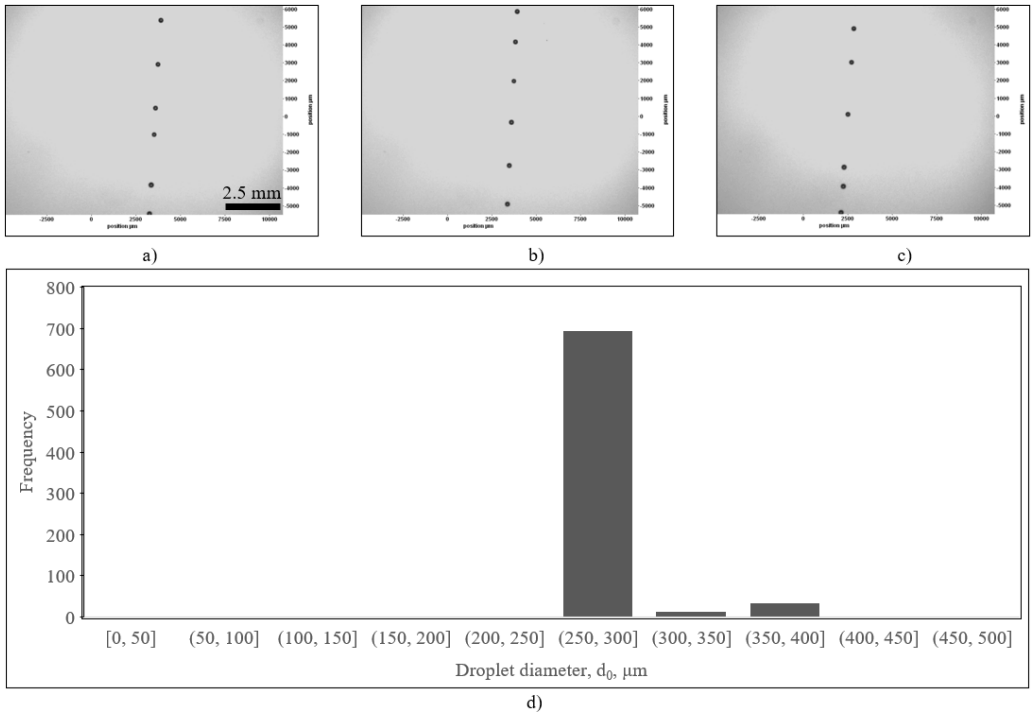

Figure A29. Images of ethylene glycol droplets from a 0.1 mm orifice with an applied frequency of 1400 Hz, presented in a), b), and c). The histogram showing the droplet size distribution, presented in d).

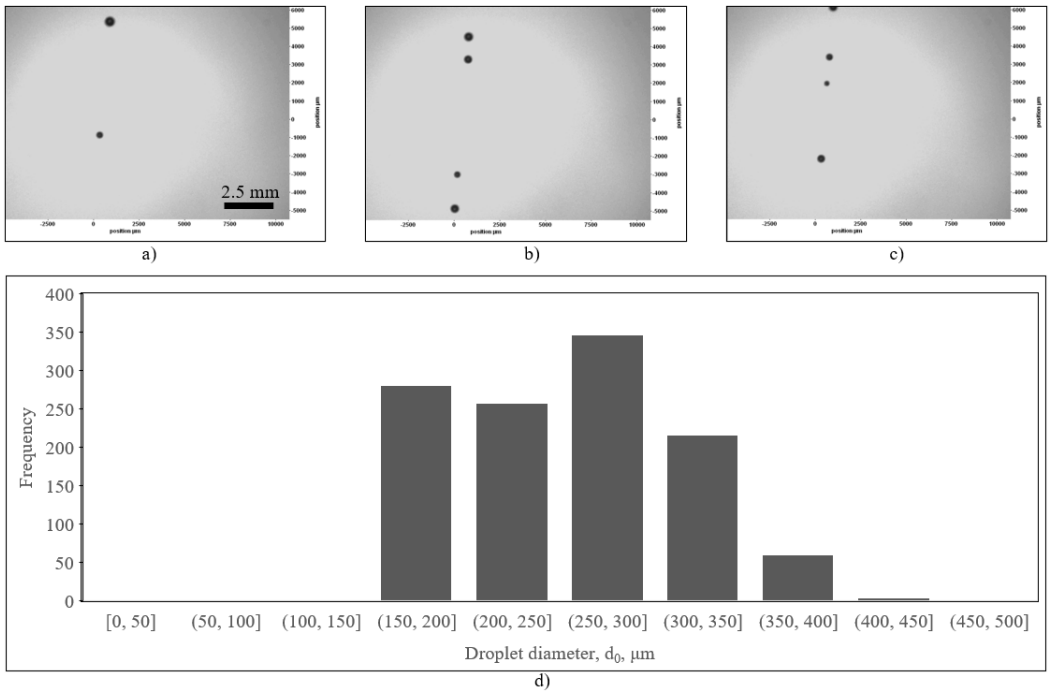

Figure A30. Images of ethylene glycol droplets from a 0.1 mm orifice without an applied frequency, presented in a), b), and c). The histogram showing the droplet size distribution, presented in d).

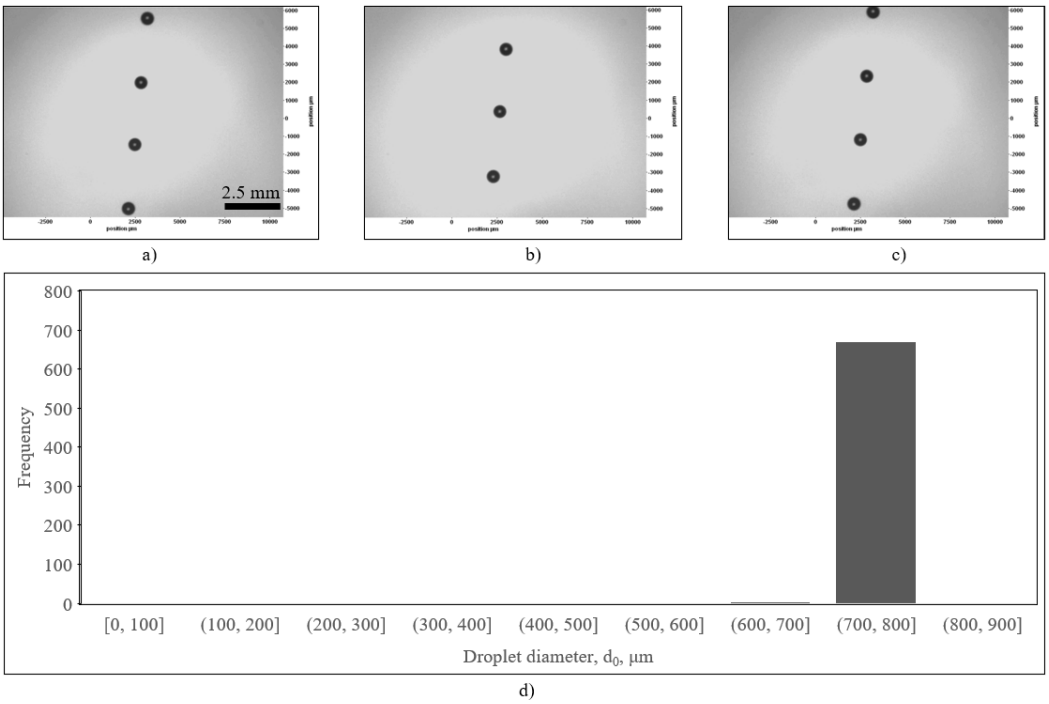

Figure A31. Images of ethylene glycol droplets from a 0.275 mm orifice with an applied frequency of 800 Hz, presented in a), b), and c). The histogram showing the droplet size distribution, presented in d).

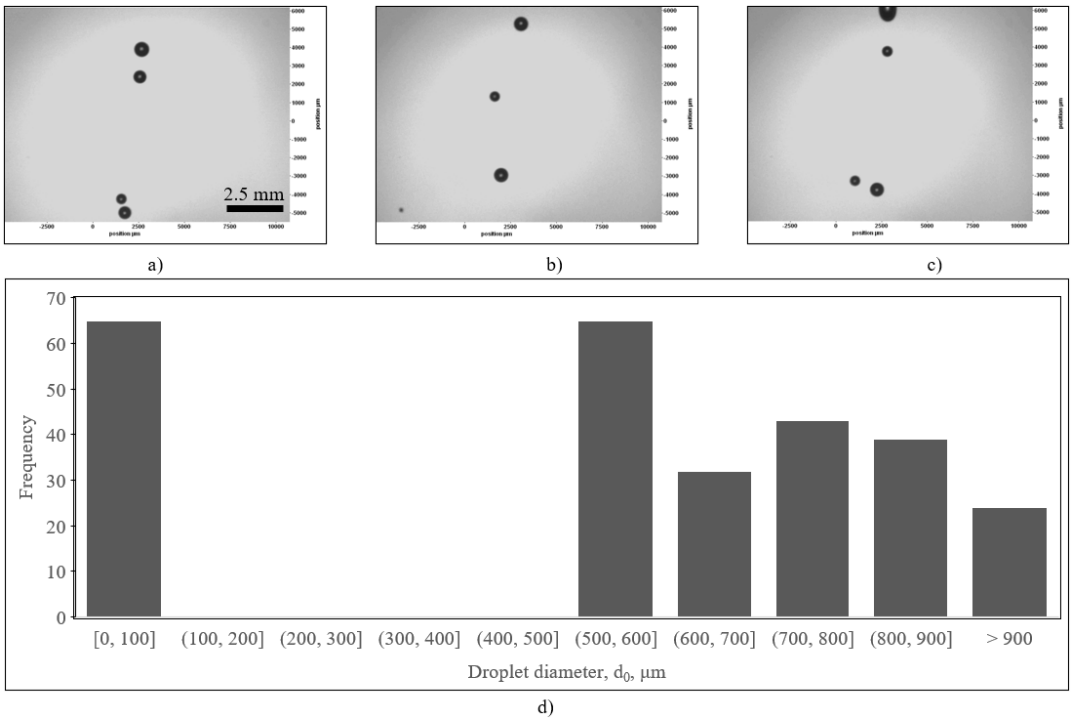

Figure A32. Images of ethylene glycol droplets from a 0.275 mm orifice without an applied frequency, presented in a), b), and c). The histogram showing the droplet size distribution, presented in d).

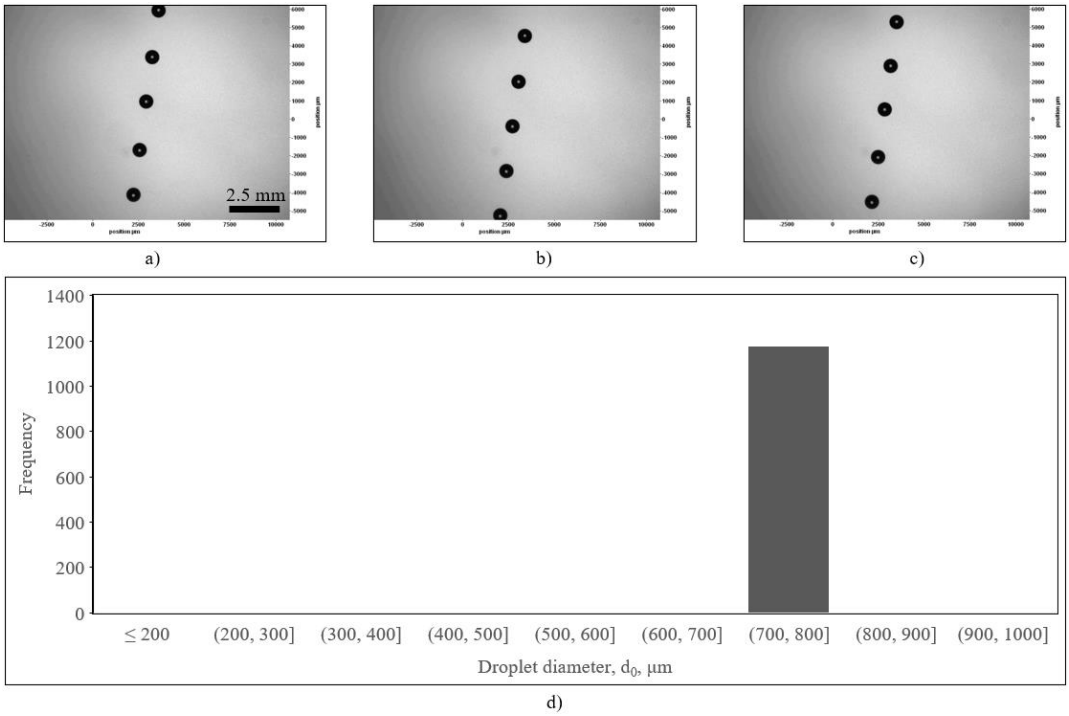

Figure A33. Images of ethylene glycol droplets from a 0.45 mm orifice with an applied frequency of 700 Hz, presented in a), b), and c). The histogram showing the droplet size distribution, presented in d).

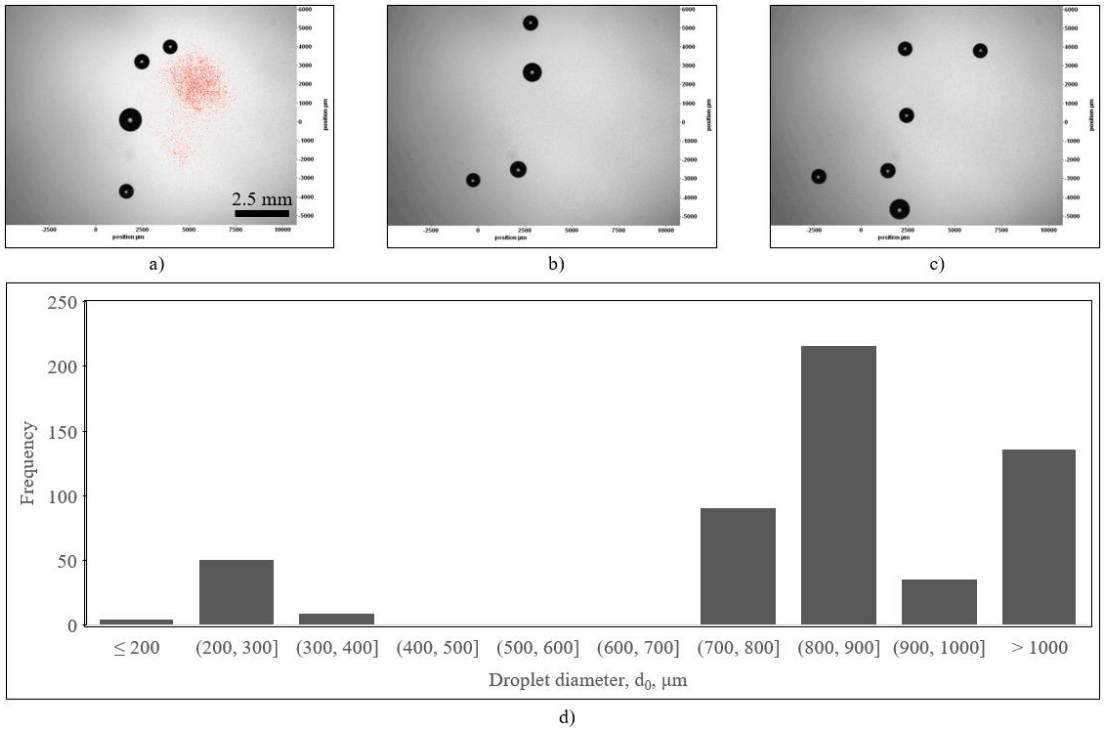

Figure A34. Images of ethylene glycol droplets from a 0.45 mm orifice without an applied frequency, presented in a), b), and c). The histogram showing the droplet size distribution, presented in d).

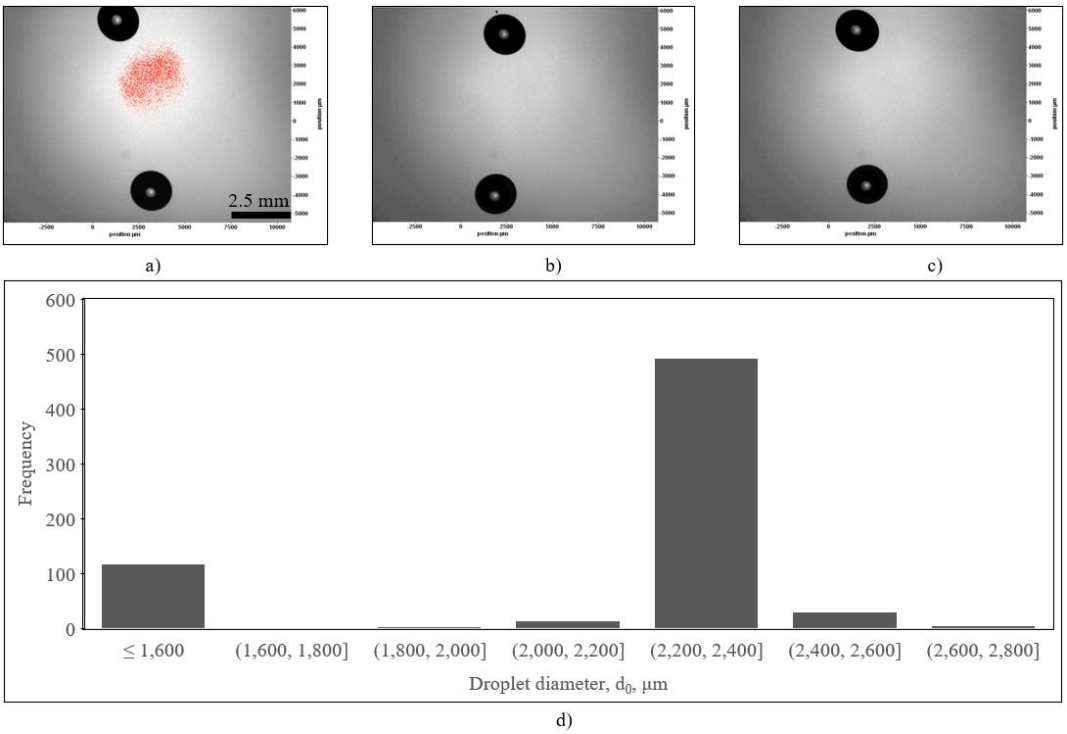

Figure A35. Images of ethylene glycol droplets from a 2 mm orifice with a head of 5.5 cm and an applied frequency of 200 Hz, presented in a), b), c). The histogram showing the droplet size distribution, presented in d).

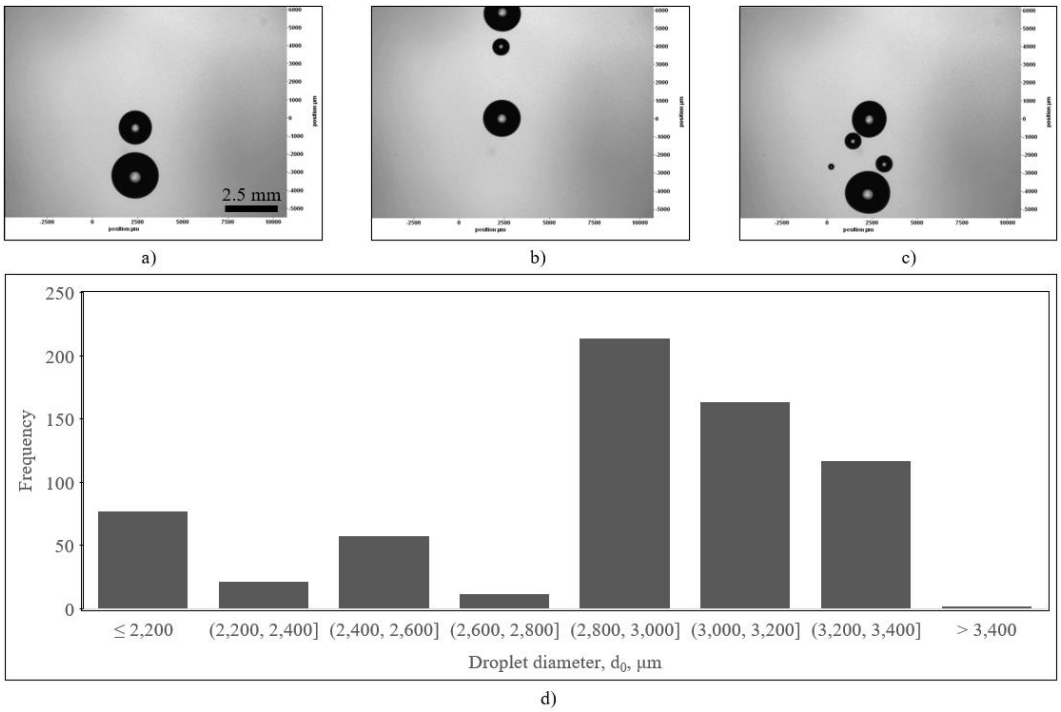

Figure A36. Images of ethylene glycol droplets from a 2 mm orifice with a head of 5.5 cm and without an applied frequency, presented in a), b), c). The histogram showing the droplet size distribution, presented in d).

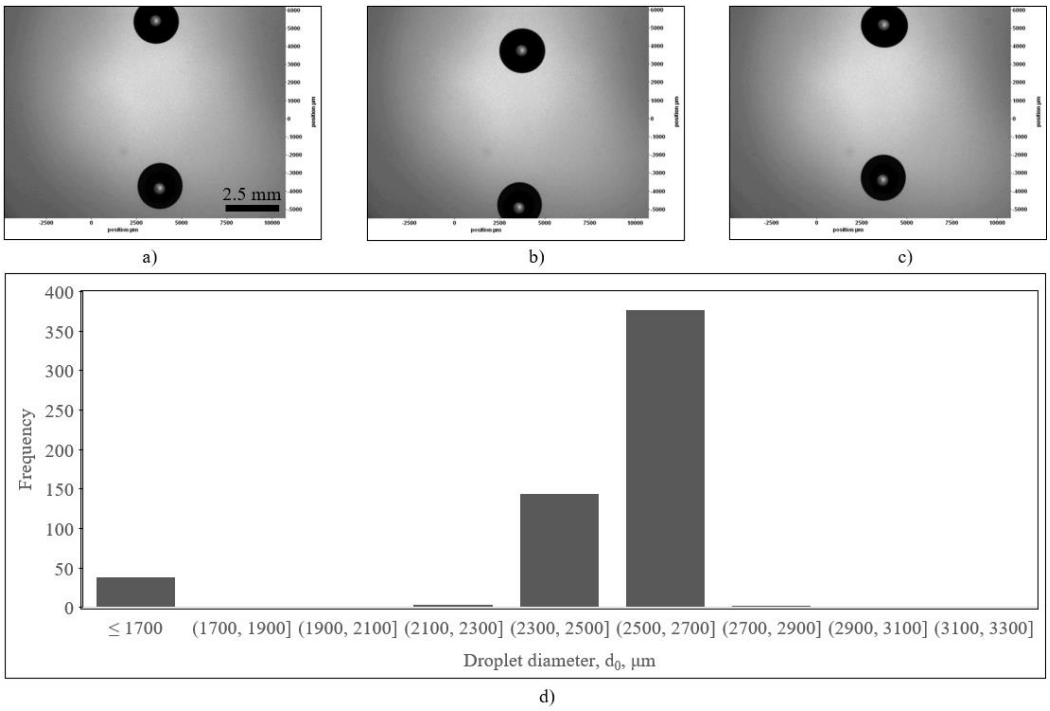

Figure A37. Images of ethylene glycol droplets from a 2 mm orifice with a head of 7.5 cm and an applied frequency of 200 Hz, presented in a), b), c). The histogram showing the droplet size distribution, presented in d).

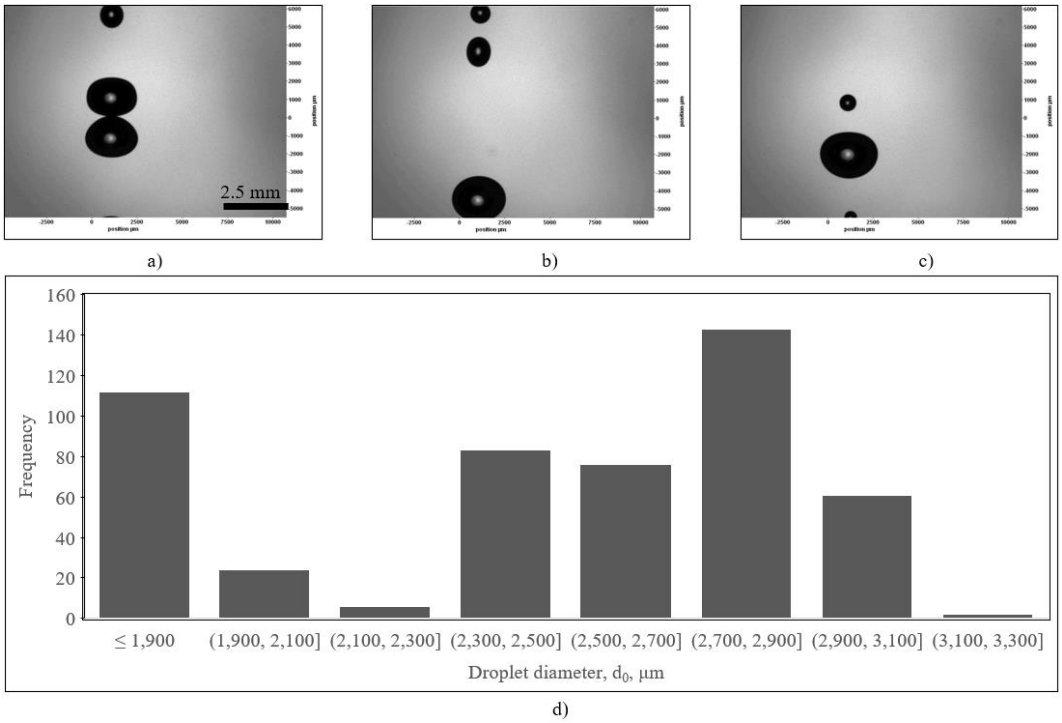

Figure A38. Images of ethylene glycol droplets from a 2 mm orifice with a head of 7.5 cm and without an applied frequency, presented in a), b), c). The histogram showing the droplet size distribution, presented in d).

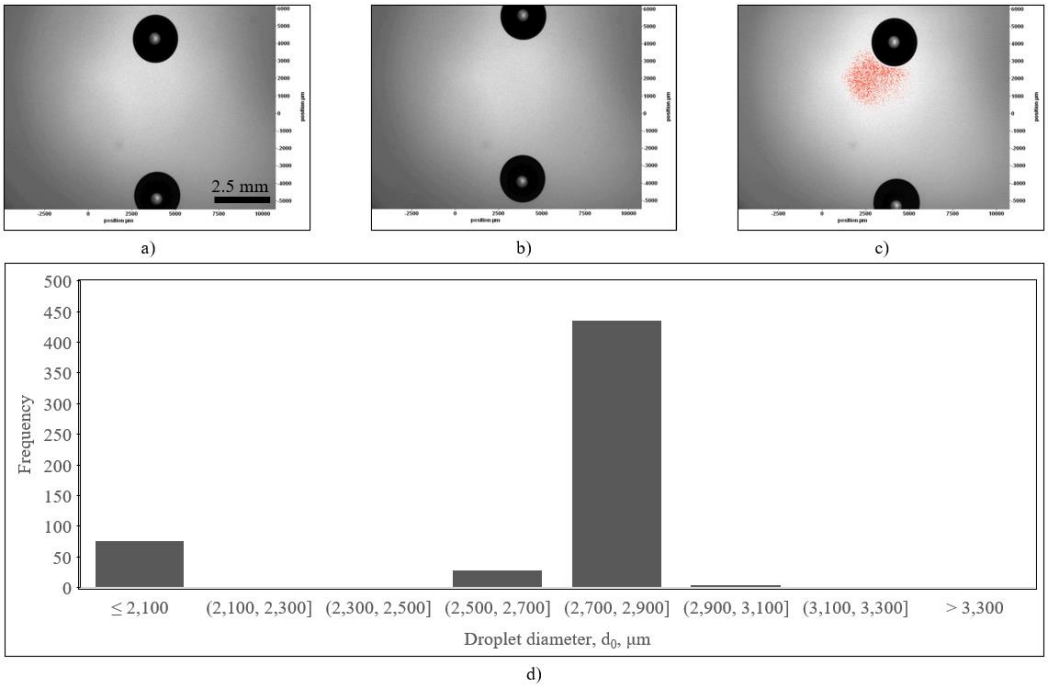

Figure A39. Images of ethylene glycol droplets from a 2 mm orifice with a head of 9.5 cm and an applied frequency of 200 Hz, presented in a), b), c). The histogram showing the droplet size distribution, presented in d).

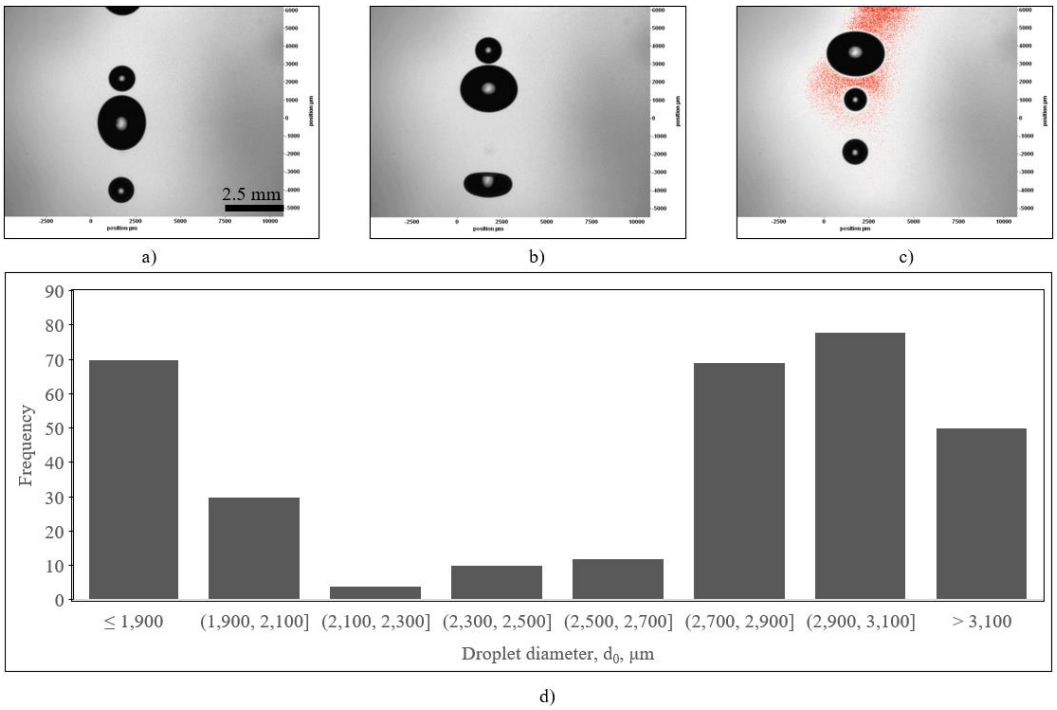

Figure A40. Images of ethylene glycol droplets from a 2 mm orifice with a head of 9.5 cm and without an applied frequency, presented in a), b), c). The histogram showing the droplet size distribution, presented in d).

A3 Experiments Using Tin, with Orifice Sizes of 0.35 and 0.45 mm

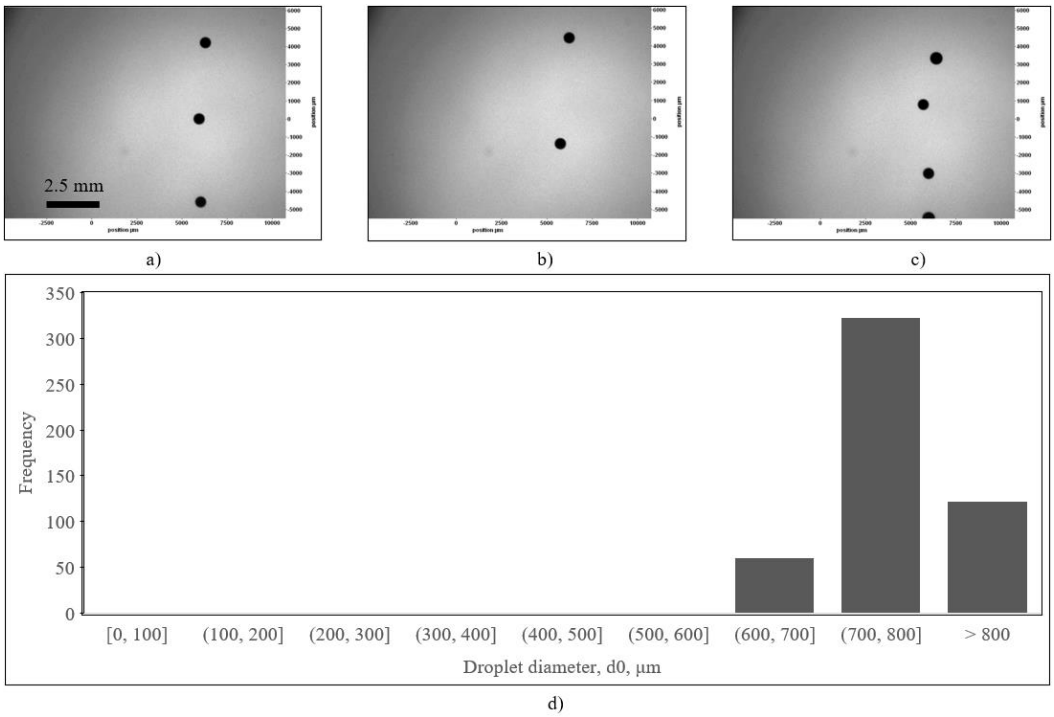

Figure A41. Images of tin droplets from a 0.35 mm orifice with an applied frequency of 1000 Hz, presented in a), b), and c). The histogram showing the droplet size distribution, presented in d).

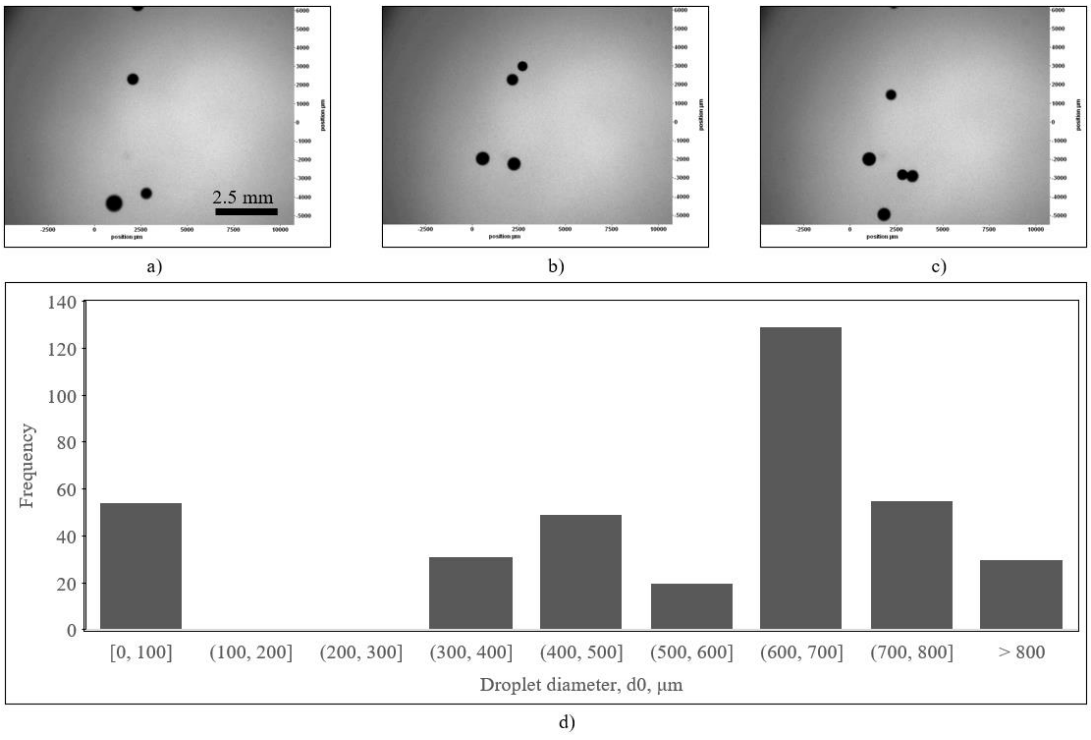

Figure A42. Images of tin droplets from a 0.35 mm orifice without an applied frequency, presented in a), b), and c). The histogram showing the droplet size distribution, presented in d).

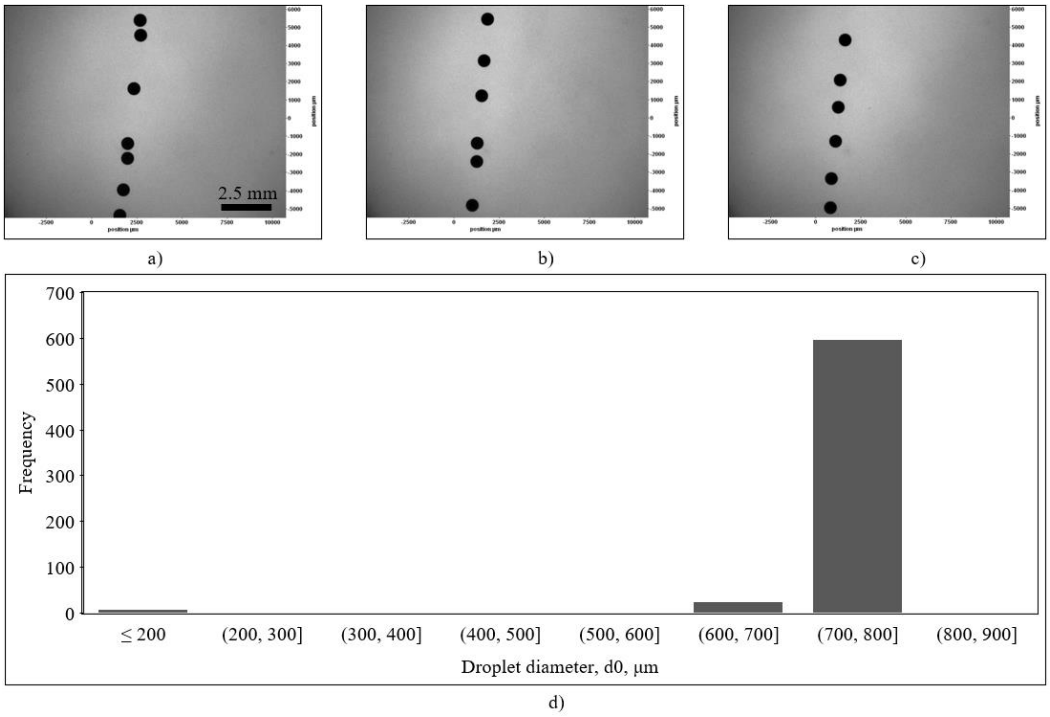

Figure A43. Images of tin droplets from a 0.45 mm orifice with an applied frequency of 900 Hz, presented in a), b), and c). The histogram showing the droplet size distribution, presented in d).

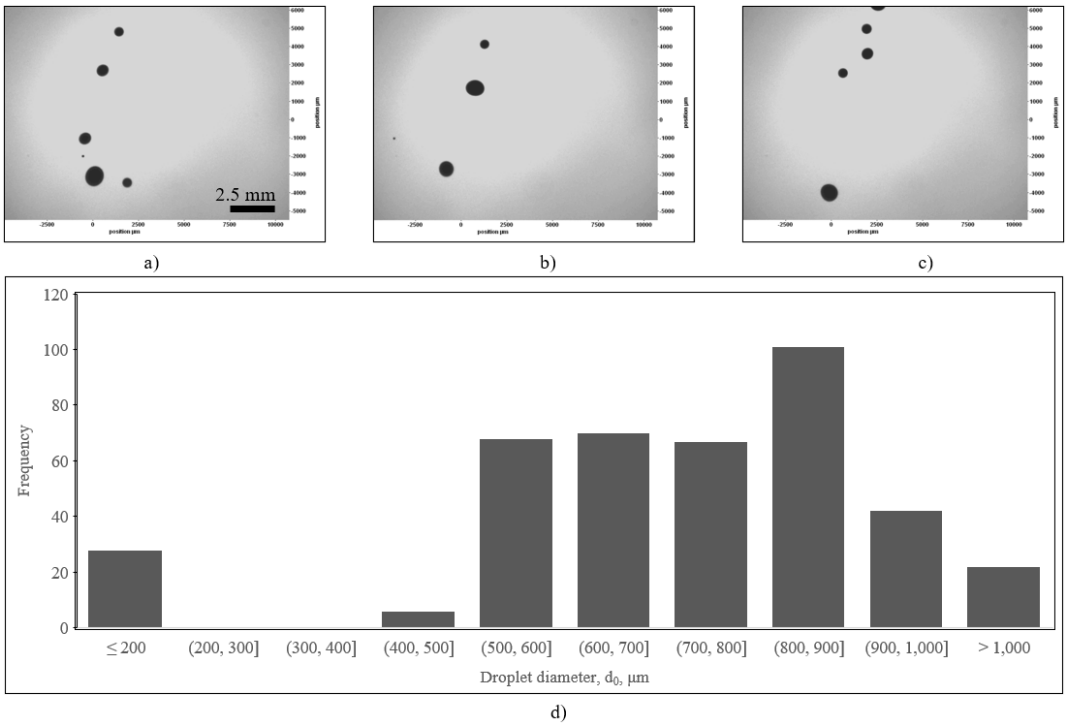

Figure A44. Images of tin droplets from a 0.45 mm orifice without an applied frequency, presented in a), b), and c). The histogram showing the droplet size distribution, presented in d).